8-18-2015

Modeling and Experimental Studies of Miniature Lithium Air Batteries and Alkaline Direct Ethanol Fuel Cells

Jing Huang
University of Connecticut - Storrs, jing.huang@engineer.uconn.edu

Modeling and Experimental Studies of Miniature Lithium Air Batteries and Alkaline Direct Ethanol Fuel Cells

Jing Huang, PhD

University of Connecticut, 2015

Batteries and fuel cells directly convert chemical energy to electricity through controlled electrochemical reactions. Batteries also serve as energy storage devices, while fuel cells rely on a continuous supply of fuel to maintain power output. In this dissertation, modeling and experimental studies on lithium air batteries and alkaline direct ethanol fuel cells are presented. Both technologies can be designed as small-scale electrochemical devices that are suitable for miniature electronics and energy systems. Innovative concepts are presented regarding miniaturization of both technologies, including detailed physical simulation. The lithium air (Li-air) battery is considered a promising candidate for next generation secondary battery technology because of its extremely high theoretical energy density. Its application, however, has been impeded by issues including electrode clogging, electrolyte degradation, low cycling efficiency, and safety concerns. A unique Li-air battery concept is proposed to enhance oxygen supply and alleviate electrode clogging. The proposed flow cell has a specific capacity of 15.5 times higher than that of a conventional Li-air cell. Based on the physical modeling, a multi-layer electrode structure is also proposed which helps to increase cell capacity by 105%. A comprehensive 2D physical model of the battery is developed at the cell-level. Through the deformed mesh technique, the change of electrolyte level in a Li-air coin cell during discharge is tracked. It is found that without considering this effect, a battery model may underestimate cell capacity by up to 22%. The model also includes an air chamber in the computation domain to account for solvent evaporation. For highly volatile solvent-based cells, the chamber size may affect the experimental results significantly. These findings provide direction for further enhancement of battery

performance and better design of experiments. Alkaline direct ethanol fuel cells (ADEFC) are considered as a replacement of direct methanol fuel cells. The alkaline environment improves reaction kinetics while ethanol is well regarded for wide availability and low toxicity. Through detailed modeling and experimental studies, it is shown that the costly anion exchange membrane in a conventional ADEFC can be replaced by a much less expensive porous separator without lowering overall cell performance.

Modeling and Experimental Studies of Miniature Lithium Air Batteries and Alkaline Direct Ethanol Fuel Cells

Jing Huang

B.S., Xi'an Jiaotong University, 1999
M.S., Xi'an Jiaotong University, 2002

A Dissertation
Submitted in Partial Fulfillment of the
Requirements for the Degree of

Doctor of Philosophy
at the
University of Connecticut

2015

2015

APPROVAL PAGE

Doctor of Philosophy Dissertation

Modeling and Experimental Studies of Miniature Lithium Air Batteries and Alkaline Direct Ethanol Fuel Cells

Presented by

Jing Huang, B.S., M.S.

Major Advisor 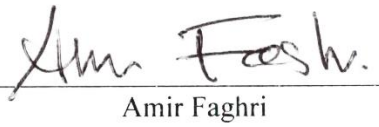
Amir Faghri

Associate Advisor 
Tai-Hsi Fan

Associate Advisor 
Tianfeng Lu

Associate Advisor 
William E. Mustain

Associate Advisor 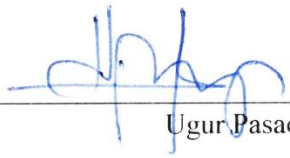
Ugur Pasaogullari

University of Connecticut
2015

Acknowledgements

In the past four and half years, I received countless help from my advisor, professors, lab-mates and family. I would like to express my deepest appreciation here.

First and foremost I want to thank my advisor Dr. Amir Faghri. It has been an honor to be able to work under his direction. His vision, encouragement, and patience have helped me to learn how to be a better researcher and present high quality works. Dr. Faghri always encourages me to think out of box, which I will keep in my mind forever.

I also want to express my thanks to my co-advisors, Dr. Fan, Dr. Lu, Dr. Mustain and Dr. Pasaogullari for their insightful advices during my PhD study.

During my stay in the heat transfer lab, I shared a lot of times with my lab mates. I would like to express my appreciation for helpful discussions with them.

Finally I would like to thank my parents for their consistent support and understanding.

Table of Contents

Table of Contents v

List of Tables xi

List of Figures xii

Chapter 1 A Critical Review of Modeling Studies on Li–O_2 and Li–Air Batteries: Challenges and Opportunities 1

1.1 Background 1

1.2 Development of continuum-scale physical models 4

1.2.1 Model formulation 4

1.2.2 Features of existing models 9

1.2.3 Cathode modeling 11

1.2.4 Anode modeling 22

1.2.5 Special features of continuum-scale models 24

1.3 Particle-scale and multi-scale models 33

1.4 Property data 34

1.4.1 Fundamentals 36

1.4.2 Summary of property data 37

1.4.3 Discussion 38

1.5 Unresolved issues and future opportunities 42

1.6 Concluding remarks 43

References 47

Tables 62

Figures 74

Chapter 2 Modeling study of a Li-O_2 battery with an active cathode 87

2.1 Introduction 87

2.2 Existing models 90

2.3 Model development 92

2.3.1 Governing equations 93

2.3.2 Boundary conditions 98

2.4 Results and discussion 101

2.4.1 Model validation 101

2.4.2 Distributions of pressure, velocity and temperature 102

2.4.3 Compare the capacity to conventional Li-O_2 battery 103

2.4.4 Discharge capacities of passive vs. active batteries 104

2.4.5 Distribution of lithium ion and oxygen 105

2.4.6 Effect of pressure difference between channels 106

2.4.7 Effect of exchange current density 107

2.4.8 Effect of porosity 107

2.5 Conclusions 109

References 111

Tables 116

Figures 117

Chapter 3 Capacity Enhancement of a Lithium Oxygen Flow Battery 132

3.1 Introduction 132

3.2 Background 134

3.3 Model development 137

3.3.1 Governing equations 138

3.3.2 Electrochemical Kinetics 144

3.3.3 Boundary and initial conditions 145

3.4 Results and discussion 147

3.4.1 Model validation 147

3.4.2 Parametric study 148

3.4.3 Energy consumption by electrolyte pump 153

3.4.4 Capacity enhancement using dual layer cathode 154

3.4.5 Capacity enhancement using alternating flow 155

3.5 Conclusion 156

References 160

Tables 166

Figures 169

Chapter 4 Analysis of Electrolyte Level Change in a Li–Air Battery 180

4.1 Introduction 180

4.2 Physical Model 183

4.2.1 Mass and charge transfer 184

4.2.2 Moving boundaries 189

4.2.3 Boundary conditions 191

4.2.4 Computational methodology 192

4.3 Results and discussion 193

4.3.1 Model validation 193

4.3.2 Tracking the electrolyte level 194

4.3.3 Effect of electrolyte level change 195

4.3.4 Effect of air chamber size 197

4.4 Conclusions 198

References 202

Tables 206

Figures 210

Chapter 5 Analysis of a Permselective Membrane-Free Alkaline Direct Ethanol Fuel Cell ... 222

5.1 Introduction 222

5.2 Physical Model 225

5.2.1 Governing equations 226

5.2.2 Boundary conditions 229

5.2.3 Electrochemical kinetics 231

5.2.4 Physical properties 232

5.3 Results and discussion 234

5.3.1 Effect of ethanol and potassium hydroxide concentration on the cell performance 234

5.3.2 Mass transport 235

5.3.3 Fuel utilization rate 238

5.3.4 Effect of separator thickness on cell performance 239

5.4 Conslusions 239

References 245

Tables 248

Figures 250

Chapter 6 Comparison of Alkaline Direct Ethanol Fuel Cells with and without Anion Exchange Membrane 264

6.1 Introduction 264

6.2 Experimental 268

6.2.1 Fuel Cell Assembly 268

6.2.2 Testing procedure 269

6.3 Results and discussion 270

6.3.1 General performance and comparison 270

6.3.2 Effect of temperature 271
6.3.3 Effect of reactants flow rate 271
6.3.4 Effect of reactant concentration 273
6.4 Conclusions 275
References 277
Tables 280
Figures 281
Chapter 7 Optimizing the Anode Structure of a Passive Tubular-Shaped Direct Methanol Fuel Cell to Operate with High Concentration Methanol 293
7.1 Introduction 293
7.2 Experimental 296
7.2.1 Structure of the passive tubular-shaped DMFC 296
7.2.2 Testing 297
7.3 Results and discussion 298
7.3.1 Effect of structure on performance 298
7.3.2 Effect of structure on fuel efficiency 302
7.3.3 Future improvement to operate with neat methanol 303
7.4 Conclusions 304
References 306
Figures 308

List of Tables

Table 1-1 Summary of governing equations for continuum-scale models for Li–O_2 batteries .. 62

Table 1-2 Features of continuum-scale physical models for Li–O_2 batteries 63

Table 1-3 Relationships between structural parameters with different pore structures for Li–O_2 battery cathode models 65

Table 1-4 Deposition layer voltage drop sub-model for Li–O_2 batteries 66

Table 1-5 Summary of commonly used electrolytes for Li–O_2 batteries 67

Table 1-6 Ionic conductivity of organic electrolytes for Li–O_2 batteries 68

Table 1-7 Salt diffusion coefficient and transference number of non-aqueous electrolytes for Li–O_2 batteries 69

Table 1-8 Oxygen related transport properties of non-aqueous electrolytes for Li–O_2 batteries 70

Table 1-9 Thermodynamic factor of non-aqueous electrolytes for Li–O_2 batteries 73

Table 2-1 Parameters used in the model. 116

Table 3-1 Summary of governing equations and boundary conditions 166

Table 3-2 Parameters used in the model 167

Table 4-1 Structural parameters of the Li–air coin cell 206

Table 4-2 Effective domains of each dependent variable and corresponding boundary and initial conditions 207

Table 4-3 Solvent/Electrolyte properties of the Li-air coin cell 208

Table 4-4 Parameters used in the simulation model of a Li-air coin cell 209

Table 5-1 Boundary conditions 248

Table 5-2 Simulation parameters 249

Table 6-1 Reported performance of ADLFCs with and without AEM 280

List of Figures

Figure 1-1 Structure and basic operation of a typical non-aqueous Li–O_2 cell. 74

Figure 1-2 Comparison of the discharge curves predicted by various models (Wang and Cho [27], Sahapatsombut et al. [17], Jung et al. [21], Li and Faghri [33]) to the experimental results of Read 2002 [34] at different discharge current densities: (a) 0.05 mA cm^{-2}, (b) 0.1 mA cm^{-2}, and (c) 0.2 mA cm^{-2}. 75

Figure 1-3 Distribution of Li_2O_2 volume fractions in the cathode at the end of discharge at various current densities [33]. 76

Figure 1-4 Simplified micro-scale structure of the electrode used in various models: (a) spherical particle, (c) spherical pore, (c) cylindrical particle, (d) cylindrical pore, and (e) flat pore. 77

Figure 1-5 Dependence of specific surface area on solid precipitation volume fraction predicted by various models and parameters. 78

Figure 1-6 Solid-phase volume and electrolyte level change in a Li–O_2 coin cell. 79

Figure 1-7 Distribution of ε_s with consideration of electrolyte level drop by (a) conceptual analysis and (b) model prediction [71]. 80

Figure 1-8 Illustration of (a) 1-D 2-phase model, (b) 2-D 2-phase model, (c) 3-phase model and (d) pseudo 3-phase model. 81

Figure 1-9 Configuration of an organic Li–O_2 flow battery (Li–O_2 battery with an active cathode). 82

Figure 1-10 Effect of ionic conductivity of electrolyte on the discharge capacity of a Li–O_2 flow cell [81]. 83

Figure 1-11 Comparison between t_+ and t_+^0 given by Capiglia et al. [107] and Nyman et al. [24]. The Electrolyte is $LiPF_6$ in EC:EMC. 84

Figure 1-12 Effect of oxygen solubility on cathode specific capacity predicted by Andrei et al. 2010 [47], Sahapatsombut et al. 2013 [17], and Huang and Faghri 2015 [81]. 85

Figure 1-13 Comparison of thermodynamics factors provided by Valøen and Reimers [94], Stewart and Newman [96], and Nyman et al. [24]. 86

Figure 2-1 A rechargeable Li-O_2 battery using an organic electrolyte. 117

Figure 2-2 a) An active Li-O_2 battery system, b) the interdigital channel at the cathode, and c) the cross-sectional view of interdigitatal channels. 118

Figure 2-3 Boundary conditions and computational domain of a Li-O_2 battery model considering convection. 119

Figure 2-4 Comparison between modeling results and experimental results [33] of cell voltage vs. specific capacities at various discharge current densities. 120

Figure 2-5 a) Pressure and b) velocity distributions in the computational domain (including the separator and electrode). The numbers in b) show magnitude of local velocity in unit of m s^{-1}. 121

Figure 2-6 Temperature distribution at the end of the discharge process. The discharge current is 1.5 mA cm^{-2}..... 122

Figure 2-7 Comparison of voltage vs. specific capacity curves between the Li-O_2 cells with passive and active cathode. The discharge current density is 0.2 mA cm^{-2}..... 123

Figure 2-8 Comparison of the discharge capacities of Li-O_2 cells with passive and active cathodes under different discharge current densities. 124

Figure 2-9 Distributions of volume fractions of Li_2O_2 in the electrode after the passive and the active Li-O_2 cells are fully discharged at different current densities. 125

Figure 2-10 Distributions of a) oxygen, b) lithium ions, and c) ORR rate at different times of the discharge process. 127

Figure 2-11 Distributions of a) Li_2O_2 volume fraction and b) relative permeability at different times of discharge process. 128

Figure 2-12 a) The cell voltage vs. specific capacity curves and b) distributions of Li_2O_2 volume fraction along the electrode of active Li-O_2 cells under different pressure differences ($0.3P_0$, $0.4P_0$ and $0.5P_0$) between adjacent channels. 129

Figure 2-13 Discharge capacities of cells with different exchange current densities. 130

Figure 2-14 a) The cell voltage vs. specific capacity curves and b) distribution of Li_2O_2 volume fractions of active Li-O_2 cells with gradient electrode porosities. 131

Figure 3-1 Structure of (a) an aprotic Li–O_2 flow battery and (b) the corresponding computation domain 169

Figure 3-2 Comparison of cell voltage vs. specific capacity between the simulation results and experimental data at different discharge current density 170

Figure 3-3 Discharge curve of the Li–O_2 flow cell at different discharge current densities and comparison of cathode specific capacity and specific energy 171

Figure 3-4 Distribution of Li_2O_2 volume fraction, $\varepsilon_{Li_2O_2}$, at the end of discharge with discharge current density of (a) 0.2 mA cm^{-2}, and (b) 1.5 mA cm^{-2} 172

Figure 3-5 Effect of ionic conductivity of electrolyte in electrolyte on cell performance 173

Figure 3-6 Distribution of Li_2O_2 volume fraction and electrolyte potential (*y*–direction averaged) with different conductivity of electrolyte 174

Figure 3-7 Effects of (a) oxygen diffusion coefficient, D_{O_2}, and (b) oxygen solubility, $c_{O_2,sat}$, on cathode specific capacity 175

Figure 3-8 Effect of cathode thickness on cathode specific capacity 176

Figure 3-9 Effects of pressure difference on the increase of energy output by the Li–O_2 flow cell and the percentage of energy consumed by the electrolyte pump 177

Figure 3-10 Comparison of cathode specific capacity between single layer and dual layer (a) conventional Li–O_2 cell, and (b) Li–O_2 flow cell 178

Figure 3-11 Comparison of cell voltage vs. cathode specific capacity between non–alternating and alternating flow at discharge current density of 0.2 mA cm^{-2} 179

Figure 4-1 Structure of a Li-air coin cell. 210

Figure 4-2 Computational domain and boundaries of the Li-air coin cell. 211

Figure 4-3 Boundary movement and mesh deformation of the Li-air coin cell. 212

Figure 4-4 Comparison of predicted battery discharge curves at various current densities with experimental results from Read [26]. 213

Figure 4-5 Variation of electrolyte surface and anode/spring interface position with time for a Li-air coin cell using (a) DMF and (b) TEGDME as electrolyte solvent. 214

Figure 4-6 Velocities of electrolyte surface caused by solvent evaporation (V_{1e}) and solid volume change (V_{1v}) for a Li-air coin cell using (a) DMF and (b) TEGDME as electrolyte solvent. 215

Figure 4-7 Variation of solvent vapor concentration with time at the cell opening and at the air chamber wall (DMF, R_o = 0.5 mm, R_{ac} = 10 cm). 216

Figure 4-8 Discharge curves with and without consideration of electrolyte level change for a Li-air coin cell using (a) DMF and (b) TEGDME as electrolyte solvent. 217

Figure 4-9 Reaction rate distribution at different states of discharge. 218
Figure 4-10 Li_2O_2 deposition on the cathode solid phase surface (a) with constant electrolyte level and (b) with electrolyte level drop. 219
Figure 4-11 Distribution of Li_2O_2 deposition volume fraction, ε_s, with and without consideration of electrolyte level drop. 220
Figure 4-12 Discharge curve with various air chamber radii and DMF as electrolyte solvent. 221
Figure 5-1 Structure of a PMF-ADEFC 250
Figure 5-2 Possible scenarios of electrolyte potential and electrolyte concentration distribution at the reservoir-ADL boundary 251
Figure 5-3 Comparison of the predictions by this study and and the experimental results of [2] ($C_{E,res}$ = 2.4 M, $C_{KOH,res}$ = 1 M, Ambient Air, 313 K) 252
Figure 5-4 Influence of ethanol concentration on performance 253
Figure 5-5 Influence of KOH concentration on polarization 254
Figure 5-6 Overpotential breakdown 255
Figure 5-7 Distribution of ethanol concentration for various cell voltages 256
Figure 5-8 Distribution of oxygen concentration for various cell voltages 257
Figure 5-9 Distribution of normalized (a) oxidation reaction rate in the ACL and (b) reduction reaction rate in the CCL 258
Figure 5-10 Distribution of electrolyte potential 259
Figure 5-11 Distribution of KOH concentration 260
Figure 5-12 Diffusion and migration molar flux of (a) K^+ and (b) OH^- ions under various voltages 261

Figure 5-13 Change of fuel utilization with different cell voltage 262
Figure 5-14 Influence of separator thickness 263
Figure 6-1 Structure of an AEM-free ADEFC 281
Figure 6-2 ADEFCs that use anion exchange membrane as electrolyte (left, Cell #1) and non-woven fabric as separator (right, Cell #2) 282
Figure 6-3 Comparison between three fuel cells that using identical anode and cathode electrodes but different separators or anion exchange membrane 283
Figure 6-4 iR-corrected anode and cathode potential and overpotential 284
Figure 6-5 Influence of temperature on the cell performance (Cell #2) 285
Figure 6-6 Influence of cathode flow rate on (a) Cell #1, (b) Cell #2, and (c) Cell #3 287
Figure 6-7 Influence of anode flow rate on (a) Cell #1, (b) Cell #2, and (c) Cell #3 289
Figure 6-8 Influence of the ethanol concentration on (a) Cell #1, (b) Cell #2 290
Figure 6-9 Influence of KOH concentration on (a) Cell #1, (b) Cell #2 291
Figure 6-10 Influence of oxygen humidity (cell #1) 292
Figure 7-1 Different anode structures tested 308
Figure 7-2 (a) Power density and (b) polarization curves for different concentrations of methanol using structure S4 309
Figure 7-3 (a) Power density and (b) polarization curves for different anode side structures with a 15 M methanol solution 310
Figure 7-4 Peak power density versus methanol solution concentration for different anode structures 311
Figure 7-5 Maximum current density versus methanol solution concentration 312
Figure 7-6 Maximum power density versus anode structure 313

Figure 7-7 Maximum temperature rise with different methanol concentrations and structures 314
Figure 7-8 Fuel efficiency versus methanol solution concentration 315
Figure 7-9 Constant voltage discharge with the same strucutre under different methanol concentrations 316
Figure 7-10 Fuel efficiency versus anode structure 317
Figure 7-11 Electricity generated by 2 ml methanol solution at 0.35 V 318

Chapter 1 A Critical Review of Modeling Studies on Li–O_2 and Li–Air Batteries: Challenges and Opportunities

A comprehensive review of the state-of-the-art modeling studies on lithium oxygen (Li–O_2) and lithium air (Li–Air) batteries is presented. As a promising device for the next generation of energy storage in portable electronics and electric vehicles, the Li–O_2 battery own the merits of rechargeability and high specific energy. To bring this technology from laboratory concept to real products, there are a number of shortcomings to be addressed. The multi-scale, multi-physics phenomena in a Li–O_2 battery encompasses a wide range of scientific disciplines, including electrochemistry, mass transport, multiphase transport, and material science. Modeling study provides a powerful tool to understand the charge-species transport phenomena inside a battery that cannot be captured by experimentation. It offers insight to optimize battery design and fabrication. Continuum-scale models will be the focus of this review since they are the most commonly studied. Although the same modeling framework was used among most of these studies, different sub-models were employed to describe electrode structure change. These sub-models are presented and compared. Recent developments and opportunities for future improvement and advancement are also discussed. Finally, a detailed summary of property data relevant to Li–O_2 batteries is provided in response to their critical role in modeling studies.

1.1 Background

Rechargeable batteries store and release electric energy through electrochemical reactions. Good batteries should have high energy density, high power density, long cycleability, and low production cost. Translated to electric vehicles, this means long driving range, fast acceleration, long life, and low price. In addition to electric vehicles, rechargeable batteries are also needed to power portable electronic devices and to serve as grid-level energy storage to accommodate the

fluctuation of renewable energy. In contrast to the rapid development in electronic and renewable energy technologies, rechargeable batteries have made made relatively slow progress, and have therefore become the bottleneck for many applications [1].

Lithium oxygen ($Li–O_2$) and lithium air (Li–Air) batteries use metallic lithium as the anode and an oxygen breathing cathode. The primary $Li–O_2$ battery was invented by Lockheed in the 1970s [2] but was not considered feasible due to safety and reliability issues. In 1996, Abraham and Jiang [3] at EIC Laboratories (Norwood, MA) found that $Li–O_2$ batteries using organic electrolyte were rechargeable, which reignited the interests in this type of battery. In the last several years, the $Li–O_2$ battery has attracted a rapid growth of research attention due to its reputation for high specific energy compared to the intercalated electrodes used in lithium ion (Li–ion) batteries. Figure 1-1 illustrates the structure and operating principles of a $Li–O_2$ battery consisting of a lithium foil anode, separator, and an oxygen cathode. The separator and cathode are porous and soaked in an ionic conductive solution, usually a lithium salt dissolved in an organic solvent, ionic fluid, or water. Depending on the type of electrolyte, $Li–O_2$ batteries are usually categorized into four different types: non-aqueous, aqueous, hybrid, or solid-state. During discharge, lithium is oxidized at the anode, as shown in eq. (1). The lithium ions enter the electrolyte and move to the cathode. Oxygen diffuses into the electrolyte through openings in the battery casing at the cathode side. The porous cathode is filled with electrolyte, and oxygen reduction reaction (ORR) takes place. The major product of ORR in non-aqueous $Li–O_2$ battery is Li_2O_2, as indicated by experimental studies. The half reactions are:

Anode: $2\ Li \rightarrow 2\ Li^+ + 2\ e^-$ (1)

Cathode (non-aqueous): $2\ Li^+ + O_2 + 2\ e^- \rightarrow 2\ Li_2O_2$ (2)

During the charging process, the above reactions are reversed and oxygen evolution occurs in the cathode. If the oxygen is provided from ambient air, the battery is called a lithium air battery. Because both Li–O_2 and Li–Air batteries use oxygen as the oxidizer, in the following discussion, we refer to them all as Li–O_2 batteries, unless otherwise specified.

The increasing demands for high energy density, high power density batteries have sparked vigorous studies both in experiment and modeling of Li–O_2 batteries. There have been many review articles that summarize experimental studies from different perspectives, such as electrolyte [4], anode material [5], cathode materials [6,7], energy density analysis [8], applications [9], etc. In contrast, modeling studies on Li–O_2 batteries are just now gaining popularity and attention.

Modeling study is an important tool to improve Li–O_2 battery technology in two key ways. First, it provides an in-depth explanation of the mass and charge transport processes and their interaction with the electrochemical reactions. Based on these principles, viable ways to further optimize electrode and battery structures can be achieved. Secondly, computational simulations are time-saving and more economical than experimental studies; thus it is useful to optimize cell design and operation parameters.

Modeling studies on Li–O_2 batteries are still in the development stage. Most of them are based on continuum-scale models for non-aqueous Li–O_2 batteries. Although the framework for continuum-scale battery modeling is well established, there are still a number of issues that should be addressed because of the novelty and uniqueness of Li–O_2 batteries. Different methodologies are used to solve these issues. This section will summarize these efforts and carry out a thorough comparison.

1.2 Development of continuum-scale physical models

In this section, the essential governing equations for a continuum-scale model based on a porous electrode and concentrated electrolyte theory are presented, followed by a table summarizing various features of existing models for easy comparison.

1.2.1 Model formulation

Continuum-scale models treat the electrode as a homogeneous medium consisting of several phases while neglecting the detailed pore structures. They are widely used for the modeling of various electrochemical systems, including fuel cells, Li–ion batteries, and flow batteries. In these models, at least two phases exist, the solid (carbon, Li_2O_2) phase and the liquid (electrolyte) phase [10]. Electrochemical reactions take place at the inter-phase surface. The driving force is the deviation of the potential difference between the two phases from its theoretical value. Electrons generated from the electrochemical reactions are transported in the solid phase and transport of ions, solvent, and oxygen occur in the electrolyte phase.. This framework is well-established based on porous electrode and concentrated solution theory [11]. A brief derivation will be given below and the essential governing equations for a Li–O_2 battery model are summarized in Table 1-1. A more rigorous derivation of these equations can be found in [11–13]. The computation domain of most modeling studies usually include the separator and cathode, as shown in Figure 1-1.

Conservation of all species in the electrolyte can be expressed as [14]:

$$\frac{\partial\left(\varepsilon c_i\right)}{\partial t} = -\nabla \cdot \boldsymbol{N}_i + r_i \tag{3}$$

where c_i is molarity of specie i, ε is porosity, $\boldsymbol{N}_i$ is the molar flux of specie i, and r_i is the species generation rate due to reactions. The number of species equations varies for different models. Some models only consider one species [15,16], while most models include Li^+, and oxygen [17–22]. If

side reactions are included [23], there are additional species to be considered such as O_2^-, CO_3^{2-}, and CO_2.

Three mechanisms of transport for the charged species (such as Li^+) are normally considered, including diffusion, migration, and convection, the driving force of which are concentration gradient, electric field, and electrolyte bulk velocity, respectively. According to the concentrated solution theory [11], the molar flux in electrolyte can be expressed as:

$$\boldsymbol{N}_{\mathrm{Li}} = -D_{\mathrm{e}}^{eff}\nabla c_{\mathrm{Li}} + \frac{\boldsymbol{i}_2 t_+^0}{F} + \boldsymbol{u}_0 c_{\mathrm{Li}} \tag{4}$$

where D_{e}^{eff} is the effective diffusion coefficient of the salt, t_+^0 is the transference number of the lithium ion with respect to the solvent velocity, F is the Faraday constant, and $\boldsymbol{i}_2$ is the current density in electrolyte. It should be noted $\boldsymbol{u_0}$ is the solvent velocity. In most analyses, the convection term is dropped since the electrolyte is assumed to be stagnant.

The current density in the binary electrolyte, $\boldsymbol{i}_2$, can be expressed as:

$$\boldsymbol{i}_2 = -k^{eff}\nabla\phi_2 - \frac{2RTk^{eff}}{F}\left(t_+^0 - 1\right)\left(1 + \frac{\partial \ln f_{\pm}}{\partial \ln c_{\mathrm{Li}}}\right)\nabla \ln c_{\mathrm{Li}} \tag{5}$$

where k^{eff} is the effective conductivity, $f_{\pm}$ is the salt activity coefficient, and $\left(1 + \frac{\partial \ln f_{\pm}}{\partial \ln c_{\mathrm{Li}}}\right)$ is the thermodynamic factor [24].

To simplify the equations, the diffusion conductivity, k_{D}, is defined [13]:

$$k_D = \frac{2RTk^{eff}}{F}\left(t_+^0 - 1\right)\left(1 + \frac{\partial \ln f_{\pm}}{\partial \ln c_{\mathrm{Li}}}\right) \tag{6}$$

Combining eqs. (3) - (6) leads to the governing equation for lithium ion transport:

$$\varepsilon\frac{\partial c_{\mathrm{Li}}}{\partial t} + \nabla\cdot\left(-D_e^{eff}\nabla c_{\mathrm{Li}}\right) + \boldsymbol{u}_0\cdot\nabla c_{\mathrm{Li}} = r_{\mathrm{Li}} - \nabla\cdot\left(\frac{\boldsymbol{i}_2 t_+}{F}\right) \tag{7}$$

Some investigations have simplified this equation further by combining it with the equation for $\boldsymbol{i}_2$, which will be discussed later.

The most prominent non-charged species is the dissolved oxygen in the electrolyte, which is transported by the electrolyte via diffusion and convection. Its molar flux is expressed as:

$$\boldsymbol{N}_{\mathrm{O_2}} = -D_{\mathrm{O_2}}^{eff} \nabla c_{\mathrm{O_2}} + \boldsymbol{u}_0 c_{\mathrm{O_2}} \tag{8}$$

Similar to eq. (7), the convection term is usually dropped. Combining eqs. (3) and (8) yields the governing equation for oxygen transport:

$$\varepsilon \frac{\partial c_{\mathrm{O_2}}}{\partial t} + \nabla \cdot \left(-D_{\mathrm{O_2}}^{eff} \nabla c_{\mathrm{O_2}} \right) + \boldsymbol{u}_0 \cdot \nabla c_{\mathrm{O_2}} = r_{\mathrm{O_2}} \tag{9}$$

The consumption rates of the lithium ion, r_{Li}, in eq. (7), and oxygen, $r_{\mathrm{O_2}}$, in eq. (9), can be related to the local transfer current density between electrolyte and electrode, j_{R}, as:

$$r_{\mathrm{Li}} = \frac{s_{\mathrm{Li}} A_{ED} j_{\mathrm{R}}}{nF}, \tag{10}$$

and

$$r_{\mathrm{O_2}} = \frac{s_{\mathrm{O_2}} A_{ED} j_{\mathrm{R}}}{nF} \tag{11}$$

where s is the stoichiometric coefficient of the corresponding species, A_{ED} is specific surface area for reaction, n is the number of electrons transferred in the reaction and the subscript R denotes the reaction shown in eq. (2).

To maintain charge balance, the divergence of electrolyte current density should be equal to the volumetric current density:

$$\nabla \cdot \boldsymbol{i}_2 = A_{ED} j_R \tag{12}$$

Combining eqs. (5) and (12) provides the equation for electrolyte potential:

$$\nabla \cdot \left(-k^{eff} \nabla \phi_2 \right) = \nabla \cdot \left(\frac{k_D}{c_{\mathrm{Li}}} \nabla c_{\mathrm{Li}} \right) + A_{ED} j_R \tag{13}$$

The current balance between the electrolyte and cathode solid phase is:

$$\nabla \cdot \boldsymbol{i}_1 + \nabla \cdot \boldsymbol{i}_2 = 0 \tag{14}$$

where i_1 is the current density in the cathode solid phase, which can be expressed simply by Ohm's law:

$$\boldsymbol{i}_1 = -k_c^{eff} \nabla \phi_1 \tag{15}$$

where k_c^{eff} is the electronic conductivity of the cathode solid phase. Cathode electric potential can be obtained from eqs. (12), (14), and (15):

$$\nabla \cdot \left(-k_c^{eff} \nabla \phi_1 \right) = -A_{ED} j_{\mathrm{R}} \tag{16}$$

Equation (7) can be further simplified by combination with eq. (12):

$$\varepsilon \frac{\partial c_{\mathrm{Li}}}{\partial t} + \nabla \cdot \left(-D_{\mathrm{e}}^{eff} \nabla c_{\mathrm{Li}} \right) + \boldsymbol{v} \cdot \nabla c_{\mathrm{Li}} = -\frac{\boldsymbol{i}_2 \nabla t_+}{F} + r_{\mathrm{Li}} - \frac{t_+ A_{ED} j_R}{F} \tag{17}$$

The effective parameters used in the above equations (4) - (9), (13), and (15) - (17), including D_{e}^{eff}, k^{eff}, $D_{\mathrm{O_2}}^{eff}$, and k_c^{eff}, can be calculated through the Bruggeman correlation [25]:

$$\Phi^{eff} = \Phi \varepsilon^{\beta} \tag{18}$$

where Φ can be D_{e}, k, and $D_{\mathrm{O_2}}$. Similarly, k_{c}^{eff} can be expressed as:

$$k_c^{eff} = k_c \left(1 - \varepsilon_0 - \varepsilon_{\mathrm{b}} \right)^{\beta} \tag{19}$$

where k_c is the electron conductivity in the carbon phase of the cathode and ε_{b} is the volume fraction of electrode binder. The Bruggeman coefficient, β, is often assumed to be a constant 1.5 [26]. The effective diffusivity can also be calculated using the Macmullin number, which is the ratio of transport resistance in a porous medium to the bulk resistance. Wang and Cho [27] gave a

summary of different expressions for Macmullin numbers under different assumptions of pore structures.

Porosity in the cathode is a function of both location and time due to the deposition of insoluble reaction products, such as Li_2O_2, during the discharge process. It can be related to the volume fraction of precipitated product, ε_s, and original porosity, ε_0, through:

$$\varepsilon = \varepsilon_0 - \varepsilon_s \tag{20}$$

When only Li_2O_2 deposition is considered, as in most models [19,20,22,27–29], the mass conservation of discharge product, Li_2O_2, can be expressed to obtain an equation for ε_s**:**

$$\frac{\partial \varepsilon_s}{\partial t} = -\frac{s_{Li_2O_2,R} M_{Li_2O_2}}{\rho_{Li_2O_2} nF} A_{ED} j_R \tag{21}$$

where $s_{Li_2O_2,R}$ is the stoichiometric coefficient of Li_2O_2, $M_{Li_2O_2}$ is the molecular weight of Li_2O_2, and $\rho_{Li_2O_2}$ is the density of Li_2O_2. The Butler-Volmer model is normally adopted to describe reaction kinetics and to obtain j_R.

In summary, there are five unknowns in the above discussion, including c_{Li}, c_{O_2}, ϕ_2, ϕ_1, and ε_s, and five governing equations, eqs. (7), (9), (13), (16), and (21). These governing equations are discretized in the computation domain, usually including the cathode and separator, and solved numerically. A constant current density is normally assumed and the cell voltage during the discharge or charge process can be obtained through the computation.

It should be emphasized that not all the models follow the framework described in the first half of this section. For example, Franco [30] used Poisson-Nernst-Planck equations to describe ion transport in the electrolyte, which applies to dilute solutions. In addition, the formulation described

in this section is only suitable for a binary system. Recently, many Li–O_2 batteries have started to use ionic liquid based electrolytes because of their stability and low vapor pressures. Such a battery is a ternary electrochemical system (two cations, one anion). Yoo et al. [31] developed a model for Li-ion batteries using ionic liquid based electrolyte which can be extended to Li–O_2 batteries.

1.2.2 Features of existing models

A comprehensive summary of existing continuum-scale models and their features is presented in Table 1-2. The first two columns of the table show the major investigators and dimension of the model. The third column shows whether it is a numerical or analytical model. The next two columns describe whether the model uses concentrated solution theory and if thermal behavior is included. The column 'Oxygen transport' indicates the mechanism of oxygen transportation in the model. Most models for non-aqueous battery assume that oxygen is supplied by dissolved oxygen molecules diffusing in electrolyte solution. The columns 'Passive/Active' and 'Convection' describe whether a pump is used to supply oxygen and if convective effects in mass transport are considered. The electrochemical kinetics model used at the two electrodes are described in the next two columns, followed with information of whether discharging or charging processes are considered. Columns 13 and 14 indicate whether side reactions and a multi-layer electrode structure are consideredd in the model, respectively. The next 5 columns show which mechanisms are considered in causing the resulting overpotential: anode reaction activation, cathode reaction activation, Ohmic loss in the electrolyte, in the electrode backbone, and in the deposition layer, respectively.

One of the most unique characteristics of a Li–O_2 battery is the precipitation of discharge product. Many models assume it contributes to the decrease in reaction surface area. The sub-model to describe this process is included in the column labeled 'Coverage model'. To build a

coverage model, the micro-structure of the cathode pores need to be considered. The next two columns describe the assumed pore shape in the corresponding model and if pore size distribution is considered. The following column shows whether the solid phase volume change during discharge is considered. The last three columns show the model electrolyte, discharge current density range, and cathode specific capacity range in the investigation. The features shown in Table 1-2 will be discussed in greater detail in the following sections.

Since the first numerical model for Li–O_2 batteries was reported by Sandhu et al. [16] in 2007, there has been an increasing number of published modeling works on Li–O_2 and Li–Air batteries. In Sandhu's model, only oxygen transport was considered, while later models incorporated charged species such as Li^+. In the model by Albertus et al. [32] in 2011, the major discharge product in the cathode was considered to be Li_2CO_3, while in later investigations it was changed to Li_2O_2 based on experimental observations. Increasingly complex physics and chemistries were considered in simulation models to closer resemble the real situation, such as inclusion of side reactions, pore size distribution, volume changes, and thermal effects.

Most existing Li–O_2 models can predict the discharge curves of a cell under different current densities and can match with experimental results reasonably well. Figure 1-2 compares the discharge curves predicted by several models (Wang and Cho [27], Sahapatsombut et al. [17], Jung et al. [21], Li and Faghri [33]) with the experimental results provided by Read [34]. The simulated curves also reflect that higher current density leads to lower discharge capacity. However, the fact that Read's experimental results [34] served as the only comparison resource for most modeling studies reflects the problem that there is a disconnection between modeling and experimental studies. Many experimental studies do not provide detailed cell parameters (such as cathode thickness and electrode porosity) which are essential for model development. Read [34] provided

this information in their publication, and is the primary reason why it is widely used in modeling studies for model calibration and validation.

In addition to improving the reliability of performance predictions, some models have served to propose better battery structure, with the proposed improvements validated and proven by experiments. Li and Faghri [33] developed a two dimensional numerical model in 2012, and obtained the distribution of the Li_2O_2 volume fraction in the cathode after discharge, as shown in Figure 1-3. The position $\chi = 1$ represents the cathode/oxygen boundary and $\chi = 0$ is the cathode/separator boundary. The Li_2O_2 volume fraction gradually increases toward the cathode/oxygen boundary. This trend is attributed to an increasingly high concentration of oxygen at the cathode/oxygen boundary which leads to high reaction rates and consequently high Li_2O_2 generation. This distribution means that the micro pores closer to the separator/cathode interface were not fully utilized. Based on this result, the authors proposed a cathode structure with gradient porosity of higher porosity closer to the air side and lower porosity at the separator/cathode interface. This concept was proven to be effective through experiments by Tan et al. [35]. Following the above work, Li et al. [29] also proposed an active cathode battery in which the electrolyte was recirculated through the cathode like a flow battery and oxygen was dissolved into the electrolyte in a tank outside of the battery. The convection effect significantly enhanced oxygen supply in the cathode porous structure and consequently increased battery capacity by a factor of ten.

1.2.3 Cathode modeling

The cathode is the focus of most modeling studies of Li–O_2 batteries, mainly because the precipitation of discharge products in the cathode pores is considered to be a determining factor of

the capacity. In this section, several key phenomena to be considered in cathode modeling are presented, along with a comparison of their treatment in the different models.

1.2.3.1 Cathode structural change

The cathode of a Li–O_2 battery is usually made from a mixture of carbon powder and a binder such as PTFE or PVDF. The carbon is considered catalytic to the oxygen reduction (discharge) and evolution (charge) reactions. Other catalysts such as gold, silver, or metal oxides are also used to improve reaction kinetics. In some cases, nickel foam is used to serve as both the electrode backbone and current collector [36]. These materials form porous media with highly complex micro-scale structures, which are not possible to be accurately described by cell-level continuum-scale models. Continuum models neglect the exact pore structure of the electrode and treat it as a homogeneous medium. Some macroscopic parameters are used to characterize the structure, such as porosity and specific surface area in these continuum scale analyses.

In most models, the porous structure of the cathode is assumed to consist of an agglomerate of ideal shaped micro-structures in order to obtain a simplified analytical expression for the dependence of these parameters on discharge state. Figure 1-4 shows the five most adopted pore shapes in battery modeling. Figure 1-4(a) assumes that the solid phase in the electrode are spherical particles with an average diameter of d_0, while the remaining space is completely filled with electrolyte. In contrast, Figure 1-4(b) assumes an open pore structure with spherical pores and the solid phase occupying the rest of the space. In Figure 1-4(c), the electrode is assumed to be comprised of carbon nanotubes or carbon fibers, and therefore the solid phase has a cylindrical shape. Figure 1-4(d) assumes that the pores are cylindrical tunnels inside the solid phase. Figure 1-4(e) treats both the solid and pore phases as flat shapes, with the average distance between the solid plates as d_0.

A simple relationship between the original electrode specific surface area, porosity, and particle or pore size can be readily obtained for each of these idealized pore structures, while neglecting the interference between individual pores or particles [37]. For example, the specific surface area of the structure in Figure 1-4(a) can be related to porosity and particle radius by $A_{ED,0} = 6(1-\varepsilon_0)/d_0$. These structural relations for each configuration are summarized in Table 1-3. It should be noted that in any battery model, experimentally measured specific surface area data are still preferable than using the proposed equations shown in Table 1-3 because of the associated assumptions made when developing these equations. These equations should be used with caution to avoid unrealistic results. For example, these relations show the specific surface area as a monotonic function of ε_0, which is not always true.

The third column in Table 1-3 shows the dependence of deposit film thickness, δ_s, on initial porosity ε_0, initial particle or pore size d_0, and volume fraction of deposit products ε_s. The last column in Table 1-3 shows the change in specific surface area with the deposit of solid products. These equations are based on two additional assumptions: i) the precipitate forms a smooth film on the reaction surface, and ii) the reactions occur on the fluid/solid interface. It should be noted that these assumptions are questionable, especially for the spherical and cylindrical particle models. Recent experimental results also show that the deposit shape is highly rate-dependent [38].

The volume fraction of the precipitates, ε_s, can be calculated by eq. (21) Once ε_s is known, deposit film thickness and specific surface area at any discharge state can be updated through the equations listed in Table 1-3.

In addition to decreasing specific reaction surface area, the precipitation of Li_2O_2 or other insoluble products in the electrode pores leads to several other consequences:

1. Increasing the transport resistance of reactants through the porous structure of the cathode at the electrode level;
2. Increasing the transport resistance of electrons through the deposit film at the pore level;
3. Changing reaction kinetics.

In most models, only the first one or two effects were considered. Li and Faghri [33] considered the last effect by expressing the ORR rate constant as a two-stage function of $\varepsilon_{Li_2O_2}$:

$$k = \begin{cases} i_0\left(1-0.9\dfrac{\varepsilon_s}{1.63\times10^{-6}}\right) & \text{for } \varepsilon_s < 1.63\times10^{-6} \\ 0.1i_0 & \text{for } \varepsilon_s \geq 1.63\times10^{-6} \end{cases} \tag{22}$$

where k is the ORR rate constant and i_0 is the exchange current density. This relationship assumes that Li_2O_2 does not normally form a complete film on the surface before ε_s reaches 1.63×10^{-6}. After that, the rate constant drops to 10% of that of the pristine electrode and does not change with further deposition of Li_2O_2. The dependence of specific surface area on ε_s is calculated based on the assumption of a spherical pore shape (case (b) in Table 1-3) [33]:

$$\frac{A_{ED}}{A_{ED,0}} = \left(1-\frac{\varepsilon_s}{\varepsilon_0}\right)^{2/3} \tag{23}$$

It should be noted that since k and A_{ED} influence reaction rate in the same manner, one could argue that eqs. (22) and (23) are redundant mathematically because they both consider the effect of Li_2O_2 deposition on reaction rate.

The effect of Li_2O_2 on the active reaction area was considered in a semi-empirical form [17,23,39]:

$$\frac{A_{ED}}{A_{ED,0}} = 1-\left[\frac{\varepsilon_s(t)}{\varepsilon_0}\right]^p \tag{24}$$

where p is a geometric factor between 0 – 1 indicating the shape of the solid precipitation layer. The term $\left[\frac{\varepsilon_s(t)}{\varepsilon_0}\right]^p$ can be interpreted as a coverage ratio of effective reaction surface area. It was stated that a relatively small value of p indicates a flat film, while a larger value means needle-shaped precipitation that barely covers the reaction surface. In these models, a constant of 0.4 or 0.5 was used for p. This relationship can be traced back to the modeling studies of Lead–Acid batteries and fuel cells.

Jung et al. [21] improved eq. (24) to make the factor p an inverse value of current density:

$$\frac{A_{ED}}{A_{ED,0}} = 1 - \left[\frac{\varepsilon_s(t)}{\varepsilon_0}\right]^{\frac{c}{i_{m,app}}} \tag{25}$$

where c is an empirical constant obtained by fitting the simulated discharge curve to experimental results, and $i_{m,app}$ is the applied mass-specific current density (A g^{-1}). This means that p, as in eq. (24), is lower at higher discharge rates, which leads to a more flat coverage while a lower discharge rate means more needle-shape (in [21] it is referred to as island-shape) coverage. The authors also considered the species mass transport resistance through the deposit film [21]. Compared to the results of other models [17,27,33], this model showed better agreement with experimental results under several different discharge current densities.

Figure 1-5 shows the decrease of specific surface area with an increase of ε_s using the different coverage models shown in Table 1-3. The initial porosity of the pristine electrode was set to 0.75, a typical porosity value for a lithium battery cathode [34]. The trends of Figure 1-5 reveal that the empirical eq. (24) generally imposes a rapid drop of reaction surface at the early stages of discharge but slows when the pores are considered fully filled by the solid products. Figure 1-5 also shows that with higher p (lower current density in [21]), the dependence is more

linear. The surface area remains unchanged for the pore structure model that assumes a flat reaction surface. Cylindrical and spherical pore structures show a different trend to that of eq. (24), with the specific reaction area decreasing almost linearly at the early stages of discharge, but more rapidly when approaching its maximum possible value of 0.75.

For the pore structures that assume spherical and cylindrical solid particles, the reaction surface area increased along with increasing deposition because the reaction is assumed to take place at the solid/liquid interface, as shown in Figure 1-4. When the deposit layer is thick enough, the particles start to combine to form void pores, and the surface area starts to decrease. This process is considered in the model developed by Chen et al. [40].

Xue et al. [41] assumed that A_{ED} is a function of deposit thickness instead of porosity:

$$\frac{A_{ED}}{A_{ED,0}} = \frac{1 - erf\left(\delta_s - 7\right)}{2} \tag{26}$$

This function assumes that when the film thickness δ_s is above 7 nm, electrons cannot penetrate the layer (tunneling limit) to reach reaction sites and therefore the surface is no longer active.

Wang [42] suggested that the Li_2O_2 growth is similar to the ice formation in a proton exchange membrane fuel cell (PEMFC) during sub-freezing conditions. This model followed a similar method developed for PEMFCs to calculate the effect of insoluble substances on surface passivation and oxygen transport in Li–O_2 batteries [28].

The Li_2O_2 deposition is assumed to be a smooth layer generated on the electrode pore surface, and the reaction is assumed to take place at the interface between this thin layer and electrolyte. However, the real physical situation is much more complex. As noted by experimental trials [38], Li_2O_2 grows in both film and toroid shapes, and the shape is highly rate-dependent. Xue et al. [43] developed a model that described Li_2O_2 growth on the electrode surface and in the electrolyte

separately. In this model, the reaction shown in eq. (2) is assumed to take place in multiple steps and mechanisms:

$$O_2 + e^- \rightarrow O_2^- \begin{cases} \rightarrow \text{Adsorption} \quad O_2^{-*} + 2Li^{+*} + e^- \rightarrow Li_2O_{2(\text{film})} \\ \rightarrow \text{Solution} \quad O_{2(\text{sol})}^- + 2Li_{(\text{sol})}^+ \rightarrow Li_2O_{2(\text{particle})} + O_2 \end{cases} \tag{27}$$

An escape function is defined to determine the ratio of the solution phase reaction to the total reaction, depending on a simplified pore network model. The decrease of specific reaction surface is expressed by eq. (26), but only the Li_2O_2 generated on the surface (adsorption path) would contribute to the increase of δ_s, which causes a decrease of reaction surface and an increase of electron transport resistance. Both film and particle shaped Li_2O_2 influence the change diffusivity of oxygen through decreasing effective porosity. The simulation results on cells that use DMSO or TEGDME based electrolytes show good agreement with experimental measurements when current density was under 1 mA cm^{-2}. This model also accounted for pore size distribution.

1.2.3.2 Voltage drop over deposition layer

The major reaction products in non-aqueous Li–O_2 batteries, including Li_2O_2, Li_2O, Li_2CO_3, are electronically insulating in their perfect crystalline form. Therefore, deposit film on the reaction surface hinders electron transfer between the electrolyte and electrode, and causes Ohmic voltage loss. While the conductivity of bulk Li_2O_2 crystal is very low ($10^{-18} - 10^{-17}$ S m^{-1} [44]), some experimental or material simulation studies indicate that the surface or grain boundary of Li_2O_2 crystals actually have a higher conductivity which leads to a much higher film conductivity than in its crystalline form [45,46].

Most models take the voltage drop across the deposit layer into account for the calculation of cell voltage. Although they are all based on Ohm's law, the calculation forms are different, as

summarized with unified symbols in Table 1-4, in which *j* is interfacial transfer current density (A m^{-2}), ρ_s is the electrical resistivity of the deposit layer, δ_s is the deposit layer thickness, and R_c is contact resistance.

Andrei et al. [13,47] and Chen et al. [40] developed the only models that considered the effect of the deposit film's curvature on ρ_s, which is included by the logarithm terms in the equations shown in Table 1-4. In other models, the voltage drop was calculated as through a flat surface even if a spherical or cylindrical pore structure was assumed.

Resistivity is assumed to be a function of thickness instead of a constant in [32]. It increases exponentially with thickness, and was later adopted by Wang [42]. However, in [32] the calculated ρ_s is obviously lower than other sources (see Table 1-4).

Wang and Cho [27] attributes cell voltage drop mainly to the electronic resistance and reaction surface area decrease caused by the solid film instead of the mass transport resistance. It can be seen that in their model, the resistance of the Li_2O_2 layer is at the order of 10^7 $\Omega \cdot m^2$, which is fairly high.

The model developed by Sahapatsombut et al. [17,23,39] is the only one that does not require information about δ_s or d_0, i.e., the pore structure information. However, the resistance parameter used by this model, R_s, has the unit of $\Omega \cdot m^2$, and is not a normally measured electric property parameter of Li_2O_2. Instead, it is a concept similar to contact resistance, as in [42]. Therefore, these model [17,23,39] treat the Ohmic loss over the deposition layer as a contact resistance which increases linearly with the volume fraction of the precipitate. The value of the parameter is obtained by fitting the simulated discharge curves to experimental measurements.

1.2.3.3 Pore size distribution

In the discussions related to pore structure and surface coverage models in section 2.3.1, one major assumption is adopted, that the electrode pore size has a uniform value of d_0 at the start of discharge. In real porous media, however, the pore size is not uniform, and varies in a wide range, which is often described by the pore size distribution function [48,49]. Franco et al. [18] and Xue et al. [41] introduced a model adapted from earlier PEMFC modeling works [50], that incorporates the pore size distribution.. In addition to the ordinary spatial mesh, a mesh on the pore radius was also introduced. The variation of specific surface area and deposition film thickness are calculated on each separate pore radius mesh. This enables the model to compare the performance of different carbon powders used for cathode fabrication, since the powders have different particle size distribution functions. The authors compared the discharge characteristics of two cathodes fabricated with Super P and Ketjen Black carbon. It was concluded that the Super P cathode showed lower discharge capacity because of a smaller surface area and faster growth of Li_2O_2 film thickness.

Chen et al. [40] developed a model to simulate a carbon nano-fiber electrode with a distribution of fiber radii considered. Initially, the deposition of Li_2O_2 is considered to be on cylindrical particles, as described in Figure 1-4(c). When the deposit film grows thick enough that the different fibers contact each other, cylindrical pores form. Then, the deposit film growth would follows that described by Figure 1-4(d). This is a more realistic presentation of the deposit film growth process than in other models.

Li [51] adopted a particle size distribution function of the following form:

$$P(d) = \frac{1}{\sqrt{2\pi}\sigma d} \exp\left(\frac{-\left(\ln d - \mu\right)^2}{2\sigma^2} \right) \tag{28}$$

where d is pore size, σ is a shape factor, and μ is the mean pore size. With the deposition of Li_2O_2, pore size d decreases consistently, and therefore the distribution function $P(d)$ needs to be updated at each time step. It is also assumed that there is a critical pore size. The pores smaller than this value are not to be filled with electrolyte and therefore do not take part in reactions. Based on this function, the specific surface area A_{ED} can be calculated as:

$$A_{ED} = \frac{\varepsilon \int_0^{\infty} P(t)\pi t^2 dt}{\int_0^{\infty} P(t)\frac{\pi t^3}{6} dt} \tag{29}$$

which assumes a spherical pore shape. The deposition film thickness δ_s, is calculated as:

$$\delta_s = \frac{\varepsilon_s}{A_{ED}} \tag{30}$$

which implicitly assumes a flat pore shape, as evidenced by Table 1-3. Using this model, the effect of mean pore size and critical pore size on discharge capacity was studied. It is concluded that there exists an optimum mean pore size under a constant porosity to reach a maximum discharge capacity. A periodical discharge mode is also proposed which uses a pulsed discharge current instead of a constant value. Simulation results indicate that this facilitates oxygen transfer into the electrode and leads to a higher discharge capacity than that for constant discharge current. This provides a unique way to increase the capacity of a battery pack.

1.2.3.4 Cathode reaction kinetics

In all existing Li–O_2 battery models, the classic Butler–Volmer model, or the simplified Tafel model, were used to describe cathode reaction (ORR and OER) kinetics. The interfacial current density, j (A m^{-2}), can be expressed as:

$$j = j_0 \cdot \left\{ \exp\left[\frac{\alpha_a nF}{RT}(E - E_{eq}) \right] - \exp\left[-\frac{\alpha_c nF}{RT}(E - E_{eq}) \right] \right\} \tag{31}$$

where j_0 is the exchange current density, α_a and α_c are the anodic and cathodic charge transfer coefficients, respectively, n is the number of electrons transferred during the reaction, E is electrode potential, and E_{eq} is the equilibrium potential. Regarding the electron transfer number, n, some models use the value of 1 [32] while others used 2 [39] as indicated by eq. (2). According to Guidelli et al. [52], using the value of 1 for n is more reasonable because it is impossible for one single reaction step to transfer more than one electron, especially for a reaction with unclear mechanism. For the charge transfer coefficient, most models adopted the assumption that $\alpha_a = \alpha_c = 0.5$ [42]. The exchange current density is usually an assumed value based on calibration of the model to match experimental results.

As discussed by Safari et al. [53], studies on the reaction kinetics at the oxygen electrodes in non-aqueous electrolytes are still very limited. However, they developed a model that depicted the formation of Li_2O_2 as a two-step reaction and considered the effect of lithium superoxide desorption via solution-mediated reactions. This model successfully explained the change of discharge product morphologies at different current densities and the curvature in Tafel-plots for ORR in non-aqueous Li–O_2 cells. A non-Tafel kinetics equation was suggested for the interfacial current density of ORR for future Li–O_2 battery models:

$$j = -\frac{F\Gamma k_{c1}\exp\left[-\dfrac{\alpha F(E-E_{eq})}{RT}\right]}{0.5+\dfrac{(k_{c1}-k_{c2})-k_{c2}}{8\left[k_{c2}\exp\left[-\dfrac{\alpha F(E-E_{eq})}{RT}\right]+\dfrac{1}{2\tau}\right]}\exp\left[-\dfrac{\alpha F(E-E_{eq})}{RT}\right]} \tag{32}$$

where Γ is the maximum surface site concentration (mol m^{-2}), k_{c1} and k_{c2} are the rate constants (s^{-1}), and τ is a characteristic time constant for lithium superoxide desorption (s).

1.2.4 Anode modeling

Anode reaction of a Li–O_2 battery occurs at the lithium/separator interface. The kinetics for the major reaction, eq. (1), is usually considered to be very fast, thus causing negligible overpotential. However, at least two phenomena occurring at this surface are of great importance but ignored by most models.

The first is the formation of the solid electrolyte interphase (SEI) [54]. This layer forms spontaneously when lithium contacts with the non-aqueous electrolyte solution. It passivates the lithium anode and protects it from further reaction with the electrolyte. During charge, it hinders a uniform plating of lithium [55]. The thickness of SEI on the carbon electrode for a Li–ion battery ranges between 10 – 100 nm, depending on the state of charge and electrolyte material. Its composition also changes during cycling [56]. The SEI layer formed on lithium metal in Li–O_2 batteries has been less studied though several groups have reported the composition and morphology of this layer [56,57]. It was estimated that the thickness of the SEI was approximately 50 nm.

While SEI forms spontaneously, in some cases an artificial anode protective layer (APL) is coated on the anode to suppress self-discharge and dendritic growth of lithium [58,59]. The most common materials for this layer are LiPON and ion conductive glass film. The thickness of this layer is usually between 50 – 200 nm [60]. In [16] and [17,23,39], such a layer was introduced in their cell structure, but how the layer was treated in the numerical and analytical computations was not discussed.

The anode protective layer imposes a transport resistance for both electrons and lithium ions whether it is spontaneously formed SEI or the artificial APL. It is very difficult to include these layers in the computation grid of continuum models since they are very thin. The overpotential

caused by these layers can be assumed as that similar to a contact resistance. This effect on battery performance should be considered in future models.

The second important phenomenon occurring at the anode is dendrite growth [61,62]. Lithium dendrites form during charge and the uncontrolled growth may cause a short-circuit, which imposes a severe safety issue in all kinds of lithium batteries. It also decreases battery cycleability. In their cell-level model, Tan and Ryan [63] incorporated a dendrite growth model, which was proposed by Monroe and Newman [64], where the dendrite tip velocity is calculated by:

$$\upsilon_{tip} = \frac{M_{Li}}{F\rho_{Li}} i_n \tag{33}$$

where M_{Li} and ρ_{Li} are the molecular weight and density of metal lithium, respectively. i_n is the dendrite tip current density, which is a function of local kinetic overpotential and Li^+ concentration:

$$i_n = i_{0,\mathrm{ref}} \frac{\exp\left(\frac{2\gamma M_{\mathrm{Li}}}{rRT\rho_{\mathrm{Li}}}\right)\exp\left(\frac{\alpha_{\mathrm{a}} F\eta}{RT}\right) - \exp\left(\frac{-\alpha_{\mathrm{c}} F\eta}{RT}\right)}{\left(\frac{c_{\mathrm{ref}}}{c_{Li^+}^{\delta'}}\right)^{\alpha_{\mathrm{a}}} + \frac{\left(1-t_+^0\right) r i_{0,\mathrm{ref}}}{FDc_{Li^+}^{\delta'}} \exp\left(\frac{-\alpha_{\mathrm{c}} F\eta}{RT}\right)} \tag{34}$$

where $i_{0,\mathrm{ref}}$ is the reference exchange current density, γ is the interfacial tension between the separator and lithium, r is the radius of curvature of the dendrite tip, and $c_{Li^+}^{\delta'}$ is the salt concentration at the vicinity of the dendrite tip. Calculation results showed that at low charge current density (needle-shape dendrites) the predicted dendrite position agreed well with experimental results.

Akolkar [62] derived a temperature-dependent dendrite tip current density:

$$i_n = i_{\mathrm{f}} \left\{ -\frac{1}{bC_0} \ln \left[e^{-bC_0} + \frac{i_f \left(1 - t_+\right) b\delta}{nFa_0 e^{\frac{E_D}{R}\left(\frac{1}{T_0} - \frac{1}{T}\right)}} \right] \right\}^A \tag{35}$$

$$A = -\frac{\alpha_c^0}{n} e^{-\frac{E}{2R}\left(\frac{1}{T_0} - \frac{1}{T}\right)}$$

where i_f is the current density at the flat lithium surface, a_0 and b are coefficients used in the exponential function to express the dependence of the salt diffusion coefficient on concentration, C_0 is bulk concentration, δ is the thickness of the mass transport boundary layer, α_c^0 is the transfer coefficient at reference temperature T_0, and E and E_D are diffusion activation energies for the SEI phase and solution phase, respectively.

These dendrite growth models may be incorporated in future continuum-scale Li–O_2 battery models to predict the growth and decomposition of dendrite formation on an anode surface and to evaluate its effect on cell safety.

1.2.5 Special features of continuum-scale models

The physical and chemical processes in a Li–O_2 battery are very complex. Various assumptions and simplifications are made in modeling studies to focus solely on the process of interest. Some models attempt to add features neglected by other studies to build a model closer to the actual processes in a Li–O_2 battery. In the sections following, these efforts are presented.

1.2.5.1 Side reactions and the charging process

In most Li–O_2 battery models, the electrolyte is assumed to be an ideal binary electrolyte, i.e., the solvent and anions do not take part in the reactions. Only the major reactions (as shown in eqs. (1) and (2)) are considered. However, one of the most challenging issues for Li–O_2 battery studies is electrolyte instability and unwanted side reactions. In actual cells, the electrolyte may

decompose because of the attack of radicals and side products may be produced depending on which electrolyte is used. In addition, water can enter the system from the ambient air through cell openings for oxygen breathing. Some experimental studies [65] show that trace quantities of water existing in the system may help improve the cell capacity, which might be attributed to a higher solubility of Li_2O_2. Carbon dioxide may also enter the system from the environment, or be produced during charging due to the oxidation of carbon based electrodes to form Li_2CO_3 [66,67]. Since Li_2CO_3 is insoluble in electrolyte and cannot be decomposed during charge, the accumulation of Li_2CO_3 in the system will lower cell cycleability. Moran et al. [4] provided a detailed review of electrolyte decomposition and side reactions on different types of electrolytes.

Sahapatsombut et al. [23] developed the only model that incorporated electrolyte degradation mechanisms in a Li–O_2 battery model. The CO_2 generated from carbonate-based electrolyte decomposition during discharge was considered. The scheme was similar to that suggested by Freunberger et al. [68]. Although carbonate based electrolyte is no longer considered as an appropriate option for Li–O_2 battery, this work still provided a framework to include side reactions into a Li–O_2 battery model.

As an energy storage device, one of the most appealing characteristics of the Li–O_2 battery is its rechargability. However, most of the modeling work focuses primarily on the discharge process. The work by Sahapatsombut et al. [17] was the first modeling work reported to include the charging process. The simulated cell potential for both discharge and charge agreed well with experimental results. The model was further developed to include the formation of Li_2CO_3 occurring from electrolyte degradation [23]. The relationship between the decrease of discharge capacity during cycling and the formation of Li_2O_2 and Li_2CO_3 was discussed. The model

introduced by Franco [30] in 2013 also showed simulated results of multiple discharge-charge cycles but no in-depth analysis was provided.

1.2.5.2 Solid phase volume change

During discharge of a non-aqueous Li–O_2 battery, the volume of the anode (metallic lithium) shrinks when metallic lithium is converted to lithium ions which enter the electrolyte. In most test cells [69,70], a spring is placed between the anode lithium foil and current collector in order to compensate for the volume change of the anode and to secure a good contact between different layers of the cell structure. At the same time, the volume of solid phase in the cathode increases because of the deposition of Li_2O_2. This pushes the liquid electrolyte out of cathode. Assuming electrolyte does not leak through the openings on the cell casing, it will flow into the back of the anode, as shown in Figure 1-6. According to the reaction in eq. (1), 1 mole of solid reactant lithium metal (13.0 cm^3) would generate 0.5 moles of solid reaction product Li_2O_2 (9.93 cm^3) during discharge. Therefore, in total, the volume of solid phase in the cell would decrease by 23.6%. This means that the void space for electrolyte in a cell increases after discharge (see the change of shaded electrolyte area in Figure 1-6), and the electrolyte level drops accordingly.

Although the phenomena described above was brought up as early as 2001 by Albertus et al. [32], in most of the Li–O_2 battery models listed in Table 1-2, it is neglected by limiting the computation domain only over the separator and cathode, so the movement of the anode electrode is not considered. In addition, the change in electrolyte level caused by solid volume change is neglected and it is assumed that the cathode is always completely immersed in electrolyte.

Yoo et al. [20] developed a one dimensional model that considered the effect of solid phase volume change in a Li–O_2 battery. In this battery design there was no spring mechanism to push the anode to the separator. Instead, it was assumed that the gap between the anode lithium foil and

separator would increase during discharge. Because of the decrease in solid phase volume during discharge, it was concluded that the electrolyte liquid level would decrease and cause a so-called dead zone in the cell. The simulation results showed that this caused a steep drop in cell voltage and loss of specific capacity [20].

Huang and Faghri [71] developed a 2-D Li–Air coin cell model which employs a deformed mesh technique to track the electrolyte level drop. In addition to the solid phase volume change, solvent evaporation is also responsible for electrolyte level drop. The air chamber to provide oxygen to the cell is included in the model to provide a more accurate physical model. It is found that the decreased electrolyte level actually helps to achieve a higher cell capacity. This is caused by a better Li_2O_2 distribution and cathode pore utilization. Figure 1-7(a) shows the electrolyte level movement at different time points during discharge. As the electrolyte level drops, the position with maximum reaction rate and Li_2O_2 deposition also drops. This alleviates electrode clogging and leads to better electrode utilization than for a constant electrolyte level. Figure 1-7(b) shows the simulation results of final ε_s distribution with and without the consideration of the electrolyte level change. The predictions agree well with the conceptual analysis as shown in Figure 1-7(a). It was noted that for a cell using a volatile solvent for electrolyte, air chamber size has significant influence on discharge capacity. This implies that the method of oxygen delivery to the cell is important.

1.2.5.3 Thermal model

Thermal management is a critical issue for lithium batteries due to the potential safety concern. This is especially important when energy and power density of future batteries become increasingly high. Thermal runaway occurs when the battery temperature rises past a threshold value, causing faster reactions, which then generates more heat and cause even higher

temperatures. This positive feedback loop can cause explosion and fire hazard. Since 2010, there has been a rapid increase of studies on thermal behavior and management of Li–ion batteries. The same trend can be predicted for Li–O_2 batteries. A detailed method to calculate heat generation and temperature distribution in Li–ion batteries can be found in [12], [72], and [73]. In a simplified form, heat generation in the battery is expressed as:

$$\dot{Q} = I\left(U - V\right) - I\left(T\frac{\partial U}{\partial T}\right) \tag{36}$$

where I is reaction rate (A m^{-3}), V is cell voltage and U is the theoretical voltage. The first term in the right side of the above equation describes irreversible heat generation, caused by charge transfer overpotential, Ohmic loss, and mass transport resistance. The second term is the reversible heat generation, also known as entropic heat. Equation (36) also applies to Li–O_2 batteries. More sophisticated models should include other effects such as concentration relaxation and material phase changes.

Thermal behavior studies on Li–O_2 batteries are still very rare, both experimentally and theoretically. This is because the power densities of even the most state-of-the-art Li–O_2 batteries are still very low. To achieve a high specific energy of a Li–O_2 battery, current density must be limited to under 1 mA cm^{-2}, which leads to a low specific power density of under 5 W kg^{-1} [8]. In comparison, the specific power of today's Li–ion batteries is usually around 300 W kg^{-1} for long term operation. As noted by Wagner et al. [74], charge and discharge rates of Li–O_2 battery must be improved by 2 orders of magnitude higher than the current values to be feasible for practical applications. However, one of the negative effects brought about by such high power density is the high heat generation and subsequent thermal management issues.

Li and Faghri [33] were the first to include the energy equation in a Li–O_2 battery model to calculate temperature rise. The anode was assumed to be at a constant temperature because of the

high heat conductivity of lithium metal. A natural convection boundary condition was considered for heat dissipation at the air side. The simulation results show that the maximum temperature rise is less than 0.01 K even at the highest discharge current density of 0.5 mA cm^{-2}. The authors attribute this to the low power density and natural convection heat dissipation. Only irreversible heat generation caused by activation overpotential was considered in this model. The reversible heat generation was not included because of the lack of data on the entropic heat coefficient $\frac{\partial U}{\partial T}$. Wang and Cho [28] also briefly discussed Li–O_2 battery temperature and provided an estimated temperature rise of 1 K at 1 mA cm^{-2}, but they also neglected reversible heat generation. It should be noted that these models were based on a single cell, for which the surface/volume ratio was very high to facilitate heat dissipation. In a battery pack, temperature rise is expected to be much higher.

Another issue with thermal modeling is that in most cases the dependence of the property data on temperature is unknown, as will be discussed in section 4.

1.2.5.4 Multi-phase multi-dimensional model

As shown in Table 1-2, most existing models are one-dimensional, and only consider the variation of all physical quantities in the direction normal to the electrode surface. This also means that the cathode is entirely exposed to oxygen (100% open area ratio), as shown in Figure 1-8(a). However, this is not true to a real situation. In a typical Li–O_2 coin cell, the cathode side casing is punctured with holes to enable oxygen breathing from its surroundings, either an oxygen pouch or ambient air. The open area ratio (the total area of these holes divided by the geometric cathode area) is usually around 10% [75,76]. This is far from the 100% open ratio assumed by 1-D models.

The open ratio is an important factor for cell performance because oxygen supply is crucial for Li–O_2 cells and because the casing/current collector impose resistance to oxygen transport. In Li

and Faghri's 2-D model [33], the open ratio on the cathode casing is considered, as shown in Figure 1-8(b). The results show that when the open area ratio decreases from 100% to 50%, cell capacity decreases from 529 mAh g^{-1} to 133 mAh g^{-1}. They further showed a 2-D distribution of Li_2O_2 at the end of discharge, indicating a maximum ε_{Li2O2} at the opening, which blocks oxygen transport.

It must be noted that Li and Faghri's 2-D model [33] is based on the assumption that all the pores of the cathode are flooded with electrolyte, and that there is no gas phase existing in the cathode. This translates to an electrolyte saturation rate of 100%, and oxygen is considered as a species dissolved in the electrolyte phase. Only two phases are considered to exist in the electrode, the solid phase (carbon, binder, catalyst) and the liquid phase (electrolyte); therefore the batteries represented in Figure 1-8(a) and (b) are referred to as 2-phase models. This assumption is adopted by most Li–O_2 battery models, but needs further examination. Franco and Xue [18] suggest that a gas phase possibly exists at the oxygen side of a well-designed cathode and that it has significant influence on capacity.

In models developed for fuel cells such as PEMFC and phosphoric acid fuel cells (PAFCs), it is usually assumed that electrolyte only partially fills the space between the solid agglomerate of particles in the cathode, and oxygen is considered to exist in the gas phase in the pores of the cathode [26,77]. Since there exists solid phase, liquid phase and gas phase simultaneously in the electrode, these models are referred to as 3-phase models (Figure 1-8(c)). The balance between the gas phase and liquid phase in the pores is described by the Leverett J-function. This leads to the question: Does the gas phase co-exist with the liquid electrolyte phase in the cathode of a Li–O_2 cell? The key to the answer is the wettability of the electrode.

When the contact angle of the electrolyte on an electrode surface is less than 90^o, the electrode is hydrophilic, and more easily flooded. Under this condition, it is more difficult for the gas phase

to exist in the pores. When the contact angle of the electrolyte on the electrode surface is larger than 90^{o}, it is easier for the gas phase to exist in the electrode. In most fuel cell electrodes, PTFE is used as a binder, which is very hydrophobic. This helps to build up the gas phase in the electrode. The effective oxygen diffusion coefficient in the gas phase is 10^{-8} m^2 s^{-1}, which is one to two orders of magnitude higher than for liquid; therefore the existence of the gas phase enhances oxygen supply and cell performance. For the non-aqueous Li–O_2 cells, usually the contact angle of organic electrolyte on the carbon electrode and PTFE is much less than 90^{o} [75,78]. This means electrolyte can infiltrate the cathode easily and the gas phase hardly exists in the pores. However, for an aqueous Li–O_2 cell, contact angle is usually much larger [79], which means that the gas phase may exist. In Horstmann's 1-D model [80] for an aqueous Li–O_2 battery, the gas phase diffusion was considered and the Leverette function was used to calculate the balance between liquid and gas phase. Detailed calculation of liquid saturation rate was not included. Bahrami and Faghri [26] provide information regarding the building of a two dimensional 3-phase model based on the porous electrode theory.

In Wang and Cho's 2-D model [27], a gas diffusion layer between casing (current collector) and cathode is assumed. The pores in this layer are occupied only by oxygen, and the electrolyte cannot enter this layer, as shown in Figure 1-8(d). This model can be regarded as a pseudo 3-phase model.

The above discussion also suggests two ways to improve non-aqueous Li–O_2 cells. The first is to choose electrolyte that has larger contact angle on the cathode surface. The second is to find new binders for the cathode which are super hydrophobic toward organic electrolyte. Both ways increase the existence of the gas phase in the cathode and enhance cell performance.

1.2.5.5 Li–O_2 flow cell

There is a unique type of Li–O_2 battery that combines the features of a fuel cell, flow battery and Li–O_2 battery: the Li–O_2 flow cell. Li et al. [29] and Huang and Faghri [81] proposed a non-aqueous Li–O_2 flow cell which they called a Li–O_2 battery with an active cathode, as shown in Figure 1-9. The electrolyte is saturated with oxygen in a tank external to the battery and pumped through the cathode end plate embedded with interdigital flow channels. Driven by the pressure difference between two adjacent channels, electrolyte seeps through the porous structure of the cathode. Convection significantly improves oxygen transfer in the electrode and therefore the specific capacity of the cathode and specific energy of the whole system are greatly increased. A similar concept was proposed by Zheng et al. [82,83] on an aqueous Li–O_2 battery. Their experimental results on a test cell show higher power output than conventional Li–O_2 batteries because of better oxygen supply.

In the models for Li–O_2 flow cells [29,81] as described above, species transport equations need to account for convection. The electrolyte potential equation remains the same because electric neutrality is still kept even with convection of the electrolyte. The velocity can be obtained from Darcy's law. A key parameter in Darcy's law is the permeability of the electrode. For a Li–O_2 flow cell, because of Li_2O_2 deposition, permeability of the cathode changes during cycling. According to the Carman–Kozeny equation, permeability of a porous medium can be related to its porosity, ε, as [84,85]:

$$K = C_{KC}\frac{\varepsilon^3}{(1-\varepsilon)^2} \tag{37}$$

where C_{kc} is an empirical value and should be measured through experiments for Li–O_2 flow cells.

An interesting result for the Li–O_2 flow cell obtained through the calculation result by Huang and Faghri [81] is that, in such a cell, an electrolyte with low conductivity would increase the

specific capacity, as shown in Figure 1-10. Only when the electrolyte conductivity drops below 1% of its normal value, would the predicted capacity drop. This is due to a much more uniform oxygen concentration in the flow cell compared to a conventional cell. A low conductivity causes a larger potential drop in the electrolyte, which consequently causes smaller activation overpotential and reaction rate at the electrolyte inlet. This alleviates cathode clogging and translates to better usage of electrode pores. Conductivity of the electrolyte should not be considered a priority compared to other properties when looking for potential electrolytes for Li–O_2 flow cells. Huang and Faghri [81] also simplified the gradient porosity cathode structure proposed by Li et al. in [29] and proposed a dual-layer cathode, which is able to increase cell capacity to as high as 105% compared to a conventional single layer cathode. Further experimental verification and a system level energy density analysis of the proposed flow battery design are necessary to prove its advantages over conventional Li-air and Li-ion batteries.

1.3 Particle-scale and multi-scale models

The phenomena in Li–O_2 batteries are intrinsically multi-scale, multi-physics. Continuum-scale models can only capture the macroscopic mass transport characteristics. Particle level or multi-scale models use detailed 2D or even 3D electrode structure and provide a more accurate description of the physical and chemical processes.

Ryan et al. [15] used a Lagrangian particle based modeling method called Smoothed Particle Hydrodynamics (SPH) to capture the particle-level phenomena in a Li–Air battery cathode. Spherical electrode particles with three different sizes are dispersed in a two dimensional computation domain with unknown width. Although no details about the computational methods were provided, the figures indicate a detailed 2D distribution of solid precipitation on the electrode particles. The effect of relative magnitude between diffusion rate and reaction rate on precipitation

was studied. The transport theory was based on an infinite dilute solution and therefore the governing equation for salt transport reduced to a simple diffusion equation. The reaction kinetics is first order without considering local kinetic overpotential. A dendrite and charge transport model was also integrated into the simulation.

Bao et al. [86] developed a multi-scale model that combined a 1-D cell-level and 3-D nano-scale (nm) and meso-scale (μm) models. The nano-scale and meso-scale 3-D structures were developed using a so-called particle-packing method which was able to recreate a structure highly resembling a real electrode. The nano-scale model provided a correlation between active surface percentages and Li_2O_2 film thickness and passed it to the meso-scale model. Then a relation between specific surface area and Li_2O_2 concentration was obtained in the meso-scale model, which was provided to the cell-level model for calculation of oxygen concentration and reaction rates. The cell-level model assumed a uniform kinetics overpotential and lithium ion concentration and electrolyte potential effects were neglected. The model was used to study the discharge characteristics of a Li–O_2 battery with different electrode micro-structure and operating conditions. This model provides a way to further develop a more practical Li–Air battery model that can help to optimize electrode structure.

1.4 Property data

During the early stages of development for Li–O_2 batteries, the salts and solvents used for electrolytes were the same as those used for lithium ion batteries. The solvent was usually a alkyl carbonate, such as EC, EMC, DMC, and EMC. They were often mixed to achieve a balance of different properties, such as low vapor pressure (volatility) and high conductivity. The salts used were mainly $LiPF_6$ and $LiClO_4$ [87]. Later it was found that carbonate based solvents have many problems in Li–O_2 battery applications, primarily the decomposition of electrolyte because of the

oxygen environment and high charging voltage. As for the salt, it was found that $LiPF_6$ could react with the discharge product Li_2O_2 [88]. These problems severely impaired the efficiency and cycleability of the batteries. Therefore, the search for new electrolytes for Li–O_2 batteries is a very active research direction. Some of the electrolytes under study are summarized in Table 1-5 [4,89]. Currently, ether based electrolytes, such as TEGDME, are the most commonly used in experiments [90,91].

For Li–O_2 batteries, electrolytes should have the following characteristics:

1. Low vapor pressure (Nonvolatile): When the battery is exposed to ambient air, electrolyte vaporization may not lead to severe loss in the long term.
2. Stable to O_2^-: O_2^- is believed to be the product of the first step of oxygen reduction reaction in the cathode. Because it is very reactive, the electrolyte should be stable enough to resist its attack.
3. Wide electrochemical window: The difference between discharge and charge voltages of Li–O_2 batteries is still higher than the desired value. This requires the electrolyte to remain stable in a wide electrochemical window.
4. A stable SEI at anode: Since lithium is very reactive, a SEI must be formed at the interface between lithium metal and electrolyte to protect the anode.
5. Good salt solubility: Without a suitable enough salt solubility and dissociation, electrolyte cannot have high conductivity, which is essential for high performance.

Most potential candidates of electrolyte for Li–O_2 batteries are under development. It poses a challenge for modeling studies since reliable and accurate property data are essential for successful simulation models. All relevant property data are collected and summarized below (Tables 1-6 to

1-9). However, this reinforces how very limited property data are available for the new electrolytes, which urgently needs to be addressed.

1.4.1 Fundamentals

For an infinitely dilute binary solution, two independent properties are needed to characterize the electrolyte. For example, the mobility of the anion and cation, u_+ and u_-. The diffusion coefficients of the ions can then be provided by the Nernst–Einstein equation:

$$D_+ = RTu_+ \tag{38}$$

and

$$D_- = RTu_- \tag{39}$$

The ionic conductivity electrolyte can be calculated as:

$$k = F^2\left(z_+^2 u_+ c + z_-^2 u_- c\right) \tag{40}$$

where z is the charge number of species and c is the electrolyte concentration. The salt diffusion coefficient can be calculated as [11]:

$$D = \frac{D_+ D_- \left(z_+ - z_-\right)}{z_+ D_+ - z_- D_-} \tag{41}$$

Transference numbers are given by:

$$t_+ = 1 - t_- = \frac{z_+ D_+}{z_+ D_+ - z_- D_-} \tag{42}$$

Typically, D and k are givens and all other quantities can be calculated through the equations above. With these parameters available, the molar flux of Li^+ ion in the electrolyte can be calculated as:

$$\boldsymbol{N}_{Li} = -D\nabla c_{Li} - \frac{k\nabla\phi_2 t_+}{F} + \boldsymbol{u}c_{Li} \tag{43}$$

where electrolyte potential, ϕ_2, and electrolyte velocity, u, can be obtained through charge balance and fluid dynamics, respectively.

In concentrated solution theory, a binary electrolyte requires three independent properties to be characterized. Usually, salt diffusion coefficient *D*, cation transference number with reference to solvent t_+^0, and ionic conductivity *k*, are the most commonly used. The expression for Li^+ flux in a concentrated solution is expressed as [11,13]:

$$\boldsymbol{N}_{Li} = -D\left(1-\frac{d\ln c_0}{d\ln c_{Li}}\right)\nabla c_{Li} + \frac{\boldsymbol{i}_2 t_+^0}{F} + \boldsymbol{u}_0 c_{Li} \tag{44}$$

where c_0 is the solvent concentration, $\boldsymbol{i}_2$ is the current density in electrolyte, and $\boldsymbol{u}_0$ is the solvent velocity. Comparing to eq. (43), it shows that that if the same form of equations is desired for concentrated solution theory, $D\left(1-\frac{d\ln c_0}{d\ln c_{Li}}\right)$ must be used as the diffusion coefficient, which is denoted as D_e in eq. (4). At the same time, the transference number is also different to that shown in eq. (42) because here the reference system is for the solvent while for dilute theory the reference is the surrounding environment [13].

The electrolyte used in Li–O_2 batteries are concentrated binary solutions. Most of their physical, thermal, and electrochemical properties are functions of both concentration and temperature, which should be considered in a comprehensive model.

1.4.2 Summary of property data

Tables 1-6 to 1-9 summarize the electrolyte property data that can be used for Li–O_2 battery models. Table 1-6 lists ionic conductivity *k* of different electrolytes. Table 1-7 summaries the salt diffusion coefficient *D*, and cation transference number of the electrolytes, t^+. Table 1-8 shows the oxygen related transport properties of various electrolytes, including oxygen solubility $c_{O_2,sat}$,

electrolyte viscosity μ, oxygen diffusivity D_{O_2}, and electrolyte density ρ. Table 1-9 shows various equations for the dependence of the thermodynamic factor, as shown in eq. (5), on electrolyte concentration. It is clear that electrolytes using alkyl carbonates as solvent and $LiPF_6$ as salt are the most readily available because they have been most widely used in the well-studied Li–ion batteries [92–98]. In contrast, transport properties on other types of electrolytes are very scarce. Because Li–O_2 batteries only became a popular research topic in the past several years, many different electrolytes are just in the development stages. Property data are not abundant, especially those used by concentrated solution theory, such as t_+^0 and $f_\pm$. The variation of these properties with regard to concentration and temperature is even scarcer.

1.4.3 Discussion

Conductivity *k* is the most readily available property data for the electrolytes used in lithium batteries. As shown in Table 1-6, its value usually ranges between 0.5 – 1.5 S m^{-1}. Assuming a 0.5 mm transfer distance (*l*) and 1 mA cm^{-2} discharge current density (*I*), the potential drop caused by electrolyte resistance can be approximated by:

$$\eta_e = \frac{lI}{k} \approx 5 \text{ mV}$$

This value is much lower than the activation overpotential to drive cathode reactions because state-of-the-art Li–O_2 battery can only work in a very small current density around 1 mA cm^{-2}. However, this does not mean conductivity is not important. If Li–O_2 batteries are going to reach practical application, the power output must improve and the current density must reach the level of current Li–ion batteries, in the order of 10^2 mA cm^{-2}. Only then will conductivity be a very important parameter to affect the battery performance.

Data for the salt diffusion coefficient and transference number reported in literature are summarized in Table 1-7. The salt diffusion coefficient determines the electrolyte concentration gradient in the battery. A higher diffusion coefficient will lower the concentration difference and thus lower the diffusion overpotential. Diffusion coefficient can be measured through AC impedance [99], cyclic voltammetry (CV) [100], or rotation disc electrode (RDE) tests [101]. RDE tests use the Levich equation while CV tests use the Randles–Sevcik equation to obtain *D*. However, it should be noted that in some publications, *D* is either simply referred to as the diffusion coefficient or mistaken for the self-diffusion coefficient of the lithium ion (D_{Li}). A revisit of the derivation of Levich equation [102] and Randles–Sevick equation [103–105] shows that in both equations *D* represents the salt diffusion coefficient, as defined in eq. (41). It depicts a combined effect of the diffusion of both anion and cation, not just the cation (Li^+). Reported measurement on the self-diffusion coefficient of Li^+, D_{Li}, is scarce. Saito et al. [106] and Capiglia et al. [107] both used a pulse field gradient-NMR technique to measure D_{Li} and D_-.

As indicated by Thomas et al. [12], transference number measurement could be problematic for lithium battery electrolytes and considerable error might be made. Different measurement techniques predict contradictory results. Zugmann et al. [93] showed that electrochemical methods obtained transference numbers that decreased with concentration while NMR measurements showed the opposite trend. Traditional methods to measure transference number t_+ (eq. (42)) include the Hittorf method and moving boundary method [108]. If the model is based on concentrated solution theory, then t_+^0 should be used instead of t_+. Figure 1-11 shows the comparison between the data of t_+ and t_+^0 given by Capiglia et al. [107] and Nyman [109], respectively. The data are based on the same concentration of salt (1 M $LiPF_6$) in the same solvent (EC:EMC). The weight ratio between EC and EMC are 2:8 for [107] and 3:7 for [109]. It shows

that when the electrolyte concentration is around 1 M, t_+^0 is only 0.26, much smaller than t_+, which is 0.43. It also shows that t_+ stays almost constant when concentration is above 0.1 M, which is consistent with the common belief that transference number does not change significantly with concentration. t_+^0, however, continues to decrease when concentration is high.

For Li–O_2 batteries, oxygen transport properties are crucial to battery performance. Figure 1-12 shows the effect of oxygen solubility on cathode specific capacity as predicted by various models. To enable the comparison between different models, all the oxygen solubility and specific capacity data are normalized. Different models show the same trend that oxygen solubility has a nearly linear influence on cell capacity. When the solubility doubles, predicted cathode specific capacity also approximately doubles from its original value. In contrast to the vast number of works regarding oxygen solubility and diffusivity in aqueous solutions [110–114], very few data sources are available for non-aqueous electrolytes. Table 1-8 summarizes the oxygen solubility and diffusivity for various different solvents and electrolytes. Comparing the oxygen solubility given by [115] and [91], reveals that the discrepancy between different sources can be significant. For example, the differences of oxygen solubility given by [115] and [91] are 38.4% for DMSO, 21.6% for PC and 8.76% for DME. These would cause almost the same level of error in prediction of cell capacity.

The diffusion coefficient of oxygen determines the flux of oxygen into the porous cathode and oxidation on the active reaction sites. There are many different ways to measure the diffusivity of oxygen in liquid [116], including using a diaphragm cell [117], electron paramagnetic resonance [118], and time response of an oxygen electrode [119]. In most Li–O_2 battery modeling studies [120], oxygen diffusivity data are from Read's work [115], in which oxygen diffusivity is estimated using the Stokes–Einstein equation [115,121]:

$$D_{O_2} = \frac{k_B T}{6\pi\mu a_{O_2}} \tag{45}$$

where a_{O_2} is the effective hydrodynamic radius of O_2 in the solution, k_B is the Boltzmann constant, and μ is the viscosity of the electrolyte. Thus, as long as the viscosity of the liquid is known, oxygen diffusivity can be obtained based on an estimate value of a_{O_2}. However, since this relation is just an empirical observation, and the radius of the solvated oxygen molecule is roughly estimated, data provided by this method are not very accurate.

In many cases, the solvent is a mixture of two different types of liquid while only the diffusivity in pure solvents is known. Further assumptions are made that oxygen solubility is an additive property, so the properties of a mixed solvent can be obtained from the properties of pure solvents by simple weighted averages. Another major assumption often made is that the electrolyte salt has little effect on oxygen diffusivity [34], thus the oxygen solubility in pure solvent can be used for the electrolyte. Most earlier studies gave the diffusivity and solubility of oxygen in electrolyte based on non-aqueous solvents [122–124], such as DME and DMSO, but the salts differ from those developed for lithium batteries. In [100], oxygen solubility in DMSO and ACN are presented. However, these data were provided by [125] and the salt is 0.1 M tetraethylammonium perchlorate (TEAP) instead of lithium salt. While the first assumption is somewhat acceptable, the second may lead to significant error. As shown by [115], adding $LiPF_6$ into non-aqueous solvent may reduce oxygen solubility by as much as 40% and higher salt concentration results in even greater reduction.

The measurement of oxygen solubility is relatively easier than that for diffusivity. In Read's work [115], a simple vial-pouch method is used to measure the Bunsen coefficient. Some delicate ways to measure oxygen solubility are reviewed by Groisman and Khomutov [110]. There are also

several publications about oxygen diffusivity and solubility in ionic fluids, which are regarded as potential electrolytes potential for Li–O_2 batteries [126–128].

An important parameter in concentrated solution theory is the thermodynamic factor ($1+\frac{d\ln f_{\pm}}{d\ln c}$), in which $f_{\pm}$ is the mean molar activity coefficient. Experimental studies to measure this factor are very limited, and the results show some major discrepancies. The data provided by different sources are listed in Table 1-9 and plotted in Figure 1-13 [24,94,96]. It should be noted that Valøen and Reimers provided $\left(1-t_{+}\right)\left(1+\frac{d\ln f_{\pm}}{d\ln c}\right)$ instead of $1+\frac{d\ln f_{\pm}}{d\ln c}$ [94]. Therefore, in Figure 1-13 a constant transference number of 0.38 was used to retrieve $1+\frac{d\ln f_{\pm}}{d\ln c}$ from this publication. Although the results by Stewart and Newman [96] and Valøen and Reimers [94] show similar dependence on concentration, the equation provided by Nyman et al. [24] was more widely used in Li–O_2 battery models.

1.5 Unresolved issues and future opportunities

The following unresolved issues and opportunities for future development of Li–O_2 and Li–Air battery models can be recognized:

- A multi-scale model that incorporates the exact details of the 3-D pore structure should be used to describe pore structure change in the Li–O_2 battery cathode more accurately. The model proposed by Xue et al. [43] and Bao et al.[86] are good examples of such a direction, thoughthey can be further improved to include more comprehensive cell-scale models and pore network models.

- Most existing models only consider the reversible reaction that generates and consumes Li_2O_2. It is well-known that side reactions also play an important role in the cycling of Li–O_2

batteries. The model developed by Sahapatsombut et al. [17,23] provides a good framework to include these side reactions in continuum models and to study the cycling behavior of the cell.

- A full cell-level, or even pack-level model is needed to study the multi-dimensional effects for future development of Li–O_2 batteries. It should be 3-D and include three phases (solid phase, liquid electrolyte phase and gas phase). Currently most models are 1-D and only consider the liquid electrolyte phase and solid phase.

- A closer collaboration between modeling and experimental studies should be formed. Many cathode reaction kinetic parameters used in Li–O_2 models are assumed instead of using direct measurement from experiments. Phenomena at the anode, including the influence of the solid electrolyte interphase and dendrite growth, are often omitted due to the lack of understanding of reaction mechanisms. To effectively tackle these issues, further collaboration between experimental and modeling studies are needed.

- Thermal effects become significant when power density of Li–O_2 batteries is enhanced to a practical level through use of new materials. Accordingly, thermal behavior and management will become an important topic for Li–O_2 battery modeling.

- Property data, especially oxygen solubility and diffusivity in the electrolyte have significant impact on modeling results. Yet there are still very limited sources to provide accurate data. Data provided by different investigators show some significant differences. More experimental efforts should be performed to address these challenges.

1.6 Concluding remarks

Most of the existing models are continuum-scale and based on non-aqueous Li–O_2 batteries. Although the framework for battery modeling on the continuum scale is well established, Li–O_2 batteries have their own unique characteristics to be captured by these models. One major feature

of non-aqueous Li–O_2 battery is the deposition of solid reaction products. This changes electrode structure and consequently affects mass transport and cell performance. Different methods to describe the pore structure change during battery discharge are summarized and compared. Recent developments to make Li–O_2 battery models more comprehensive and accurate are presented. The property data relevant to Li–O_2 battery models are summarized and reviewed. The reliability of these data and discrepancies between different sources are discussed.

Most state-of-the-art Li–O_2 battery models can predict experimental results fairly well after reasonable parameter adjustment. These models have already revealed some important information about the battery that could not be obtained through experimental studies, such as the reaction rate and Li_2O_2 distribution. New electrode structure and cell structures have been proposed based on simulation results. These physical models provide a valuable optimization tool for future development of Li–O_2 and Li–Air batteries. The methods developed can then be extended to other emerging types of batteries.

Nomenclature

A_{ED}	specific surface area of the electrode ($m^2\ m^{-3}$)
c	concentration (mol m^{-3})
D	diffusivity ($m^2\ s^{-1}$)
d	electrode pore diameter (m)
E_0	thermodynamic equilibrium voltage (V)
F	Faraday constant (96,485 C mol^{-1})
$f_{\pm}$	salt activity coefficient
I	discharge current density (A m^{-2})
i_0	exchange current density (A m^{-3})
$\boldsymbol{i}$	current density vector (A m^{-2})
j	interfacial transfer current density between electrode and electrolyte (A m^{-2})
K	permeability (m^2)
k	ionic conductivity (S m^{-1}), reaction rate constant (A m^{-2})
k_c	electron conductivity in carbon phase of electrode (S m^{-1})
k_D	diffusion conductivity (A m^{-1})
M	molecular weight (kg mol^{-1})
n	number of electrons transferred in reaction
p	pressure (Pa); dimensionless geometric factor
r	consumption rate (mol $m^{-3}\ s^{-1}$)
s	stoichiometric coefficient
s_m	mass source term (s^{-1})
T	temperature (K)

t	time (s)
t_+	transference number of Li^+
$\boldsymbol{u}$	electrolyte velocity vector (m s^{-1})
V	cell voltage (V)
α	transfer coefficient
ε	porosity
η	overpotential (V)
μ_{EL}	electrolyte viscosity (kg m^{-1} s^{-1})
ρ	density (kg m^{-3})
ϕ	electric potential (V)

Superscripts and Subscripts

1	electrode solid phase
2	electrolyte phase
a	anode
c	cathode
eff	effective value

References

[1] R. Van Noorden, The Rechargeable Revolution: A Better Battery, Nature. 507 (2014) 26–28. doi:10.1038/507026a.

[2] W.R. Momyer, E.L. Littauer, Development of a Lithium-Water-Air Primary Battery, Proc. Intersoc. Energy Convers. Eng. Conf. 2 (1980) 1480–1486.

[3] K.M. Abraham, Z. Jiang, A Polymer Electrolyte-Based Rechargeable Lithium/Oxygen Battery, J. Electrochem. Soc. 143 (1996) 1. doi:10.1149/1.1836378.

[4] M. Balaish, A. Kraytsberg, Y. Ein-Eli, A Critical Review on Lithium-Air Battery Electrolytes., Phys. Chem. Chem. Phys. 16 (2014) 2801–22. doi:10.1039/c3cp54165g.

[5] W. Xu, J. Wang, F. Ding, X. Chen, E. Nasybulin, Y. Zhang, et al., Lithium Metal Anodes for Rechargeable Batteries, Energy Environ. Sci. 7 (2014) 513–537. doi:10.1039/c3ee40795k.

[6] Z.-L. Wang, D. Xu, J.-J. Xu, X.-B. Zhang, Oxygen Electrocatalysts in Metal-Air Batteries: From Aqueous to Nonaqueous Electrolytes., Chem. Soc. Rev. 43 (2013) 7746–7786. doi:10.1039/c3cs60248f.

[7] Y. Shao, S. Park, J. Xiao, J.G. Zhang, Y. Wang, J. Liu, Electrocatalysts for Nonaqueous Lithium-Air Batteries: Status, Challenges, and Perspective, ACS Catal. 2 (2012) 844–857. doi:10.1021/cs300036v.

[8] J. Christensen, P. Albertus, R.S. Sanchez-Carrera, T. Lohmann, B. Kozinsky, R. Liedtke, et al., A Critical Review of Li/Air Batteries, J. Electrochem. Soc. 159 (2012) R1–R30. doi:10.1149/2.086202jes.

[9] M. Park, H. Sun, H. Lee, J. Lee, J. Cho, Lithium-Air Batteries: Survey on the Current Status and Perspectives towards Automotive Applications from a Battery Industry Standpoint, Adv. Energy Mater. 2 (2012) 780–800. doi:10.1002/aenm.201200020.

[10] M.L. Perry, Mass Transport in Gas-Diffusion Electrodes: A Diagnostic Tool for Fuel-Cell Cathodes, J. Electrochem. Soc. 145 (1998) 5–15. doi:10.1149/1.1838202.

[11] J. Newman, K.E. Thomas-Alyea, Electrochemical Systems, 3rd ed., John Wiley & Sons, Hoboken, NJ, 2004.

[12] K.E. Thomas, J. Newman, R.M. Darling, Mathematical Modeling of Lithium Batteries, in: W.A. van Schalkwijk, B. Scrosati (Eds.), Adv. Lithium-Ion Batter., Springer US, New York City, 2002: pp. 345–392. doi:10.1007/0-306-47508-1_13.

[13] P. Andrei, J.P. Zheng, M. Hendrickson, E.J. Plichta, Modeling of Li-Air Batteries with Dual Electrolyte, J. Electrochem. Soc. 159 (2012) A770–A780. doi:10.1149/2.010206jes.

[14] A. Faghri, Y. Zhang, Transport Phenomena in Multiphase Systems, Academic Press, 2006. doi:10.1016/0167-2738(81)90101-6.

[15] E.M. Ryan, K.F. Ferris, A.M. Tartakovsky, M.A. Khaleel, Computational Modeling of Transport Limitations in Li-Air Batteries, in: ECS Trans., 2013: pp. 123–136. doi:10.1149/04529.0123ecst.

[16] S.S. Sandhu, J.P. Fellner, G.W. Brutchen, Diffusion-Limited Model for a Lithium/air Battery with an Organic Electrolyte, J. Power Sources. 164 (2007) 365–371. doi:10.1016/j.jpowsour.2006.09.099.

[17] U. Sahapatsombut, H. Cheng, K. Scott, Modelling the Micro–macro Homogeneous Cycling Behaviour of a Lithium–air Battery, J. Power Sources. 227 (2013) 243–253. doi:10.1016/j.jpowsour.2012.11.053.

[18] A.A. Franco, K.-H. Xue, Carbon-Based Electrodes for Lithium Air Batteries: Scientific and Technological Challenges from a Modeling Perspective, ECS J. Solid State Sci. Technol. 2 (2013) M3084–M3100. doi:10.1149/2.012310jss.

[19] V.Y. Nimon, S.J. Visco, L.C. De Jonghe, Y.M. Volfkovich, D.A. Bograchev, Modeling and Experimental Study of Porous Carbon Cathodes in Li-O_2 Cells with Non-Aqueous Electrolyte, ECS Electrochem. Lett. 2 (2013) A33–A35. doi:10.1149/2.004304eel.

[20] K. Yoo, S. Banerjee, P. Dutta, Modeling of Volume Change Phenomena in a Li–air Battery, J. Power Sources. 258 (2014) 340–350. doi:10.1016/j.jpowsour.2014.02.044.

[21] C.Y. Jung, T.S. Zhao, L. An, Modeling of Lithium–oxygen Batteries with the Discharge Product Treated as a Discontinuous Deposit Layer, J. Power Sources. 273 (2015) 440–447. doi:10.1016/j.jpowsour.2014.09.103.

[22] A. V. Sergeev, A. V. Chertovich, D.M. Itkis, E. a. Goodilin, A.R. Khokhlov, Effects of Cathode and Electrolyte Properties on Lithium-Air Battery Performance: Computational Study, J. Power Sources. 279 (2015) 707–712. doi:10.1016/j.jpowsour.2015.01.024.

[23] U. Sahapatsombut, H. Cheng, K. Scott, Modelling of Electrolyte Degradation and Cycling Behaviour in a Lithium-Air Battery, J. Power Sources. 243 (2013) 409–418. doi:10.1016/j.jpowsour.2013.06.043.

[24] A. Nyman, M. Behm, G. Lindbergh, Electrochemical Characterisation and Modelling of the Mass Transport Phenomena in $LiPF_6$–EC–EMC Electrolyte, Electrochim. Acta. 53 (2008) 6356–6365. doi:10.1016/j.electacta.2008.04.023.

[25] W. Lai, F. Ciucci, Mathematical Modeling of Porous Battery electrodes—Revisit of Newman's Model, Electrochim. Acta. 56 (2011) 4369–4377. doi:10.1016/j.electacta.2011.01.012.

[26] H. Bahrami, A. Faghri, Review and Advances of Direct Methanol Fuel Cells: Part II: Modeling and Numerical Simulation, J. Power Sources. 230 (2013) 303–320. doi:10.1016/j.jpowsour.2012.12.009.

[27] Y. Wang, S.C. Cho, Analysis and Multi-Dimensional Modeling of Lithium-Air Batteries, J. Electrochem. Soc. 162 (2015) A114–A124. doi:10.1149/2.0731501jes.

[28] Y. Wang, S.C. Cho, Analysis of Air Cathode Perfomance for Lithium-Air Batteries, J. Electrochem. Soc. 160 (2013) A1847–A1855. doi:10.1149/2.092310jes.

[29] X.L. Li, J. Huang, A. Faghri, Modeling Study of a Li-O_2 Battery with an Active Cathode, Energy. 81 (2015) 489–500. doi:10.1016/j.energy.2014.12.062.

[30] A.A. Franco, A Multiscale Physical Model of Electrochemical Energy Storage Devices, in: ECS Trans., 2013: pp. 11–19. doi:10.1149/04527.0011ecst.

[31] K. Yoo, A. Deshpande, S. Banerjee, P. Dutta, Electrochemical Model for Ionic Liquid Electrolytes in Lithium Batteries, Electrochim. Acta. (2015). doi:10.1016/j.electacta.2015.07.003.

[32] P. Albertus, G. Girishkumar, B. McCloskey, R.S. Sánchez-Carrera, B. Kozinsky, J. Christensen, et al., Identifying Capacity Limitations in the Li/Oxygen Battery Using Experiments and Modeling, J. Electrochem. Soc. 158 (2011) A343–A351. doi:10.1149/1.3527055.

[33] X. Li, A. Faghri, Optimization of the Cathode Structure of Lithium-Air Batteries Based on a Two-Dimensional, Transient, Non-Isothermal Model, J. Electrochem. Soc. 159 (2012) A1747–A1754. doi:10.1149/2.043210jes.

[34] J. Read, Characterization of the Lithium/Oxygen Organic Electrolyte Battery, J. Electrochem. Soc. 149 (2002) A1190–A1195. doi:10.1149/1.1498256.

[35] P. Tan, W. Shyy, L. An, Z.H. Wei, T.S. Zhao, A Gradient Porous Cathode for Non-Aqueous Lithium-Air Batteries Leading to a High Capacity, Electrochem. Commun. 46 (2014) 111–114. doi:10.1016/j.elecom.2014.06.026.

[36] L. Li, A. Manthiram, Decoupled Bifunctional Air Electrodes for High-Performance Hybrid Lithium-Air Batteries, Nano Energy. 9 (2014) 94–100. doi:10.1016/j.nanoen.2014.07.002.

[37] I.M. Development, W.B. Gu, Micro-Macroscopic Coupled Modeling of Batteries and Fuel Cells, J. Electrochem. Soc. 145 (1998) 3418–3427. doi:10.1149/1.1838821.

[38] B. Horstmann, B. Gallant, R. Mitchell, W.G. Bessler, Y. Shao-Horn, M.Z. Bazant, Rate-Dependent Morphology of Li_2O_2 Growth in $Li–O_2$ Batteries, J. Phys. Chem. Lett. 4 (2013) 4217–4222. doi:10.1021/jz401973c.

[39] U. Sahapatsombut, H. Cheng, K. Scott, Modelling of Operation of a Lithium-Air Battery with Ambient Air and Oxygen-Selective Membrane, J. Power Sources. 249 (2014) 418–430.

[40] X.J. Chen, V. V. Bevara, P. Andrei, M. Hendrickson, E.J. Plichta, J.P. Zheng, Combined Effects of Oxygen Diffusion and Electronic Resistance in Li-Air Batteries with Carbon Nanofiber Cathodes, J. Electrochem. Soc. 161 (2014) A1877–A1883. doi:10.1149/2.0721412jes.

[41] K.-H. Xue, T.-K. Nguyen, A. A. Franco, Impact of the Cathode Microstructure on the Discharge Performance of Lithium Air Batteries: A Multiscale Model, J. Electrochem. Soc. 161 (2014) E3028–E3035. doi:10.1149/2.002408jes.

[42] Y. Wang, Modeling Discharge Deposit Formation and Its Effect on Lithium-Air Battery Performance, Electrochim. Acta. 75 (2012) 239–246. doi:10.1016/j.electacta.2012.04.137.

[43] K. Xue, E. Mcturk, L. Johnson, P.G. Bruce, A.A. Franco, A Comprehensive Model for Non-Aqueous Lithium Air Batteries Involving Different Reaction Mechanisms, J. Electrochem. Soc. 162 (2015) 614–621. doi:10.1149/2.0121504jes.

[44] M.D. Radin, D.J. Siegel, Charge Transport in Lithium Peroxide: Relevance for Rechargeable Metal–air Batteries, Energy Environ. Sci. 6 (2013) 2370–2379. doi:10.1039/c3ee41632a.

[45] W.T. Geng, B.L. He, T. Ohno, Grain Boundary Induced Conductivity in Li_2O_2, J. Phys. Chem. C. (2013) 131122161534000. doi:10.1021/jp405315k.

[46] M.D. Radin, J.F. Rodriguez, F. Tian, D.J. Siegel, Lithium Peroxide Surfaces Are Metallic, While Lithium Oxide Surfaces Are Not, J. Am. Chem. Soc. 134 (2012) 1093–1103. doi:10.1021/ja208944x.

[47] P. Andrei, J.P. Zheng, M. Hendrickson, E.J. Plichta, Some Possible Approaches for Improving the Energy Density of Li-Air Batteries, J. Electrochem. Soc. 157 (2010) A1287–A1295. doi:10.1149/1.3486114.

[48] J.R. Nimmo, Porosity and Pore Size Distribution, in: Encycl. Soils Environ., 2004: pp. 295–303. doi:10.1016/B978-0-12-409548-9.05265-9.

[49] C. Lastoskie, K.E. Gubbins, N. Quirke, Pore Size Distribution Analysis of Microporous Carbons: A Density Functional Theory Approach, J. Phys. Chem. 97 (1993) 4786–4796. doi:10.1021/j100120a035.

[50] A.A. Franco, PEMFC Degradation Modeling and Analysis, in: C. Hartnig, C. Roth (Eds.), Polym. Electrolyte Membr. Direct Methanol Fuel Cell Technol. (PEMFCs DMFCs)-Volume 1 Fundam. Perform., Woodhead, Cambridge, UK, 2011.

[51] X. Li, A Modeling Study of the Pore Size Evolution in Lithium-Oxygen Battery Electrodes, J. Electrochem. Soc. 162 (2015) A1636–A1645. doi:10.1149/2.0921508jes.

[52] R. Guidelli, R.G. Compton, J.M. Feliu, E. Gileadi, J. Lipkowski, W. Schmickler, et al., Defining the Transfer Coefficient in Electrochemistry: An Assessment (IUPAC Technical Report), Pure Appl. Chem. 86 (2014) 245–258. doi:10.1515/pac-2014-5026.

[53] M. Safari, B.D. Adams, L.F. Nazar, Kinetics of Oxygen Reduction in Aprotic Li−O_2 Cells: A Model-Based Study, J. Phys. Chem. Lett. 5 (2014) 3486−3491. doi:10.1021/jz5018202.

[54] E. Peled, The Electrochemical Behavior of Alkali and Alkaline Earth Metals in Nonaqueous Battery Systems - The Solid Electrolyte Interphase Model, J. Electrochem. Soc. 126 (1979) 2047–2051. doi:10.1149/1.2128859.

[55] J.B. Goodenough, K.S. Park, The Li-Ion Rechargeable Battery: A Perspective, J. Am. Chem. Soc. 135 (2013) 1167–1176. doi:10.1021/ja3091438.

[56] M. Nie, D. Chalasani, D.P. Abraham, Y. Chen, A. Bose, B.L. Lucht, Lithium Ion Battery Graphite Solid Electrolyte Interphase Revealed by Microscopy and Spectroscopy, J. Phys. Chem. C. 117 (2013) 1257–1267. doi:10.1021/jp3118055.

[57] R. Younesi, M. Hahlin, K. Edstro, Surface Characterization of the Carbon Cathode and the Lithium Anode of Li−O_2 Batteries Using $LiClO_4$ or LiBOB Salts, ACS Appl. Mater. Interfaces. (2013). doi:10.1021/am3026129.

[58] H.S. Jadhav, R.S. Kabubarme, C.-J. Park, Protective Layers of B Containing Glass Ceramic and LiPON for Lithium Electrode in Rechargeable Li-O_2 Batteries, in: 223rd ECS Meet., Electrochemical Society, 2013: p. 216.

[59] D.J. Lee, H. Lee, J. Song, M.H. Ryou, Y.M. Lee, H.T. Kim, et al., Composite Protective Layer for Li Metal Anode in High-Performance Lithium-Oxygen Batteries, Electrochem. Commun. 40 (2014) 45–48. doi:10.1016/j.elecom.2013.12.022.

[60] S.J. Yoo, J.W. Lim, B. Choi, Y.-E. Sung, Enhanced Reliability of Electrochromic Devices with a LiPON Protective Layer, J. Electrochem. Soc. 154 (2007) P6–P10. doi:10.1149/1.2404787.

[61] R. Akolkar, Mathematical Model of the Dendritic Growth during Lithium Electrodeposition, J. Power Sources. 232 (2013) 23–28. doi:10.1016/j.jpowsour.2013.01.014.

[62] R. Akolkar, Modeling Dendrite Growth during Lithium Electrodeposition at Sub-Ambient Temperature, J. Power Sources. 246 (2014) 84–89. doi:10.1016/j.jpowsour.2013.07.056.

[63] E.M. Tan, J; Ryan, Numerical Modeling of Dendrite Growth in a Lithium Air Battery System, ECS Trans. 53 (2013) 35–43.

[64] C. Monroe, J. Newman, Dendrite Growth in Lithium/Polymer Systems, J. Electrochem. Soc. 150 (2003) A1377–A1384. doi:10.1149/1.1606686.

[65] N.B. Aetukuri, B.D. Mccloskey, J.M. Garcia, L.E. Krupp, V. Viswanathan, A.C. Luntz, On the Origin and Implications of Li_2O_2 Toroid Formation in Nonaqueous Li-O_2 Batteries, arXiv Prepr. (2014) 1406.3335.

[66] W. Xu, J. Hu, M.H. Engelhard, S.A. Towne, J.S. Hardy, J. Xiao, et al., The Stability of Organic Solvents and Carbon Electrode in Nonaqueous Li-O_2 Batteries, J. Power Sources. 215 (2012) 240–247. doi:10.1016/j.jpowsour.2012.05.021.

[67] M.M. Ottakam Thotiyl, S.A. Freunberger, Z. Peng, P.G. Bruce, The Carbon Electrode in Nonaqueous Li-O_2 Cells, J. Am. Chem. Soc. 135 (2013) 494–500. doi:10.1021/ja310258x.

[68] S.A. Freunberger, Y. Chen, Z. Peng, J.M. Griffin, L.J. Hardwick, F. Bardé, et al., Reactions in the Rechargeable Lithium-O_2 Battery with Alkyl Carbonate Electrolytes, J. Am. Chem. Soc. 133 (2011) 8040–8047. doi:10.1021/ja2021747.

[69] V. Garlapati, Thesis: Development of High Performance Air-Cathodes for Solid State Lithium-Air Cells, University of Dayton, 2010.

[70] J. Deboever, Thesis: Characterization of Lithium Peroxide Formation in Lithium Air Battery Electrode via Titration Techniques and EIS, Oregon Institute of Technology, 2014.

[71] J. Huang, A. Faghri, Investigating the Effect of Electrolyte Level Change in a Li–Air Coin Cell, (2015).

[72] D. Bernardi, E. Pawlikowski, J. Newman, A General Energy Balance for Battery Systems, J. Electrochem. Soc. 132 (1985) 5–12. doi:doi: 10.1149/1.2113792.

[73] T.M. Bandhauer, S. Garimella, T.F. Fuller, A Critical Review of Thermal Issues in Lithium-Ion Batteries, J. Electrochem. Soc. 158 (2011) R1–R25. doi:10.1149/1.3515880.

[74] F.T. Wagner, B. Lakshmanan, M.F. Mathias, Electrochemistry and the Future of the Automobile, J. Phys. Chem. Lett. 1 (2010) 2204–2219. doi:10.1021/jz100553m.

[75] W. Xu, J. Xiao, D. Wang, J. Zhang, J.-G. Zhang, Effects of Nonaqueous Electrolytes on the Performance of Lithium/Air Batteries, J. Electrochem. Soc. 157 (2010) A219–A224. doi:10.1149/1.3269928.

[76] H.-G. Jung, J. Hassoun, J.-B. Park, Y.-K. Sun, B. Scrosati, An Improved High-Performance Lithium–air Battery, Nat. Chem. 4 (2012) 579–585. doi:10.1038/nchem.1376.

[77] S.R. Choudhury, M.B. Deshmukh, R. Rengaswamy, A Two-Dimensional Steady-State Model for Phosphoric Acid Fuel Cells (PAFC), J. Power Sources. 112 (2002) 137–152. doi:10.1016/S0378-7753(02)00369-5.

[78] W. Xu, J. Xiao, J.J.-G. Zhang, D. Wang, Optimization of Nonaqueous Electrolytes for Primary Lithium/Air Batteries Operated in Ambient Environment, J. Electrochem. Soc. 156 (2009) A773–A779. doi:10.1149/1.3168564.

[79] H. Ohkuma, I. Uechi, M. Matsui, Y. Takeda, O. Yamamoto, N. Imanishi, Stability of Carbon Electrodes for Aqueous Lithium-Air Secondary Batteries, J. Power Sources. 245 (2014) 947–952. doi:10.1016/j.jpowsour.2013.06.146.

[80] B. Horstmann, T. Danner, W.G. Bessler, Precipitation in Aqueous Lithium-Oxygen Batteries: A Model-Based Analysis, Energy Environ. Sci. 6 (2013) 1299–1314.

[81] J. Huang, A. Faghri, Capacity Enhancement of a Lithium Oxygen Flow Battery, Electrochim. Acta. 174 (2015) 908–918. doi:10.1016/j.electacta.2015.06.071.

[82] J.P. Zheng, P. Andrei, M. Hendrickson, E.J. Plichta, The Theoretical Energy Densities of Dual-Electrolytes Rechargeable Li-Air and Li-Air Flow Batteries, J. Electrochem. Soc. 158 (2011) A43–A46. doi:10.1149/1.3515330.

[83] X.J. Chen, a. Shellikeri, Q. Wu, J.P. Zheng, M. Hendrickson, E.J. Plichta, A High-Rate Rechargeable Li-Air Flow Battery, J. Electrochem. Soc. 160 (2013) A1619–A1623. doi:10.1149/2.012310jes.

[84] D.A. Nield, A. Bejan, Convection in Porous Media, 3rd ed., Springer, New York, 2006. doi:10.1007/0-387-33431-9.

[85] A. Costa, Permeability-Porosity Relationship: A Reexamination of the Kozeny-Carman Equation Based on a Fractal Pore-Space Geometry Assumption, Geophys. Res. Lett. 33 (2006) L02318. doi:10.1029/2005GL025134.

[86] J. Bao, W. Xu, P. Bhattacharya, M.L. Stewart, J.-G. Zhang, W. Pan, Discharge Performance of Li-O_2 Batteries Using a Multiscale Modeling Approach, J. Phys. Chem. C. (2015). doi:10.1021/acs.jpcc.5b01441.

[87] G.M. Veith, J. Nanda, L.H. Delmau, N.J. Dudney, Influence of Lithium Salts on the Discharge Chemistry of Li-Air Cells, J. Phys. Chem. Lett. 3 (2012) 1242–1247. doi:10.1021/jz300430s.

[88] D. Chalasani, B.L. Lucht, Reactivity of Electrolytes for Lithium-Oxygen Batteries with Li_2O_2, ECS Electrochem. Lett. 1 (2012) A38–A42. doi:10.1149/2.010202eel.

[89] V. Bryantsev, V. Giordani, Predicting Solvent Stability in Aprotic Electrolyte Li–air Batteries: Nucleophilic Substitution by the Superoxide Anion Radical (O_2^-), J. Phys. Chem. A. 115 (2011) 12399–12409. doi:10.1021/jp2073914.

[90] D. Sharon, V. Etacheri, A. Garsuch, M. Afri, A.A. Frimer, D. Aurbach, On the Challenge of Electrolyte Solutions for Li-Air Batteries: Monitoring Oxygen Reduction and Related Reactions in Polyether Solutions by Spectroscopy and EQCM, J. Phys. Chem. Lett. 4 (2013) 127–131. doi:10.1021/jz3017842.

[91] J. Read, Ether-Based Electrolytes for the Lithium/Oxygen Organic Electrolyte Battery, J. Electrochem. Soc. 153 (2006) A96–A100. doi:10.1149/1.2131827.

[92] M. Riley, P.S. Fedkiw, S. a. Khan, Transport Properties of Lithium Hectorite-Based Composite Electrolytes, J. Electrochem. Soc. 149 (2002) A667–A674. doi:10.1149/1.1470652.

[93] S. Zugmann, M. Fleischmann, M. Amereller, R.M. Gschwind, H.D. Wiemhöfer, H.J. Gores, Measurement of Transference Numbers for Lithium Ion Electrolytes via Four Different Methods, a Comparative Study, Electrochim. Acta. 56 (2011) 3926–3933. doi:10.1016/j.electacta.2011.02.025.

[94] L.O. Valøen, J.N. Reimers, Transport Properties of LiPF6-Based Li-Ion Battery Electrolytes, J. Electrochem. Soc. 152 (2005) A882–A891. doi:10.1149/1.1872737.

[95] S.G. Stewart, J. Newman, The Use of UV/vis Absorption to Measure Diffusion Coefficients in $LiPF_6$ Electrolytic Solutions, J. Electrochem. Soc. 155 (2008) F13–F16. doi:10.1149/1.2801378.

[96] S. Stewart, J. Newman, Measuring the Salt Activity Coefficient in Lithium-Battery Electrolytes, J. Electrochem. Soc. 155 (2008) A458–A463. doi:10.1149/1.2904526.

[97] T. Nishida, K. Nishikawa, Y. Fukunaka, Diffusivity Measurement of $LiPF_6$, LiTFSI, $LiBF_4$ in PC, ECS Trans. 6 (2008) 1–14. doi:10.1149/1.2831921.

[98] J. Zhao, L. Wang, X. He, C. Wan, C. Jiang, Determination of Lithium-Ion Transference Numbers in $LiPF_6$–PC Solutions Based on Electrochemical Polarization and NMR Measurements, J. Electrochem. Soc. 155 (2008) A292–A296. doi:10.1149/1.2837832.

[99] X. Andrieu, Ultracapacitors for Portable Electronics, in: T. Osaka, M. Datta (Eds.), Energy Storage Syst. Electron., CRC Press, Amsterdam, 2000: pp. 521–548.

[100] C.O. Laoire, S. Mukerjee, K.M. Abraham, E.J. Plichta, M.A. Hendrickson, Influence of Nonaqueous Solvents on the Electrochemistry of Oxygen in the Rechargeable Lithium−Air Battery, J. Phys. Chem. C. 114 (2010) 9178–9186. doi:10.1021/jp102019y.

[101] S.-I. Lee, U.-H. Jung, Y.-S. Kim, M.-H. Kim, D.-J. Ahn, H.-S. Chun, A Study of Electrochemical Kinetics of Lithium Ion in Organic Electrolytes, Korean J. Chem. Eng. 19 (2002) 638–644. doi:10.1007/BF02699310.

[102] C.W. Tobias, M. Eisenberg, C.R. Wilke, Diffusion and Convection in Electrolysis - A Theoretical Review, Electrochem. Ion. Cryst. 99 (1952) 359–365.

[103] R.S. Nicholson, I. Shain, Theory of Stationary Electrode Polarography: Single Scan and Cyclic Methods Applied to Reversible, Irreversible, and Kinetic Systems, Anal. Chem. 36 (1964) 706–723. doi:10.1021/ac60210a007.

[104] J.E.B. Randles, A Cathode Ray Polarograph, Trans. Faraday Soc. 44 (1948) 322–327.

[105] A. Sevcik, Oscillographic Polarography with Periodical Triangular Voltage, Collect. Czechoslov. Chem. Commun. 13 (1948) 349–377. doi:10.1135/cccc19480349.

[106] Y. Saito, H. Yamamoto, H. Kageyama, O. Nakamura, Investigation of the Solution Condition of Lithium Electrolyte Solutions with $LiCF_3SO_3$ Salt, J. Mater. Sci. 5 (2000) 809–812. doi:10.1023/A:1004717517628.

[107] C. Capiglia, Y. Saito, H. Kageyama, P. Mustarelli, T. Iwamoto, T. Tabuchi, et al., ^{7}Li and ^{19}F Diffusion Coefficients and Thermal Properties of Non-Aqueous Electrolyte Solutions for Rechargeable Lithium Batteries, J. Power Sources. 81-82 (1999) 859–862. doi:10.1016/S0378-7753(98)00237-7.

[108] M. Mizuhata, F. Ito, S. Deki, Transport Properties of Non-Aqueous Lithium Electrolyte Coexisting with Porous Solid Materials, J. Power Sources. 146 (2005) 365–370. doi:10.1016/j.jpowsour.2005.03.020.

[109] A. Nyman, Thesis: An Experimental and Theoretical Study of the Mass Transport in Lithium-Ion Battery Electrolytes, 2011.

[110] A.S. Groisman, N.E. Khomutov, Solubility of Oxygen in Electrolyte Solutions, Russ. Chem. Rev. 59 (2007) 707–727. doi:10.1070/RC1990v059n08ABEH003550.

[111] K.E. Gubbins, R.D. Walker, The Solubility and Diffusivity of Oxygen in Electrolytic Solutions, J. Electrochem. Soc. 112 (1965) 469–471. doi:10.1149/1.2423575.

[112] C.S. Ho, L.-K. Ju, R.F. Baddour, D.I.C. Wang, Simultaneous Measurement of Oxygen Diffusion Coefficients and Solubilities in Electrolyte Solutions with a Polarographic Oxygen Electrode, Chem. Eng. Sci. 43 (1988) 3093–3107. doi:10.1016/0009-2509(88)80061-7.

[113] G.W. Hung, R.H. Dinius, Diffusivity of Oxygen in Electrolyte Solutions, J. Chemcal Eng. Data. 17 (1972) 449–451.

[114] R. Battino, T.R. Rettich, T. Tominaga, The Solubility of Oxygen and Ozone in Liquids, J. Phys. Chem. Ref. Data. 12 (1983) 163–177. doi:10.1063/1.555680.

[115] J. Read, K. Mutolo, M. Ervin, W. Behl, J. Wolfenstine, A. Driedger, et al., Oxygen Transport Properties of Organic Electrolytes and Performance of Lithium/Oxygen Battery, J. Electrochem. Soc. 150 (2003) A1351–A1356. doi:10.1149/1.1606454.

[116] P. Han, D.M. Bartels, Temperature Dependence of Oxygen Diffusion in H2O and D2O, J. Phys. Chem. 100 (1996) 5597–5602. doi:10.1021/jp952903y.

[117] J.E. Vivian, C.J. King, Diffusivity of Slightly Soluble Gases in Water, AIChE J. 10 (1964) 220–221. doi:10.1002/aic.690100217.

[118] T. Sridhar, O.E. Potter, Gas-Liquid Diffusion Coefficients Measured by Esr Linewidths, Can. J. Chem. Eng. 56 (1978) 399–400. doi:10.1002/cjce.5450560321.

[119] L.-K. Ju, C.S. Ho, Measuring Oxygen Diffusion Coefficients with Polarographic Oxygen Electrodes: I. Electrolyte Solutions, Biotechnol. Bioeng. 27 (1985) 1495–1499. doi:10.1002/bit.260271015.

[120] I. Kowalczk, J. Read, M. Salomon, Li-Air Batteries: A Classic Example of Limitations Owing to Solubilities, Pure Appl. Chem. 79 (2007) 851–860. doi:10.1351/pac200779050851.

[121] S.G. Stewart, Thesis: Determination of Transport Properties and Optimization of Lithium-Ion Batteries, University of California, Berkeley, 2007.

[122] D. Vasudevan, H. Wendt, Electroreduction of Oxygen in Aprotic Media, J. Electroanal. Chem. 192 (1995) 69–74. doi:10.1016/0022-0728(95)04044-O.

[123] D.L. Maricle, W.G. Hodgson, Reduction of Oxygen to Superoxide Anion in Aprotic Solvents, Anal. Chem. 37 (1965) 1562–1565. doi:10.1021/ac60231a027.

[124] C. Song, J. Zhang, Electrocatalytic Oxygen Reduction Reaction, in: J.J. Zhang (Ed.), PEM Fuel Cell Electrocatal. Catal. Layers Fundam. Appl., Springer-Verlag, London, 2008: pp. 89–134. doi:10.1007/978-1-84800-936-3_2.

[125] D.T. Sawyer, G. Chlerlcato, C.T. Angells, E.J. Nannl, T. Tsuchlya, Effects of Media and Electrode Materials on the Electrochemical Reduction of Dioxygen, Anal. Chem. 54 (1982) 1720–1724. doi:10.1021/ac00248a014.

[126] I.M. AlNashef, M.L. Leonard, M.C. Kittle, M.A. Matthews, J.W. Weidner, Electrochemical Generation of Superoxide in Room-Temperature Ionic Liquids, Electrochem. Solid-State Lett. 4 (2001) D16–D18. doi:10.1149/1.1406997.

[127] I.M. AlNashef, M.L. Leonard, M.A. Matthews, J.W. Weidner, Superoxide Electrochemistry in an Ionic Liquid, Ind. Eng. Chem. Res. 41 (2002) 4475–4478. doi:10.1021/ie010787h.

[128] D. Zhang, T. Okajima, F. Matsumoto, T. Ohsaka, Electroreduction of Dioxygen in 1-N-Alkyl-3-Methylimidazolium Tetrafluoroborate Room-Temperature Ionic Liquids, J. Electrochem. Soc. 151 (2004) D31–D37. doi:10.1149/1.1649748.

[129] M.M. Ottakam Thotiyl, S. a Freunberger, Z. Peng, Y. Chen, Z. Liu, P.G. Bruce, A Stable Cathode for the Aprotic Li-O_2 Battery., Nat. Mater. 12 (2013) 1050–6. doi:10.1038/nmat3737.

[130] Z. Peng, S. a Freunberger, Y. Chen, P.G. Bruce, A Reversible and Higher-Rate Li-O_2 Battery, Science. 337 (2012) 563–566. doi:10.1126/science.1223985.

[131] D. Xu, Z. Wang, J. Xu, L. Zhang, X. Zhang, Novel DMSO-Based Electrolyte for High Performance Rechargeable Li–O_2 Batteries, Chem. Commun. 48 (2012) 6948–6950. doi:10.1039/c2cc32844e.

[132] D. Sharon, M. Afri, M. Noked, A. Garsuch, A.A. Frimer, D. Aurbach, Oxidation of Dimethyl Sulfoxide Solutions by Electrochemical Reduction of Oxygen, J. Phys. Chem. Lett. 4 (2013) 3115–3119.

[133] S.S. Zhang, K. Xu, J. Read, A Non-Aqueous Electrolyte for the Operation of Li/air Battery in Ambient Environment, J. Power Sources. 196 (2011) 3906–3910. doi:10.1016/j.jpowsour.2010.12.092.

[134] C.M. Doyle, Thesis: Design and Simulation of Lithium Rechargeable Batteries, University of California, Berkeley, 1995.

[135] Y.-C. Lu, D.G. Kwabi, K.P.C. Yao, J.R. Harding, J. Zhou, L. Zuin, et al., The Discharge Rate Capability of Rechargeable Li-O_2 Batteries, Energy Environ. Sci. 4 (2011) 2999–3007. doi:10.1039/c1ee01500a.

[136] Y.R. Dougassa, J. Jacquemin, L. El Ouatani, C. Tessier, M. Anouti, Viscosity and Carbon Dioxide Solubility for $LiPF_6$, LiTFSI, and LiFAP in Alkyl Carbonates: Lithium Salt Nature and Concentration Effect, J. Phys. Chem. B. 118 (2014) 3973–3980. doi:10.1021/jp500063c.

Table 1-1 Summary of governing equations for continuum-scale models for Li–O_2 batteries

Independent variables	Governing Equations	Field variables	
Oxygen concentration c_{O_2} [mol m^{-3}]	$\varepsilon \frac{\partial c_{O_2}}{\partial t} + \nabla \cdot \left(-D_{O_2}^{eff} \nabla c_{O_2} \right) = r_{O_2}$	Oxygen generation rate [mol m^{-3} s^{-1}]	$r_{O_2} = \frac{s_{O_2,R} A_{ED} j_R}{n_R F}$
		Li^+ generation rate [mol m^{-3} s^{-1}]	$r_{Li} = \frac{s_{Li,R} A_{ED} j_R}{n_R F}$
Electrolyte concentration c_{Li} [mol m^{-3}]	$\varepsilon \frac{\partial c_{Li}}{\partial t} + \nabla \cdot \left(-D_{Li}^{eff} \nabla c_{Li} \right) = r_{Li} - \nabla \cdot \left(\frac{\boldsymbol{i}_2 t_+}{F} \right)$	Electrolyte current density [A m^{-2}]	$\boldsymbol{i}_2 = -k^{eff} \nabla \phi_2 - \frac{2RTk^{eff}}{F} \left(t_+^0 - 1 \right) \left(1 + \frac{\partial \ln f_\pm}{\partial \ln c_{Li}} \right) \nabla \ln c_{Li}$
Electric potential in the electrolyte ϕ_2 [V]	$\nabla \cdot \left(-k^{eff} \nabla \phi_2 \right) = \nabla \cdot \left(\frac{k_D}{c_{Li}} \nabla c_{Li} \right) + A_{ED} j_R$	Diffusion conductivity [A m^{-1}]	$k_D = \frac{2RTk^{eff}}{F} \left(t_+^0 - 1 \right) \left(1 + \frac{\partial \ln f_\pm}{\partial \ln c_{Li}} \right)$
		Interfacial current density [A m^{-2}]	$j_R = f\left(c_{O_2}, c_{Li}, \eta_c \right)$
Electric potential in the electrode ϕ_1 [V]	$\nabla \cdot \left(-k_c^{eff} \nabla \phi_1 \right) = -A_{ED} j_R$	Activation overpotential [V]	$\eta_c = \phi_1 - \phi_2 - \Delta \phi_{Li_2O_2} - E_c^{\,0}$

Table 1-2 Features of continuum-scale physical models for Li–O_2 batteries

Investigators	1-D/2-D	Numerical/Analytical	Concentrated solution	Temperature	Oxygen transport	Passive/Active	Convection	Anode Kinetics	Cathode Kinetics	Discharging	Charging	Side reactions	Multi-layer electrode	Overpotentials: Anode kinetics	Overpotentials: Cathode kinetics	Overpotentials: Ohmic loss	Overpotentials: Electrode backbone	Overpotentials: Deposition layer	Coverage model	Pore shape	Pore/Particle size distribution	Volume change	Model Electrolyte	Current (mA cm^{-2})	Capacity (mAh g^{-1})
Sandhu et al. 2007[16]	1-D	Ana	N	Y	D	P	N	BV	BV	Y	N	N	N	Y	Y	Y	Y	N	N	N/A	N	N	$LiPF_6$ in PC:DME	0.2	3,863 mAh g^{-1}Li
Andrei et al. 2010 [47]	1-D	Num	Y	N	D	P	N	BV	BV	Y	N	N	N	Y	Y	Y	N	Y	Y	CPo	N	N	Organic	0.05 ─ 1	100 – 2,750 mAh g_c^{-1}
Albertus et al. 2011 [32]	1-D	Num	Y	N	D	P	N	BV	T	Y	N	N	N	Y	Y	Y	N	Y	N	SPa	N	N	LiTFSI in PC	0.75×10^{-3} -3.76×10^{-3}	200 – 800 mAh g_c^{-1}
Li and Faghri 2012[33]	2-D	Num	N	Y	D	P	N	R	T	Y	N	N	N	N	Y	Y	N	N	Y	SPo	N	N	Organic	0.05 – 0.5	200 – 1,500
Wang 2012[42]	1-D	Ana	N	Y	D	P	N	N/A	T	Y	N	N	N	N	Y	Y	N	Y	Y	SPa, CPo, FPo	N	N	Organic	0.001 – 2	40 – 100 mAh cm^{-2}
Andrei et al. 2012[13]	1-D	Num	Y	N	D	P	N	BV	BV	Y	N	N	N	N	Y	Y	N	Y	Y	CPo	N	N	Hybrid	0.05 ─ 8	280 – 1,000 mAh g_c^{-1}
Wang and Cho 2013[28]	1-D	Ana	N	N	D	P	N	N/A	T	Y	N	N	N	N	Y	Y	N	N	Y	SPa	N	N	Organic	0.05 – 0.1	900 – 1,900
Horstmann et al. 2013[80]	1-D	Num	N	N	Tw	P	Y	BV	BV	Y	N	N	N	Y	Y	Y	Y	N	Y	N/A	N	N	Aqueous	0.01 – 10	100 – 900 mAh g^{-1}_{H2O}
Sahapatsombut et al. 2013[17]	1-D	Num	Y	N	D	P	N	BV	BV	Y	Y	N	N	Y	Y	Y	Y	Y	Y	N/A	N	N	$LiPF_6$ in ACN	0.05 – 1.0	100 – 1,500
Sahapatsombut et al. 2013[23]	1-D	Num	Y	N	D	P	N	BV	BV	Y	Y	Y	N	Y	Y	Y	Y	Y	Y	N/A	N	N	$LiPF_6$ in ACN	0.1	400 – 650
Franco and Xue 2013[18]	1-D	Num	N	N	D	P	N	N	T	Y	N	N	N	N	Y	Y	N	N	Y	N/A	Y	N	N/A	0.5	~225
Franco 2013[30]	1-D	Num	N	N	D	P	N	N/A	E	Y	Y	N	N	N	Y	Y	N	N	Y	N/A	N	N	Organic	N/A	1,500 – 3,000
Nimon et al. 2013 [19]	1-D	Num	N	N	D	P	N	N/A	BV	Y	N	N	N	N	Y	N	Y	N	N	N/A	N	N	0.5 M $LiN(CF_3SO_2)_2$ in DMF	0.1 – 0.25	40 – 60 mAh cm^{-2}
Sahapatsombut	1-D	Num	Y	N	D	P	N	BV	BV	Y	Y	Y	N	Y	Y	Y	Y	Y	Y	N/A	N	N	$LiPF_6$ in ACN	0.05 – 0.1	100 – 1200

et al. 2014[39]																								
Xue, et al 2014 [41]	1-D	Num	N	N	D	P	N	N/A	T	Y	N	N	N	N	Y	Y	N	Y	Y	SPo	Y	N	Organic	0.5 – 1.0	200 – 500
Yoo et al. 2014[20]	1-D	Num	Y	N	D	P	N	BV	BV	Y	Y	N	N	Y	Y	Y	Y	Y	N	N/A	N	Y	$LiPF_6$ in PC:DME	0.1 – 0.3	0 – 1,000
Chen, et al 2014 [40]	1-D	Num	Y	N	D	P	N	N/A	T	Y	N	N	N	N	Y	Y	Y	Y	Y	CPa/ CPo	Y	N	$LiPF_6$ in TEGDME	0.2 ─ 1.0	100 –1,300 mAh g_c^{-1}
Wang and Cho 2015 [27]	2-D	Num	Y	N	D	P	N	BV	BV	Y	N	N	N	Y	Y	Y	Y	Y	Y	SPa, CPo, FPo	N	N	Organic	0.05 – 0.2	10 – 1,500
Li et al. 2015 [29]	2-D	Num	N	Y	D	A	Y	R	T	Y	N	N	Y	N	Y	Y	Y	Y	Y	SPo	N	N	$LiPF_6$ in PC:DME	0.1 – 2.5	200 – 1,500
Li 2015 [51]	2-D	Num	N	Y	D	P	N	R	T	Y	N	N	N	N	Y	Y	Y	Y	Y	SPo	Y	N	Organic	0.05 – 0.5	200 – 1,500
Huang and Faghri 2015 [81]	2-D	Num	Y	Y	D	A	Y	R	T	Y	N	N	Y	N	Y	Y	Y	Y	Y	SPo	N	N	$LiPF_6$ in EC:EMC	0.1 – 2.0	100 – 1,600
Xue et al. 2015 [43]	1-D	Num	N	N	D	P	N	N/A	BV	Y	N	N	N	N	Y	Y	N	Y	Y	SPo	Y	N	Li Triflate in DMSO and TEGDME	0.2 – 1.0	450 - 2000
Jung et al. 2015 [21]	1-D	Num	Y	N	D	P	N	N/A	BV	Y	N	N	N	Y	Y	Y	Y	Y	Y	SPa	N	N	$LiPF_6$ in PC:DME	0.05 – 1.0	500 – 2,800
Sergeev et al. 2015[22]	1-D	Num	N	N	D	P	N	BV	BV	T	N	N	N	Y	Y	N	Y	N	N	N/A	N	N	1M unknown salt in MeCN, DME, DMSO	0.1 – 3	1,000 – 4,700

1-D: One dimensional model; 2-D: Two dimensional model; 2-D-m: Two dimensional meso-scale; A: Active; Ana: Analytical; BV: Butler–Volmer; C: Constant; CPa: Cylindrical Particle; CPo: Cylindrical Pore; D: Oxygen dissolved in electrolyte; E: Empirical differential rate equation; F: Fick's law; FO: 1st order reaction; FPo: Flat Pore; N: No; N/A: Not vailable; Ns: Non-smooth; Num: Numerical; P: Passive; R: Reversible; S: Smooth; SM: Stefan–Maxwell model; SPa: Spherical Particle; SPo: Spherical Pore; T: Tafel; Tw: Two phase model; Y: Yes.

Table 1-3 Relationships between structural parameters with different pore structures for Li–O_2 battery cathode models

Case	Pore structure	Specific surface area, $A_{ED,0}$	Deposit layer thickness, δ_s	Specific surface area change, $A_{ED}/A_{ED,0}$
(a)	Spherical particle	$\frac{6(1-\varepsilon_0)}{d_0}$	$\frac{d_0}{2}\left[\left(1+\frac{\varepsilon_s}{1-\varepsilon_0}\right)^{1/3}-1\right]$	$\left(1+\frac{\varepsilon_s}{1-\varepsilon_0}\right)^{2/3}$
(b)	Spherical pore	$\frac{6\varepsilon_0}{d_0}$	$\frac{d_0}{2}\left[1-\left(1-\frac{\varepsilon_s}{\varepsilon_0}\right)^{1/3}\right]$	$\left(1-\frac{\varepsilon_s}{\varepsilon_0}\right)^{2/3}$
(c)	Cylindrical particle	$\frac{4(1-\varepsilon_0)}{d_0}$	$\frac{d_0}{2}\left[\left(1+\frac{\varepsilon_s}{1-\varepsilon_0}\right)^{1/2}-1\right]$	$\left(1+\frac{\varepsilon_s}{1-\varepsilon_0}\right)^{1/2}$
(d)	Cylindrical pore	$\frac{4\varepsilon_0}{d_0}$	$r_0\left[1-\left(1-\frac{\varepsilon_s}{\varepsilon_0}\right)^{1/2}\right]$	$\left(1-\frac{\varepsilon_s}{\varepsilon_0}\right)^{1/2}$
(e)	Flat shape	$\frac{2\varepsilon_0}{d_0}$	$\frac{D_0\varepsilon_s}{2\varepsilon_0}$	1

Table 1-4 Deposition layer voltage drop sub-model for Li–O_2 batteries

Investigators	Micro-structure	Overpotential caused by insulate deposition layer, $\Delta\phi_s$	Parameters
Andrei et al. 2010, 2012 [13,47]	CPo*	$j\rho_s r \ln\frac{r}{r_0} = j\rho_s r_0\sqrt{\frac{\varepsilon}{\varepsilon_0}}\ln\sqrt{\frac{\varepsilon}{\varepsilon_0}}$	ρ_s: $5\times10^8 - 6\times10^{10}$ Ω·m, r_0 : 20 nm
Albertus et al. 2011 [32]	Spa	$j\rho_s\delta_s = j\delta_s e^{c_1(\delta_s - c_2)}$	ρ_s: 9.4×10^{-8} Ω·m @ δ_s =30nm
Wang 2012 [42] Wang and Cho 2015 [27]	SPo, CPo, FPo	$j\left(R_s e^{c_1\delta_s} + R_c\right)$	R_s: 8.5×10^7 Ω·m^2, R_c: contact resistance
Sahapatsombut, et al. 2013, 2014 [17,23,39]	Am	$jR_s\varepsilon_s$	R_s : 50 Ω·m^2
Chen et al. 2014 [40]	CPo/CPa	$j\rho_s r_0\sqrt{\frac{1-\varepsilon}{1-\varepsilon_0}}\ln\sqrt{\frac{1-\varepsilon}{1-\varepsilon_0}}$ $\Delta\phi_s' + j\rho_s r_0'\sqrt{\frac{\varepsilon}{\varepsilon_0'}}\ln\sqrt{\frac{\varepsilon}{\varepsilon_0'}}$	ρ_s: 2×10^{10} Ω·m, r_0 : 5 – 60 nm
Xue et al. 2014 [41]	SPo	$j\rho_s\delta_s$	ρ_s: 10^8 Ω·m
Jung et al. 2015 [21]	Spa	$j\frac{\delta_s^2}{\int k_{eff}\,d\delta_s}$	

* CPo: Cylindrical pore; SPa: Spherical particle; SPo: Spherical pore; Am: Amorphous; CPa: Cylindrical particle; FPo: Flat pore

Table 1-5 Summary of commonly used electrolytes for Li–O_2 batteries

Solvent	Examples	Advantages	Disadvantages
Alkyl carbonate	PC, EC, EMC, DMC, DEC	Widely studied, property data readily available	High vapor pressure Decomposition due to O_2^- attack and oxidation during charging
Ether	TEGDME[129], DME[91]	Low vapor pressure Stable Good salt solubility Wide electrochemical window	Autoxidation
Ester	BL MF	Can have low viscosity and high salt dissolution	High vapor pressure, Susceptible to O_2^- attack
Nitrile	ACN, TMA	Stable to O_2^-	High vapor pressure,
Amide	DMA, DMF, NMP	Stable to O_2^-	High vapor pressure, side reactions, unstable SEI
DMSO[129–131]		Stable to O_2^- with non-carbon electrode [132]	Side reactions, reactive with Li metal, high vapor pressure
Sulfones	TMSO	Stable to O_2^-, low vapor pressure	High melting temperature
Ionic Fluids	EMITFSI	Low vapor pressure, low flammability, hydrophobicity, wide electrochemical window, stable	Poor salt solubility Susceptible to moisture

Table 1-6 Ionic conductivity of organic electrolytes for Li–O_2 batteries

Ref.	c (M)	Salt	Solvent	k (S m^{-1})
Read et al. 2003 [115]	1	$LiPF_6$	PC:EC(1:1 wt)	0.65
			PC	0.55
			PC:DME(1:1 wt)	1.32
			PC:DMC(1:1 wt)	0.94
			PC:DEC(1:1 wt)	0.67
			PC:DME (1:2 wt)	1.59
	0.5		PC:DME (1:2 wt)	1.22
Xu et al. 2009 [78]	1	LiTFSI	PC:EC(1:1 wt)	0.504
			PC:DME(1:1 wt)	1.141
			PC:DEE(1:1 wt)	0.787
			PC:BEE(1:1 wt)	0.478
			PC:DG(1:1 wt)	0.726
			PC:DPG(1:1 wt)	0.519
			PC:EDG(1:1 wt)	0.553
			PC:BDG(1:1 wt)	0.347
	1	$LiPF_6$	PC:EC (1:1 wt)	0.624
	1	$LiClO_4$	PC:EC (1:1 wt)	0.563
	1	LiI	PC:EC (1:1 wt)	0.627
	1	LiBr	PC:EC (1:1 wt)	0.273
	1	$LiSO_3CF_3$	PC:EC (1:1 wt)	0.208
	1	LiBOB	PC:EC (1:1 wt)	0.313
	1	LiTFSI	PC:EC (1:1 wt)	0.504
Laoire et al. 2010 [100]	0.1	$LiPF_6$	DMSO	0.211
			MeCN	1.439
			DME	0.116
			TEGDME	0.03
Zhang et al. 2011 [133]	0.2	$LiSO_3CF_3$	PC:TFP(1:1)	0.0937
			PC	0.165
Read 2006 [91]	1	LiBr	DOL:DME (1:1 wt)	0.105
		LiTriflate	DOL:DME (1:1 wt)	0.238
		LiImide	DOL:DME (1:1 wt)	1.120
		LiBETI	DOL:DME (1:1 wt)	1.109
Nyman 2008, 2011 [24,109]	0 – 2	$LiPF_6$	EC:EMC(3:7 wt)	$0.1297c^3 - 2.51c^{1.5} + 3.329$
Doyle 1995 [134]	0.1 – 4	$LiPF_6$	EC:DMC (2:1 v)	$0.0911 + 1.9101c - 1.052c^2 + 0.1554c^3$
Valøen and Reimers 2005 [94]	0 – 4	$LiPF_6$	PC:EC:DMC(10:27:63 v)	0 – 2.1 (function of c and T)

Table 1-7 Salt diffusion coefficient and transference number of non-aqueous electrolytes for $Li–O_2$ batteries

Ref.	c (M)	Salt	Solvent	D ($\times 10^{-9}$ m^2 s^{-1})	t_+
Jung et al. 2012 [76]	1	$LiCF_3SO_3$	TEGDME	0.0003	
	0.1–1	$LiClO_4$	PC	$0.476+0.126c$	
Lee et al. 2002 [101]	0.1–1	$LiPF_6$	EC:DEC (1:1)	$e^{-0.784+0.969c}$	
	0.1–1	$LiPF_6$	EC:DMC (1:1)	$e^{-0.1884-0.1605c+0.6696c^2}$	
Stewart and Newman 2008 [95]	0–1	$LiPF_6$	EC:DEC (1:1 wt)	$3.018e^{-0.357c}$	
	0–2	$LiPF_6$	ACN	$2.582e^{-2.856c}$	
Nyman 2008, 2011 [24,109]	0–2	$LiPF_6$	EC:EMC(3:7 wt)		$-0.1287c^3+0.4106c^2-0.4717c+0.4492$ *
Saito et al. 2000 [106]	0.002–2	$LiCF_3SO_3$	PC or DME	0.1–0.2 (PC), 0.8–1.4 (DME)**	
Capiglia et al. 1999 [107]	0.1–1.5	$LiPF_6$	EC:EMC(2:8 wt)	$0.534e^{-0.65c}$ **	$0.4242-0.09599\times\left(4.6723e^{-13}\right)^c$
Lu et al. 2011 [135]	1	$LiBF_4$	PC:DME(1:2)	0.077**	0.43
Stewart and Newman 2008 [96]	0−2	$LiPF_6$	EC:EMC(1:1 wt)		0.38
Zhao et al. 2008 [98]	0.25–1.5	$LiPF_6$	PC		$0.3424+0.315*0.2052^c$
Zugmann et al. 2011 [93]	0.05–0.93 mol kg^{-1}	LiDFOB	EC:DEC (3:7 wt)		$0.4407+0.00894c_m+0.00073408c_m^2+0.01276c_m^3$ ***
		$LiPF_6$	EC:DEC (3:7 wt)		0.24 – 0.28 @1mol kg^{-1}
Valøen and Reimers, 2005 [94]	0–4	$LiPF_6$	PC:EC:DMC (10:27:63 v)		function of both c and T

* t_+^0

** D_{Li}

*** c_m: mol kg^{-1}

Table 1-8 Oxygen related transport properties of non-aqueous electrolytes for Li–O_2 batteries

Ref.	c (M)	Salt	Solvent	$c_{O_2,sat}$ ($\times10^{-3}$ mol L^{-1})	Viscosity ($\times10^{-3}$ Pa s)	D_{O_2} ($\times10^{-9}$ m^2 s^{-1})	density (kg m^{-3})
Read et al. 2003 [115] (25 °C)	1	$LiPF_6$	PC:EC(1:1 wt)	2.122	7.73	0.233	1,282*
	1	$LiPF_6$	PC	2.272	8.06	0.224	1,230*
	1	$LiPF_6$	PC:DME(1:1 wt)	3.179	2.59	0.697	1,057*
	1	$LiPF_6$	PC:DMC(1:1 wt)	3.210	3.50	0.516	1,168*
	1	$LiPF_6$	PC:DEC(1:1 wt)	3.465	4.78	0.378	1,118*
	1	$LiPF_6$	PC:DME (1:2 wt)	4.395	1.98	0.912	1,011*
	0.5	$LiPF_6$	PC:DME (1:2 wt)	5.363	1.19	0.152	984*
Dougassa et al. 2014 [136]**	1	$LiPF_6$	EC:DMC(1:1 wt)		4.152	0.435	1,214*
Xu et al. 2009 [78] (25 °C)	1	LiTFSI	PC:EC(1:1 wt)	0.1775	7.10		
	1	LiTFSI	PC:DME(1:1 wt)	0.3235	2.59		
	1	LiTFSI	PC:DEE(1:1 wt)	0.3806	3.54		
	1	LiTFSI	PC:BEE(1:1 wt)	0.3175	5.78		
	1	LiTFSI	PC:DG(1:1 wt)	0.2566	4.31		
	1	LiTFSI	PC:DPG(1:1 wt)	0.2394	5.99		
	1	LiTFSI	PC:EDG(1:1 wt)	0.2688	5.72		
	1	LiTFSI	PC:BDG(1:1 wt)	0.2319	8.81		
	1	$LiPF_6$	PC:EC (1:1 wt)	0.1622	7.41		
	1	$LiClO_4$	PC:EC (1:1 wt)	0.1631	7.17		
	1	LiI	PC:EC (1:1 wt)	0.1216	7.70		
	1	LiBr	PC:EC (1:1 wt)	0.1209	7.02		
	1	$LiSO_3CF_3$	PC:EC (1:1 wt)	0.1663	6.63		
	1	LiBOB	PC:EC (1:1 wt)	0.1350	11.3		
Laoire et al. 2010 [100]	0.1	$LiPF_6$	DMSO	2.10	1.948	1.67	
			DME	9.57	0.46	1.22	
			MeCN	8.10	0.361	4.64	
			TEGDME	4.43	4.05	0.217	
Sawyer et al. 1982 [125]	0.1	TEAP	DMSO	2.10			
			MeCN	8.10			
			DMF	4.80			
			Pyr	4.90			
Zhang et al.	0.2	$LiSO_3CF_3$	PC:TFP(1:1)		3.492		
			PC		2.520		

2011 [133] (25 °C)			TFP		3.879		
Read et al. 2003 [115] (25 °C)	0		TMSO	1.572			
			EC	1.682			
			DMSO	1.832			
			BL	2.422			
			PC	3.162			
			NMP	3.175			
			TEGDME	4.373			
			Triglyme	4.641			
			DMC	7.186			
			DPC	7.729			
			DEC	7.807			
			EMC	7.838			
			THF	8.710			
			DME	9.437			
			PC:DMSO (1:4 wt)	1.889			
			PC:EC (1:3 wt)	1.977			
			PC:EC (1:1 wt)	2.571			
			PC:DME (3:1 wt)	3.796			
			PC:DMC (1:1 wt)	4.399			
			PC:DEC (1:1 wt)	5.143			
			PC:DME (1:1 wt)	5.218			
			BL:DME (1:2 wt)	5.517			
			PC:DME (1:2 wt)	5.879			
			PC:DME (1:4 wt)	6.746			
Read 2006 [91] (21 °C)	0		EC	1.738	1.85	0.962	1,338
			DMSO	2.535	1.99	0.895	1,096
			BL	3.754	1.75	1.02	1,125
			PC	3.844	2.53	0.704	1,198
			DOL	6.673	0.58	3.07	1,060
			DMC	8.616	0.59	3.02	1,070
			DME	8.677	0.46	3.87	860
			EMC	9.323	0.65	74	1,007
			DEC	9.850	0.75	2.37	969
			THF	10.09	0.46	3.87	889
			2-MeTHF	10.95	0.47	3.79	848
			DOL:DME	7.524	0.51	3.49	952
	1	LiBr	DOL:DME (1:1 wt)	5.385	0.866	2.06	1,028
	1	LiTriflate	DOL:DME (1:1 wt)	6.011	1.036	1.72	1,050
	1	LiImide	DOL:DME (1:1 wt)	6.575	1.255	1.42	1,114

1	LiBETI	DOL:DME (1:1 wt)	6.354	1.908	0.933	1,172

*Calculated based on ideal mixture assumption

** Temperature dependent, showing value at 25^{o}C

Table 1-9 Thermodynamic factor of non-aqueous electrolytes for Li–O_2 batteries

Ref	Salt	Solvent	Themodynamic factor @ Concentration c (mol L^{-1})
Valøen and Reimers 2005 [94]	$LiPF_6$	PC:EC:DMC (10:27:63 v)	$\frac{0.601-0.24c^{0.5}+0.982\left[1-0.0052\left(T-293\right)\right]c^{1.5}}{1-t_0^+}$
Nyman et al. 2008 [24]	$LiPF_6$	EC:EMC	$\frac{0.28687\times c^2-0.74678\times c+0.44103}{0.1287\times c^3-0.4106\times c^2+0.4717\times c+0.5508}$
Stewart and Newman 2008 [96]	$LiPF_6$	PC	$1+c\left[\frac{-1.6934}{2\left(1+3.92\sqrt{c}\right)}\left(\frac{1}{\sqrt{c}}-\frac{3.92}{1+3.92\sqrt{c}}\right)+1.5223\right]$
		EC:EMC	$1+c\left[\frac{-1.0178}{2\left(1+0.9831\sqrt{c}\right)}\left(\frac{1}{\sqrt{c}}-\frac{0.9831}{1+0.9831\sqrt{c}}\right)+1.5842\right]$

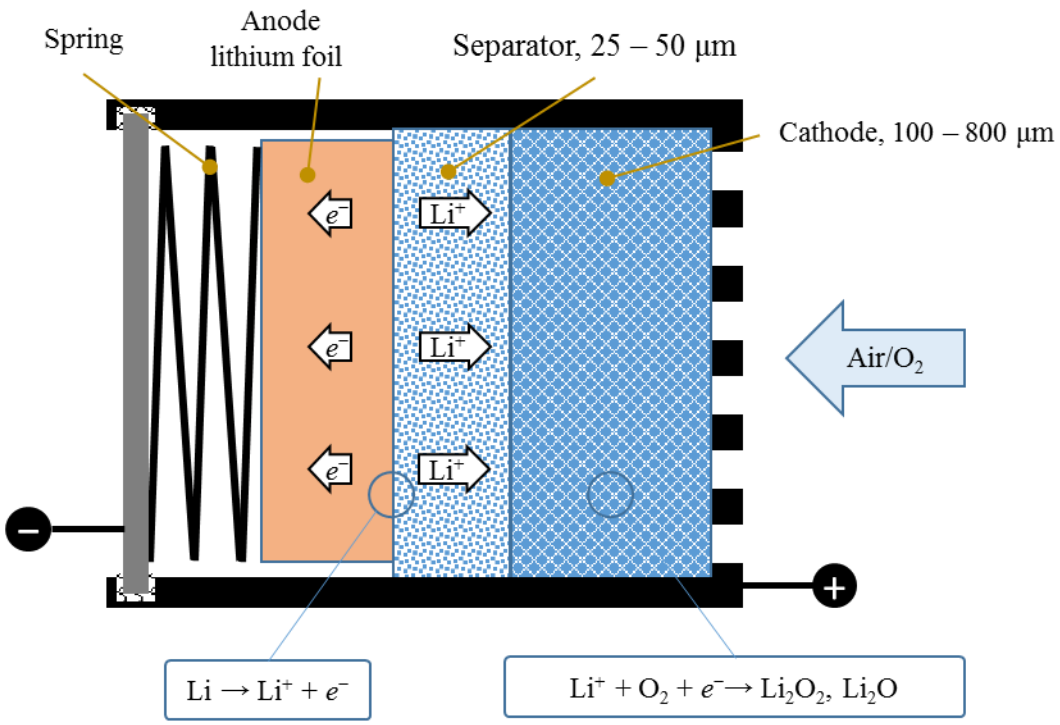

Figure 1-1 Structure and basic operation of a typical non-aqueous Li–O_2 cell.

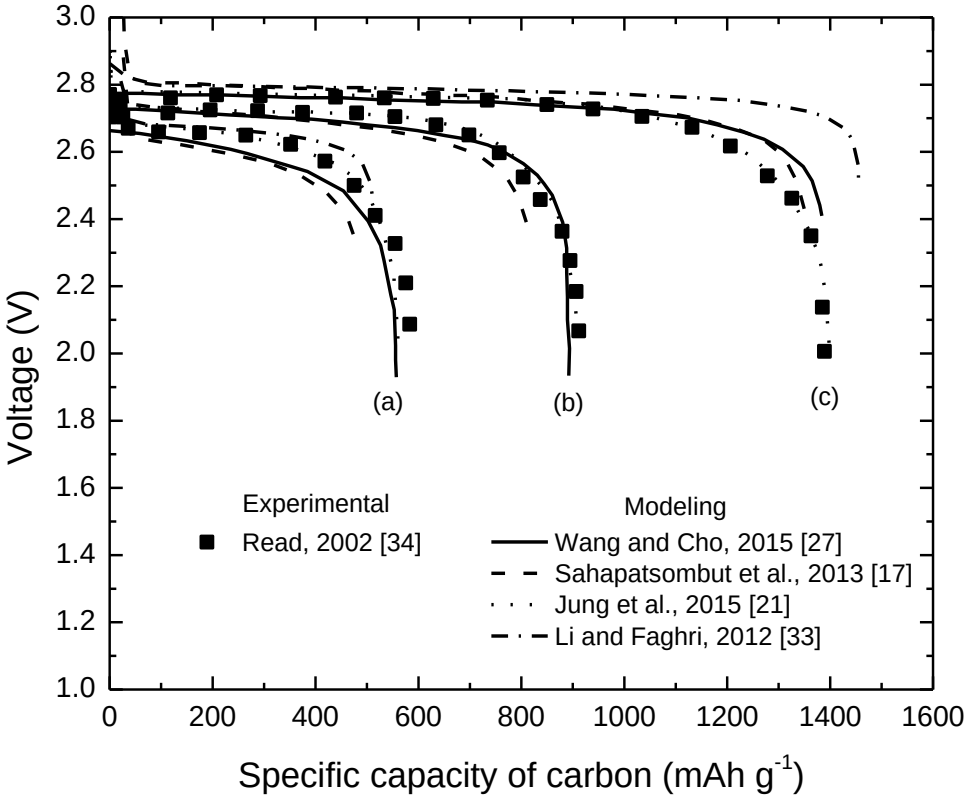

Figure 1-2 Comparison of the discharge curves predicted by various models (Wang and Cho [27], Sahapatsombut et al. [17], Jung et al. [21], Li and Faghri [33]) to the experimental results of Read 2002 [34] at different discharge current densities: (a) 0.05 mA cm^{-2}, (b) 0.1 mA cm^{-2}, and (c) 0.2 mA cm^{-2}.

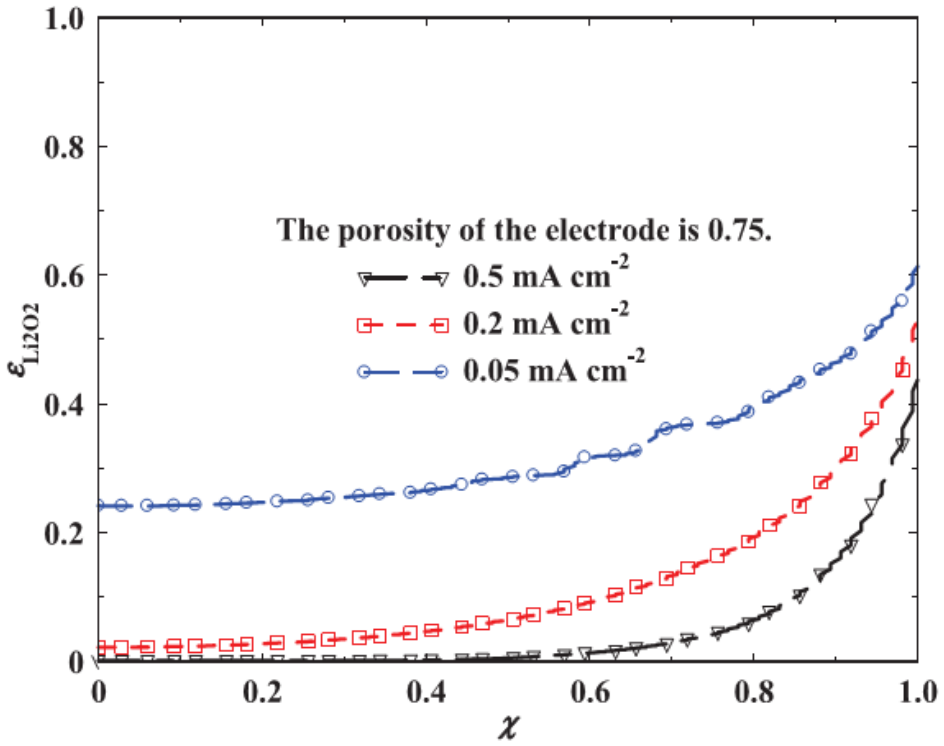

Figure 1-3 Distribution of Li_2O_2 volume fractions in the cathode at the end of discharge at various current densities [33].

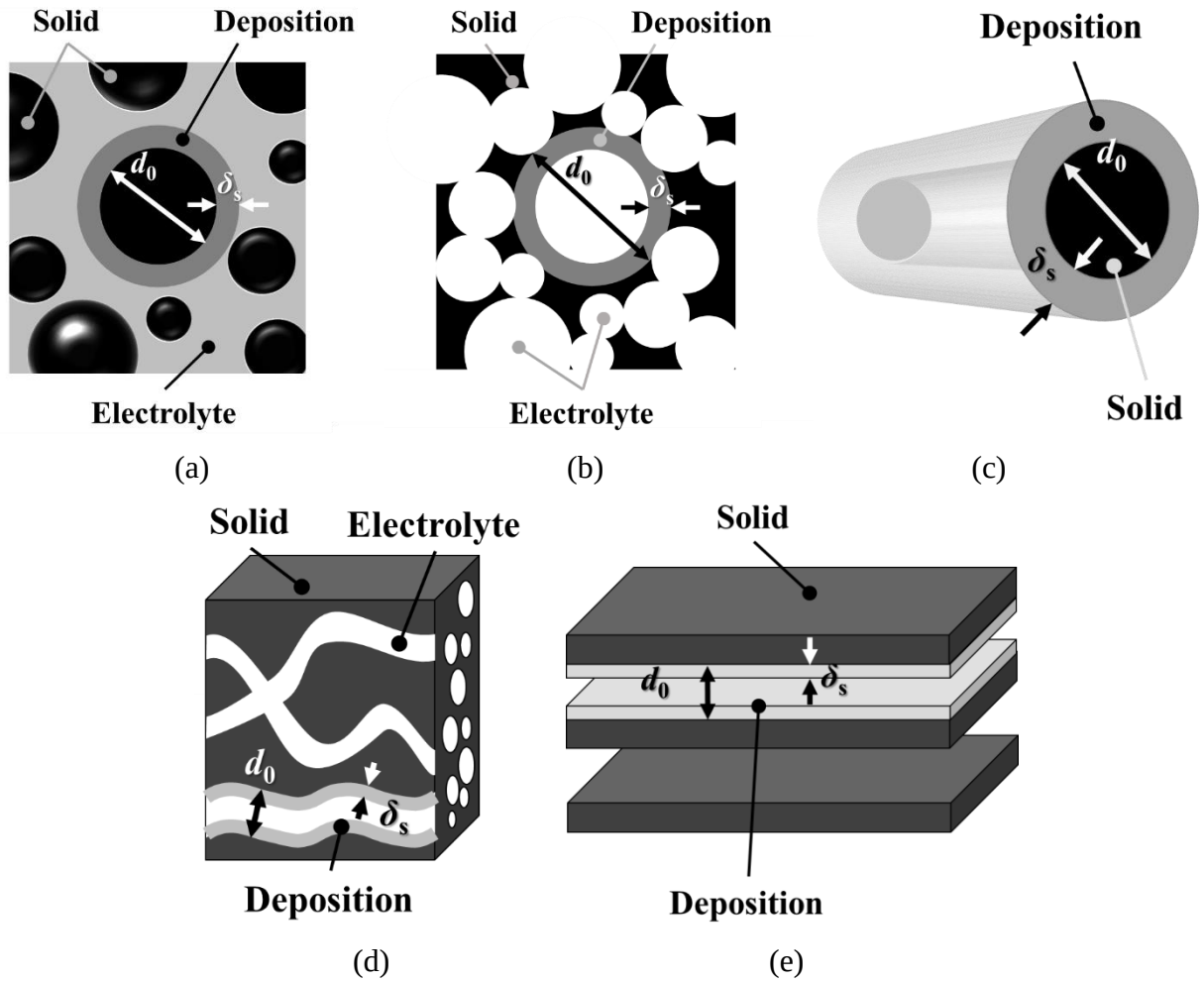

Figure 1-4 Simplified micro-scale structure of the electrode used in various models: (a) spherical particle, (c) spherical pore, (c) cylindrical particle, (d) cylindrical pore, and (e) flat pore.

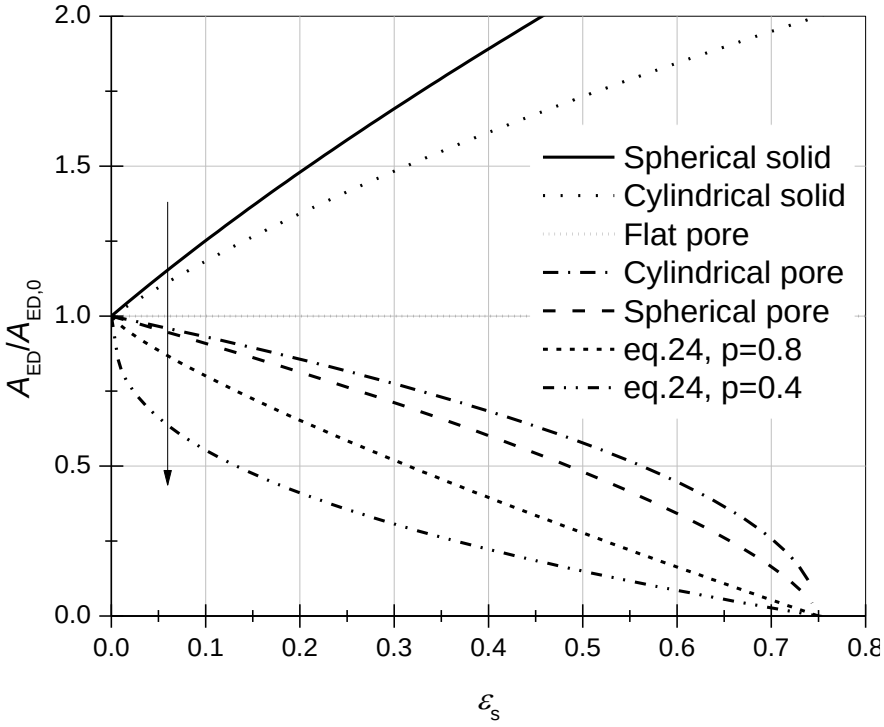

Figure 1-5 Dependence of specific surface area on solid precipitation volume fraction predicted by various models and parameters.

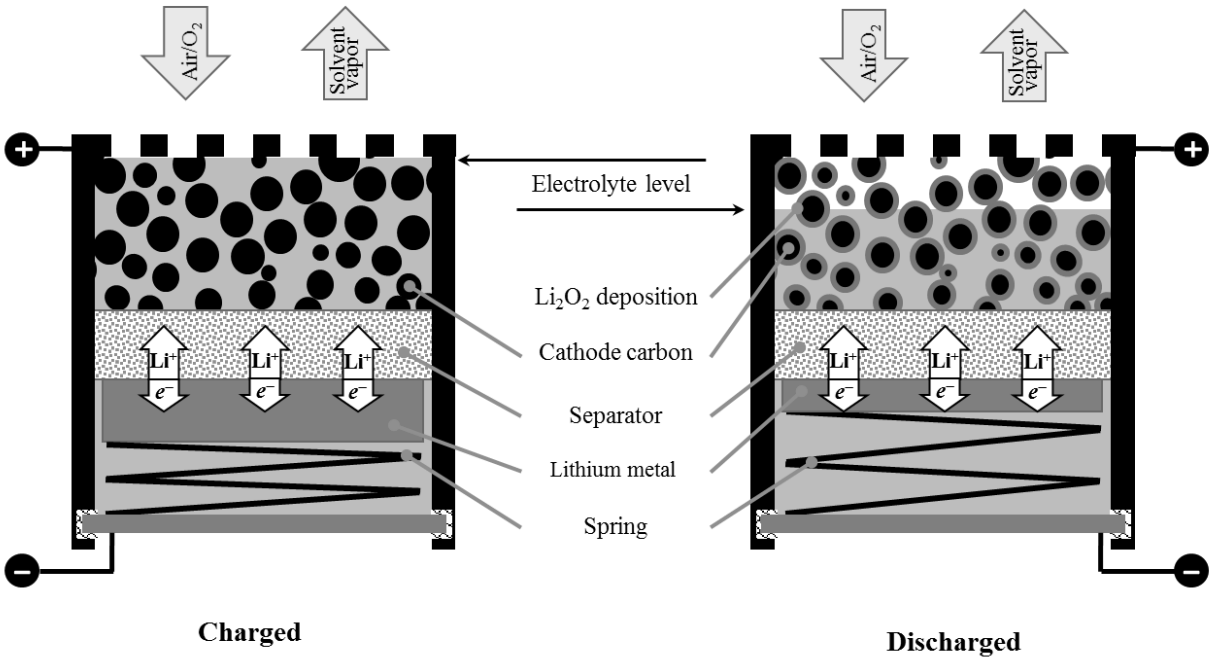

Figure 1-6 Solid-phase volume and electrolyte level change in a Li–O_2 coin cell.

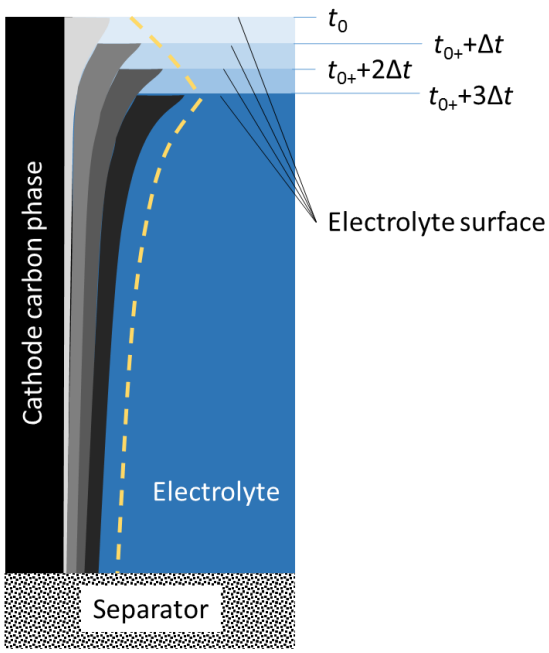

(a)

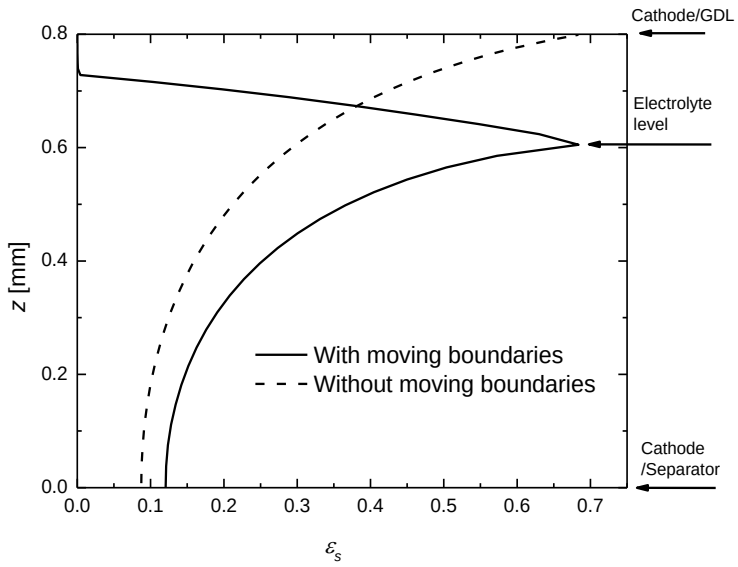

(b)

Figure 1-7 Distribution of ε_s with consideration of electrolyte level drop by (a) conceptual analysis and (b) model prediction [71].

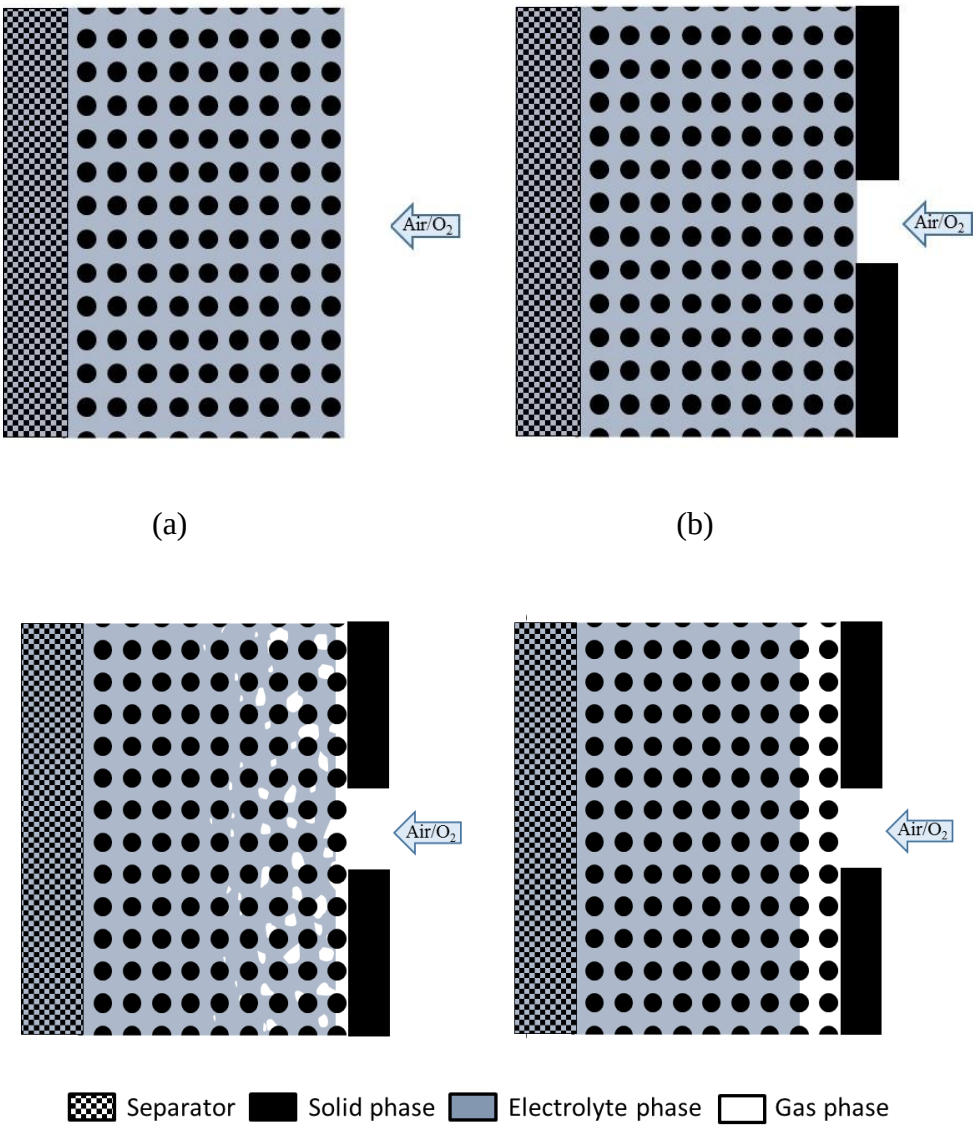

Figure 1-8 Illustration of (a) 1-D 2-phase model, (b) 2-D 2-phase model, (c) 3-phase model and (d) pseudo 3-phase model.

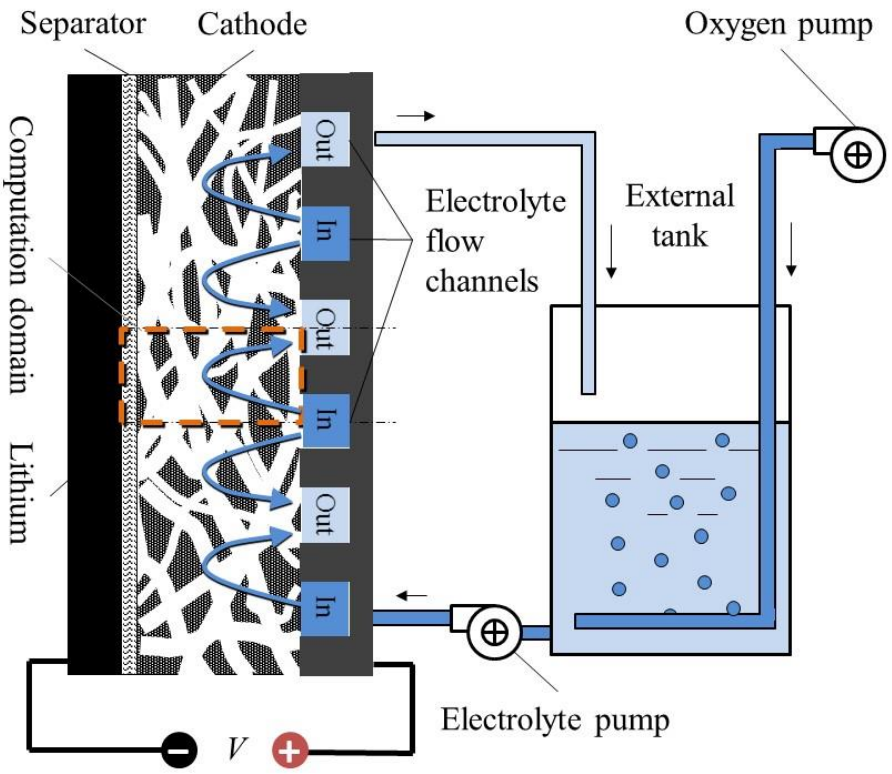

Figure 1-9 Configuration of an organic Li–O_2 flow battery (Li–O_2 battery with an active cathode).

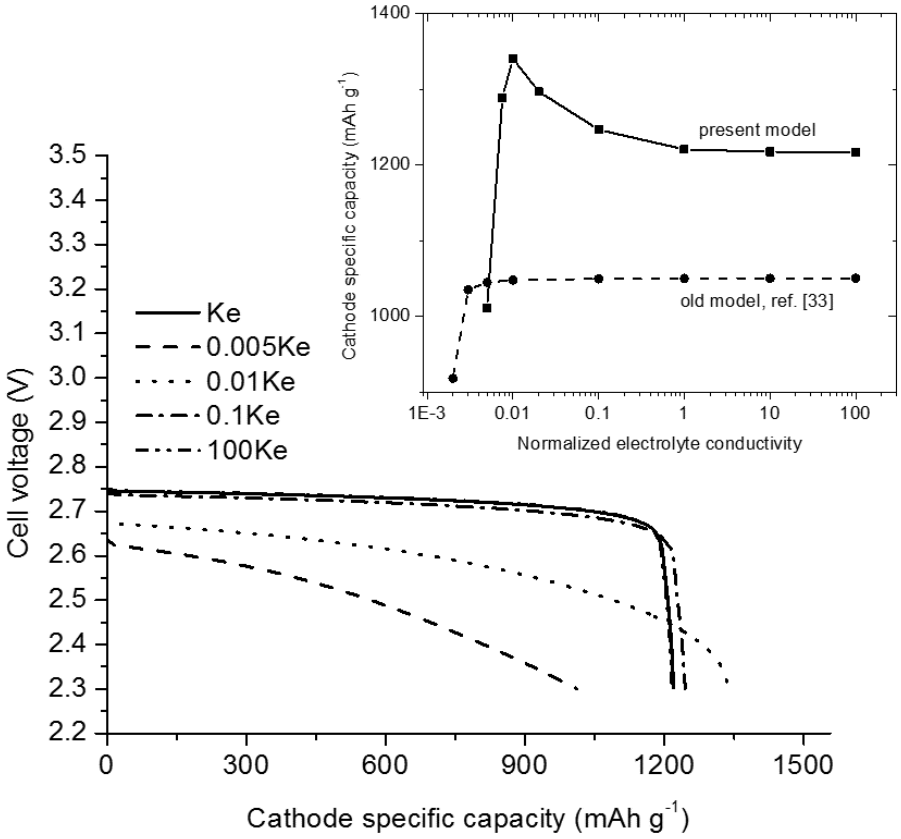

Figure 1-10 Effect of ionic conductivity of electrolyte on the discharge capacity of a $Li–O_2$ flow cell [81].

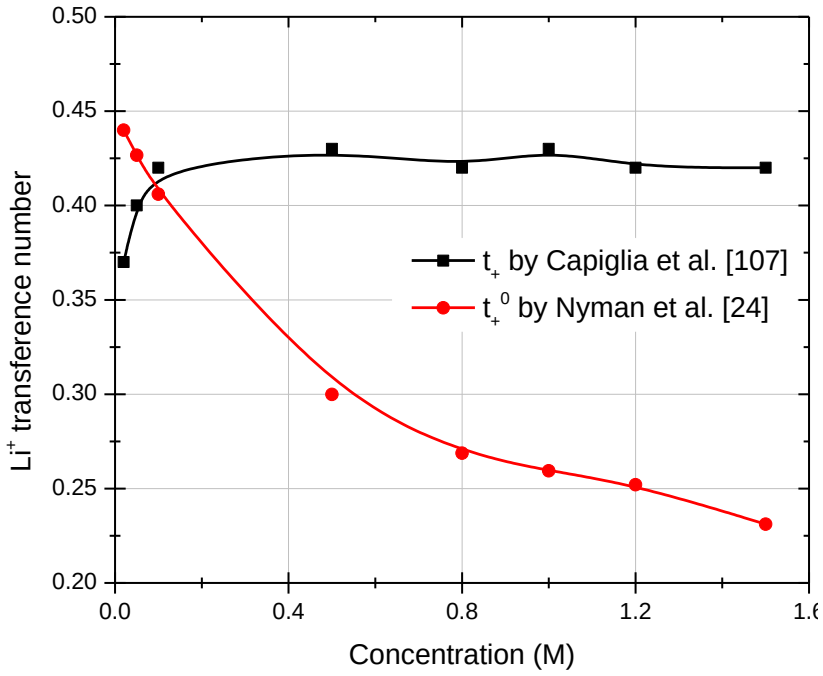

Figure 1-11 Comparison between t_+ and t_+^0 given by Capiglia et al. [107] and Nyman et al. [24]. The Electrolyte is $LiPF_6$ in EC:EMC.

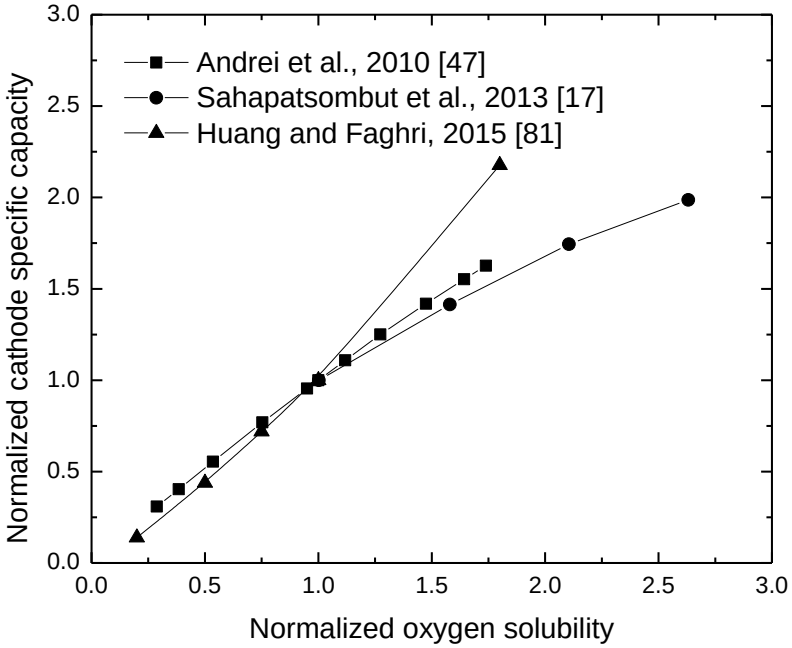

Figure 1-12 Effect of oxygen solubility on cathode specific capacity predicted by Andrei et al. 2010 [47], Sahapatsombut et al. 2013 [17], and Huang and Faghri 2015 [81].

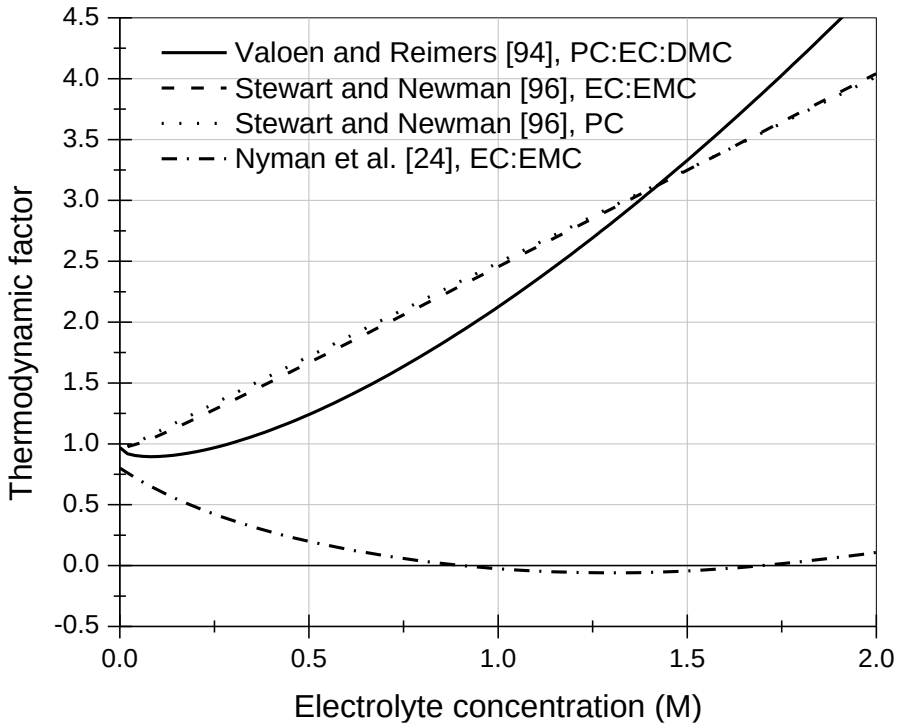

Figure 1-13 Comparison of thermodynamics factors provided by Valøen and Reimers [94], Stewart and Newman [96], and Nyman et al. [24].

Chapter 2 Modeling study of a Li-O_2 battery with an active cathode

In this chapter, a new organic lithium oxygen (Li-O_2) battery structure is proposed to enhance battery capacity. The electrolyte is forced to recirculate through the cathode and then saturated with oxygen in a tank external to the battery. The forced convection enhances oxygen transport and alleviates the problem of electrode blockage during discharge. A two dimensional, transient, non-isothermal simulation model is developed to study the heat and mass transfer within the battery and validate the proposed design. Results show that this novel active cathode design improves the battery capacity at all discharge current densities. The capacity of the Li-O_2 battery is increased by 15.5 times (from 12.2 mAh g^{-1} to 201 mAh g^{-1}) at the discharge current of 2.0 mA cm^{-2} when a conventional passive electrode is replaced by the newly designed active electrode. Furthermore, a cathode with non-uniform porosity is suggested and simulation results show that it can reach a higher discharge capacity without decreasing its power density. Detailed mass transport processes in the battery are also studied.

2.1 Introduction

The demand for rechargeable batteries in portable electronics, military applications, electric vehicles, and smart grids increases significantly each year. In 2001, the United States Advanced Battery Consortium (USABC) set the goal of 150 Wh kg^{-1} for batteries used in electric vehicles with acceptable driving range. [1] Commercial Li-ion batteries almost reached that goal, but the need for longer driving range and higher efficiency requires a specific energy above 400 Wh kg^{-1}, at significantly lower cost [2]. In order to meet the driving range of 300 miles, a typical electric vehicle requires an energy capacity of 75 kWh [3]. This translates to a weight over 600 kg for a state-of-the-art Li-ion batteries (120 Wh kg^{-1} specific energy, 80% state of charge window, and

95% discharge efficiency [4,5]), which makes the vehicle much heavier and less efficient than gasoline powered vehicles. Reliable and lasting batteries are also required for other applications, such as military and soldier specific systems, including power instrumentation for long range data acquisition systems. The specific energy and power for vehicle instrumentation and human-carried instrumentation are expected to exceed 600 Wh kg^{-1} and 25 W kg^{-1}, respectively.

New batteries with substantially higher specific energy should be deployed in order to decrease weight and reduce cost. Li-O_2 batteries are considered to be promising alternatives to current rechargeable batteries due to the exceptionally high specific energy of lithium metal (12 kWh kg^{-1}) and the inexhaustible supply of oxygen from the ambient. There are four types of Li-O_2 batteries categorized by the electrolyte: organic electrolyte, aqueous electrolyte, mixed organic and aqueous electrolyte, and solid state electrolyte [6]. Within these four types of Li-O_2 batteries, the battery using the organic electrolyte, shown in Figure 2-1, has recently attracted the most attention [7].

The first rechargeable Li-O_2 battery using organic electrolytes was developed by Abraham and Jiang at EIC Laboratories (Norwood, MA) in 1996 [8]. The overall reactions during charge and discharge of a Li-O_2 battery using an organic electrolyte are:

$$2Li + O_2 \leftrightarrow Li_2O_2 \qquad (3.10\,V) \tag{1}$$

and/or

$$4Li + O_2 \leftrightarrow 2Li_2O \qquad (2.91\,V) \tag{2}$$

It has been experimentally verified that the two-electron process in eq. (1) is the dominant oxygen reduction reaction (ORR) under normal operating conditions [8].

The high energy density of the Li-O_2 battery cannot be fully utilized with current technology primarily because the cathode capacity is limited by oxygen transport and electrode blockage. Typically less than 10% of its theoretical value can be achieved [9,10]. Conventional passive Li-O_2 batteries breathe oxygen from the ambient. Oxygen transfer in the porous carbon electrode filled with organic electrolyte is done by diffusion only. This causes a large oxygen concentration gradient within the porous carbon electrode because the diffusivity of oxygen in organic electrolytes is low. Pores further away from the electrode-oxygen interface are not fully utilized because of insufficient oxygen transport. In addition, the insoluble production of Li_2O_2 blocks the oxygen path and further impedes the oxygen diffusion. At the end of the discharge, battery voltage drops sharply due to the lack of oxygen supply and electrode passivation. During recharge the deposited Li_2O_2 decomposes to Li^+ and oxygen.

In this chapter, an innovative Li-O_2 battery with an actively recirculated electrolyte through the cathode, as shown in Figure 2-2, is proposed to achieve higher cathode specific capacity and better thermal management than present Li-O_2 batteries. In the proposed battery, the electrolyte is saturated with oxygen in a tank outside of the battery then pumped into the cathode end plate embedded with interdigital flow channels. Driven by the pressure difference between two adjacent channels, electrolyte seeps through cathode. Convection significantly improves mass transfer in the electrode. Enhanced oxygen transport significantly increases the specific capacity of the cathode; consequently, the specific energy of the whole system is increased. The forced convection of electrolyte through the cathode may also suppress the deposition of Li_2O_2 and improve cell capacity. It should be noted that the group led by Zheng proposed a Li-air flow battery concept and analyzed its theoretical energy density in 2013 [11]. Later experiments further demonstrated that this design could maintain a high power output [12]. However, Zhang et al. investigated a

battery design using aqueous electrolyte at the anode, while we propose a totally organic electrolyte system.

To prove the feasibility of the proposed Li-O_2 battery with active cathode, a two-dimensional, transient, non-isothermal numerical model was developed. Compared to existing Li-O_2 battery models, this model features two dimensional simulation and includes convection effects. Simulation results show that this new design can significantly increase the discharge capacity of the Li-O_2 battery over conventional designs.

2.2 Existing models

Compared to the vast number of modeling works of other electrochemical energy conversion and storage devices, such as Li-ion batteries, fuel cells, and flow batteries, modeling studies are relatively scarce for Li-O_2 batteries. As early as 2007, Sandhu et al. developed the first model for a Li-O_2 battery which assumed cylindrical pores in the cathode and focused on the limiting effect of oxygen transport [13]. In 2010, Andrei et al. reported a model that considered oxygen and lithium ion transport. The electrolyte potential and thermal effect were also included [14]. Wang suggested that the Li_2O_2 growth is similar to the ice formation in a proton exchange membrane fuel cell during sub-freezing conditions. His model followed a similar method developed for a proton exchange membrane fuel cell to calculate the effect of an insoluble substance on surface passivation and oxygen transport in Li-O_2 batteries. Different shapes of the reaction surfaces were considered, including cylindrical, spherical and planar surfaces [15,16]. Although one of the main attractions of Li-O_2 battery is its rechargeability, most of the modeling work only focused on the discharging process. The work by Sahapatsombut was the first modeling work reported to consider the charging process. The simulated cell potential for both discharging and charging agreed well with experimental results [17]. In a more recent paper by the same authors, the model was further

developed to include the formation of Li_2CO_3 occurring from electrolyte degradation. The relationship between capacity loss during cycling and the formation of Li_2O_2 and Li_2CO_3 was discussed [18]. Jung et al. improved the reaction surface coverage model by relating the model parameter to discharge current density [10]. Chen et al. considered particle size distribution in their model and simulated a cathode made from carbon nanotube and nanofiber [19]. Similarly, Xue et al. incorporated pore size distribution [20]. In the model developed by Yoo et al., the effective volume change during battery cycling was addressed by adopting moving boundary technique [21].

It should be noted that the proposed battery configuration resembles that of redox flow batteries, particularly those with a flow-through electrode. Flow batteries have been widely studied by both experiments and modeling [22]. The group led by Shah developed a transient modeling framework for a vanadium flow battery to study the effect of flow rate, concentration and electrode porosity on the battery performance [23]. Later, it was further developed to include thermal effects and oxygen evolution [24,25]. Vynnycky developed a 2D transient model for a redox battery using the asymptotic method, which was more efficient for battery stack simulation [26]. Very recently, a 3D non-isothermal model for redox flow battery was also reported [27]. A major difference between the redox flow battery and a Li-O_2 battery is that the electrode structure does not change during operation in a flow battery while in a Li-O_2 battery the deposited Li_2O_2 changes the porosity and structure of the electrode. This inevitably influences the modeling method. In addition, unlike redox flow batteries, the electrolyte in the proposed battery does not serve as an energy storage medium. Increasing the reservoir size of a redox flow battery increases the energy stored in the system, but the energy that can be retrieved in the proposed battery is not determined by the reservoir size but by the capacity of the cathode.

2.3 Model development

The model considers the two-dimensional mass transfer and electrochemical reaction in the two adjacent flow channels in the proposed Li-O_2 battery with an active cathode. The computational domain includes the electrolyte and the oxygen cathode, as shown in Figure 2-3. During discharge, oxygen-saturated electrolyte is actively driven through the cathode by the pressure gradient between adjacent channels. The complex reaction paths and kinetics during the charging process of organic Li-O_2 batteries are still under study [28]; therefore the current model does not consider the charging process.

The velocities of the electrolyte, distributions of oxygen concentration, Li^+ concentration, reaction rate, and volume fraction of solid product are solved in this model. To simplify the analysis and examine only the key parameters and phenomena, the following assumptions are adopted in this model:

- The overpotential of the anode reaction is negligible [29].
- All pores in the electrode are filled with electrolyte solution and contribute to the discharge of the battery.
- There is no gas phase in the electrode. The oxygen transport solely depends on the dissolved oxygen diffusion in liquid phase.
- Li_2O_2 deposits as a smooth film in the electrode because the size of Li_2O_2 particles is typically several orders of magnitude smaller than the size of a Li-O_2 battery electrode [30].
- Due to the high thermal conductivity of lithium metal (84.8 W m^{-1} K^{-1}) and commonly used materials for the end plate of an active cathode, such as stainless steel (16 W m^{-1} K^{-1}), their thermal resistances are negligible.

2.3.1 Governing equations

The continuity equation in porous media can be written as:

$$\frac{\partial\left(\varepsilon\rho_{\mathrm{EL}}\right)}{\partial t}+\nabla\cdot\left(\varepsilon\rho_{\mathrm{EL}}\boldsymbol{u}\right)=\dot{m}_{\mathrm{EL}} \tag{3}$$

where subscript 'EL' stands for electrolyte.

The relationship between the pressure gradient and velocity vector is described by the momentum equations, which reduces to Darcy's law for porous medium:

$$\varepsilon\boldsymbol{u}=-\frac{K}{\mu_{\mathrm{EL}}}\nabla p \tag{4}$$

By substituting the momentum equations into the continuity equation, we obtain an equation for pressure:

$$\frac{\partial\left(\varepsilon\rho_{\mathrm{EL}}\right)}{\partial t}+\nabla\cdot\left(-\frac{K}{\mu_{\mathrm{EL}}}\rho_{\mathrm{EL}}\nabla p\right)=\dot{m}_{\mathrm{EL}} \tag{5}$$

The permeability of the electrode, K, changes with time because the Li_2O_2 produced does not dissolve in the electrolyte, but adheres to the pore surfaces. In time, the permeability of the electrode could be detrimentally changed by an order of magnitude due to the accumulation of Li_2O_2. The Carman-Kozeny equation relates the permeability of the porous medium as a collection of solid spheres of diameter d_{p} to the porosity, ε [31]:

$$K=\frac{d_{\mathrm{p}}^{2}\varepsilon^{3}}{180\left(1-\varepsilon\right)^{2}} \tag{6}$$

We assume that particle size d_p is of the same magnitude to pore size d_{avg}, so d_p can be replaced with d_{avg} in the above equation. Both the porosity of the electrode and the average pore diameter can be related to the volume fraction of the Li_2O_2 by the following equation:

$$\varepsilon = \varepsilon^0 - \varepsilon_{Li2O2} \tag{7}$$

$$d_{avg} = d_{avg}^0 - 2\delta_{Li2O2} = \left(1 - \frac{\varepsilon_{Li2O2}}{\varepsilon^0}\right)^{1/3} d_{avg}^0 = \left(\frac{\varepsilon}{\varepsilon^0}\right)^{1/3} d_{avg}^0 \tag{8}$$

where ε^0 and d_{avg}^0 (0.1 μm [32]) are the porosity and average diameter of the pores before Li_2O_2 deposition and δ_{Li2O2} is the thickness of the precipitated Li_2O_2. The volume fraction of Li_2O_2, ε_{Li2O2}, changes with time and can be calculated from the generation rate of Li_2O_2 based on local reaction rate. Combining equations (6) to (8), the relative change of permeability of the porous medium can be calculated by the following equation:

$$\frac{K}{K^0} = \left(\frac{d_{avg}}{d_{avg}^0}\right)^2 \cdot \left(\frac{\varepsilon}{\varepsilon^0}\right)^3 \cdot \left(\frac{1-\varepsilon^0}{1-\varepsilon}\right)^2 = \left(\frac{\varepsilon}{\varepsilon^0}\right)^{3\frac{2}{3}} \cdot \left(\frac{1-\varepsilon^0}{1-\varepsilon}\right)^2 \tag{9}$$

The concentration of lithium ion and dissolved oxygen are solved by:

$$\frac{\partial\left(\varepsilon\rho_{EL}\omega_{Li+}\right)}{\partial t} + \nabla\cdot\left(\varepsilon\rho_{EL}\boldsymbol{u}\omega_{Li+}\right) = \nabla\cdot\left(\rho_{EL}D_{Li+}^{eff}\nabla\omega_{Li+}\right) - \nabla\cdot\left(\frac{\boldsymbol{i}_{el}t_+}{F}M_{Li+}\right) + \dot{m}_{Li+} \tag{10}$$

and

$$\frac{\partial\left(\varepsilon\rho_{EL}\omega_{O2}\right)}{\partial t} + \nabla\cdot\left(\varepsilon\rho_{EL}\boldsymbol{u}\omega_{O2}\right) = \nabla\cdot\left(\rho_{EL}D_{O2}^{eff}\nabla\omega_{O2}\right) + \dot{m}_{O2} \tag{11}$$

The effective diffusivity, D_i^{eff}, is determined by the diffusion coefficients, D_i, porosity of the porous media, ε, and tortuosity of the porous media, τ:

$$D_{\mathrm{i}}^{\mathrm{eff}} = D_{\mathrm{i}} \varepsilon^{\tau} \tag{12}$$

where the tortuosity is a function of porosity [33]:

$$\tau(\varepsilon) = 1 - 0.77 \ln \varepsilon \tag{13}$$

The second term on the right hand side of eq. (10) considers the migration of Li^+, where $\boldsymbol{i}_{el}$ is the current density vector in electrolyte and t_+ is the transference number of Li^+. Based on charge conservation, $\boldsymbol{i}_{el}$ can be related to $\dot{m}_{\mathrm{Li+}}$ as:

$$\nabla \cdot \boldsymbol{i}_{el} = \frac{\dot{m}_{\mathrm{Li+}}}{M_{\mathrm{Li+}}} F \tag{14}$$

The consumption rates in the species equations of Li^+, and O_2 are, respectively:

$$\dot{m}_{\mathrm{Li+}} = -\frac{R_{\mathrm{ORR}}}{F} M_{\mathrm{Li+}} \quad [\frac{\mathrm{g}}{\mathrm{m}^3 \cdot \mathrm{s}}] \tag{15}$$

$$\dot{m}_{\mathrm{O2}} = -\frac{R_{\mathrm{ORR}}}{2F} M_{\mathrm{O2}} \quad [\frac{\mathrm{g}}{\mathrm{m}^3 \cdot \mathrm{s}}] \tag{16}$$

where R_{ORR} is the reaction rate of the oxygen reduction reaction (A m^{-3}), and M is the molecular weight (g mol^{-1}).

The energy balance equation is expressed as:

$$\frac{\partial \left(\left[\rho C_p \right]^{\mathrm{eff}} T \right)}{\partial t} + \nabla \cdot \left[\left(\varepsilon \rho_{\mathrm{EL}} C_{p,\mathrm{EL}} \boldsymbol{u} \right) T \right] = \nabla \cdot \left(\kappa_{\mathrm{T}}^{\mathrm{eff}} \nabla T \right) + \dot{m}_{\mathrm{T}} \tag{17}$$

where the effective specific heat, $\left[\rho C_p \right]^{\mathrm{eff}}$, and the effective thermal conductivity, $\kappa_{\mathrm{T}}^{\mathrm{eff}}$, are related to the properties of the electrode, Li_2O_2 precipitate, and electrolyte:

$$\left[\rho C_p\right]^{\text{eff}} = (1-\varepsilon)\rho_{\text{ED}} C_{p,\text{ED}} + \varepsilon_{\text{Li2O2}}\rho_{\text{Li2O2}} C_{p,\text{Li2O2}} + (\varepsilon - \varepsilon_{\text{Li2O2}})\rho_{\text{EL}} C_{p,\text{EL}} \tag{18}$$

$$\kappa_{\text{T}}^{\text{eff}} = (1-\varepsilon)\kappa_{\text{ED}} + \varepsilon_{\text{Li2O2}}\kappa_{\text{Li2O2}} + (\varepsilon - \varepsilon_{\text{Li2O2}})\kappa_{\text{EL}} \tag{19}$$

The source terms used in the energy equations are also related to the electrochemical reaction:

$$\dot{m}_{\text{T}} = R_{\text{ORR}}\left(E_0 - V\right) \tag{20}$$

where E_0 is the thermodynamic equilibrium voltage and V is the cell voltage. In eq.(20), only the irreversible heating is considered. The reversible heat that arises from entropy change is neglected due to lack of data.

The local ORR rate of the Li-O_2 battery is related to the concentrations of lithium ion and oxygen, the standard constant rate of ORR, k_{ORR}, the specific surface area of the electrode, A_{ED}, and the overpotential, η_{c}, by the following equation:

$$R_{\text{ORR}} = \left(\frac{\omega_{\text{Li+}}}{\omega_{\text{Li+}}^{\text{ref}}}\right)^2 \cdot \left(\frac{\omega_{\text{O2}}}{\omega_{\text{O2}}^{\text{ref}}}\right) \cdot k_{\text{ORR}} \cdot A_{\text{ED}} \cdot \exp\left(\frac{\alpha_{\text{ORR}} F}{RT}\eta_c\right) \tag{21}$$

The standard rate constant, k_{ORR}, in the above equation is a function of temperature:

$$k_{\text{ORR}} = i_0 \cdot \exp\left[\frac{E_{\text{ORR}}}{R}\left(\frac{1}{295} - \frac{1}{T}\right)\right] \tag{22}$$

where i_0 is the exchange current density at 295 K, and E_{ORR} is the activation energy of the ORR, which has an approximate value of 21 kJ mol^{-1} [34]. In all calculations of the current work, the initial temperature is set at 293 K.

Since the cathode reaction product Li_2O_2 is both insoluble and insulating, it causes electrode passivation during discharge. On the electrode level, the solid Li_2O_2 decreases porosity and

increases transport resistance. This is considered in the electrolyte and oxygen concentration equations through increased effective diffusivities. On the pore level, the formed Li_2O_2 film increases transport resistance for lithium ions, oxygen molecules, and electrons from the electrolyte to the electrode surface. In this model, these effects are generalized by assuming a decreasing effective active area. The effective active area of electrode per volume, A_{ED}, is calculated by the following equation:

$$\frac{A_{ED}(t)}{A_{ED,0}} = 1 - \left(\frac{\varepsilon_{L2O2}}{\varepsilon^0} \right)^z \tag{23}$$

where $A_{ED,0}$ is the effective active area of the electrode before discharge and the value of z indicates different modes of surface coverage. In this work, a fixed value of 0.4 is used for z [18]. The Li_2O_2 production rate from the ORR is calculated by:

$$\dot{m}_{Li2O2} = \frac{R_{ORR}}{2F} M_{Li2O2} \tag{24}$$

and the local volume fraction of Li_2O_2, ε_{Li2O2}, is calculated based on the amount of accumulated Li_2O_2:

$$\varepsilon_{Li2O2}(t) = \frac{\int R_{ORR} \cdot dt}{2F} \frac{M_{Li2O2}}{\rho_{Li2O2}} \tag{25}$$

The integration of the ORR rates within the whole electrode equals the discharge current density:

$$I = \frac{\int_{\text{Electrode}} R_{ORR} \, dxdy}{\delta_Y} \tag{26}$$

where δ_Y is the height of the computation domain, as shown in Figure 2-3.

In summary, there are five primary unknowns in the system, p, $\boldsymbol{u}$, ω_{O2}, ω_{Li+} and T. They are described by five coupled equations (4), (5), (10), (11), and (17). Their boundary conditions are described below.

2.3.2 Boundary conditions

Boundaries for the computational domain are numbered in Figure 2-3. The upper (I) and lower (II) boundaries are considered to be symmetric boundaries and the corresponding boundary conditions are:

$$\frac{\partial \Phi}{\partial y} = 0 \tag{27}$$

where Φ can be T, P, ω_{Li+}, and ω_{O2}.

At the lithium/separator interface (boundary III), the flux of lithium ion is proportional to the discharge current density:

$$N_{Li+} = -\rho D_{Li+}^{eff} \nabla \omega_{Li+} + \frac{i_{el,x} t_+}{F} M_{Li+} = \frac{I}{F} M_{Li+} \tag{28}$$

The electrolyte current density in the x direction, $i_{el,x}$, at boundary III equals to the discharge current density I, while at boundary IV, V and VI $i_{el,x}$ equals zero.

The flux of oxygen at boundary III is 0, and the temperature at boundary III is set as the room temperature (293 K). At the electrode/rib interface (boundary IV), the flux of lithium ion and oxygen are 0 and the temperature is room temperature (293 K). At the electrode/channel interface (boundary V), the electrolyte flows into the electrode. The lithium ion and the oxygen concentrations are set as constant:

$$\omega_{Li+} = 6.86 \times 10^{-3} \tag{29}$$

and

$$\omega_{O2} = 1.41 \times 10^{-4} \tag{30}$$

The pressure at boundary V is set as constant:

$$P_{EL} = 1.2 \times P_0 \tag{31}$$

where P_0 is the atmospheric pressure, 1 atm. At the electrode-channel interface (boundary VI), the electrolyte flows out of the electrode. The gradients of lithium ion and the oxygen concentration are set to 0. The pressure is set as constant:

$$P_{EL} = 0.8 \times P_0 \tag{32}$$

The temperature at boundaries III, IV, V is set to be constant:

$$T = T_\infty \tag{33}$$

At boundary VI, electrolyte flows out of the electrode, and an outflow boundary condition is applied.

The computational grids are generated based on the finite volume method (FVM) [35], governing equations were discretized and solved by in-house code developed with Fortran. In each time step, governing equations (5), (10), (11) and (17) are discretized and implicitly solved by an iteration to get pressure, electrolyte concentration, oxygen concentration and temperature. Velocity is obtained from eq. (4) based on the central differencing scheme. Source terms and coefficients of the equations, which involve reaction rate, species consumption rate, Li_2O_2 volume fraction, etc., are updated at each iterative step to guarantee a numerically stable result. The calculation does

not enter the next time step until the relative error for each variable is under 10^{-5}. The grid number is 160×50 and the time step is 1 second. All the model results are both grid independent and time step independent. After the results are converged in each time step, the cell voltage is determined by the following equation:

$$V = E_0 - \eta_c - \eta_m - I \times \left(\delta_{\mathrm{EL}} + 0.5\delta_{\mathrm{ED}} \right) / \sigma_{\mathrm{EL}}^{eff} \tag{34}$$

where δ_{EL} is the thickness of the separator, δ_{ED} is the thickness of the cathode, σ_{EL} is the conductivity of the electrolyte, and η_m is the potential drop over the deposited Li_2O_2 film. Not all charge transfer ions (Li^+) travel the length of δ_{ED}, instead, charge transfer takes place throughout the length of the cathode from electrolyte to carbon phase. Therefore, a factor of 0.5 is used in eq. (34) to approximate the resistance of the electrolyte along the thickness of the cathode. The kinetic and concentration overpotential on the cathode, η_c, is obtained through an iterative method to fulfill eqs. (21) and (26) simultaneously with a specified discharge current density *I*. Since the reaction rate and Li_2O_2 thickness vary at different locations in the electrode, η_m is averaged over the whole cathode:

$$\eta_m = \frac{1}{\delta_{\mathrm{ED}} \delta_{\mathrm{Y}}} \int \frac{R_{ORR} \delta_{Li2O2}}{A_{ED} \sigma_{Li2O2}} dxdy \tag{35}$$

where δ_{Li2O2} can be calculated through eq. (8) and σ_{Li2O2} is the estimated electrical conductivity of Li_2O_2 formed during discharge.

The overpotential in the solid backbone phase of the cathode is neglected in the current work, because this phase has very high conductivity in comparison to the electrolyte (~10^2 S m^{-1} vs. 0.5 S m^{-1}). Since the thickness of the electrode is 0.8 mm, the overpotential caused by the electrode

backbone phase would be less than 0.025 mV with a current density of 1 mA cm^{-2}, which is far less than the other overpotentials.

Values of parameters used in the model are each presented in Table 2-1. Transport properties are obtained from published data of the electrolyte of 1M $LiPF_6$ in propylene carbonate/dimethoxyethane (1:2 wt). It should be noted that many new electrolytes for Li-O_2 batteries are currently under study to achieve higher ionic conductivity, higher oxygen solubility and diffusivity, and better cycling stability. The conclusions of the modeling studies closely depend on the properties of the materials, and must be re-inspected for each new electrolytes when the property data become available. In the simulations discussed below, if not otherwise specified, the pressure difference between the inlet and outlet is $0.4P_0$, the battery is discharged at a constant current of 0.2 mA cm^{-2}, and the ambient temperature is 293 K.

2.4 Results and discussion

2.4.1 Model validation

After grid and time-independence verification, the model is used to simulate a conventional Li-O_2 cell. The simulation results of discharge capacity vs. cell voltage at various discharge current densities are compared to the experimental data provided by Read [36] in Figure 2-4. Generally, the predicted specific capacities of our model agree well with experimental results. The errors in specific capacity are 17.7%, –3.60%, –10.5% and –3.04%, at 0.1 mA cm^{-2}, 0.2 mA cm^{-2}, 0.5 mA cm^{-2}, and 1.0 mA cm^{-2}, respectively. The predicted cell voltage is higher than that of experimental results, especially at the later stages of discharge, because in the present model all of the side reactions are neglected and the electrolyte is considered to be perfect without any decomposition.

The following results are based on the validated model and parameters to compare the performance of active and passive cathode cells.

2.4.2 Distributions of pressure, velocity and temperature

Figure 2-5 depicts the distributions of pressure and velocity in the computational domain at the end of discharging. The pressure difference between the electrode inlet and outlet, shown in Figure 2-5, drives the electrolyte from the inlet to the outlet. Compared to a passive cathode, the forced convection of the lithium ion and oxygen-saturated electrolyte leads to better mass transfer of both lithium ions and oxygen.

The velocity calculation is based on Darcy's law, which is only suitable when the flow is laminar. To confirm the integrity of this assumption, the maximum local Re number of the flow should be checked. This value occurs at the start of discharging. It is calculated using the maximum local velocity (6.81×10^{-4} m s^{-1}), average pore size as characteristic length, electrolyte viscosity, and electrolyte density, to result in:

$$\mathrm{Re} = \frac{\rho u L}{\mu} = 3.5\times10^{-5}$$

which is far smaller than 1, and ensures that the flow is in the laminar regime and Darcy's law is suitable for use.

The temperature rise in the battery is directly affected by the current density and thermal properties of the materials. The temperature distribution at the end of a discharging process is shown in Figure 2-6. The discharge current density is 1.5 mA cm^{-2} and the temperatures at the inlet, boundaries III and IV are kept at constant. Because of the high reaction rate at the inlet, electrolyte temperature rises and causes a high temperature zone at the lower center area. Boundaries III and IV are kept at ambient temperature and cool down the electrolyte on their way from inlet to outlet. Even with a relatively high discharge current, the maximum temperature rise

during the discharging is much less than 1 K. Therefore the effect of temperature is not significant for kinetics and mass transport.

2.4.3 Compare the capacity to conventional Li-O_2 battery

Since most Li-O_2 battery studies are still on the laboratory scale, it would be impractical to conduct a system level comparison of effective capacity between a conventional Li-O_2 and the active cathode battery we proposed here. However, the following analysis would justify the effort of using an active cathode as proposed.

Primarily, liquid cooling methods are already used in commercial Li-ion battery stacks, for example battery stacks in the Chevrolet Volt to keep the battery at a safe working temperature [37]. The cooling liquid is circulated between the stack and a radiator to dissipate heat generated by the battery during operation. Therefore, in future battery applications with higher power and energy density, it is foreseeable that liquid cooling would be used. Under this condition, peripheral devices like pumps and storage tanks are inevitable. The proposed active cathode battery can be integrated with a liquid cooling system seamlessly. The circulation of electrolytic solution through an air cooled radiator will keep the battery at an optimal temperature.

Secondly, flow channels are not only required by the proposed battery with an active cathode, they are also needed in the conventional battery with a passive cathode to distribute air/oxygen throughout the battery package.

Lastly, the power consumption required for the pumping of the electrolyte is considered. Under the condition of $0.4P_0$ pressure difference (40530 Pa), the above results show that the volume flow rate on the computation domain (1 cm^2 reaction area) is 0.00413 $cm^3\ s^{-1}$; therefore the pump power consumption is 0.17 mW cm^{-2}. When the discharge current density and voltage are 0.2 mA cm^{-2} and 2.65 V, respectively, the power output of the battery is 0.53 mW cm^{-2}. This means that about

32% of the power output is consumed by pumping the electrolyte through the cathode. With the improvement of Li-O_2 battery technology, such as finding high performance catalysts and low viscosity electrolytes, an increase of the current density and power density will decrease the percentage of pump power consumption.

2.4.4 Discharge capacities of passive vs. active batteries

Figure 2-7 compares the variation of battery voltage of Li-O_2 batteries with passive and active cathodes with the same discharge current density of 0.2 mA cm^{-2}. The cut-off voltages for active and passive cells are 2.45 V and 2.4 V, respectively. In both cases, the rib width is equal to the flow channel width (a 50% open ratio of the cathode to oxygen). However, for passive mode there is no pressure gradient between the inlet and outlet channel so there is no bulk velocity of electrolyte movement. It can be seen that the discharge capacity of the Li-O_2 battery is greatly increased from 178 mAh g^{-1} to 1217 mAh g^{-1} by adopting an active cathode design.

The discharge capacities of passive and active Li-O_2 cells at different current densities are compared in Figure 2-8. Both cathodes have a 50% open ratio because of the existence of the ribs. It is clearly shown in the figure that the discharge capacity of an active battery is always higher than that of a passive battery. The absolute amount of increase is higher at a lower current density. At the discharge current density of 0.1 mA cm^{-2}, the discharge capacity of the active cathode battery increases from 455 mAh g^{-1} to 1523 mAh g^{-1}, while the relative capacity increases (the columns in Figure 2-8) show a maximum value of 15.5 times at 2.0 mA cm^{-2} (12.2 mAh g^{-1} to 201 mAh g^{-1}).

The increase of the discharge capacity is mainly caused by the improved utilization of the electrode. The volume fractions of Li_2O_2 in both the active and passive battery electrodes after

being fully discharged are compared in Figure 2-9. The non-dimensional χ in this figure and following figures is defined as:

$$\chi = \left(x - \delta_{\mathrm{EL}}\right) / \delta_{\mathrm{ED}}$$

where δ_{EL} and δ_{ED} are the thickness of separator and electrode, respectively. It can be seen from the figure that in the active cathode battery Li_2O_2 is distributed more uniformly. Compared with the passive battery, pores further away from the electrode/oxygen interface in the active battery are much better utilized due to the improved mass transfer. At the end of discharge with current density of 0.1 mA cm^{-2}, the volume fraction of Li_2O_2 at the electrode/separator interface (χ=0) in the active battery is 0.30, as compared to 0.024 in the passive battery.

2.4.5 Distribution of lithium ion and oxygen

To better understand the mass transport in the electrode, the distributions of oxygen and lithium ions at different stages of discharge (denoted by increasing specific capacity) are plotted in Figure 2-10(a) and (b), respectively. At the inlet, oxygen concentration is kept at the saturated value. At every location except near the inlet, the oxygen concentration slowly decreases until the oxygen is depleted in the electrode due to its consumption by the ORR. The decrease of the permeability at the inlet impedes the oxygen delivery into the electrode and completely stops the battery discharging at 1217 mAh g^{-1}. For the lithium ion, the constant mass flux from the anode causes a negative concentration gradient along the *x*-direction which drives lithium ions from the anode to the cathode. The lithium ion concentration around the outlet is higher because the flow of electrolytes brings all the reactants to the outlet. At the end of the discharging process, the lithium ion concentration closer to the anode rises because of a higher transport resistance caused by a deteriorated convective effect.

As indicated by eq. (21), lithium ion concentration and oxygen concentration directly affect the distribution of the local ORR rate, R_{ORR}. Figure 2-10(c) shows the distribution of R_{ORR} at different times and that it is mainly controlled by oxygen concentration. During the discharging process, the reaction rate around the inlet increases while around the outlet and separator, the reaction rate decreases. Comparing to Figure 2-10(a), it can be seen that the decrease of R_{ORR} is due to the decreasing oxygen concentration in the same area. To maintain a constant discharge current and compensate for the R_{ORR} decrease, the inlet area where oxygen is still relatively high must have an increased reaction rate and lower voltage. Combining this with the fact that the effective reaction area is decreasing, there is a sharp increase of R_{ORR} around the inlet after the discharge depth of 1100 mAh g^{-1}.

Figure 2-11 shows the distribution of Li_2O_2 volume fraction and relative permeability at different times of discharging. Between 1100mAh/g and the end of discharge, at the inlet Li_2O_2 volume fraction increases quickly and permeability continues decreasing, which leads to deteriorated electrolyte flow and oxygen transport. This causes the reaction rate at the inlet to rise and causes more Li_2O_2 deposition. This cycle leads to a rapid drop of battery voltage, as evidenced in Figure 2-7.

2.4.6 Effect of pressure difference between channels

Figure 2-12(a) shows the discharging processes when the pressure difference between adjacent flow channels changes. The discharge current density is kept at 1.5 mA cm^{-2}. As can be seen from Figure 2-12(b), the volume fraction of Li_2O_2 along the cathode increases when the pressure difference between the inlet and outlet increases. This means that a higher pressure difference makes utilization of the electrode more efficient due to the improved mass transfer, which consequently improves the discharge capacity of a Li-O_2 battery. The discharge capacity increases

from 205 mAh g^{-1} to 314 mAh g^{-1} and to 401 mAh g^{-1} when the pressure difference increases from $0.3P_0$ to $0.4P_0$ and to $0.5P_0$. However, for an interdigital flow channel design, high pressure differences lead to a higher possibility of damage to the flow channel, and shorter lifetime of the current collector. At the same time, the pump power to circulate electrolyte will be higher. Thus, an optimum pressure difference in an actual battery design should be a balance between the above factors.

2.4.7 Effect of exchange current density

Exchange current density is a very important parameter to depict the ORR kinetics. In this study, the exchange current density is calibrated so that the voltage vs. specific capacity curve can be compared to experimental results. However, exchange current density is affected by many factors, including electrode material, electrolyte, etc. As can be seen from Figure 2-13, the simulation with different exchange current density shows that higher i_0 would lead to a higher voltage at the same discharge current. The increase of battery voltage is in proportion to the logarithm of i_0. A higher voltage means the battery has better energy efficiency, but it will not help to increase the specific capacity, which is mainly determined by the porosity and the mass transfer properties of the electrode.

2.4.8 Effect of porosity

As discussed above, electrode porosity determines the discharge capacity of the battery. Therefore, a higher porosity is preferred to increase the specific capacity of a Li-O_2 battery. Conversely, the change of porosity also influences specific surface area. A very high and very low porosity both lead to a low specific surface area, and consequently a low power density. In the current model, specific surface area is set to a constant value because of the difficulty in finding a reliable analytical expression for the dependence of surface area on porosity. This depends on both

the electrode material and fabrication method. Thus, studying the effect of porosity on the battery performance cannot be done by simply assuming a constant specific surface area and changing electrode porosity. In the current study, an electrode with a linearly distributed porosity is tested by placing the electrode in two opposite directions, first the higher porosity side faces the cathode flow channel then the lower porosity side faces the cathode flow channel. This keeps the total surface area constant and its dependence on porosity is avoided. The comparison at a relatively high discharge current of 1.5 mA cm^{-2} is shown in Figure 2-14. From Figure 2-14(a) it can be seen that the battery with the high porosity side facing the flow channel will have 104% higher capacity, from 195 mAh g^{-1} to 398 mAh g^{-1}. Since the surface area is constant, discharge voltage should also be at the same level. Figure 2-14(b) shows that volume fraction of Li_2O_2 is higher when the porosity close to the electrolyte flow channel is higher. This higher utilization of the electrode pores helps to increase battery capacity. At low discharge current such as 0.2 mA cm^{-2}, this improvement is less significant. Simulation results show a 20.5% higher specific capacity if the oxygen side has higher porosity. This is reasonable because a lower discharge current requires lower oxygen flux, thus the advantage of higher porosity at the oxygen side would not be as notable as the case at a higher discharge current.

Future works include experimental validation of the design, improvement of the model and system-level analysis. Modeling studies on Li-O_2 batteries are still in the preliminary stage. To include the charging process, consideration of side reactions and thermal effects on battery performance are several of the most urgent tasks in future studies. Experiments on the proposed Li-O_2 battery with the active cathode will be carried out soon to validate the idea and to seek further improvements.

2.5 Conclusions

The lithium oxygen battery is one of the most promising next generation energy storage devices for long-range electric vehicles and portable devices. With the aim of enhanced oxygen transport and increased specific capacity, an innovative battery structure with active cathode is proposed. In the proposed Li-O_2 battery, electrolyte is recirculated between the battery cathode and an oxygen saturation tank outside of the battery. Forced convection improves oxygen transport and battery capacity. The proposed design can be integrated with the battery cooling systems seamlessly.

A two-dimensional, transient, non-isothermal simulation model is developed to study the discharging process of such a Li-O_2 battery. Compared to other existing Li-O_2 battery models, this model features two dimensional simulation and includes convection effect.

Based on the simulation results, it can be concluded that:

1. The active cathode design can significantly enhance the Li-O_2 battery discharge capacity at a certain range of discharge current densities. At the discharge current of 2.0 mA cm^{-2}, the capacity can be increased 15.5 times (from 12.2 mAh g^{-1} to 201 mAh g^{-1}) compared to the conventional passive cathode Li-O_2 battery. This is caused by a better oxygen supply in the electrode and thus the micro scale pores in the electrode further away from oxygen can be more efficiently utilized.

2. An electrode with a higher porosity at the current collector side and a lower porosity at the separator side is preferred. A higher porosity allows oxygen-saturated electrolyte to penetrate into a deeper area of the electrode, while a lower porosity can be used to maintain an optimal reaction area. For a variable porosity cathode, placing the high porosity side closer to the current collector

can lead to a 104% higher capacity than the opposite arrangement, assuming a discharge current of 1.5 mA cm^{-2}.

References

[1] Åhman M. Primary energy efficiency of alternative powertrains in vehicles. Energy 2001;26:973–89. doi:10.1016/S0360-5442(01)00049‑4.

[2] Noorden R Van. The rechargeable revolution: A better battery. Nature 2014;507:26–8. doi:10.1038/507026a.

[3] Colmenar-Santos A, Alberdi-Jiménez L, Nasarre-Cortés L, Mora-Larramona J. Residual heat use generated by a 12kW fuel cell in an electric vehicle heating system. Energy 2014;68:182–90. doi:10.1016/j.energy.2014.02.092.

[4] Scrosati B, Hassoun J, Sun Y-K. Lithium-ion batteries. A look into the future. Energy Environ Sci 2011;4:3287. doi:10.1039/c1ee01388b.

[5] Molenda J. Material problems and prospects of Li-ion batteries for vehicles appliations. Funct Mater Lett 2011;04:107–12. doi:10.1142/S1793604711001816.

[6] Girishkumar G, McCloskey B, Luntz AC, Swanson S, Wilcke W. Lithium-air battery: Promise and challenges. J Phys Chem Lett 2010;1:2193–203. doi:10.1021/jz1005384.

[7] Balaish M, Kraytsberg A, Ein-Eli Y. A critical review on lithium-air battery electrolytes. Phys Chem Chem Phys 2014;16:2801–22. doi:10.1039/c3cp54165g.

[8] Abraham KM. A Polymer Electrolyte-Based Rechargeable Lithium/Oxygen Battery. J Electrochem Soc 1996;143:1. doi:10.1149/1.1836378.

[9] Garcia-Araez N, Novák P. Critical aspects in the development of lithium-air batteries. J Solid State Electrochem 2013;17:1793–807. doi:10.1007/s10008-013-1999-1.

[10] Jung CY, Zhao TS, An L. Modeling of lithium–oxygen batteries with the discharge product treated as a discontinuous deposit layer. J Power Sources 2015;273:440–7. doi:10.1016/j.jpowsour.2014.09.103.

[11] Zheng JP, Andrei P, Hendrickson M, Plichta EJ. The Theoretical Energy Densities of Dual-Electrolytes Rechargeable Li-Air and Li-Air Flow Batteries. J Electrochem Soc 2011;158:A43. doi:10.1149/1.3515330.

[12] Chen XJ, Shellikeri a., Wu Q, Zheng JP, Hendrickson M, Plichta EJ. A High-Rate Rechargeable Li-Air Flow Battery. J Electrochem Soc 2013;160:A1619–23. doi:10.1149/2.012310jes.

[13] Sandhu SS, Fellner JP, Brutchen GW. Diffusion-limited model for a lithium/air battery with an organic electrolyte. J Power Sources 2007;164:365–71. doi:10.1016/ j.jpowsour.2006.09.099.

[14] Andrei P, Zheng JP, Hendrickson M, Plichta EJ. A physics-based drift-diffusion approach to model Li-air batteries with organic electrolyte. ICSICT-2010 - 2010 10th IEEE Int. Conf. Solid-State Integr. Circuit Technol. Proc., 2010, p. 2016–8.

[15] Wang Y, Cho SC. Analysis of Air Cathode Perfomance for Lithium-Air Batteries. J Electrochem Soc 2013;160:A1847–55. doi:10.1149/2.092310jes.

[16] Wang Y. Modeling discharge deposit formation and its effect on lithium-air battery performance. Electrochim Acta 2012;75:239–46. doi:10.1016/j.electacta.2012.04.137.

[17] Sahapatsombut U, Cheng H, Scott K. Modelling the micro-macro homogeneous cycling behaviour of a lithium-air battery. J Power Sources 2013;227:243–53. doi:10.1016/j.jpowsour.2012.11.053

[18] Sahapatsombut U, Cheng H, Scott K. Modelling of electrolyte degradation and cycling behaviour in a lithium-air battery. J Power Sources 2013;243:409–18. doi:10.1016/j.jpowsour.2013.06.043.

[19] Chen XJ, Bevara VV., Andrei P, Hendrickson M, Plichta EJ, Zheng JP. Combined Effects of Oxygen Diffusion and Electronic Resistance in Li-Air Batteries with Carbon Nanofiber Cathodes. J Electrochem Soc 2014;161:A1877–83. doi:10.1149/2.0721412jes.

[20] Xue K-H, Nguyen T-K, Franco AA. Impact of the Cathode Microstructure on the Discharge Performance of Lithium Air Batteries: A Multiscale Model. J Electrochem Soc 2014;161:E3028–35. doi:10.1149/2.002408jes.

[21] Yoo K, Banerjee S, Dutta P. Modeling of volume change phenomena in a Li–air battery. J Power Sources 2014;258:340–50. doi:10.1016/j.jpowsour.2014.02.044.

[22] Weber AZ, Mench MM, Meyers JP, Ross PN, Gostick JT, Liu Q. Redox flow batteries: A review. J Appl Electrochem 2011;41:1137–64. doi:10.1007/s10800-011-0348-2.

[23] Shah AA, Watt-Smith MJ, Walsh FC. A dynamic performance model for redox-flow batteries involving soluble species. Electrochim Acta 2008;53:8087–100. doi:10.1016/j.electacta.2008.05.067.

[24] Al-Fetlawi H, Shah AA, Walsh FC. Non-isothermal modelling of the all-vanadium redox flow battery. Electrochim Acta 2009;55:78–89. doi:10.1016/j.electacta.2009.08.009.

[25] Al-Fetlawi H, Shah AA, Walsh FC. Modelling the effects of oxygen evolution in the all-vanadium redox flow battery. Electrochim Acta 2010;55:3192–205. doi:10.1016/j.electacta.2009.12.085.

[26] Vynnycky M. Analysis of a model for the operation of a vanadium redox battery. Energy 2011;36:2242–56. doi:10.1016/j.energy.2010.03.060.

[27] Oh K, Yoo H, Ko J, Won S, Ju H. Three-dimensional, transient, nonisothermal model of all-vanadium redox flow batteries. Energy 2014. doi:10.1016/j.energy.2014.05.020.

[28] Kang S, Mo Y, Ong SP, Ceder G. A facile mechanism for recharging Li_2O_2 in Li-O_2 batteries. Chem Mater 2013;25:3328–36. doi:10.1021/cm401720n.

[29] Zhang SS, Foster D, Read J. Discharge characteristic of a non-aqueous electrolyte Li/O_2 battery. J Power Sources 2010;195:1235–40. doi:10.1016/j.jpowsour.2009.08.088.

[30] Mitchell RR, Gallant BM, Thompson C V., Shao-Horn Y. All-carbon-nanofiber electrodes for high-energy rechargeable Li-O_2 batteries. Energy Environ Sci 2011;4:2952. doi:10.1039/c1ee01496j.

[31] Nield DA, Bejan A. Convection in Porous Media. 3rd ed. New York: Springer; 2006. doi:10.1007/978-0-387-76543-3.

[32] Ren X, Zhang SS, Tran DT, Read J. Oxygen reduction reaction catalyst on lithium/air battery discharge performance. J Mater Chem 2011;21:10118. doi:10.1039/c0jm04170j.

[33] Matyka M, Khalili A, Koza Z. Tortuosity-porosity relation in porous media flow. Phys Rev E - Stat Nonlinear, Soft Matter Phys 2008;78. doi:10.1103/PhysRevE.78.026306.

[34] Anderson AB, Roques J, Mukerjee S, Murthi VS, Markovic NM, Stamenkovic V. Activation energies for oxygen reduction on platinum alloys: Theory and experiment. J Phys Chem B 2005;109:1198–203. doi:10.1021/jp047468z.

[35] Patankar S V. Numerical Heat Transfer and Fluid Flow. 1st ed. New York: CRC Press; 1980.

[36] Read J. Characterization of the lithium/oxygen organic electrolyte battery. J Electrochem Soc 2002;149:A1190–5. doi:10.1149/1.1498256.

[37] Smith B. Chevrolet Volt Battery Incident Summary Report. Washington, DC: 2012.

[38] O'Laoire CM. Dissertation: Investigations of oxygen reduction reactions in non-aqueous electrolytes and the lithium-air battery. Northeastern University, 2010.

[39] Read J, Mutolo K, Ervin M, Behl W, Wolfenstine J, Driedger A, et al. Oxygen Transport Properties of Organic Electrolytes and Performance of Lithium/Oxygen Battery. J Electrochem Soc 2003;150:A1351. doi:10.1149/1.1606454.

[40] Lu Y-C, Kwabi DG, Yao KPC, Harding JR, Zhou J, Zuin L, et al. The discharge rate capability of rechargeable Li-O_2 batteries. Energy Environ Sci 2011;4:2999. doi:10.1039/c1ee01500a.

[41] Lu Y-C, Shao-Horn Y. Probing the Reaction Kinetics of the Charge Reactions of Nonaqueous Li-O_2 Batteries. J Phys Chem Lett 2013;4:93–9. doi:10.1021/jz3018368.

[42] Li XL, Faghri A. Local entropy generation analysis on passive high-concentration DMFCs (direct methanol fuel cell) with different cell structures. Energy 2011;36:403–14. doi:10.1016/j.energy.2010.10.024.

Table 2-1 Parameters used in the model.

Parameter	Symbol	Value
Room temperature	T_∞	293 K
Thermal diffusivity of air	α	2.22×10^{-5} m^2 s^{-1}
Kinematic viscosity of air	ν	1.51×10^{-5} m^2 s^{-1}
Thermal expansion coefficient of air	β	3.43×10^{-3} K^{-1}
Prandtl number of air	Pr	0.713
Active area of electrode per volume	$A_{ED,0}$	3.67×10^{5} cm^2 cm^{-3} [32]
Exchange current density	i_0	3.11×10^{-6} A m^{-2} [Assumed]
Transfer coefficient of cathode	α_{ORR}	0.5 [38]
Thermodynamic equilibrium voltage	E_0	3.1 [8]
Reference concentration of O_2	$\omega_{O_2}^{ref}$	1.41×10^{-3} kg kg^{-1} [Assumed]
Reference concentration of lithium ion	$\omega_{Li^+}^{ref}$	6.86×10^{-3} kg kg^{-1} [Assumed]
Density of PTFE	ρ_{PTFE}	2.2 g cm^{-3}
Density of lithium	ρ_{Li}	0.534 g cm^{-3}
Density of carbon	ρ_{C}	2.26 g cm^{-3}
Density of lithium peroxide	ρ_{Li2O2}	2.31 g cm^{-3}
Density of electrolyte	ρ_{EL}	1.011 g cm^{-3} [39]
Conductivity of electrolyte	σ_{EL}	15.9×10^{-3} S cm^{-1} [39]
Conductivity of electrode	σ_{ED}	3 S cm^{-1} [40]
Conductivity of Li_2O_2	σ_{Li2O2}	2×10^{-13} S cm^{-1} [41]
Specific heat of electrolyte	$Cp_{,EL}$	0.5 J g^{-1} K^{-1}
Specific heat of carbon	$Cp_{,ED}$	0.71 J g^{-1} K^{-1}
Specific heat of Li_2O_2	$Cp_{,Li2O2}$	1.81 J g^{-1} K^{-1}
Diffusivity of oxygen in electrolyte	D_{O2}	8.35×10^{-6}cm^2 s^{-1} [39]
Diffusivity of Li^+ in electrolyte	D_{Li+}	8×10^{-7} cm^2 s^{-1} [40]
Thermal conductivity of electrolyte	k_{EL}	0.2 W m^{-1} K^{-1}
Thermal conductivity of electrode	k_{ED}	1.5 W m^{-1} K^{-1} [42]
Thermal conductivity of Li_2O_2	k_{Li2O2}	14.5 W m^{-1} K^{-1}
Solubility of oxygen in electrolyte		4.45×10^{-3} M [39]
Molecular weight of lithium	M_{Li}	6.94 g mol^{-1}
Molecular weight of lithium peroxide	M_{Li2O2}	45.88 g mol^{-1}
Porosity of electrode	ε_{ED}	0.75 [32]
Porosity of separator	ε_{EL}	0.5 [32]
Thickness of the electrode	δ_{ED}	800 μm [36]
Thickness of the separator	δ_{EL}	25 μm [32]
Width of the battery	δ_{Y}	2 mm
Width of the rib	δ_{RIB}	1.0 mm
Viscosity of Electrolyte	μ	1.98×10^{-3} kg m^{-1} s^{-1} [40]

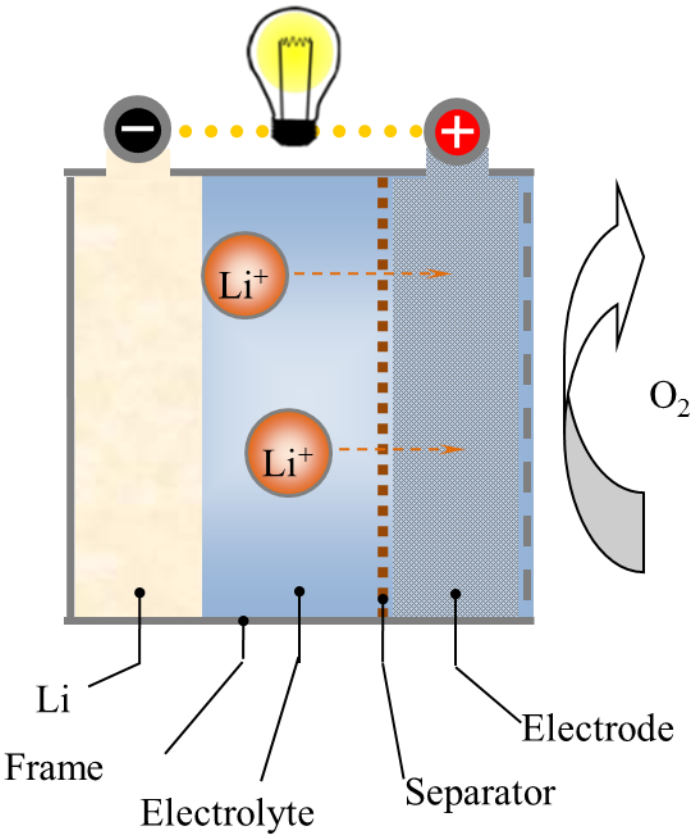

Figure 2-1 A rechargeable Li-O_2 battery using an organic electrolyte.

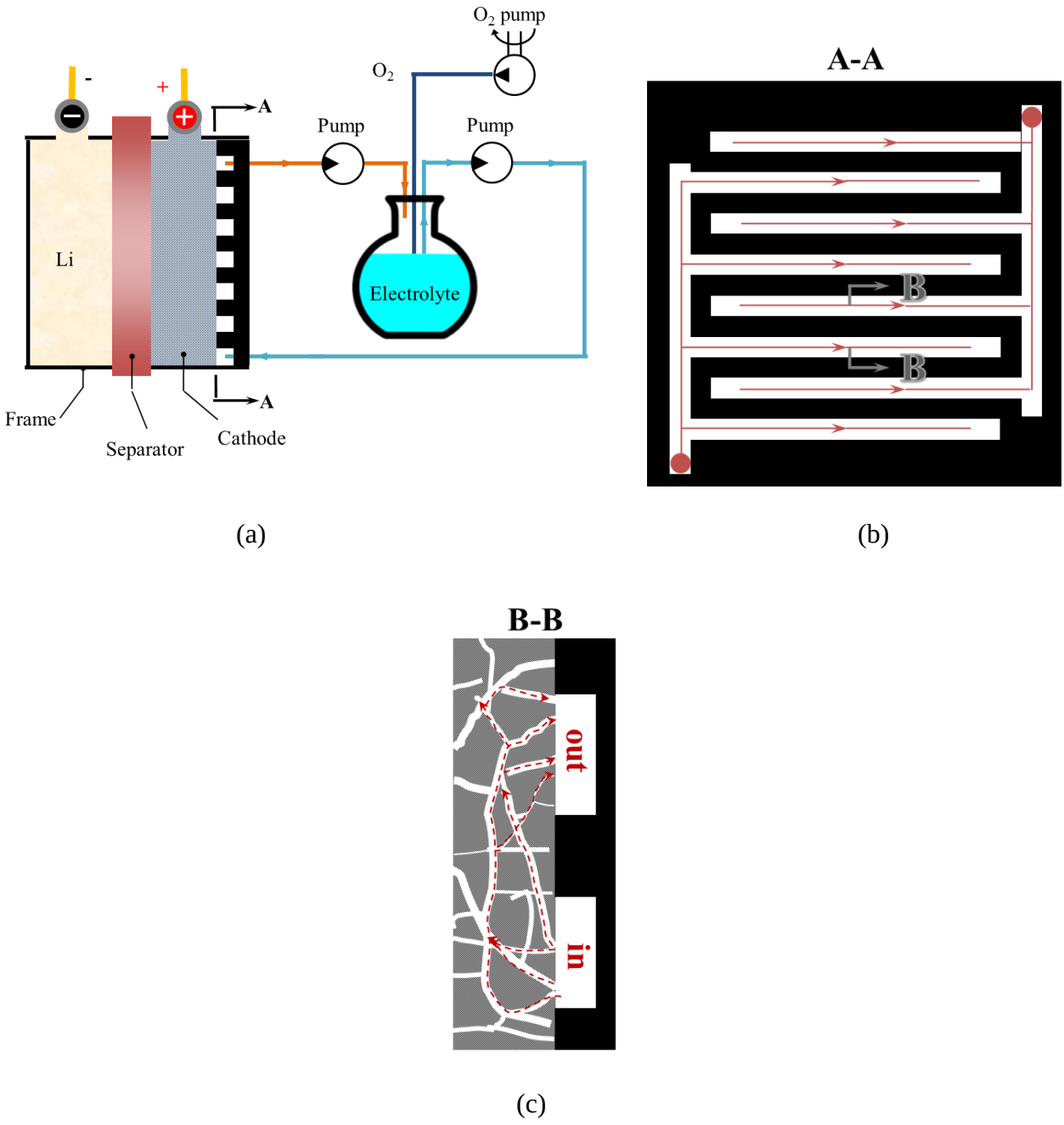

(a) (b)

(c)

Figure 2-2 a) An active Li-O_2 battery system, b) the interdigital channel at the cathode, and c) the cross-sectional view of interdigitatal channels.

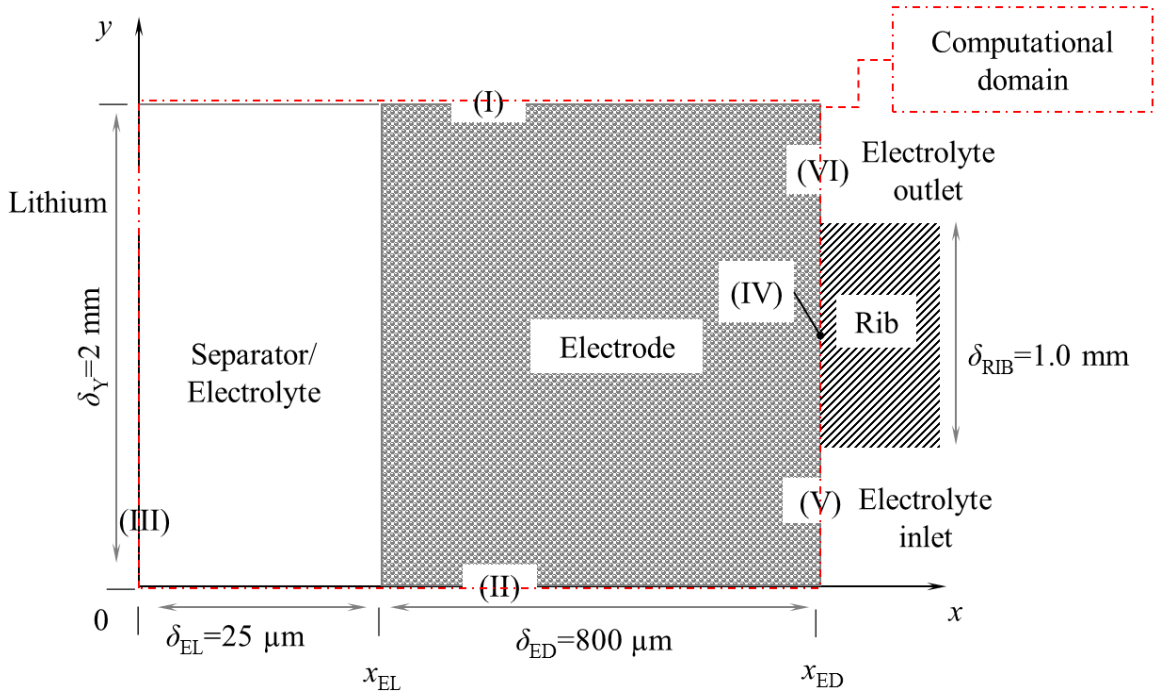

Figure 2-3 Boundary conditions and computational domain of a Li-O_2 battery model considering convection.

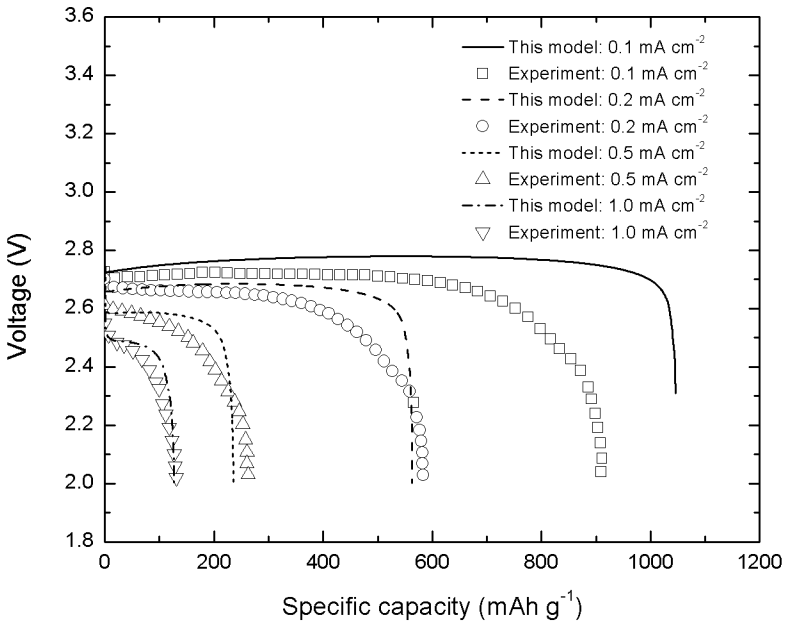

Figure 2-4 Comparison between modeling results and experimental results [33] of cell voltage vs. specific capacities at various discharge current densities.

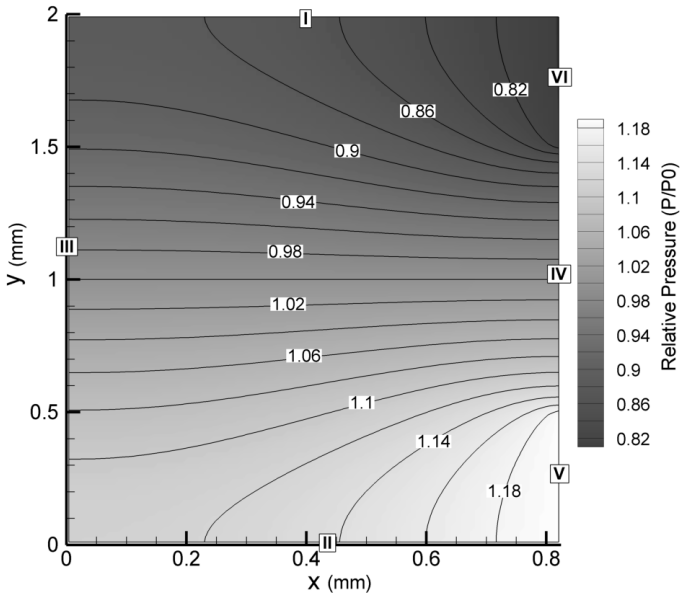

(a)

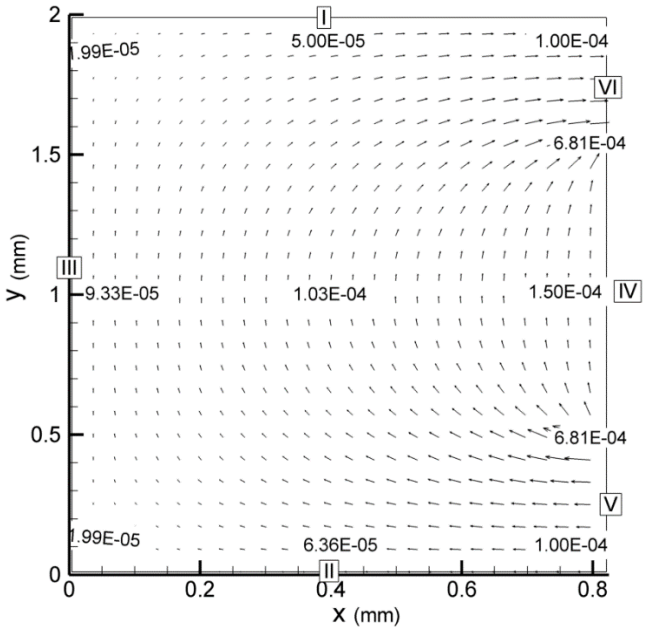

(b)

Figure 2-5 a) Pressure and b) velocity distributions in the computational domain (including the separator and electrode). The numbers in b) show magnitude of local velocity in unit of m s^{-1}.

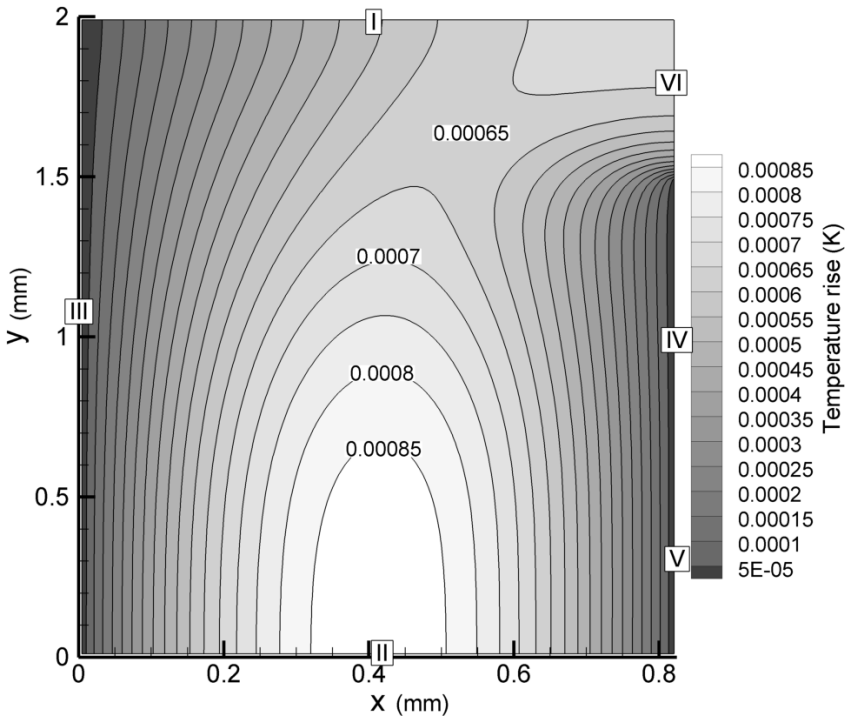

Figure 2-6 Temperature distribution at the end of the discharge process. The discharge current is 1.5 mA cm^{-2}.

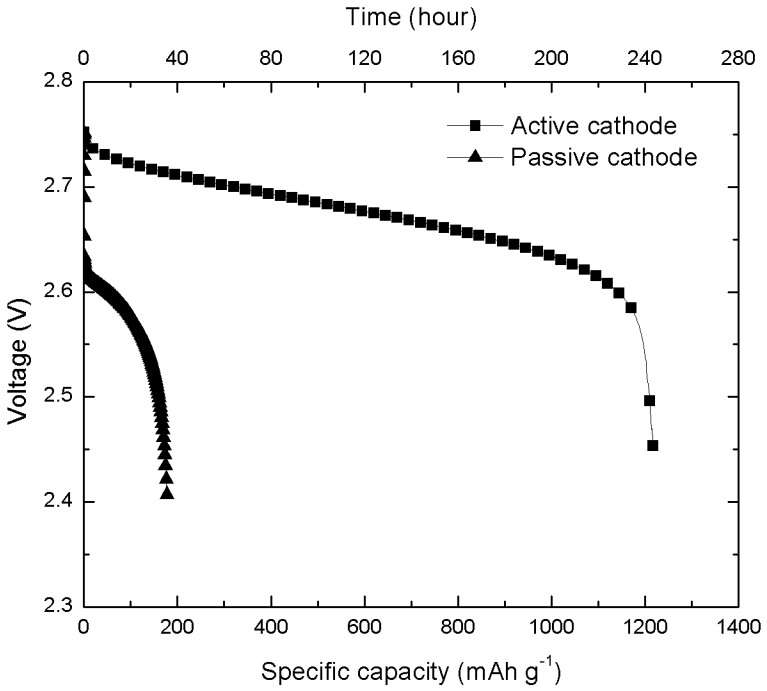

Figure 2-7 Comparison of voltage vs. specific capacity curves between the Li-O_2 cells with passive and active cathode. The discharge current density is 0.2 mA cm^{-2}.

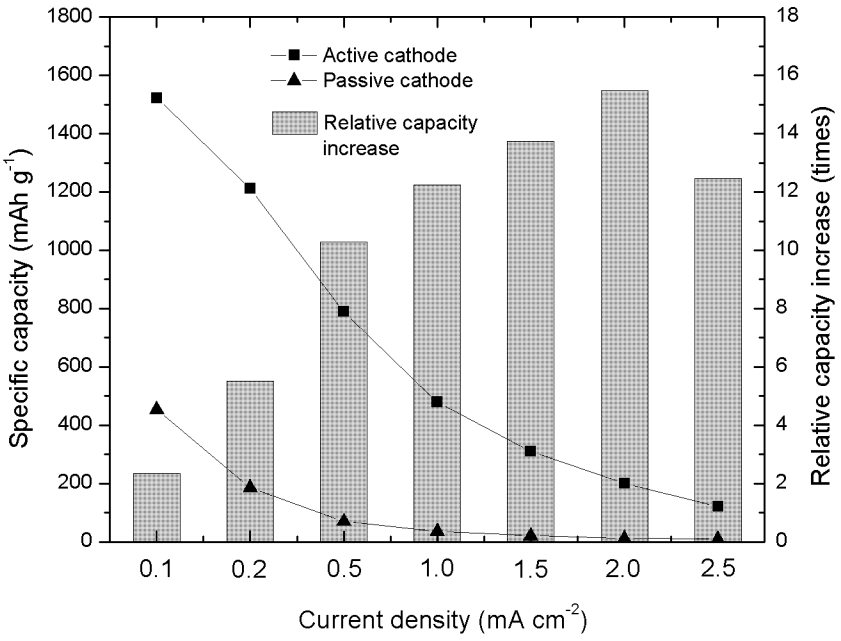

Figure 2-8 Comparison of the discharge capacities of Li-O_2 cells with passive and active cathodes under different discharge current densities.

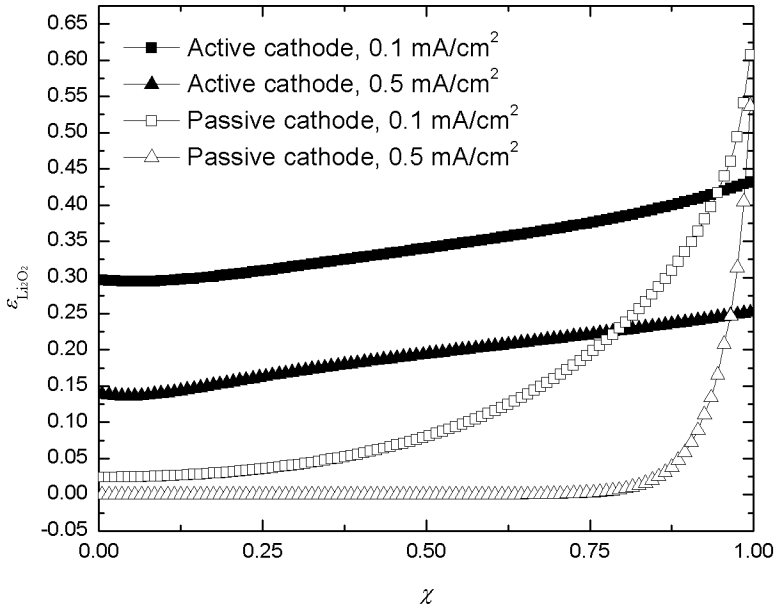

Figure 2-9 Distributions of volume fractions of Li_2O_2 in the electrode after the passive and the active Li-O_2 cells are fully discharged at different current densities.

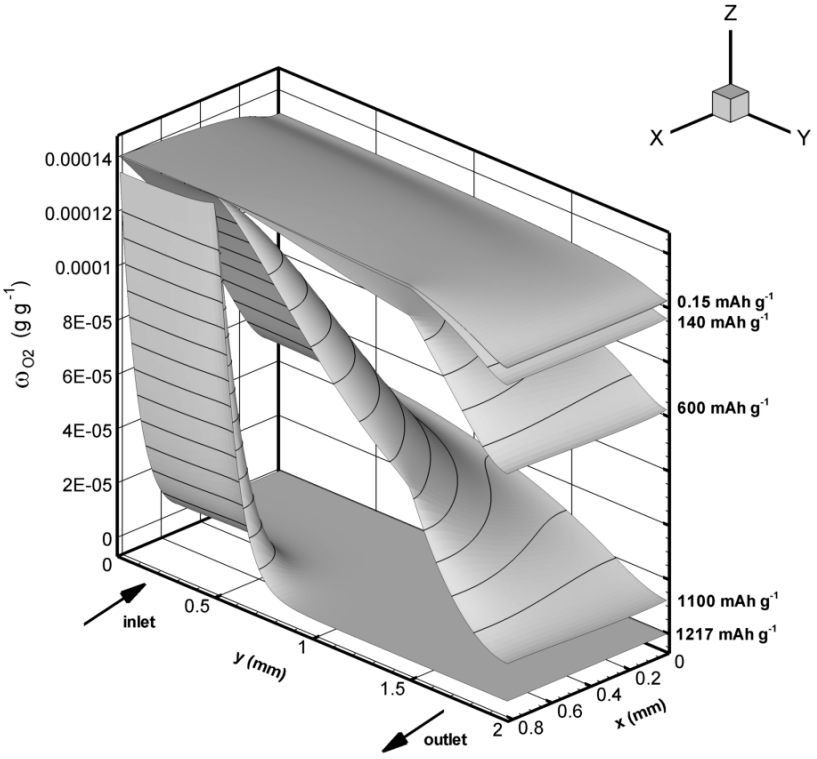
Z
X
Y
0.00014
0.00012
0.0001
8E-05
6E-05
4E-05
2E-05
0
ω_{O2} (g g^{-1})
0.15 mAh g^{-1}
140 mAh g^{-1}
600 mAh g^{-1}
1100 mAh g^{-1}
1217 mAh g^{-1}
inlet
y (mm)
outlet
x (mm)

(a)

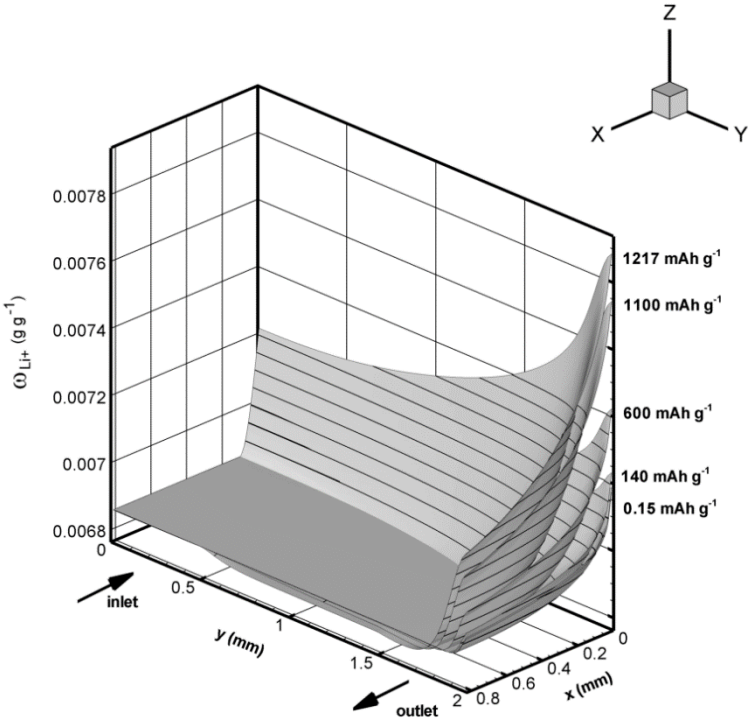
Z
X
Y
0.0078
0.0076
0.0074
0.0072
0.007
0.0068
ω_{Li+} (g g^{-1})
1217 mAh g^{-1}
1100 mAh g^{-1}
600 mAh g^{-1}
140 mAh g^{-1}
0.15 mAh g^{-1}
inlet
y (mm)
outlet
x (mm)

(b)

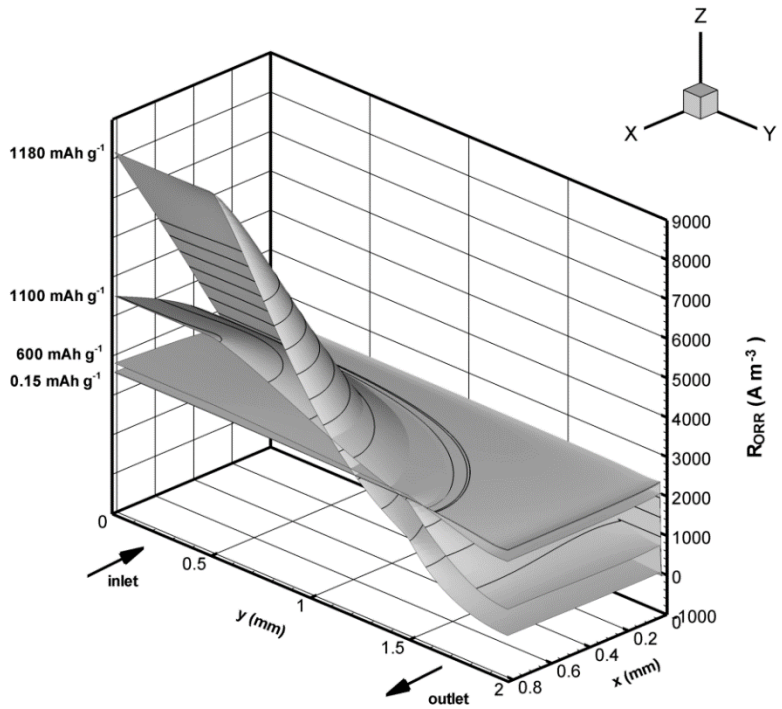

(c)

Figure 2-10 Distributions of a) oxygen, b) lithium ions, and c) ORR rate at different times of the discharge process.

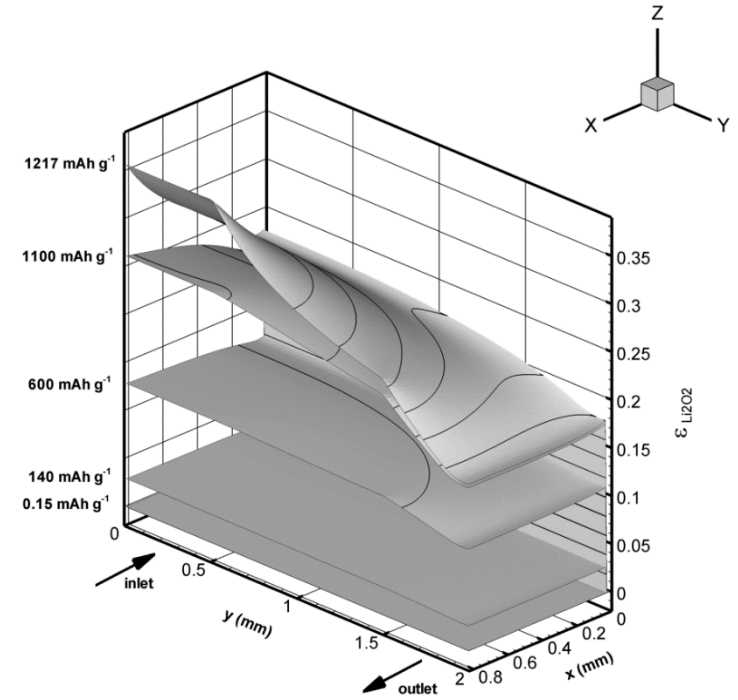

(a)

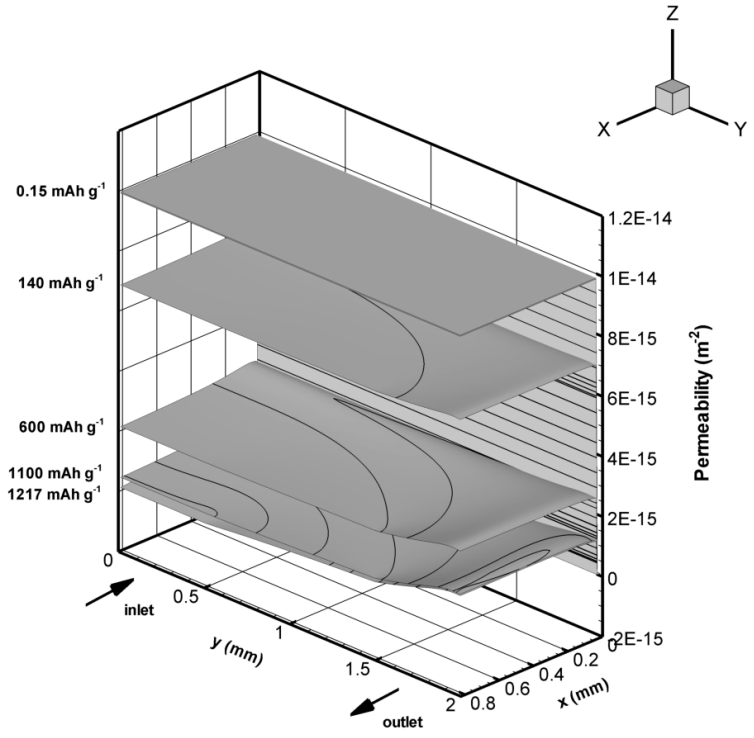

(b)

Figure 2-11 Distributions of a) Li_2O_2 volume fraction and b) relative permeability at different times of discharge process.

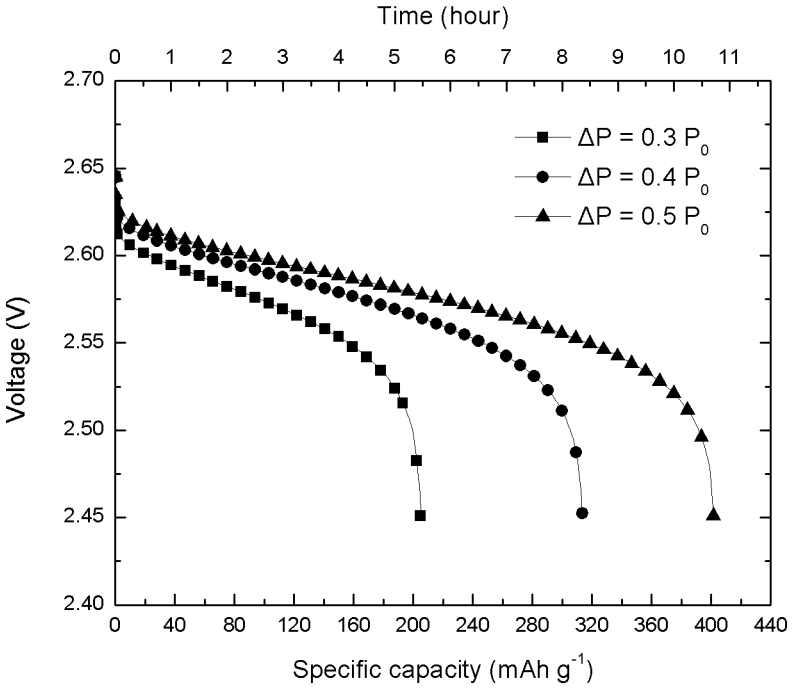

(a)

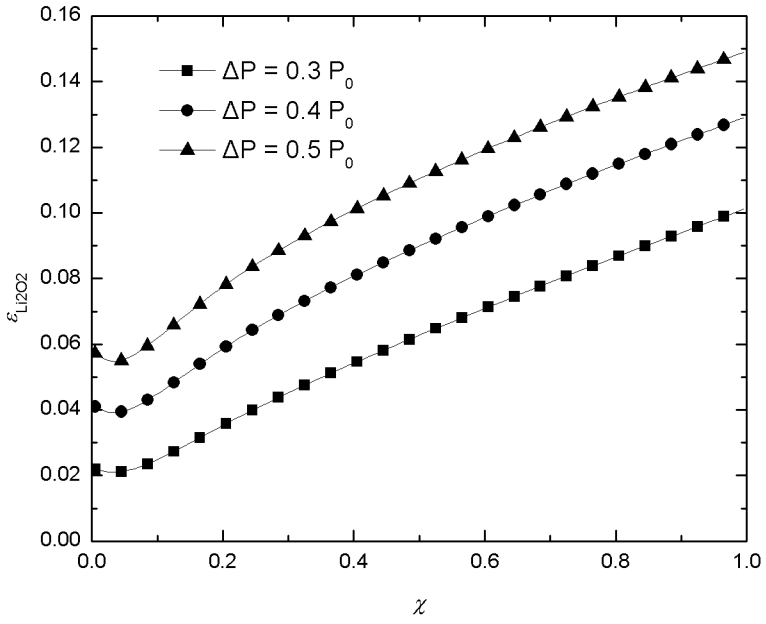

(b)

Figure 2-12 a) The cell voltage vs. specific capacity curves and b) distributions of Li_2O_2 volume fraction along the electrode of active Li-O_2 cells under different pressure differences ($0.3P_0$, $0.4P_0$ and $0.5P_0$) between adjacent channels.

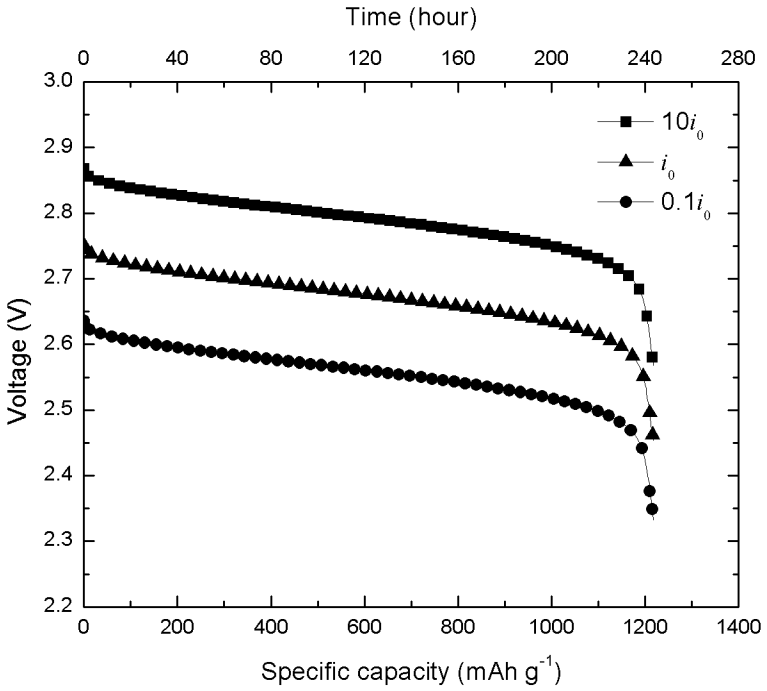

Figure 2-13 Discharge capacities of cells with different exchange current densities.

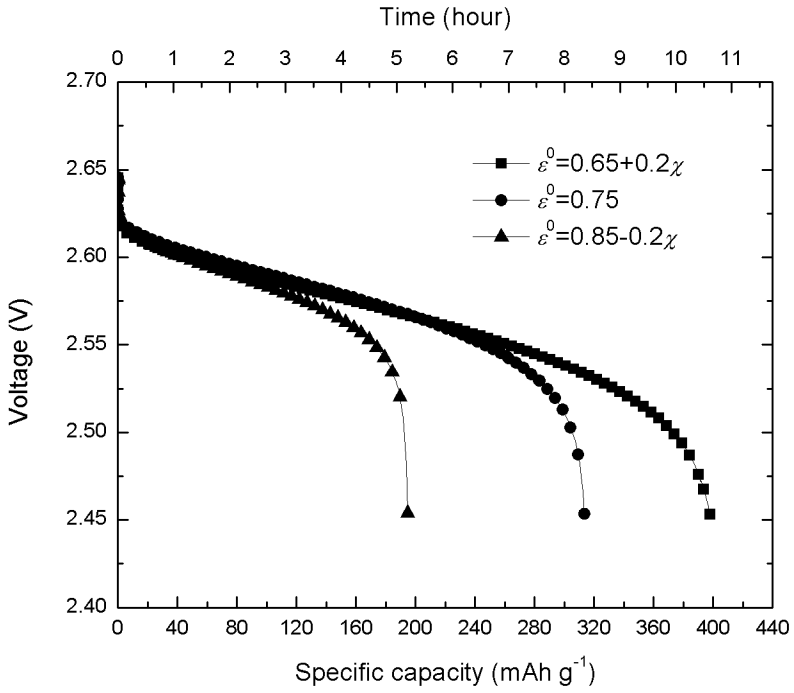

(a)

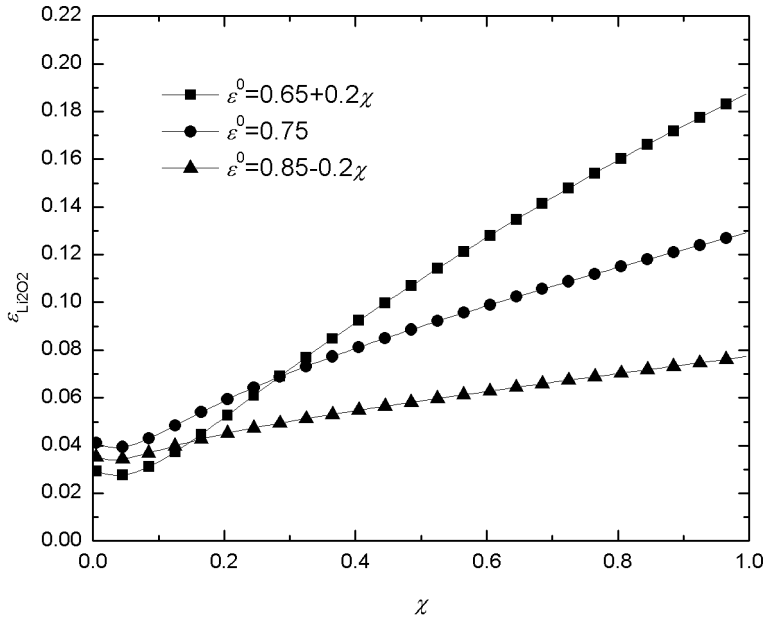

(b)

Figure 2-14 a) The cell voltage vs. specific capacity curves and b) distribution of Li_2O_2 volume fractions of active Li-O_2 cells with gradient electrode porosities.

Chapter 3 Capacity Enhancement of a Lithium Oxygen Flow Battery

A two-dimensional model is developed for an aprotic lithium oxygen ($Li–O_2$) flow battery, in which the organic electrolyte is recirculated through the cathode to enhance oxygen supply. The conventional $Li–O_2$ battery model is extended to incorporate convection effects. In contrast to the classic flow battery models, the pore structure change caused by the insoluble discharge product of $Li–O_2$ batteries is considered. A parametric study is performed to study the influence of model parameters on cathode specific capacity. Results show that contrary to conventional $Li–O_2$ cells, electrolyte with a lower conductivity would increase the specific capacity of the $Li–O_2$ flow cell. The results also reveal those parameters that are influential to battery capacity. Based on the analysis, two methods, dual layer cathode and alternating electrolyte flow, are proposed to enhance battery capacity. The dual layer cathode has 105% higher capacity than a single layer cathode at the current density of 1.5 mA cm^{-2}. Alternating electrolyte flow can increase the cathode capacity by 3.7% at the current density of 0.2 mA cm^{-2}.

3.1 Introduction

The next generation of electrochemical energy storage devices should have high capacity, long cycleability and low cost. To achieve these goals, secondary batteries are researched from different perspectives, including integration of new materials, improving reaction kinetics, building more effective electrodes, and other novel research strategies [1].

Among the numerous different types of batteries, some can be well categorized, such as lithium ion batteries, metal air batteries, lithium sulfur batteries, all-vanadium redox flow batteries, etc. Some others are a hybrid of two different battery types, such as the semi-solid lithium flow battery proposed by Duduta et al. (2011) [2]. It was a combination of flow battery and lithium ion (Li–ion) battery. The active materials for the conventional Li–ion batteries were liquidified to a semi-solid slurry, to be pumped out of the battery and stored in external tanks. Another example is the semi-liquid lithium sulfur flow battery proposed by Yang et al. (2013) [3]. Like in a conventional lithium sulfur (Li–S) battery its anode was metallic lithium, while the cathode resembled that of a flow battery. Operation relied on the transition between various lithium polysulfides (Li_2S_8, Li_2S_4, and Li_2S_2) to store and release energy.

Two other batteries combined the features of the flow battery and the lithium oxygen battery (Li–O_2) designs. To enhance the oxygen transport in aqueous Li–O_2 battery, Xu et al. (2013) proposed to saturate the electrolyte with oxygen external to the battery and to pump it through the cathode of the battery [4]. The electrolyte was water based and separated from the anode by an ion conducting glass-ceramic membrane. Experimental results showed that the battery could be cycled at a high discharge rate of 5mA cm^{-2}. Similarly, Li et al. (2015) proposed an aprotic Li–O_2 design in which the electrolyte was recirculated through the cathode like a fuel cell and oxygen was dissolved into the electrolyte in a tank external to the battery. Simulation results showed that the convection effect significantly enhanced oxygen supply in the cathode and hence increased battery capacity significantly [5]. However, in their model a constant cathode activation overpotential was

assumed so electrolyte potential equation was neglected. The transportation equations for lithium ion and oxygen were based on dilute solution theory.

In this work, the model developed by Li et al. [5] is improved based on the porous electrode method and concentrated solution theory developed by Newman's group [6–9]. Compared to the models for conventional flow batteries, this model considers the effects of the insoluble and insulate discharge product deposition in the electrode. Compared to conventional Li–O_2 battery models, this model includes the effect of convection in species transportation. A parametric study is performed to find the influence of modeling parameters on the prediction of cathode specific capacity and energy. Based on the analysis of the results, two methods: i) a dual porosity cathode structure, and ii) an alternating electrolyte flow method, are proposed to further increase the capacity of the aprotic Li–O_2 flow battery.

3.2 Background

Modeling study on batteries can provide in-depth details of the mass transport process and its interdependence with the electrochemical reactions for future battery structure optimization. Li et al. (2012) conducted a lithium and oxygen diffusion model and found that the micro-pores closer to the separator/cathode interface were not fully utilized [10]. Based on this result, they proposed a cathode structure with a gradient porosity of higher porosity closer to the air side and lower porosity closer to the separator/cathode interface. This idea was proven to be effective through experiments by another group led by Zhao (2014) [11].

In 2007, Sandhu et al. developed the first numerical model for Li–O_2 batteries. This model assumed that the cathode has a cylindrical pore geometry. The effect of oxygen partial pressure on the battery capacity was studied [12]. In 2010, Andrei et al. reported a model that considered electrolyte potential and thermal effect, as well as oxygen and lithium ion transport [13]. The importance of oxygen transport and Li_2O_2 growth in a Li–O_2 battery were recognized later. Wang (2012) formed an analogy between the Li_2O_2 growth in a Li–O_2 battery and the ice formation in a proton exchange membrane fuel cell (PEMFC) under sub-freezing conditions [14]. Based on this assumption, a Li–O_2 battery model was developed to study the effect of insoluble substance deposition on surface passivation and oxygen transport in Li–O_2 batteries. Different micro-structures of the porous electrode were considered, including cylindrical, spherical and planar pores [15]. In 2013, Sahapatsombut et al. became the first to model the charging process of a lithium air (Li–air) battery. The predicted cell potential for both discharging and charging processes agreed well with the experimental results [16]. The model was further developed to include the formation of Li_2CO_3 occurring from electrolyte degradation [17]. The model attributed the decrease of discharge capacity during cycling to the irreversible formation of Li_2CO_3. Wang and Cho (2014) developed a 2D Li–air battery model that incorporated a gas diffusion layer. It was concluded that a low Damköhler number in the diffusion layer should be kept to alleviate voltage loss [18]. Other recent developments in Li–O_2 battery modeling include the consideration of pore size or particle size distribution [19,20], the improvement of reaction surface covering model [21], and the consideration of the volume change effect caused by Li_2O_2 deposition [22].

Redox flow batteries have also been the focus of modeling studies. Shah and co-workers (2008) developed a transient model for all-vanadium flow batteries to examine the effect of flow rate, concentration and electrode porosity on the performance [23]. It was later developed to include thermal effects, oxygen evolution and hydrogen evolution [24–26]. Recent advancements in flow battery modeling include multi-dimensional models [27] and stack scale models [28]. Brunini et al. (2012) developed a 3D model for the aforementioned semi-solid lithium ion flow battery [2], from which it was concluded that a weak dependence of cell voltage on the state of charge would result in uniform current density distribution and higher energy efficiency [29].

It should be noted that the Li–O_2 flow battery studied in this chapter has fundamental differences to the conventional all-vanadium redox flow battery, other than the apparent difference in chemistries. The most prominent difference is that the electrode structure in a flow battery does not change during operation while in a Li–O_2 battery the Li_2O_2 deposition decreases the porosity of the electrode. Therefore, the capacity of the system is limited by the blocking effect of Li_2O_2 deposition in cathode. From the perspective of energy conversion and storage, the circulated electrolyte in the Li–O_2 flow battery only serves as a vehicle to transport oxygen. The oxygen-depleted electrolyte does not go to a low energy storage tank but returns to the aeration tank and is re-saturated with oxygen. Therefore, the external tank size is determined by the aeration efficiency, not by the amount of energy to be stored. It is also observed that in most all-vanadium redox flow battery models, dilute solution theory was used while most lithium battery models used concentrated solution theory.

In this chapter, a comprehensive 2D, transient model based on porous electrode and concentrated solution theory is developed for the aprotic Li–O_2 flow battery proposed by Li et al. [5]. Electrolyte concentration, oxygen concentration, electrolyte potential, electrode potential, and the porosity change caused by Li_2O_2 precipitation are considered in the model. Efforts are made to keep the property data consistent for the same type of electrolyte. It should be noted that although most state-of-the-art Li–O_2 cells use an ether, amide or ionic fluid based electrolyte, property data on these solutions are not as abundant as alkyl carbonate based electrolytes. Therefore, the model electrolyte in this work is carbonate based.

3.3 Model development

The structure of the aprotic Li–O_2 flow battery is shown in Figure 3-1(a). Lithium foil and a porous carbon electrode serve as the anode and cathode, respectively. A porous dielectric film is placed between them to serve as the separator. An endplate embedded with interdigital flow channels is pressed onto the cathode to provide electrolyte circulation and serve as cathode current collector. The dashed line depicts the computation domain of the model. Because of the symmetry of the flow, the computation domain covers only half of the inlet and outlet channels. In all calculations, the rib covers half of the cathode electrode surface (50% open ratio). As a comparison, the conventional Li–O_2 cell has the same structure but the electrolyte is stagnant and the flow channels are filled with oxygen, instead of oxygen-saturated electrolyte.

The pressure, velocities of the electrolyte, oxygen concentration, electrolyte concentration, electrolyte potential, electrode potential, reaction rate, and volume fraction of the solid product are

solved in the computation domain as shown in Figure 3-1(b). To simplify the analysis and focus on the key parameters and phenomena, the following assumptions are adopted:

- Only the following reaction is considered in the cathode:

$$2Li^+ + O_2 + 2e^- \rightarrow Li_2O_2 \qquad (E_0 = 3.10\text{V vs. } Li/Li^+) \tag{1}$$

- The overpotential of the anode reaction is negligible [30].
- The electrolyte fully fills the pores in the cathode electrode. Oxygen and lithium ion transfer occur only in the electrolyte (liquid phase).
- Li_2O_2 is insoluble in the electrolyte and deposits as a smooth film in the electrode because the size of Li_2O_2 particles is typically several orders of magnitude smaller than the size of a Li–O_2 battery electrode [31].

3.3.1 Governing equations

The electrode and separator are regarded as porous media in the model. Based on the calculations, the maximum velocity in the computation domain occurs at the start of discharge around the inlet, which is 2.86×10^{-3} m s^{-1}. Using the average pore size (0.1 μm) as characteristic length, the maximum local Re number is 8.3×10^{-5}, which is far smaller than 1. This ensures that the flow is in the laminar regime and Darcy's law is applicable [5]. Conservation of mass in porous media can be written as [32]:

$$\frac{\partial \varepsilon}{\partial t} + \nabla \cdot \boldsymbol{u} = s_m \tag{2}$$

where ε is porosity, $\boldsymbol{u}$ is the spatial averaged electrolyte velocity, and s_m is the source term caused by the consumption of oxygen and lithium ions. It is defined by:

$$s_m = \frac{r_{\mathrm{Li}} M_{\mathrm{Li}} + r_{\mathrm{O_2}} M_{\mathrm{O_2}}}{\rho_{\mathrm{EL}}}$$

where r is the consumption rate, M is the molecular weight and ρ_{EL} is the electrolyte density. Subscripts Li and O_2 stand for lithium ion and oxygen, respectively.

According to Darcy's law, the relation between pressure and velocity in porous media can be expressed as:

$$\boldsymbol{u} = -\frac{K}{\mu_{\mathrm{EL}}} \nabla p \tag{3}$$

where K is permeability, μ_{EL} is the viscosity of the electrolyte and p is pressure. The permeability of the electrode, K, is a function of porosity, and therefore changes during discharge. In this chapter, the cathode is assumed to consist of a collection of solid spheres. The Carman–Kozeny equation relates the permeability of such a porous media to the porosity, ε [32,33]:

$$K = C_{\mathrm{KC}} \frac{\varepsilon^3}{\left(1-\varepsilon\right)^2} \tag{4}$$

where C_{KC} is an empirical factor. The porosity of the electrode can be related to the volume fraction of the Li_2O_2, $\varepsilon_{\mathrm{Li_2O_2}}$, by:

$$\varepsilon = \varepsilon^0 - \varepsilon_{\mathrm{Li_2O_2}} \tag{5}$$

where ε^0 is the porosity of a pristine cathode. The volume fraction of Li_2O_2 changes with time and position and can be calculated from the generation rate of Li_2O_2. Combining eqs. (4) and (5), the relative change of permeability of the porous medium can be calculated by the following equation:

$$\frac{K}{K^0}=\left(1-\frac{\varepsilon_{\mathrm{Li_2O_2}}}{\varepsilon^0}\right)^3\cdot\left(\frac{1-\varepsilon^0}{1-\varepsilon^0+\varepsilon_{\mathrm{Li_2O_2}}}\right)^2 \tag{6}$$

where K^0 is the original permeability at the start of discharge.

Combining eq. (2) and (3) leads to the equation for pressure:

$$\frac{\partial\varepsilon}{\partial t}+\nabla\cdot\left(-\frac{K}{\mu_{\mathrm{EL}}}\nabla p\right)=s_{\mathrm{m}} \tag{7}$$

Equation (7) is solved implicitly to obtain the pressure distribution and then the velocity field may be obtained through eq. (3).

Conservation of all species in the electrolyte can be expressed as:

$$\frac{\partial\left(\varepsilon c_i\right)}{\partial t}=-\nabla\cdot\boldsymbol{N}_i+r_i \tag{8}$$

where c_i is molarity of specie i, $\boldsymbol{N}_i$ is the molar flux of specie i, and r_i is the species generation rate due to reactions.

Lithium ion transport in the electrolyte occurs by diffusion, migration, and convection. According to the concentrated solution theory [9], its molar flux is expressed as:

$$\boldsymbol{N}_{\mathrm{Li}}=-D_{\mathrm{Li}}^{eff}\nabla c_{\mathrm{Li}}+\frac{\boldsymbol{i}_2 t_+^0}{F}+\boldsymbol{u}c_{\mathrm{Li}} \tag{9}$$

where D_{Li}^{eff} is the effective diffusion coefficient of the salt, t_+^0 is the transference number of lithium ion with respect to the solvent velocity, F is the Faraday constant, and $\boldsymbol{i}_2$ is the current density vector in the electrolyte. Strictly speaking the term $\boldsymbol{u}$ in eq. (9) is the solvent velocity. In the present model it is approximated by the mass averaged velocity as determined by eq. (3). The current density in the binary electrolyte, $\boldsymbol{i}_2$, can be expressed as:

$$\boldsymbol{i}_2 = -k^{\text{eff}}\nabla\phi_2 - \frac{2RTk^{\text{eff}}}{F}\left(t_+^0 - 1\right)\left(1 + \frac{\partial \ln f_\pm}{\partial \ln c_{\text{Li}}}\right)\nabla \ln c_{\text{Li}} \tag{10}$$

where k^{eff} is the effective conductivity, $f_\pm$ is the salt activity coefficient, and $\left(1 + \frac{\partial \ln f_\pm}{\partial \ln c_{\text{Li}}}\right)$ is the thermodynamic factor [34].

To simplify the equations, a diffusion conductivity, k_{D}, is defined [13]:

$$k_{\text{D}} = \frac{2RTk^{\text{eff}}}{F}\left(t_+^0 - 1\right)\left(1 + \frac{\partial \ln f_\pm}{\partial \ln c_{\text{Li}}}\right) \tag{11}$$

Combining eqs. (2) and (8) – (11) yields the governing equation for lithium ion transport:

$$\varepsilon\frac{\partial c_{\text{Li}}}{\partial t} + \nabla\cdot\left(-D_{\text{Li}}^{\text{eff}}\nabla c_{\text{Li}}\right) + \boldsymbol{u}\cdot\nabla c_{\text{Li}} = r_{\text{Li}} - \nabla\cdot\left(\frac{\boldsymbol{i}_2 t_+}{F}\right) - s_{\text{m}}c_{\text{Li}} \tag{12}$$

Dissolved oxygen is transported in the electrolyte by diffusion and convection. Its molar flux is expressed as:

$$\boldsymbol{N}_{\text{O}_2} = -D_{\text{O}_2}^{\text{eff}}\nabla c_{\text{O}_2} + \boldsymbol{u}c_{\text{O}_2} \tag{13}$$

Combining eqs. (2), (8) and (13) leads to the governing equation for oxygen transport:

$$\varepsilon\frac{\partial c_{\text{O}_2}}{\partial t} + \nabla\cdot\left(-D_{\text{O}_2}^{\text{eff}}\nabla c_{\text{O}_2}\right) + \boldsymbol{u}\cdot\nabla c_{\text{O}_2} = r_{\text{O}_2} - s_{\text{m}}c_{\text{O}_2} \tag{14}$$

The consumption rates of the lithium ion, r_{Li} in eq. (12), and oxygen, r_{O_2} in eq. (14), can be related to the local interfacial transfer current density between electrolyte and electrode, j_{R}, as:

$$r_{\text{Li}} = \frac{s_{\text{Li,R}}A_{\text{ED}}j_{\text{R}}}{n_{\text{R}}F} \tag{15}$$

$$r_{\text{O}_2} = \frac{s_{\text{O}_2,\text{R}}A_{ED}j_{\text{R}}}{n_{\text{R}}F} \tag{16}$$

where *s* is the stoichiometric coefficient of species, *n* is the number of electrons transferred in the reaction and the subscript R is the reaction to be considered. In this model, R represents the reaction shown in eq. (1).

To maintain charge balance, the divergence of electrolyte current density should be equal to the local reaction rate:

$$\nabla \cdot \boldsymbol{i}_2 = A_{\mathrm{ED}} j_{\mathrm{R}} \tag{17}$$

Combining eqs. (10) and (17) gives the equation for electrolyte potential:

$$\nabla \cdot \left(-k^{\mathrm{eff}} \nabla \phi_2 \right) = \nabla \cdot \left(\frac{k_{\mathrm{D}}}{c_{\mathrm{Li}}} \nabla c_{\mathrm{Li}} \right) + A_{\mathrm{ED}} j_{\mathrm{R}} \tag{18}$$

The current balance between the electrolyte and cathode solid phase indicates that:

$$\nabla \cdot \boldsymbol{i}_1 + \nabla \cdot \boldsymbol{i}_2 = 0 \tag{19}$$

where $\boldsymbol{i}_1$ is the current density in the cathode solid phase, which can be expressed by Ohm's law:

$$\boldsymbol{i}_1 = -k_{\mathrm{c}}^{\mathrm{eff}} \nabla \phi_1 \tag{20}$$

Therefore, cathode electric potential can be obtained from eqs. (17), (19), and (20) as:

$$\nabla \cdot \left(-k_{\mathrm{c}}^{\mathrm{eff}} \nabla \phi_1 \right) = -A_{\mathrm{ED}} j_{\mathrm{R}} \tag{21}$$

The effective parameters used in the above equations, including $D_{\mathrm{Li}}^{\mathrm{eff}}$, k^{eff}, $D_{\mathrm{O_2}}^{\mathrm{eff}}$, and $k_{\mathrm{c}}^{\mathrm{eff}}$, can be calculated through the Bruggeman correlation:

$$k^{\mathrm{eff}} = k\varepsilon^{\beta} \tag{22}$$

$$D_{\mathrm{O_2}}^{\mathrm{eff}} = D_{\mathrm{O_2}} \varepsilon^{\beta} \tag{23}$$

$$D_{\mathrm{Li}}^{\mathrm{eff}} = D_{\mathrm{Li}} \varepsilon^{\beta} \tag{24}$$

$$k_{\mathrm{c}}^{\mathrm{eff}} = k_{\mathrm{c}}\left(1-\varepsilon_0-\varepsilon_{\mathrm{PTFE}}\right)^{\beta} \tag{25}$$

where k, $D_{\mathrm{O_2}}$, D_{Li}, k_{c} are the ionic conductivity in bulk electrolyte, diffusion coefficients of O_2 and Li^+, and electron conductivity in the carbon phase of cathode, respectively. $\varepsilon_{\mathrm{PTFE}}$ is the volume fraction of PTFE used as the electrode binder and β is the Bruggeman coefficient, assumed to be 1.5.

In an all-vanadium flow battery, the porosity of the porous electrode does not change, therefore all the parameters in eqs. (22) – (24) do not change during battery cycling. However, in a Li–O_2 flow cell, porosity in the cathode is a function of location and increases overtime due to the deposition of Li_2O_2, which increases the transport resistance over time. Eventually, when the resistance becomes too high to sustain reactant transport, battery voltage drops. The increase of $\varepsilon_{\mathrm{Li_2O_2}}$ can be calculated according to mass conservation of the Li_2O_2**:**

$$\frac{\partial \varepsilon_{\mathrm{Li_2O_2}}}{\partial t} = -\frac{s_{\mathrm{Li_2O_2,R}} M_{\mathrm{Li_2O_2}}}{\rho_{\mathrm{Li_2O_2}} n_{\mathrm{R}} F} A_{\mathrm{ED}} j_{\mathrm{R}} \tag{26}$$

where $s_{\mathrm{Li_2O_2,R}}$ is the stoichiometric coefficient, $M_{\mathrm{Li_2O_2}}$ is the molecular weight, and $\rho_{\mathrm{Li_2O_2}}$ is the density of Li_2O_2. To arrive at this equation, it is assumed that the Li_2O_2 immediately deposits on the reaction surface once it is generated. The convection effect on Li_2O_2 is not considered in the present model. The Li_2O_2 deposition also reduces the effective reaction surface area. This effect is considered by an empirical correlation in the next section.

Seven equations are introduced above, including eqs. (3), (7), (12), (14), (18), (21), and (26). They are coupled together to determine seven unknowns: p, $\boldsymbol{u}$, c_{Li}, $c_{\mathrm{O_2}}$, ϕ_1, ϕ_2, and $\varepsilon_{\mathrm{Li_2O_2}}$. The

other unknown, j_R, is to be determined by reaction kinetics and connects the species consumption rates r_i to electrolyte and electrode potentials.

3.3.2 Electrochemical Kinetics

The driving force of the reaction is the local activation overpotential η_c, which can be defined as:

$$\eta_c = \phi_1 - \phi_2 - \Delta\phi_{Li_2O_2} - E_c^{\ 0} \tag{27}$$

where $\Delta\phi_{Li_2O_2}$ is the voltage drop over the Li_2O_2 film and $E_c^{\ 0}$ is the cathode theoretical potential. Voltage drop over the Li_2O_2 film is calculated by Ohm's law [17]:

$$\Delta\phi_{Li_2O_2} = j_R R_{Li_2O_2} \varepsilon_{Li_2O_2} \tag{28}$$

where $R_{Li_2O_2}$ is the electrical resistivity across Li_2O_2 film.

The Tafel equation is used to approximate the reaction kinetics:

$$j_R = -k_R \left(\frac{c_{Li}}{c_{Li}^{ref}} \right)^2 \left(\frac{c_{O_2}}{c_{O_2}^{ref}} \right) \exp\left(-\frac{\alpha_c F}{RT} \eta_c \right) \tag{29}$$

where k_R is the rate constant for cathode reaction, and α_c is the transfer coefficient equal to 0.5. Reference concentrations c_{Li}^{ref} and $c_{O_2}^{ref}$ are set to be 1 M and the saturated oxygen concentration, $c_{O_2,sat}$, respectively. The rate constant, k_R, is a function of temperature:

$$k_R = i_0 \cdot \exp\left[-\frac{E_R}{R} \left(\frac{1}{T^0} - \frac{1}{T} \right) \right] \tag{30}$$

where i_0 is the exchange current density at reference temperature T^0, and E_R is the activation energy of the reaction. Because the current density considered in this model is low, thermal effect is insignificant. Therefore, temperature is considered to be a constant T^0.

The effect of reaction area loss due to Li_2O_2 deposition is considered by the following empirical equation:

$$A_{\mathrm{ED}} = A_{\mathrm{ED},0}\left[1-\left(\frac{\varepsilon_{\mathrm{Li_2O_2}}}{\varepsilon_0}\right)^{z}\right] \tag{31}$$

where $A_{\mathrm{ED},0}$ is the original specific area and the value for z is set to 0.5 by ref. [16].

3.3.3 Boundary and initial conditions

At the electrolyte inlet (boundary I in Figure 3-1(b)), electrolyte and oxygen concentrations are both prescribed. The lithium ion concentration is fixed at 1 M and the oxygen concentration is assumed to be the saturated concentration at room temperature.

At the electrolyte outlet (boundary II), an outflow condition is assigned for electrolyte and oxygen concentration. The value of a boundary element is set to be the same as the value of the adjacent element to its left. The pressures at the inlet and outlet are 121,590 Pa and 81,060 Pa, respectively.

At the flow channel rib (boundary III), the x-direction gradient of pressure is zero; the x-direction flux of oxygen and electrolyte are also zero. Electrolyte potential at the right boundaries (I, II and III) is determined by:

$$i_{2,x} = -k^{\mathrm{eff}}\frac{\partial \phi_2}{\partial x} - \frac{k_{\mathrm{D}}}{c_{\mathrm{Li}}}\frac{\partial c_{\mathrm{Li}}}{\partial x} = 0$$

At the left boundary (boundary IV), the pressure gradient, oxygen concentration gradient, and velocity are zero. Electrolyte concentration at this boundary is determined by:

$$N_{\mathrm{Li},x} = -D_{\mathrm{Li}}^{\mathrm{eff}} \frac{\partial c_{\mathrm{Li}}}{\partial x} + \frac{i_{2,x} t_+^0}{F} = \frac{I}{F}$$

where I is the discharge current density. Because anode reaction is assumed to be reversible, the anode activation overpotential is zero. Electrolyte potential at the left boundary, therefore, is determined by

$$\phi_2 = \phi_{1,\mathrm{a}} - E_{\mathrm{a}}{}^0 - \eta_a .$$

Since both $\phi_{1,\mathrm{a}}$ and $E_{\mathrm{a}}{}^0$ are set to zero, ϕ_2 at left boundary is set to zero.

At the separator/cathode interface (boundary V) and electrolyte inlet and outlet, the electrode carbon phase current density is zero, which describes the boundary condition for ϕ_1:

$$\boldsymbol{i}_1 = -k_{\mathrm{c}}^{\mathrm{eff}} \nabla \phi_1 = 0$$

At the rib, the boundary condition for ϕ_1 is determined by:

$$i_{1,x} = -k_{\mathrm{c}}^{\mathrm{eff}} \frac{\partial \phi_1}{\partial x} = \frac{I}{(1-\mathrm{OR})}$$

where OR is the open ratio of the cathode to current collector. In this model, the open ratio is 0.5.

Because of the symmetry of the computation domain, all the variables, denoted by Φ, have a zero *y*-direction gradient on the upper and lower boundary (VI – IX):

$$\frac{\partial \Phi}{\partial y} = 0$$

All the governing equations and boundary conditions used in the model are summarized in Table 3-1. The equation system is solved by employing the mathematics module in COMSOL MultiPhysics®. The complete mesh consists of 9,792 elements with a maximum time step range

between 10 and 100 seconds depending on the discharge current density. Higher discharge current densities require a smaller time step. All the model results are both proven grid independent and time step independent.

At the start of the calculation, pressure is considered to be at the ambient condition of 101,325 Pa, the electrolyte and oxygen concentrations are all uniform, at the value of 1 M and saturated value $c_{O_2,sat}$, respectively. The properties of various materials used in the calculations are listed in Table 3-2. Most electrolyte data are based on those of 1 M $LiPF_6$ in Ethylene carbonate : Ethyl methyl carbonate (EC:EMC). Oxygen solubility and the diffusion coefficient are based on 1 M $LiPF_6$ in Propylene carbonate : Diethyl carbonate (PC:DEC) [35]. Cathode material loading is the mass of cathode material per unit area of electrode, which is calculated based on porosity, carbon density, PTFE density and weight percentage. When the electrode thickness is 800 μm, porosity is 0.8, and PTFE weight percentage is 10%, cathode material loading is 32.3 mg cm^{-2}.

3.4 Results and discussion

3.4.1 Model validation

Before conducting the parametric study, the model is validated by comparison of the simulation results to the experimental data provided by Read (2002) [36]. The exchange current density, i_0 in eq. (30), and the coefficient for reaction surface loss, z in eq. (31), are adjusted to match experimental results. Because the experiment was on conventional Li–O_2 batteries without electrolyte circulation, the model is modified in accordance. The modified model uses the same battery structure, mathematical method, and parameters as the flow battery model described in the

above sections except that convection terms are removed in all equations and the oxygen concentration at both the inlet and outlet are set to be at the saturation value. Figure 3-2 shows the dependence of cell voltages on cathode specific capacity for both simulation and experimental results, which agree reasonably well. The discrepancies may be attributed to the various assumptions adopted by the model.

3.4.2 Parametric study

There are over thirty different parameters involved in the current model. Some are fixed constants such as the molecular weight of lithium and the Faraday constant. Others are material properties, such as the ionic conductivity of the electrolyte, oxygen diffusion coefficient, and some are cell structural parameters such as thickness, electrolyte flow channel width. Carrying out a parametric study on the model has at least two folds of significance. Firstly, it will reveal the system's sensitivity to material property data provided by experiments. If the results indicate a high sensitive to a specific property parameter, then extra effort should be paid to provide a more accurate measurement of this parameter. Secondly, it will provide direction to improve cell performance and inspiration for new cell design.

One of the most important parameters that affects battery performance is the discharge current density. Figure 3-3 shows the dependence of cell voltage on time, which is translated to cathode specific capacity. Similar to the conventional Li–O_2 cell, higher discharge current density leads to lower voltage and shorter discharge time for a Li–O_2 flow cell, which translates to both lower

specific capacity and energy. When the current density is 0.1 mA cm^{-2}, the cell can provide 16.1 times more capacity and 17.8 times more energy than those with a current density of 2 mA cm^{-2}.

It is well accepted that Li_2O_2 deposition in the pores of cathode limits the full release of Li–O_2 battery capacity. Figure 3-4 shows the Li_2O_2 volume fraction at the end of discharge with different discharge current densities. Several features are of importance. First, lower discharge current leads to a higher Li_2O_2 volume fraction at the end. When the current density is 1.5 mA cm^{-2}, the maximum $\varepsilon_{Li_2O_2}$ is under 0.1, while the potential maximum value of $\varepsilon_{Li_2O_2}$ is equal to the original porosity of the electrode, 0.8. Secondly, the Li_2O_2 fraction close to the inlet is higher than at all other parts of the electrode. This is caused by a higher oxygen concentration and consequently, a higher reaction rate. At the outlet and the cathode/separator interface, the Li_2O_2 volume fraction is low, which means that the electrode in these areas is not well utilized. It should be noted that these characteristics may change when operation parameters or material properties change. For example, when an electrolyte with extremely low conductivity is used, the distribution of Li_2O_2 at the end of discharge is different to what is shown in Figure 3-4. This will be discussed below.

To investigate the effect of a parameter on the cathode capacity, the discharge process is simulated with the parameter multiplied by a variation factor between 10^{-3} to 10^{3}, while all other parameters remain unchanged. The original values for each parameter are listed in Table 3-1. The resulting specific capacities and specific energies are compared to analyze the effect of each parameter.

Ionic conductivity of the electrolyte determines the potential drop in the electrolyte. Normally, higher conductivity is desirable. However, Figure 3-5 indicates that for a Li–O_2 flow cell, when the conductivity decreases, at first the cathode specific capacity becomes higher. If the conductivity is two orders of magnitude lower than the normal value ($0.01k_e$), cathode specific capacity increases by 9.8%. When conductivity further decreases, cathode specific capacity starts to drop sharply. To explain this phenomenon, the profile of the *y*-direction–averaged electrolyte potential and Li_2O_2 distributions in both normal and ultra-low (1% of normal value) conductivities are plotted in Figure 3-6. It shows that with a low conductivity, the distribution of $\varepsilon_{Li_2O_2}$ is very different to that at a normal conductivity. At the cathode/separator side of the electrode, where oxygen concentration is low and thus a lower reaction rate and Li_2O_2 production is expected, $\varepsilon_{Li_2O_2}$ is instead higher, which is opposite to the situation seen for normal conductivity, as shown in Figure 3-4. This is because the reaction rate is not only determined by oxygen concentration, but also by activation overpotential. For an electrolyte with very low conductivity, the drop of potential increases from several millivolts to over 100 millivolts. According to eq. (27), this leads to a low activation overpotential at the oxygen-rich area (electrolyte inlet). Although the oxygen concentration in this area is high, the combined effect produces a smaller reaction rate. This acts to alleviate the blockage of pore orifices at the inlet and increases the overall electrode utilization. When the conductivity is too low, such as $0.005k_e$, a large part of cell overpotential is caused by electrolyte resistance, therefore cell voltage drops under the cut-off voltage of 2.3 V even before Li_2O_2 blocks the inlet. This causes a sharp drop in capacity when conductivity is lower than $0.01k_e$.

When the same calculations are carried out on a conventional Li–O_2 cell, lower conductivities always cause shorter discharge time and lower specific capacity. For the passive cathode, because only diffusion drives oxygen transport, the oxygen concentration difference between the inlet and separator side is much higher than that in a flow cell. The reaction rate around the inlet is always higher than the separator side even when a low conductivity leads to lower overpotential at the inlet. Therefore lower conductivity does not alleviate electrode blockage as in a flow cell discussed above. It causes lower discharge voltage and lower specific capacity in a conventional cell with passive cathode. These results show that the Li–O_2 flow cell's cathode becomes activation overpotential controlled at low conductivity while conventional cathode remains oxygen controlled.

As evident by the above analysis, oxygen transportation in Li–O_2 cells is crucial to their performance. The two most important parameters for oxygen transport are the oxygen diffusion coefficient, D_{O_2}, and oxygen solubility, $c_{O_2,sat}$. Figure 3-7 shows the effects of D_{O_2} and $c_{O_2,sat}$ on the cathode specific capacity and energy. In Figure 3-7(a), cathode specific capacity of a conventional cell drops to zero when D_{O_2} decreases. The flow cell, however, can still maintain a high specific capacity even at very low D_{O_2}. This is because convection still acts to transport oxygen into the cathode even when diffusion is very low. Another finding is that when D_{O_2} increases to more than 10 times its current value, the flow cell shows lower capacity than the conventional cell. This means that the oxygen diffusion flux is comparable to the convection flux when D_{O_2} is high enough. However, a conventional cell has a higher contact area to oxygen while

a flow cell only receives oxygen-saturated electrolyte only at the inlet. The effects of $c_{O_2,sat}$ is similar to those of D_{O_2}, except that for both conventional and flow cell cathodes, when $c_{O_2,sat}$ decreases, cell capacity approaches zero.

Electrode thickness plays an important role in defining the power density and energy density of a lithium battery. In a Li–ion battery, a thicker cathode usually leads to higher capacity. This is not necessarily true for Li–O_2 batteries because of the clogging effect by Li_2O_2 deposition. Using the developed model, the effect of cathode thickness on specific capacity is studied for both conventional and Li–O_2 flow cells, with the result shown in Figure 3-8. The thickness of the electrode varies between 400 μm and 1,000 μm. It shows that, for a conventional cathode with a thicker electrode, specific capacity decreases. This is because the electrode further away from oxygen side is poorly utilized and generally wasted. For a Li–O_2 flow cell, convection helps move oxygen into the electrode. When the electrode increases from 400 μm to 800 μm, specific capacity further increases. However, when the electrode is over 800 μm, the specific capacity starts to drop. After inspection of the simulation results, it is found that a thicker electrode leads to higher flow rate. This is reasonable because for a thicker electrode, the boundary effect posed by the ribs is less prominent. Under the same pressure difference (0.4 atm), the maximum velocity at the start of discharge for a 800μm thickness cathode is 8.27×10^{-4} m s^{-1} while for a 400μm thickness cathode it decreases to 8.09×10^{-4} m s^{-1}. Higher velocity leads to better oxygen supply, therefore the specific capacity is increased. When the thickness further increases, the increase of velocity is not

enough to offset the increase in electrode mass, therefore the specific capacity starts to drop. This shows that there is an optimum cathode thickness for a Li–O_2 flow cell.

In addition to those discussed above, other important parameters used in the model (as shown in section 3.2) are examined, including thermodynamic factor, Li^+ diffusion coefficient, transference number, etc. The results, however, show that each has an insignificant influence on the specific capacity. For example, the diffusion coefficient of Li^+, D_{Li}, directly affect electrolyte concentration distribution. Lower D_{Li} leads to higher electrolyte concentration gradient. However, even when D_{Li} is three orders of magnitude lower than normal value, the electrolyte concentration gradient is still too low to change the result for capacity. These results are expected because of the low discharge current densities.

3.4.3 Energy consumption by electrolyte pump

One concern of Li–O_2 flow cell design is the parasitic pump work consumption due to electrolyte recirculation. Although it is reasonable to argue that a cooling system, including pumps and tubing, is also needed to pump coolant through a conventional battery system, the battery pack, an analysis of pump work consumption is still necessary. The work consumed by the pump is equal to the volume flow rate multiplied by the pressure difference. In the model presented, a constant pressure difference between the outlet and inlet is assumed. Volume flow rates decrease during discharge because of the increase in flow resistance through the electrode. The integration of pump work over time yields the energy consumed by the pump during the discharge. Figure 3-9 shows the percentage of energy consumed by the electrolyte pump at different pressure differences. It

also shows the relative increase of energy output by the Li–O_2 flow cell compared to a conventional cell. With higher pressure gradient, the advantage of the flow cell over the conventional cell is more evident. The energy consumed by the pump, however, is also higher. A reasonable pressure difference is 0.4 atm, when the flow cell can provide 15 times more capacity than the conventional cell, while the pump uses 10% of the energy generated by the flow cell.

3.4.4 Capacity enhancement using dual layer cathode

The above results illustrate that cathode porosity has significant influence on battery capacity. Figure 3-4 also shows that $\varepsilon_{Li_2O_2}$ closer to the oxygen side (larger x) is greater because of Li_2O_2 deposition, which in consequence, hinders oxygen transport. To enhance battery capacity, a dual layer cathode structure is proposed. In the above calculations, the cathode electrode is assumed to have a uniform porosity of 0.8. For a dual layer cathode, the oxygen side has higher porosity (0.9) while the separator side has lower porosity (0.7). Another case with opposite porosity distribution is calculated for comparison. The three designs use the same amount of electrode material, have the same weight and volume, and they would have the same reaction area, assuming a linear dependence of reaction area on porosity.

Figure 3-10 shows the comparison among the specific capacities of the single layer and dual layer cathode batteries at different discharge current densities. It can be seen that for both conventional cell and flow cell cathodes, a dual layer structure with porosity of 0.7 at the separator side and 0.9 at the oxygen side (mentioned as 0.7 – 0.9 below) shows the maximum cathode capacity, while the opposite configuration has the lowest. For the conventional Li–O_2 cell,

enhancement from a dual layer structure (0.7 – 0.9) than single layer structure is more significant at low current density. When the current density is 0.05 mA cm^{-2}, battery capacity increases by 40.8%. Accordingly, maximum $\varepsilon_{Li_2O_2}$ increased from 0.654 to 0.744. For a flow cell, the dual layer cathode (0.7 – 0.9) shows greater advantage at higher discharge currents. At 1.5 mA cm^{-2}, the specific capacity of the dual layer electrode (0.7 – 0.9) was 105% higher than that of a single layer electrode. Maximum $\varepsilon_{Li_2O_2}$ occurs at the center of the rib at the right boundary and increases from 0.095 to 0.256.

3.4.5 Capacity enhancement using alternating flow

The previous calculations show that the key to enhance Li–O_2 battery capacity is to fully utilize the micro-pores in the electrode structure. From Figure 3-4, it can be seen that for a single layer cathode, the electrode around the outlet (larger *y*) still has low $\varepsilon_{Li_2O_2}$ at the end of discharge, which means the electrode is not fully used. To better use the pores at both openings, an alternating flow of electrolyte for the Li–O_2 flow cell is proposed. In practice, a directional control valve can be installed between the electrolyte pump and the battery pack to alternate the flow direction of electrolyte in the cathode. Oxygen-saturated electrolyte would enter from the lower channel and exit from the upper channel for a period of time, then the valve would change polarity to direct electrolyte flow to enter from the upper channel and exit from the lower channel. This change of direction will make the micro-pore utilization more uniform and in consequence, increase battery capacity.

Figure 3-11 compares the discharge curves for a single layer battery with single direction and alternating electrolyte flow. In the calculation, the flow direction is alternated at the 180th hour of discharge (1,125 mAh g^{-1}) and with a discharge current density of 0.2 mA cm^{-2}. The result shows that alternating flow can increase the cathode specific capacity of the flow cell by 3.7%. With an alternating flow, the volume fraction of Li_2O_2, $\varepsilon_{Li_2O_2}$, at the upper opening (original outlet) becomes higher, which translates to better usage of pores in this area. However, $\varepsilon_{Li_2O_2}$ at the lower opening (original inlet) also becomes lower. The combined result is a minor increase in capacity (3.7%), as shown in Figure 3-11. This method is less effective for high discharge current such as 1.5 mA cm^{-2}.

The modeling study presented in this chapter is still preliminary research on the aprotic Li–O_2 flow battery. Its advantage over conventional Li–O_2 battery and operation characteristics still need to be studied through experiments, which will be the next step of our work. In addition, there are still many assumptions made in the current model, such as no side reactions, and no discharging process considered. These need to be addressed in future modeling studies.

3.5 Conclusion

A 2D, transient simulation model is developed for an aprotic Li–O_2 flow cell. Electrolyte concentration, oxygen concentration, electrolyte potential, electrode potential, and Li_2O_2 deposition caused porosity changes are calculated based on porous electrode and concentrated solution theory. A parametric study is carried out to identify the effect of each variable on simulation results. Dual layer cathode structure and alternating electrolyte flow are proposed to

increase specific capacity of the battery. Based on the simulation results, the following conclusions are made:

1. For a Li–O_2 flow cell, when the ionic conductivity of the electrolyte is lower, the cathode specific capacity and energy are increased. This is because a low conductivity causes larger electrolyte potential drop, which in consequence causes smaller activation overpotential and reaction rate at the electrolyte inlet. This alleviates cathode clogging and translates to better used electrode pores. For a conventional cell this is not true because the reaction rate is more controlled by oxygen concentration.

2. If the oxygen diffusion coefficient can be enhanced by over 10 times its original value, the Li–O_2 flow cell loses its advantage over a conventional Li–O_2 cell in terms of cathode specific capacity and energy.

3. There exists an optimum cathode thickness for a Li–O_2 flow cell. When the discharge current density is 0.2 mA cm^{-2}, the cathode with 800 μm thickness will lead to the highest cathode specific capacity.

4. By adopting a dual layer cathode structure without changing weight, thickness, and amount of material used, the capacity of the flow cell can be increased by 105 % at 1.5 mA cm^{-2}.

5. To fully use the pores in the cathode at both openings to the flow channel, an alternating electrolyte flow is proposed to increase capacity. By alternating the electrolyte flow direction, the specific capacity can be increased by 3.7% with a discharge current density of 0.2 mA cm^{-2}.

Nomenclature

A_{ED}	specific area of the electrode (m^{-1})
c	concentration (mol m^{-3})
D	diffusivity (m^2 s^{-1})
E_0	thermodynamic equilibrium voltage (V)
E_R	activation energy (kJ mol^{-1})
F	Faraday constant (96,485 C mol^{-1})
$f_{\pm}$	$LiPF_6$ salt activity coefficient
I	discharge current density (A m^{-2})
i_0	exchange current density (A m^{-3})
$\boldsymbol{i}$	current density vector (A m^{-2})
j_R	local transfer current density between electrode and electrolyte (A m^{-2})
K	permeability (m^2)
k	electrolyte conductivity (S m^{-1})
k_c	electron conductivity in carbon phase of electrode (S m^{-1})
k_D	diffusion conductivity (A m^{-1})
k_R	reaction rate constant (A m^{-2})
M	molecular weight (kg mol^{-1})
$\boldsymbol{N}$	molar flux (mol m^{-2} s^{-1})
n	number of electrons transferred in reaction
p	pressure (Pa)
r	consumption rate (mol m^{-3} s^{-1})
s	stoichiometric coefficient

s_m	mass source term (s^{-1})
T	temperature (K)
t	time (s)
t_+^0	transference number of Li^+ in reference to solvent
$\boldsymbol{u}$	electrolyte velocity vector (m s^{-1})
α	transfer coefficient
β	Bruggeman coefficient
ε	porosity
η	overpotential (V)
μ_{EL}	electrolyte viscosity (kg m^{-1} s^{-1})
ρ	density (kg m^{-3})

Superscripts and Subscripts

0	initial value
1	electrode phase
2	electrolyte phase
a	anode
c	cathode
eff	effective value

References

[1] R. Van Noorden, The rechargeable revolution: A better battery, Nature. 507 (2014) 26–28. doi:10.1038/507026a.

[2] M. Duduta, B. Ho, V.C. Wood, P. Limthongkul, V.E. Brunini, W.C. Carter, et al., Semi-solid lithium rechargeable flow battery, Adv. Energy Mater. 1 (2011) 511–516. doi:10.1002/aenm.201100152.

[3] Y. Yang, G. Zheng, Y. Cui, A membrane-free lithium/polysulfide semi-liquid battery for large-scale energy storage, Energy Environ. Sci. 6 (2013) 1552–1558. doi:10.1039/C3EE00072A.

[4] X.J. Chen, a. Shellikeri, Q. Wu, J.P. Zheng, M. Hendrickson, E.J. Plichta, A High-Rate Rechargeable Li-Air Flow Battery, J. Electrochem. Soc. 160 (2013) A1619–A1623. doi:10.1149/2.012310jes.

[5] X.L. Li, J. Huang, A. Faghri, Modeling study of a Li-air battery with an active cathode, Energy. 81 (2015) 489–500. doi:10.1016/j.energy.2014.12.062.

[6] J. Newman, K.E. Thomas, H. Hafezi, D.R. Wheeler, Modeling of lithium-ion batteries, J. Power Sources. 119-121 (2003) 838–843. doi:10.1016/S0378-7753(03)00282-9.

[7] K.E. Thomas, J. Newman, R.M. Darling, Mathematical Modeling of Lithium Batteries, in: Adv. Lithium-Ion Batter., Springer US, 2002: pp. 345–392. doi:10.1007/0-306-47508-1_13.

[8] J. Newman, W. Tiedemann, Porous-electrode theory with battery applications, AIChE J. 21 (1975) 25–41. doi:10.1002/aic.690210103.

[9] J. Newman, K.E. Thomas-Alyea, Electrochemical Systems, 3rd ed., John Wiley & Sons, Hoboken, NJ, 2004.

[10] X. Li, a. Faghri, Optimization of the cathode structure of lithium-air batteries based on a two-dimensional, transient, non-isothermal model, J. Electrochem. Soc. 159 (2012) A1747–A1754. doi:10.1149/2.043210jes.

[11] P. Tan, W. Shyy, L. An, Z.H. Wei, T.S. Zhao, A gradient porous cathode for non-aqueous lithium-air batteries leading to a high capacity, Electrochem. Commun. 46 (2014) 111–114. doi:10.1016/j.elecom.2014.06.026.

[12] S.S. Sandhu, J.P. Fellner, G.W. Brutchen, Diffusion-limited model for a lithium/air battery with an organic electrolyte, J. Power Sources. 164 (2007) 365–371. doi:10.1016/j.jpowsour.2006.09.099.

[13] P. Andrei, J.P. Zheng, M. Hendrickson, E.J. Plichta, Modeling of Li-air batteries with dual electrolyte, J. Electrochem. Soc. 159 (2012) A770–A780. doi:10.1149/2.010206jes.

[14] Y. Wang, Modeling discharge deposit formation and its effect on lithium-air battery performance, Electrochim. Acta. 75 (2012) 239–246. doi:10.1016/j.electacta.2012.04.137.

[15] Y. Wang, S.C. Cho, Analysis of Air Cathode Perfomance for Lithium-Air Batteries, J. Electrochem. Soc. 160 (2013) A1847–A1855. doi:10.1149/2.092310jes.

[16] U. Sahapatsombut, H. Cheng, K. Scott, Modelling the micro–macro homogeneous cycling behaviour of a lithium–air battery, J. Power Sources. 227 (2013) 243–253. doi:10.1016/j.jpowsour.2012.11.053.

[17] U. Sahapatsombut, H. Cheng, K. Scott, Modelling of electrolyte degradation and cycling behaviour in a lithium-air battery, J. Power Sources. 243 (2013) 409–418. doi:10.1016/j.jpowsour.2013.06.043.

[18] Y. Wang, S.C. Cho, Analysis and Multi-Dimensional Modeling of Lithium-Air Batteries, J. Electrochem. Soc. 162 (2015) A114–A124. doi:10.1149/2.0731501jes.

[19] X.J. Chen, V. V. Bevara, P. Andrei, M. Hendrickson, E.J. Plichta, J.P. Zheng, Combined Effects of Oxygen Diffusion and Electronic Resistance in Li-Air Batteries with Carbon Nanofiber Cathodes, J. Electrochem. Soc. 161 (2014) A1877–A1883. doi:10.1149/2.0721412jes.

[20] K.-H. Xue, T.-K. Nguyen, a. a. Franco, Impact of the Cathode Microstructure on the Discharge Performance of Lithium Air Batteries: A Multiscale Model, J. Electrochem. Soc. 161 (2014) E3028–E3035. doi:10.1149/2.002408jes.

[21] C.Y. Jung, T.S. Zhao, L. An, Modeling of lithium–oxygen batteries with the discharge product treated as a discontinuous deposit layer, J. Power Sources. 273 (2015) 440–447. doi:10.1016/j.jpowsour.2014.09.103.

[22] K. Yoo, S. Banerjee, P. Dutta, Modeling of volume change phenomena in a Li–air battery, J. Power Sources. 258 (2014) 340–350. doi:10.1016/j.jpowsour.2014.02.044.

[23] A.A. Shah, M.J. Watt-Smith, F.C. Walsh, A dynamic performance model for redox-flow batteries involving soluble species, Electrochim. Acta. 53 (2008) 8087–8100. doi:10.1016/j.electacta.2008.05.067.

[24] H. Al-Fetlawi, A.A. Shah, F.C. Walsh, Non-isothermal modelling of the all-vanadium redox flow battery, Electrochim. Acta. 55 (2009) 78–89. doi:10.1016/j.electacta.2009.08.009.

[25] H. Al-Fetlawi, A.. Shah, F.C. Walsh, Modelling the effects of oxygen evolution in the all-vanadium redox flow battery, Electrochim. Acta. 55 (2010) 3192–3205. doi:10.1016/j.electacta.2009.12.085.

[26] A. A. Shah, H. Al-Fetlawi, F.C. Walsh, Dynamic modelling of hydrogen evolution effects in the all-vanadium redox flow battery, Electrochim. Acta. 55 (2010) 1125–1139. doi:10.1016/j.electacta.2009.10.022.

[27] K. Oh, H. Yoo, J. Ko, S. Won, H. Ju, Three-dimensional, transient, nonisothermal model of all-vanadium redox flow batteries, Energy. (2014). doi:10.1016/j.energy.2014.05.020.

[28] Z. Wei, J. Zhao, M. Skyllas-Kazacos, B. Xiong, Dynamic thermal-hydraulic modeling and stack flow pattern analysis for all-vanadium redox flow battery, J. Power Sources. 260 (2014) 89–99. doi:10.1016/j.jpowsour.2014.02.108.

[29] V.E. Brunini, Y.M. Chiang, W.C. Carter, Modeling the hydrodynamic and electrochemical efficiency of semi-solid flow batteries, Electrochim. Acta. 69 (2012) 301–307. doi:10.1016/j.electacta.2012.03.006.

[30] S.S. Zhang, D. Foster, J. Read, Discharge characteristic of a non-aqueous electrolyte Li/O2 battery, J. Power Sources. 195 (2010) 1235–1240. doi:10.1016/j.jpowsour.2009.08.088.

[31] R.R. Mitchell, B.M. Gallant, C. V. Thompson, Y. Shao-Horn, All-carbon-nanofiber electrodes for high-energy rechargeable Li–O2 batteries, Energy Environ. Sci. 4 (2011) 2952. doi:10.1039/c1ee01496j.

[32] D.A. Nield, A. Bejan, Convection in Porous Media, 3rd ed., Springer, New York, 2006. doi:10.1007/978-0-387-76543-3.

[33] A. Costa, Permeability-porosity relationship: A reexamination of the Kozeny-Carman equation based on a fractal pore-space geometry assumption, Geophys. Res. Lett. 33 (2006) L02318. doi:10.1029/2005GL025134.

[34] A. Nyman, M. Behm, G. Lindbergh, Electrochemical characterisation and modelling of the mass transport phenomena in LiPF6–EC–EMC electrolyte, Electrochim. Acta. 53 (2008) 6356–6365. doi:10.1016/j.electacta.2008.04.023.

[35] J. Read, K. Mutolo, M. Ervin, W. Behl, J. Wolfenstine, A. Driedger, et al., Oxygen Transport Properties of Organic Electrolytes and Performance of Lithium/Oxygen Battery, J. Electrochem. Soc. 150 (2003) A1351. doi:10.1149/1.1606454.

[36] J. Read, Characterization of the lithium/oxygen organic electrolyte battery, J. Electrochem. Soc. 149 (2002) A1190 – A1195. doi:10.1149/1.1498256.

[37] X. Ren, S.S. Zhang, D.T. Tran, J. Read, Oxygen reduction reaction catalyst on lithium/air battery discharge performance, J. Mater. Chem. 21 (2011) 10118. doi:10.1039/c0jm04170j.

[38] K.M. Abraham, Z. Jiang, A Polymer Electrolyte-Based Rechargeable Lithium/Oxygen Battery, J. Electrochem. Soc. 143 (1996) 1. doi:10.1149/1.1836378.

[39] H. Bahrami, A. Faghri, Transport phenomena in a semi-passive direct methanol fuel cell, Int. J. Heat Mass Transf. 53 (2010) 2563–2578. doi:10.1016/j.ijheatmasstransfer.2009.12.050.

[40] Y.R. Dougassa, J. Jacquemin, L. El Ouatani, C. Tessier, M. Anouti, Viscosity and carbon dioxide solubility for LiPF6, LiTFSI, and LiFAP in alkyl carbonates: Lithium salt nature and concentration effect, J. Phys. Chem. B. 118 (2014) 3973–3980. doi:10.1021/jp500063c.

[41] Y.-C. Lu, D.G. Kwabi, K.P.C. Yao, J.R. Harding, J. Zhou, L. Zuin, et al., The discharge rate capability of rechargeable Li-O2 batteries, Energy Environ. Sci. 4 (2011) 2999. doi:10.1039/c1ee01500a.

[42] C. Capiglia, Y. Saito, H. Kageyama, P. Mustarelli, T. Iwamoto, T. Tabuchi, et al., 7Li and 19F diffusion coefficients and thermal properties of non-aqueous electrolyte solutions for rechargeable lithium batteries, J. Power Sources. 81-82 (1999) 859–862. doi:10.1016/S0378-7753(98)00237-7.

Table 3-1 Summary of governing equations and boundary conditions

Governing Equations	Boundaries								
	I	II	III	IV	V	VI	VII	VIII	IX
$\varepsilon \frac{\partial c_{O_2}}{\partial t} + \nabla \cdot \left(-D_{O_2}^{eff} \nabla c_{O_2}\right) + \boldsymbol{u} \cdot \nabla c_{O_2} = r_{O_2} - s_m c_{O_2}$	$c_{O_2} = c_{O_2,sat}$	$\frac{\partial c_{O_2}}{\partial x} = 0$	$\frac{\partial c_{O_2}}{\partial x} = 0$	$\frac{\partial c_{O_2}}{\partial x} = 0$	N/A	$\frac{\partial c_{O_2}}{\partial y} = 0$			
$\varepsilon \frac{\partial c_{Li}}{\partial t} + \nabla \cdot \left(-D_{Li}^{eff} \nabla c_{Li}\right) + \boldsymbol{u} \cdot \nabla c_{Li} = r_{Li} - \nabla \cdot \left(\frac{\boldsymbol{i}_2 t_+}{F}\right) - s_m c_{Li}$	$c_{Li} = c_{in}$	$\frac{\partial c_{Li}}{\partial x} = 0$	$\frac{\partial c_{Li}}{\partial x} = 0$	$-D_{Li}^{eff} \frac{\partial c_{Li}}{\partial x} = \frac{\left(1 - t_+^0\right) I}{F}$	N/A	$\frac{\partial c_{Li}}{\partial y} = 0$			
$\nabla \cdot \left(-k^{eff} \nabla \phi_2\right) = \nabla \cdot \left(\frac{k_D}{c_{Li}} \nabla c_{Li}\right) + A_{ED} j_R$	$-k^{eff} \frac{\partial \phi_2}{\partial x} = \frac{k_D}{c_{Li}} \frac{\partial c_{Li}}{\partial x}$			$\phi_2 = \phi_{l,a} = 0$	N/A	$\frac{\partial \phi_2}{\partial y} = 0$			
$\nabla \cdot \left(-k_c^{eff} \nabla \phi_1\right) = -A_{ED} j_R$	$\frac{\partial \phi_1}{\partial x} = 0$		$-k_c^{eff} \frac{\partial \phi_1}{\partial x} = \frac{I}{1 - OR}$		$\frac{\partial \phi_1}{\partial x} = 0$	N/A	$\frac{\partial \phi_1}{\partial y} = 0$	N/A	$\frac{\partial \phi_1}{\partial y} = 0$
$\frac{\partial \varepsilon}{\partial t} + \nabla \cdot \left(-\frac{K}{\mu_{EL}} \nabla p\right) = s_m$	$p = p_h$	$p = p_l$	$\frac{\partial p}{\partial x} = 0$		N/A	$\frac{\partial p}{\partial y} = 0$			

Table 3-2 Parameters used in the model

Parameter	Symbol	Value
Porosity of electrode	ε_{ED}	0.80
Porosity of separator	ε_{EL}	0.5 [37]
Thickness of the electrode	δ_{ED}	800 μm [36]
Thickness of the separator	δ_{EL}	25 μm [37]
Width of the battery	δ_{Y}	2 mm
Width of the rib	δ_{RIB}	1.0 mm
Cathode specific area	$A_{ED,0}$	3.75×10^{6} m^2 m^{-3} [17]
Exchange current density	i_0	2.5×10^{-9} A m^{-2}
Transfer coefficient	α_c	0.5
Cathode theoretical potential	E_c^0	3.1 V [38]
Carman–Kozeny factor	C_{KC}	1.5×10^{-15} m^2 [39]
Oxygen solubility	$c_{O_2,sat}$	3.46 mol m^{-3} [35]
Electrolyte concentration	c_{Li}	1000 mol m^{-3}
Density of lithium	ρ_{Li}	0.534 g cm^{-3}
Density of carbon	ρ_c	2.0 g cm^{-3}
Density of lithium peroxide	$\rho_{Li_2O_2}$	2.14 g cm^{-3}
Density of electrolyte	ρ_{EL}	1.2141 g cm^{-3} [40]
Density of PTFE	ρ_{PTFE}	2.2 g cm^{-3}
Viscosity of Electrolyte	μ	4.15×10^{-3} kg m^{-1} s^{-1} [40]
Ionic conductivity of electrolyte	k	$0.1297c_{Li}^{3} - 2.51c_{Li}^{1.5} + 3.329c_{Li}$ S m^{-1} [34] *
Electric conductivity of electrode	k_c	3 S cm^{-1} [41]
Electric resistivity of Li_2O_2	$R_{Li_2O_2}$	50 Ω m^2 [17]
Diffusivity of O_2 in electrolyte	D_{O_2}	3.98×10^{-10} m^2 s^{-1} [40]
Diffusivity of Li^+ in electrolyte	D_{Li}	$5.34\times10^{-10}e^{-0.65c_{Li}}$ m^2 s^{-1} [42] *
Molecular weight of lithium	M_{Li}	6.94 g mol^{-1}
Molecular weight of Li_2O_2	$M_{Li_2O_2}$	45.88 g mol^{-1}
Transference number of Li^+	t_0^+	$-0.1287c_{Li}^{3} + 0.4106c_{Li}^{2} - 0.4717c_{Li} + 0.4492$ [34] *

$LiPF_6$ thermodynamic factor	$1+d\ln f_{\pm}/d\ln c$	$\frac{0.28687c_{Li}^{\ 2}-0.74678c_{Li}+0.44103}{0.1287c_{Li}^{\ 3}-0.4106c_{Li}^{\ 2}+0.4717c_{Li}+0.5508}$	[34] *

* The unit for c_{Li} is (mol dm^{-3}).

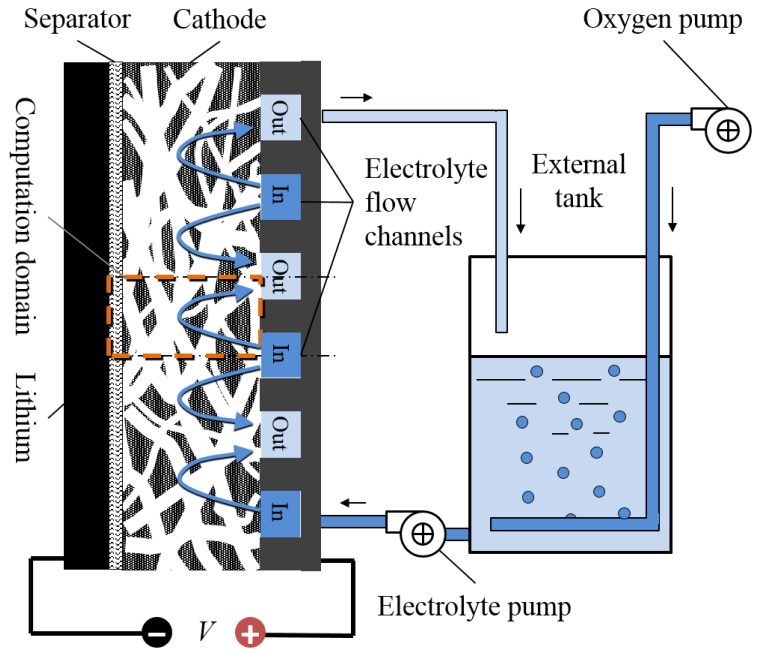

(a)

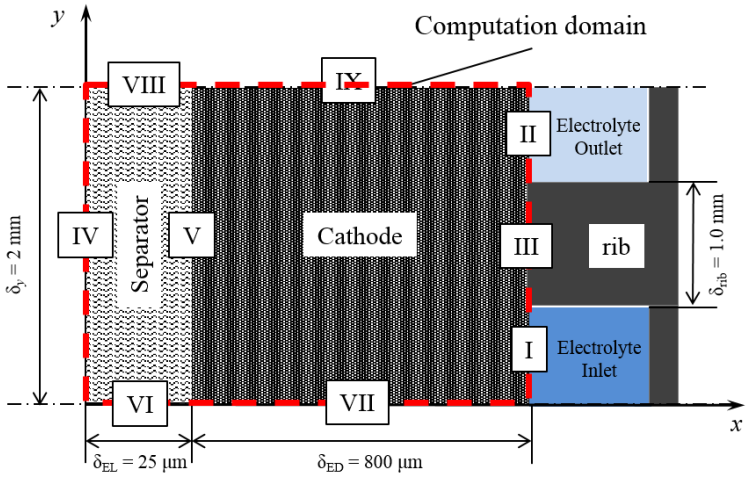

(b)

Figure 3-1 Structure of (a) an aprotic Li–O_2 flow battery and (b) the corresponding computation domain

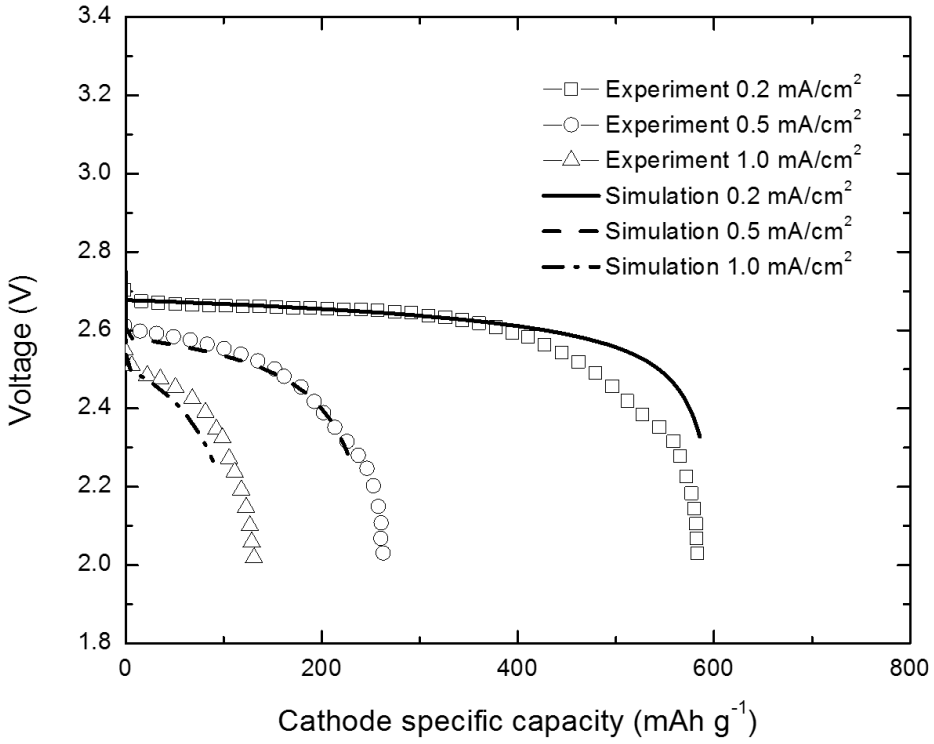

Figure 3-2 Comparison of cell voltage vs. specific capacity between the simulation results and experimental data at different discharge current density

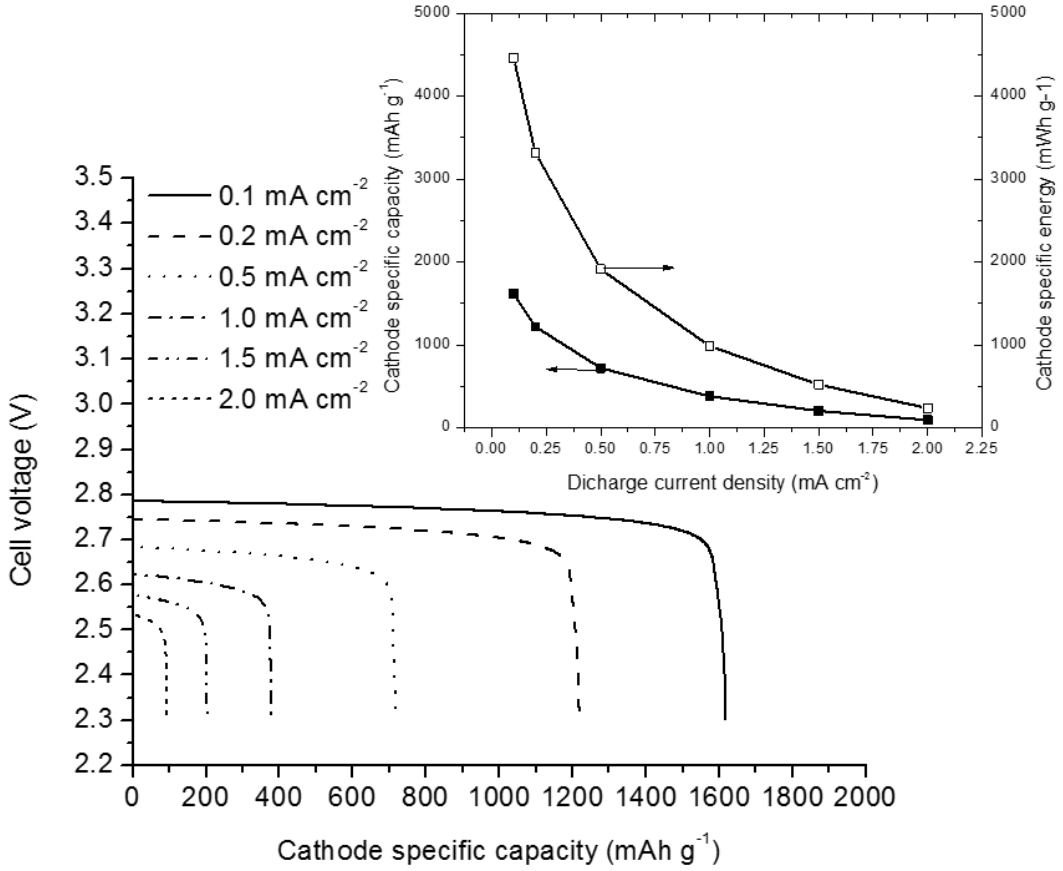

Figure 3-3 Discharge curve of the Li–O_2 flow cell at different discharge current densities and comparison of cathode specific capacity and specific energy

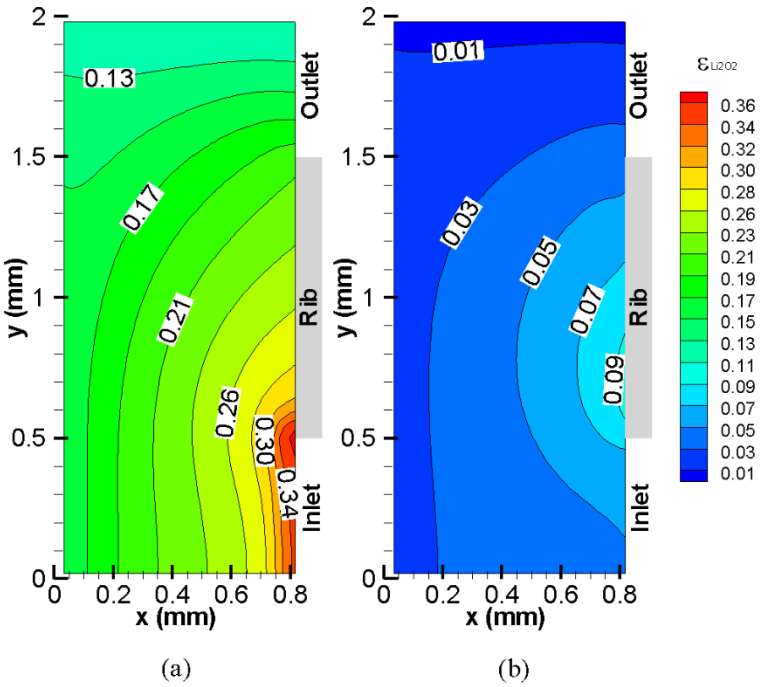

(a) (b)

Figure 3-4 Distribution of Li_2O_2 volume fraction, $\varepsilon_{Li_2O_2}$, at the end of discharge with discharge current density of (a) 0.2 mA cm^{-2}, and (b) 1.5 mA cm^{-2}

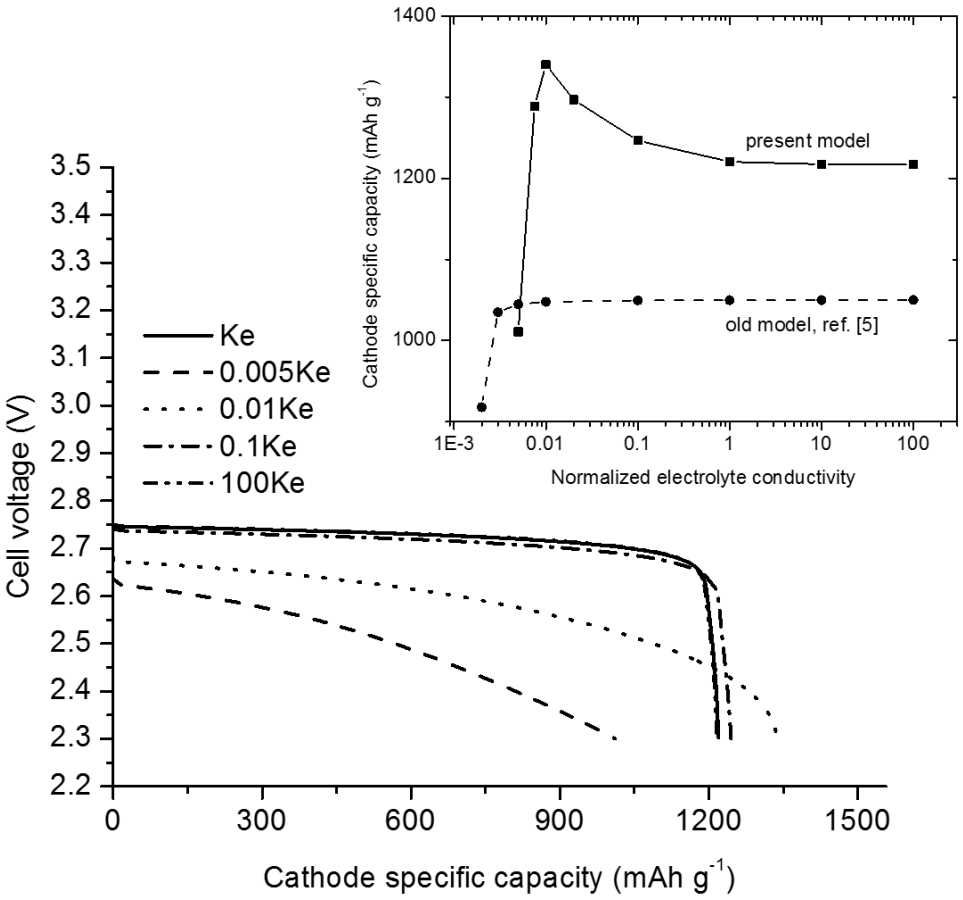

Figure 3-5 Effect of ionic conductivity of electrolyte in electrolyte on cell performance

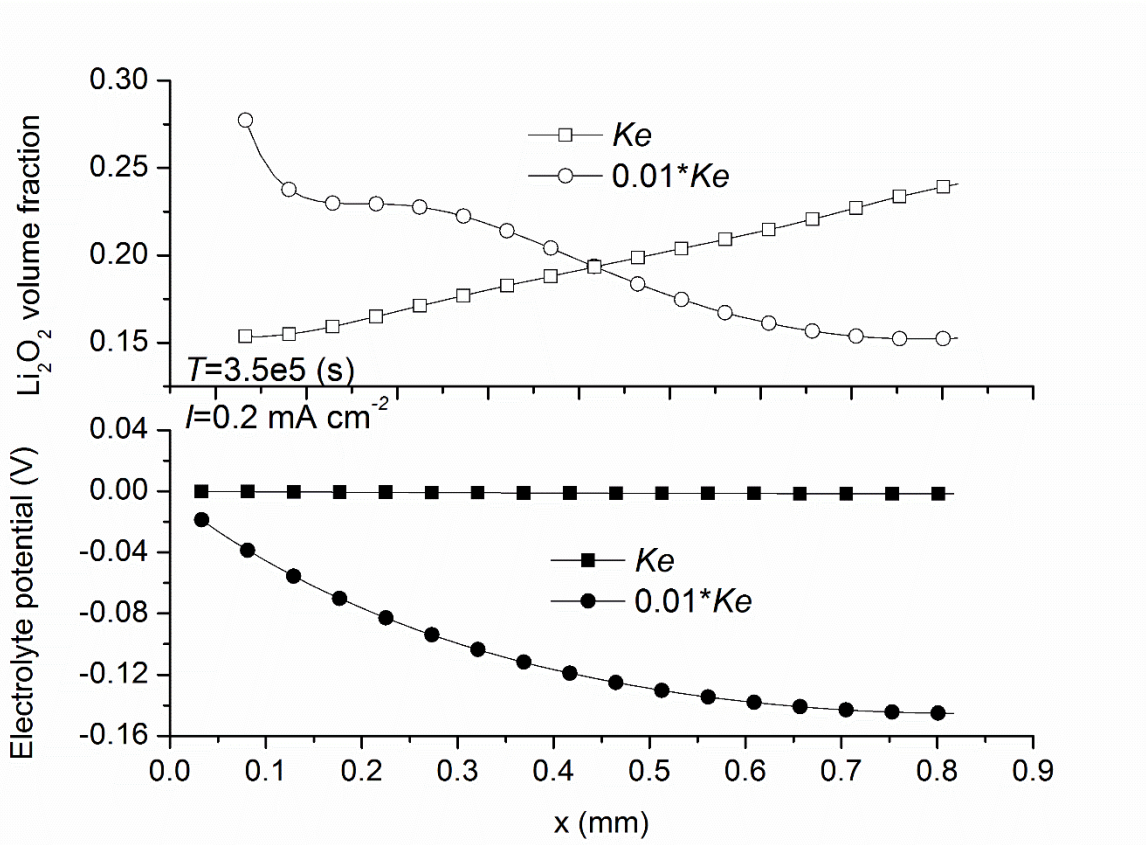

Figure 3-6 Distribution of Li_2O_2 volume fraction and electrolyte potential (*y*–direction averaged) with different conductivity of electrolyte

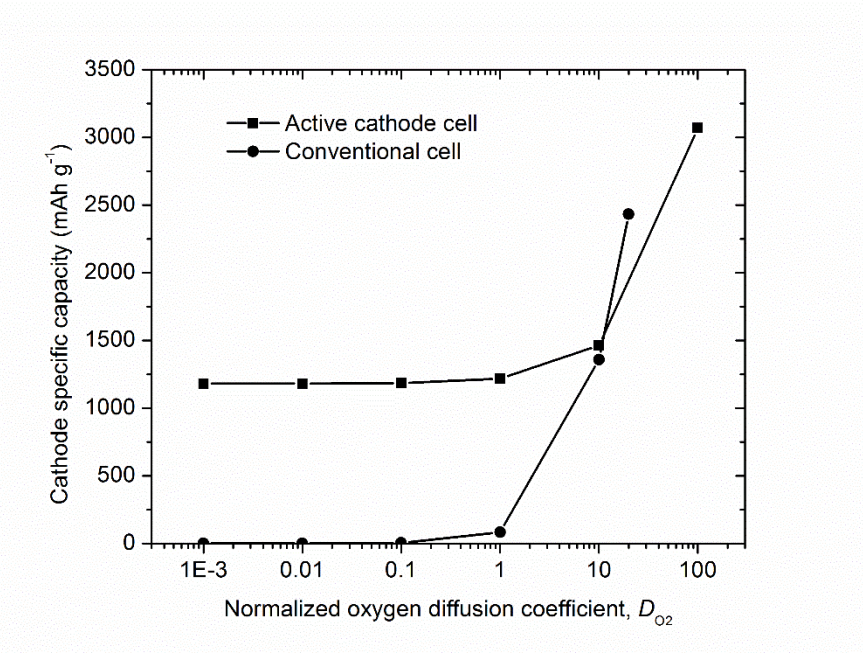

(a)

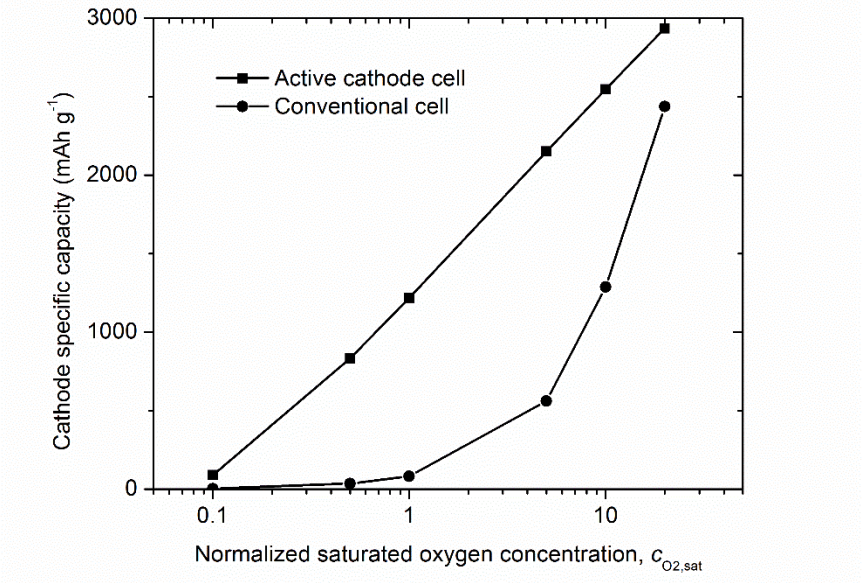

(b)

Figure 3-7 Effects of (a) oxygen diffusion coefficient, D_{O_2}, and (b) oxygen solubility, $c_{O_2,sat}$, on cathode specific capacity

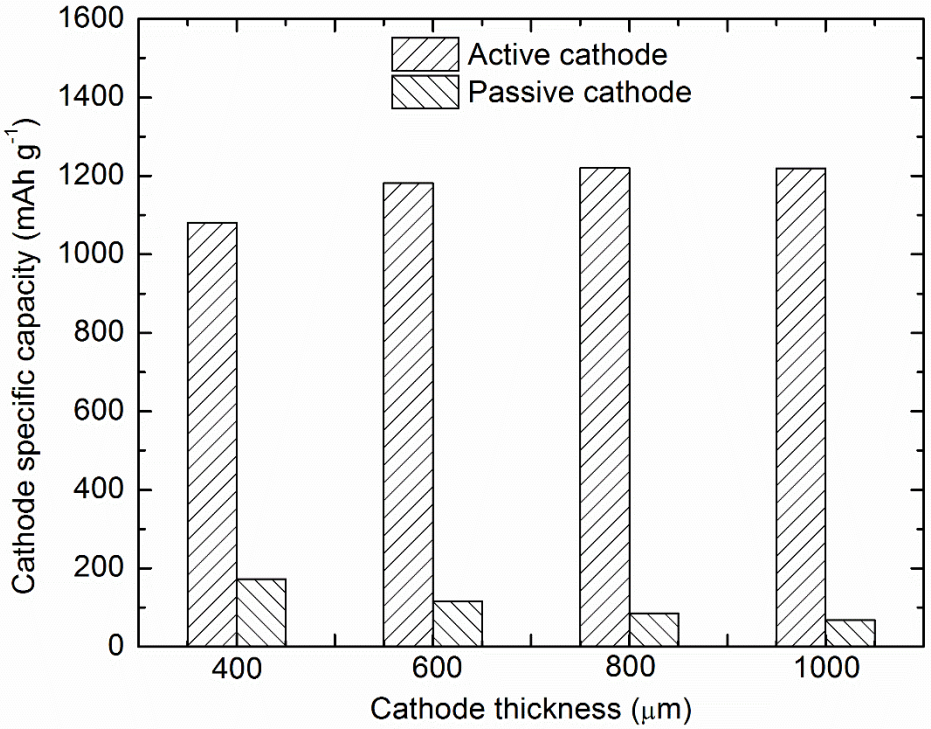

Figure 3-8 Effect of cathode thickness on cathode specific capacity

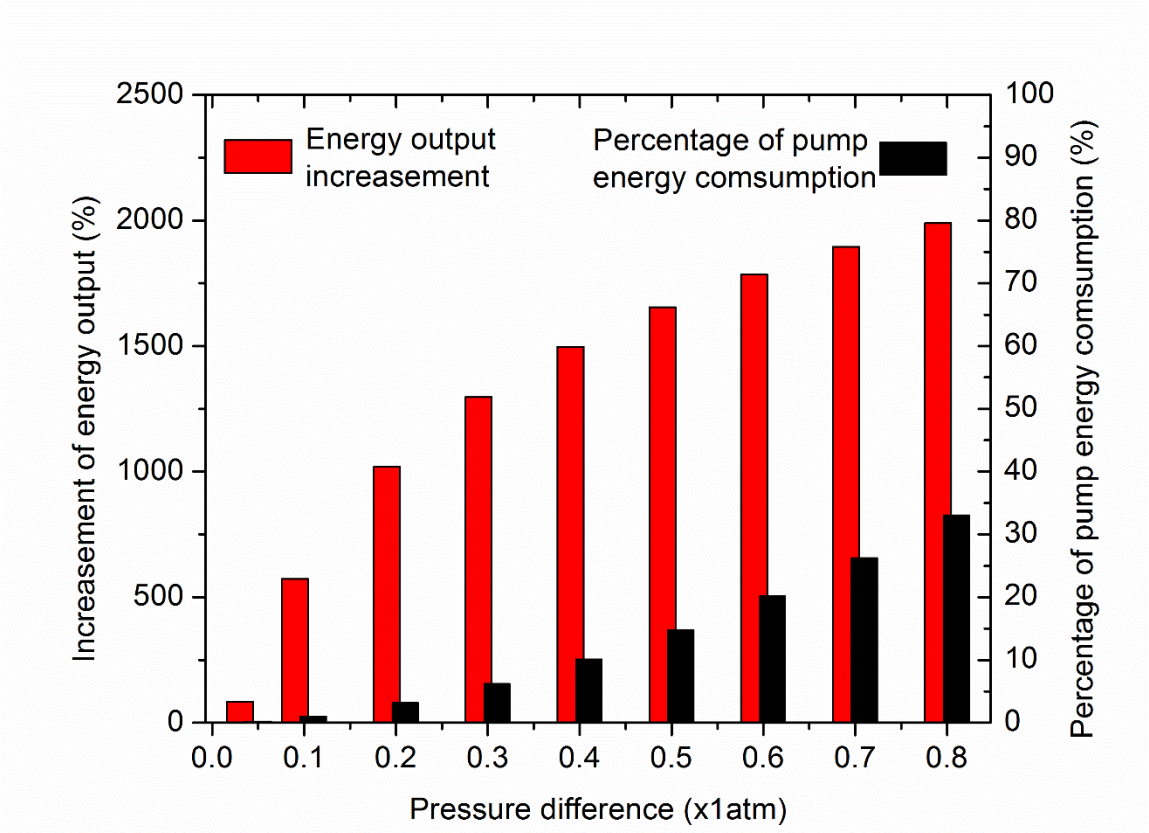

Figure 3-9 Effects of pressure difference on the increase of energy output by the Li–O_2 flow cell and the percentage of energy consumed by the electrolyte pump

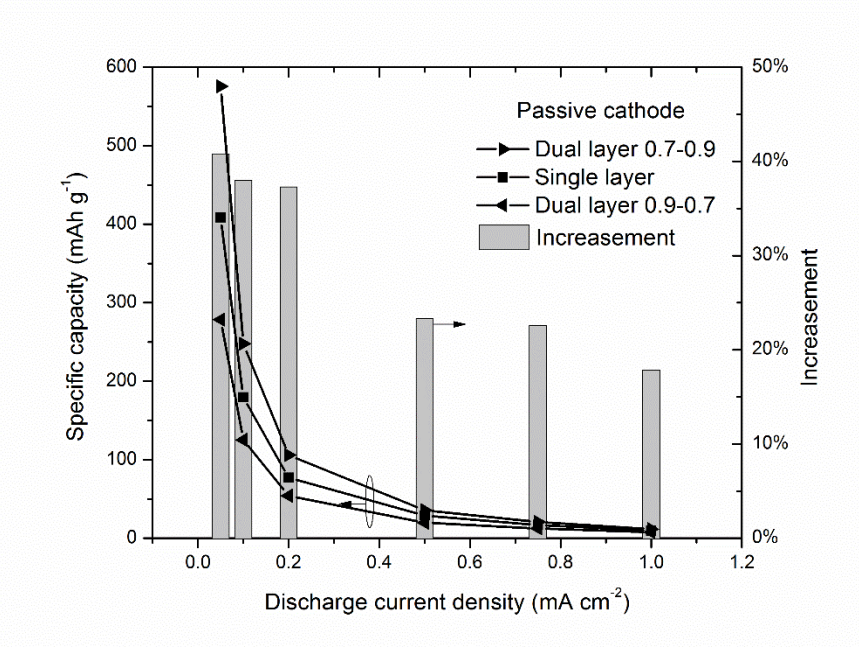

(a)

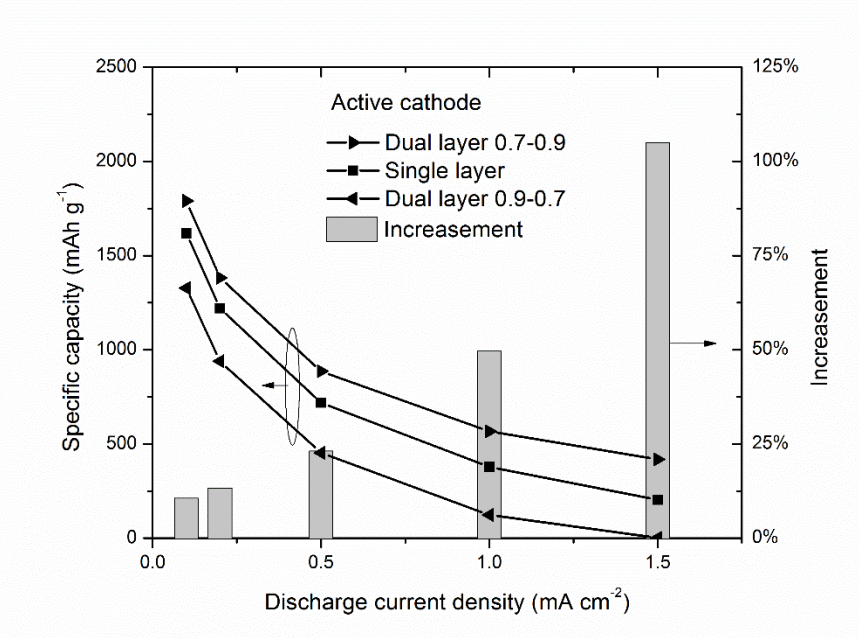

(b)

Figure 3-10 Comparison of cathode specific capacity between single layer and dual layer (a) conventional Li–O_2 cell, and (b) Li–O_2 flow cell

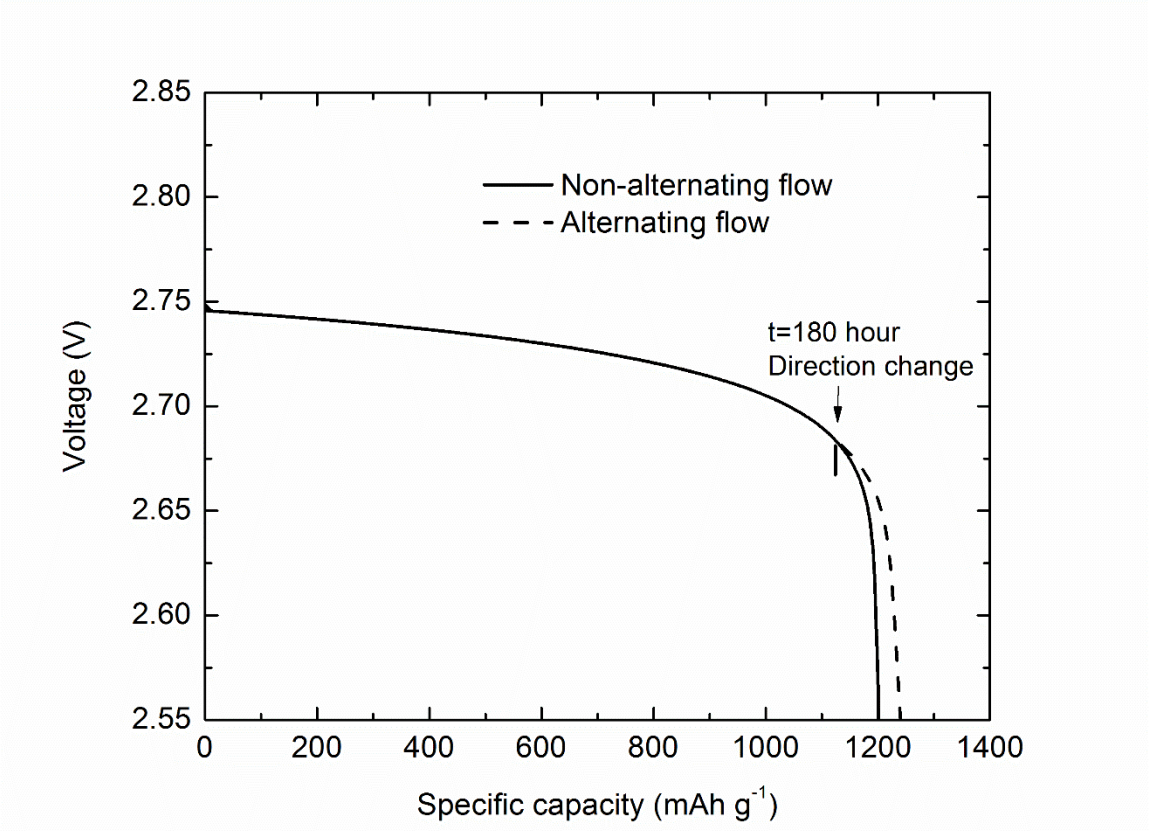

Figure 3-11 Comparison of cell voltage vs. cathode specific capacity between non–alternating and alternating flow at discharge current density of 0.2 mA cm^{-2}

Chapter 4 Analysis of Electrolyte Level Change in a Li–Air Battery

A two-dimensional physical model that employs the deformed mesh method to track the electrolyte level in a Li-air coin cell battery is presented and used to investigate the effects of electrolyte level drop during cell discharge. The electrolyte level drop is caused by solid phase volume decrease and electrolyte solvent evaporation. Simulation results show that by neglecting the drop in electrolyte level, a Li-air battery model would under-estimate cell discharge capacity by as much as 22.5%. This counter-intuitive result is explained by an in-depth analysis of simulation results. A more realistic prediction of Li_2O_2 deposit distribution is obtained, with the peak value of Li_2O_2 volume fraction in the middle of the cathode instead of on the top surface, as predicted by previous studies. The interaction between the battery and its surroundings is considered by incorporating the air chamber into the computation domain. The diffusion of solvent vapor and oxygen in this chamber is included. For batteries using volatile solvents such as DMF, increasing the air chamber radius from 5 cm to 15 cm would result in a 72% increase of discharge capacity at the cost of losing a large amount of electrolyte.

4.1 Introduction

Because of their high theoretical energy density, lithium air (Li–air) batteries, including lithium oxygen (Li–O_2) batteries, are considered to be promising candidates as the next generation secondary power supplies for portable devices and electric vehicles. A number of continuum–scale models have been developed to study the detailed charge and mass transport processes inside a Li–air battery. The first reported simulation model for Li–air batteries was by Sandhu et al. in 2007 [1]. Since then, various research groups have incorporated additional details to build more comprehensive models. Albertus et al. [2] was the first to consider solid product precipitation. Wang and Cho [3] developed a model to consider the coverage of reaction surface for different

electrode pore shapes. The model by Sahapatsombut et al. [4,5] was the first reported to include the charging process and side reactions. Li and Faghri [6] developed a 2-D model and found that the micro pores closer to the separator/cathode interface were not fully utilized. They proposed a gradient cathode structure to increase specific capacity. Several models [7–9] considered the size distribution function of the pores or carbon particles in the cathode.

All previous studies neglected two important physical phenomena in a Li–air cell. The first is the electrolyte level drop during discharge caused by a decrease in solid phase volume. During discharge, the metallic lithium of the anode is converted to lithium ions, enters the electrolyte and moves to the cathode. In the micro–pores of the cathode, oxygen reduction reaction (ORR) occurs and consumes the lithium ions and electrons. Experimental studies [10] prove that insoluble and partially insulating Li_2O_2 is the major product of this reaction in non-aqueous electrolyte; therefore the overall reaction can be expressed as:

$$2Li + O_2 \rightarrow Li_2O_2 \quad (1)$$

According to the above equation, for each mole of lithium consumed 0.5 moles of Li_2O_2 are generated, which translates to 13.0 cm^3 of solid consumed and 9.93 cm^3 of solid generated. This means a 23.6% decrease of solid phase volume for each unit volume of lithium anode consumed during discharge. This vacated space must be replaced by the liquid electrolyte and therefore electrolyte level drops during discharge.

Figure 4-1 shows the structure of a typical Li–air coin cell used in previous experimental studies [11,12]. The cell is normally placed on a solid surface with breathing holes facing upward, exposed to an air chamber. To compensate for the volume change, a spring is placed under the anode current collector in the cell. This ensures a tight contact between anode, separator, cathode, and current collectors in the cell. Solid volume decreases during discharge and electrolyte level

drops. This effect is noted as an unsolved issue by Yuan et al. [13]. Yoo et al. [14] attempted to address this problem through a 1D model. However, the proposed model assumed a fixed anode and the battery is placed vertically.

The solid phase volume change is not the only factor to cause electrolyte level change. The evaporation of solvent is another phenomenon that is often neglected in modeling works. Most experimental studies on non-aqueous Li–air batteries used volatile solvents such as 1,2–dimethoxyethane (DME) and acetonitril (ACN), as indicated by Balaish et al. [15], to achieve a high oxygen solubility and diffusivity. Evaporated solvent escapes the battery through the breathing openings and is lost in ambient air. To our best knowledge, no previous modeling studies of the effect of solvent evaporation on cell performance have been reported.

Another often neglected physical phenomenon in Li–air battery models is the interaction of the cell with its surroundings. Lithium air batteries normally interact with their surroundings by consuming or releasing oxygen during the discharge and charge cycles, respectively. However, the computation domain of most existing Li-air battery models is generally bound by the interface of the cathode and ambient air, and assumes a constant dissolved oxygen concentration as the boundary condition. The diffusion of oxygen from the environment into the cell and solvent diffusion into the environment have not been considered in prior studies.

In this section, the previously neglected physical phenomena are included in our proposed two dimensional transient Li–air coin cell model. These effects on cell performance are examined and discussed based on simulated results. The Arbitrary Lagrangian–Eulerian (ALE) method is employed to describe the deformed computation domain and to track the moving electrolyte level. The air chamber that provides oxygen to the cell is included in the computation domain. The

simulation results, both with and without consideration of these effects, are compared and discussed.

4.2 Physical Model

The battery to be modeled has a typical coin cell structure, as shown in Figure 4-1, and has been widely used in previous experimental studies. Structural parameters of the cell are listed in Table 4-1. It is assumed that the gas diffusion layer (GDL), cathode, separator and anode lithium metal have the same radius. To reduce the model to two dimensions, a single breathing hole is located at the center of the cathode casing. An axisymmetric assumption is adopted and the total computation domain is shown by the grey area in Figure 4-2, which contains five sub–domains: the air chamber, GDL, cathode, separator, and anode. The governing equations developed below are used on one or several sub-domains depending on the physical phenomena.

The following assumptions are included to make the computation feasible:

1. Li_2O_2 is considered completely insoluble in electrolyte and precipitates on the cathode pore surface immediately upon generation.
2. The reaction shown in eq. (1) is considered. Side reactions are neglected.
3. The charging process is not considered due to the lack of an established understanding of the mechanisms of these reactions.
4. Bulk velocity of the electrolyte is negligible and convection is not considered in mass transport, since the length scale in the cell is in the order of 10^{-3} m and the time scale of discharge is in the order of 1~10 hours.
5. Thermal effect is assumed to be negligible, including the temperature drop caused by solvent evaporation and consequent change of saturation vapor pressure. This is justifiable due to the small size of the cell and a long time scale of discharge (10^2 - 10^3 minutes).

4.2.1 Mass and charge transfer

The governing equations to describe the mass and charge transport inside the cell follow the common framework used in most previous Li–air continuum-scale models based on concentrated solution and porous electrode theory [16].

Conservation of all species in the electrolyte can be expressed as:

$$\frac{\partial(\varepsilon c_i)}{\partial t} = -\nabla \cdot \boldsymbol{N}_i + r_i \tag{2}$$

where c_i is molarity of species i, ε is local porosity, $\boldsymbol{N}_i$ is the molar flux of species i, and r_i is the species generation rate. According to concentrated solution theory [16], the molar flux of Li^+ ions in electrolyte can be expressed as:

$$\boldsymbol{N}_{\mathrm{Li}} = -D_e^{eff}\nabla c_{\mathrm{Li}} + \frac{\boldsymbol{i}_2 t_+^0}{F} \tag{3}$$

where D_e^{eff} is the effective diffusion coefficient of the salt, t_+^0 is the transference number of lithium ion with respect to the solvent velocity, and F is the Faraday constant. The current density in electrolyte, $\boldsymbol{i}_2$, can be expressed as:

$$\boldsymbol{i}_2 = -k_e^{eff}\nabla\phi_2 - \frac{2RTk^{eff}}{F}\left(t_+^0 - 1\right)\left(1 + \frac{\partial \ln f_{\pm}}{\partial \ln c_{\mathrm{Li}}}\right)\nabla \ln c_{\mathrm{Li}} \tag{4}$$

where k_e^{eff} is the effective ionic conductivity of the electrolyte, $f_{\pm}$ is the salt activity coefficient, and $\left(1 + \frac{\partial \ln f_{\pm}}{\partial \ln c_{\mathrm{Li}}}\right)$ is the thermodynamic factor [17].

To simplify the equations, the diffusion conductivity, k_{D}, is defined [18]:

$$k_D = \frac{2RTk^{eff}}{F}\left(t_+^0 - 1\right)\left(1 + \frac{\partial \ln f_{\pm}}{\partial \ln c_{\mathrm{Li}}}\right) \tag{5}$$

Combining eqs. (2) – (5) yields the following equation for lithium ion transport:

$$\varepsilon \frac{\partial c_{\mathrm{Li}}}{\partial t} + \nabla \cdot \left(-D_e^{eff} \nabla c_{\mathrm{Li}} \right) = r_{\mathrm{Li}} - \nabla \cdot \left(\frac{\boldsymbol{i}_2 t_+}{F} \right) \tag{6}$$

Dissolved oxygen is transported in the electrolyte by diffusion and therefore its molar flux can be expressed as [19]:

$$\boldsymbol{N}_{\mathrm{O}_2} = -D_{\mathrm{O}_2}^{eff} \nabla c_{\mathrm{O}_2} \tag{7}$$

Combining eqs. (2) and (7) leads to the following equation for dissolved oxygen transport:

$$\varepsilon \frac{\partial c_{\mathrm{O}_2}}{\partial t} + \nabla \cdot \left(-D_{\mathrm{O}_2}^{eff} \nabla c_{\mathrm{O}_2} \right) = r_{\mathrm{O}_2} \tag{8}$$

The generation rates of the lithium ion, r_{Li}, in eq. (6), and oxygen, r_{O_2}, in eq. (8), can be related to the local transfer current density between electrolyte and electrode, j_{R}, as:

$$r_{\mathrm{Li}} = \frac{A_{ED} j_{\mathrm{R}}}{F}, \tag{9}$$

and

$$r_{\mathrm{O}_2} = \frac{A_{ED} j_{\mathrm{R}}}{2F} \tag{10}$$

where A_{ED} is the specific reaction surface. The product $A_{\mathrm{ED}} j_{\mathrm{R}}$ is the cathode volumetric current density which is the direct indicator of local electrochemical reaction rate.

To maintain charge balance, the divergence of electrolyte current density should be equal to the volumetric current density:

$$\nabla \cdot \boldsymbol{i}_2 = A_{ED} j_R \tag{11}$$

Combining eqs. (4) and (11) results in the following equation for electrolyte potential:

$$\nabla \cdot \left(-k^{eff} \nabla \phi_2 \right) = \nabla \cdot \left(\frac{k_D}{c_{\mathrm{Li}}} \nabla c_{\mathrm{Li}} \right) + A_{ED} j_R \tag{12}$$

The governing equations for c_{Li}, $c_{\mathrm{O_2}}$, and ϕ_2 (eqs. (6), (8), and (12)) are computed over a set of deforming meshes covering the subdomains of the cathode and separator shown in Figure 4-2. The moving boundary of the deforming mesh reflects the drop in electrolyte level during discharge.

The current balance between the electrolyte and cathode solid phase indicates that:

$$\nabla \cdot \boldsymbol{i}_1 + \nabla \cdot \boldsymbol{i}_2 = 0 \tag{13}$$

where i_1 is the current density in the cathode solid phase, which can be expressed simply by Ohm's law:

$$\boldsymbol{i}_{1c} = -k_c^{eff} \nabla \phi_{1c} \tag{14}$$

where k_c^{eff} is the electronic conductivity of the cathode solid phase. Therefore, cathode electric potential can be obtained from eqs. (11), (13), and (14) as:

$$\nabla \cdot \left(-k_c^{eff} \nabla \phi_{1c} \right) = -A_{ED} j_{\mathrm{R}} \tag{15}$$

which is computed on a set of fixed meshes covering the GDL and cathode subdomains, shown in Figure 4-2.

Oxygen and solvent vapor transport in the GDL and air chamber are controlled by diffusion according to Fick's law:

$$\varepsilon \frac{\partial c_{oa}}{\partial t} + \nabla \cdot \left(-D_{oa}^{eff} \nabla c_{oa} \right) = 0 \tag{16}$$

$$\varepsilon \frac{\partial c_{sa}}{\partial t} + \nabla \cdot \left(-D_{sa}^{eff} \nabla c_{sa} \right) = 0 \tag{17}$$

where c_{oa} and c_{sa} are the concentrations of oxygen and solvent vapor in air, respectively; D_{oa}^{eff} and D_{sa}^{eff} are the effective diffusion coefficients of oxygen and solvent vapor in air, respectively.

Equations (16) and (17) are solved on the subdomains of the GDL and air chamber shown in Figure 4-2.

The effective parameters used in the above equations, including D_{Li}^{eff}, k^{eff}, $D_{\mathrm{O_2}}^{eff}$, D_{oa}^{eff}, and D_{sa}^{eff}, can be calculated through the Bruggeman correlation [20]:

$$\Phi^{eff} = \Phi \varepsilon^{\beta} \tag{18}$$

where Φ can be D_{Li}, k_e, $D_{\mathrm{O_2}}$, D_{oa}, and D_{sa}. Similarly, k_{c}^{eff} can be expressed as:

$$k_c^{eff} = k_c \left(1 - \varepsilon_0 - \varepsilon_{\mathrm{b}}\right)^{\beta} \tag{19}$$

where k_c is the electron conductivity in the carbon phase of the cathode and ε_{b} is the volume fraction of electrode binder. The Bruggeman coefficient, β, is assumed to be a constant 1.5 [21].

Due to the deposition of the insoluble reaction product Li_2O_2, porosity in the cathode is a function of both location and time during the discharge process. It can be related to the volume fraction of precipitated product ε_{s}, and original porosity ε_0, through:

$$\varepsilon = \varepsilon_0 - \varepsilon_{\mathrm{s}} \tag{20}$$

The mass conservation of discharge product, Li_2O_2, is used to obtain ε_{s}:

$$\frac{\partial \varepsilon_{\mathrm{s}}}{\partial t} = -\frac{M_{\mathrm{Li_2O_2}}}{\rho_{\mathrm{Li_2O_2}} F} A_{ED} j_{\mathrm{R}} \tag{21}$$

where $M_{\mathrm{Li_2O_2}}$ is the molecular weight of Li_2O_2, and $\rho_{\mathrm{Li_2O_2}}$ is the density of Li_2O_2. The transfer current density j_{R}, is to be determined by reaction kinetics. Equation (21) is computed on a set of fixed meshes covering the subdomain of the cathode shown in Figure 4-2.

The driving force for the cathode reaction is the local activation overpotential η_c, which can be defined as:

$$\eta_{\mathrm{c}} = \phi_{1c} - \phi_2 - \Delta\phi_{\mathrm{Li_2O_2}} - E_{\mathrm{c}}^{\ 0} \tag{22}$$

where $\Delta\phi_{\mathrm{Li_2O_2}}$ is the voltage drop over the Li_2O_2 film and $E_{\mathrm{c}}^{\ 0}$ is the cathode theoretical potential. The voltage drop across the Li_2O_2 film is calculated by Ohm's law [4]:

$$\Delta\phi_{\mathrm{Li_2O_2}} = j_{\mathrm{R}} R_{\mathrm{Li_2O_2}} \varepsilon_{\mathrm{s}} \tag{23}$$

where $R_{\mathrm{Li_2O_2}}$ is the electrical resistivity across the Li_2O_2 film.

The Tafel equation [22] is used to express the cathode reaction kinetics:

$$j_{\mathrm{R}} = -k_{\mathrm{R}} \left(\frac{c_{\mathrm{Li}}}{c_{\mathrm{Li}}^{\mathrm{ref}}} \right)^2 \left(\frac{c_{\mathrm{O_2}}}{c_{\mathrm{O_2}}^{\mathrm{ref}}} \right) \exp\left(-\frac{\alpha_{\mathrm{c}} F}{RT} \eta_{\mathrm{c}} \right) \tag{24}$$

where k_{R} is the rate constant for the cathode reaction, and α_{c} is the transfer coefficient, equal to 0.5. Reference concentrations $c_{\mathrm{Li}}^{\mathrm{ref}}$ and $c_{\mathrm{O_2}}^{\mathrm{ref}}$ are set to be 1 M and the saturated oxygen concentration, $c_{\mathrm{O_2,sat}}$, respectively.

Anode reaction kinetics is described by the Butler–Volmer equation [22]:

$$j_{\mathrm{a}} = i_0 \left[\exp\left(\frac{(1-\alpha_a) F}{RT} \eta_{\mathrm{a}} \right) - \exp\left(-\frac{\alpha_a F}{RT} \eta_{\mathrm{a}} \right) \right] \tag{25}$$

where j_{a} is the transfer current density at the anode/separator interface (denoted as ④ in Figure 4-2), and i_0 is the exchange current density for the anode. The anode activation overpotential, η_{a}, is defined as:

$$\eta_{\mathrm{a}} = \phi_{1a} - \phi_2 - E_{\mathrm{a}}^{\ 0} \tag{26}$$

where ϕ_{1a} is the anode electrode potential and $E_a^{\ 0}$ is the anode theoretical potential, 0 V. The anode electrode potential is governed by Ohm's law:

$$\nabla \cdot \left(-k_{\mathrm{Li}} \nabla \phi_{1a} \right) = 0 \tag{27}$$

where k_{Li} is the conductivity of lithium metal. This governing equation is computed on the moving mesh set covering the subdomain of the anode shown in Figure 4-2. The moving mesh reflects the shrinking of the anode lithium foil during discharge.

The effect of reaction area loss due to Li_2O_2 deposition is described by the following empirical relation [5]:

$$A_{\mathrm{ED}} = A_{\mathrm{ED},0} \left[1 - \left(\frac{\varepsilon_{\mathrm{s}}}{\varepsilon_0} \right)^z \right] \tag{28}$$

where $A_{\mathrm{ED},0}$ is the original specific area and the value for z is set to 0.5. In summary, there are eight unknowns in the model described above: electrolyte concentration c_{Li}, dissolved oxygen concentration c_{O_2}, electrolyte potential ϕ_2, cathode electrode potential, ϕ_{1c}, oxygen gas concentration c_{oa}, solvent vapor concentration c_{sa}, anode electrode potential ϕ_{1a} and deposit layer volume fraction ε_{s}. They are described by seven partial differential equations (6), (8), (12), (15), (16), (17), (27), and one ordinary differential equation (21).

4.2.2 Moving boundaries

As discussed in section 1, the velocity of the moving electrolyte level (① in Figure 4-2) consists of two parts:

$$V_1 = -\left(V_{1v} + V_{1e} \right) \tag{29}$$

where V_{1v} is the velocity due to the liquid replacing the vanishing solid phase, and V_{1e} is caused by solvent evaporation. The negative sign is due to the surface moving in the negative direction of *z*. V_{1v} is related to discharge current density *I*:

$$V_{1v} = \frac{I}{\varepsilon_1 F}\left(\frac{M_{\mathrm{Li}}}{\rho_{\mathrm{Li}}} - \frac{M_{\mathrm{Li_2O_2}}}{2\rho_{\mathrm{Li_2O_2}}}\right) \tag{30}$$

where ε_1 is the average porosity of the cathode at the electrolyte level, and *M* and ρ are the molecular weight and density, respectively. The subscripts Li and Li_2O_2 denote lithium and deposited lithium peroxide, respectively. V_{1e} is related to the molar flux of solvent vapor N_{sv} on the electrolyte surface:

$$V_{1e} = \frac{\int_{Aes} N_{sv} dA}{A_{es}} \frac{M_{sv}}{\varepsilon_1 \rho_s} \tag{31}$$

where A_{es} denotes the area of the electrolyte surface and the subscript *sv* denotes solvent. The molar flux of evaporated solvent N_{sv} is calculated by:

$$N_{sv} = -D_{sv} \left.\frac{\partial c_{sv}}{\partial z}\right|_{A_{es}} \tag{32}$$

where D_{sv} is the diffusion coefficient of solvent vapor in air and c_{sv} is the concentration of solvent vapor in air.

The bottom of the anode lithium foil (② in Figure 4-2), moves upward during discharge and its velocity is:

$$V_2 = \frac{M_{Li}}{F\rho_{Li}} I \tag{33}$$

This velocity is expected to be constant since the discharge is under constant current.

4.2.3 Boundary conditions

At the anode/separator interface (③ in Figure 4-2), the electrolyte current density is equal to the discharge current density and the molar flux of dissolved oxygen is zero. At the separator/cathode interface (④ in Figure 4-2), the cathode electrode current is zero. At the cathode/GDL interface (① in Figure 4-2), the electrolyte current and Li^+ molar flux are both equal to zero, and the concentration of the dissolved oxygen is determined based on Henry's law:

$$c_{O_2} = \frac{c_{oa}}{c_0} c_{O_2,sat} \tag{34}$$

where c_0 is the total molar concentration of ideal gas at 1 bar and 25 °C and $c_{O_2,sat}$ is the solubility of oxygen in the electrolyte. Concentration of solvent vapor at this boundary is determined by the ideal gas law and its vapor saturation pressure p_{sa}:

$$c_{sa} = \frac{p_{sa}}{p_0} c_0 \tag{35}$$

where p_0 is 1 bar. The effect of lithium salt on solvent vapor pressure is neglected. The molar flux of oxygen and solvent vapor are zero at the air chamber wall (⑧ in Figure 4-2). The current density is equal to the discharge current density divided by the open ratio at the cathode casing (⑥ in Figure 4-2). The thickness of the cathode casing is neglected in the model. It should be noted that eqs. (34) and (35) are derived based on the assumption that pressure in the air chamber is constant. This is considered to be a reasonable assumption because the influx of evaporated DMF in the air chamber would cause an increase in pressure of less than 0.52% (516 Pa vapor pressure vs. 1 bar initial air chamber pressure) even if oxygen consumption is not considered, which conversely decreases pressure. The governing equations, boundary conditions and initial conditions are summarized in Table 4-2.

At the start of discharge, the air chamber and GDL are filled with air at 1 bar and with 0 pa solvent vapor. The electrolyte and dissolved oxygen concentrations are all uniform, at the values of 1 M and the saturated value $c_{O_2,sat}$, respectively. The cathode, separator, anode and spring are all immersed in electrolyte.

4.2.4 Computational methodology

The above governing equations are discretized and solved using the finite element method in COMSOL Multiphysics 4.4. Two sets of meshes are used. The first mesh set has 3643 elements, and it covers all the subdomains shown in Figure 4-2. The air chamber domain is discretized using a free triangular mesh while the other domains are discretized using a mapped rectangular mesh. In this mesh set, boundaries ① and ② can translate along the *z* direction, therefore the GDL, cathode, and anode sub–domains deform during the time–dependent calculation. The velocities of the moving boundaries are defined in eqs. (29) – (31) and (33). The ALE method [23] is used to enable geometry deformation. The second mesh set (4000 elements) is fixed and includes the cathode and GDL. Governing equations for ε_s and ϕ_{1c} are solved on this mesh set. Cathode specific surface area A_{ED} and transfer current density j_R are mapped from the deformed mesh onto this fixed mesh. The resulting values of ε_s and ϕ_{1c} are then mapped back to the deformed mesh through linear projection on a spatial frame. A time–dependent solver is employed to solve all the governing equations. A constant discharge current density I is imposed and the cell voltage is obtained through the difference between the cathode electrode potential at boundary ⑥ and the anode electrode potential at boundary ② for each time step. The maximum time step ranges between 10 and 100 seconds depending on the discharge current density; higher discharge current densities require a smaller time step. All results are proven to be mesh independent and time step independent.

Two different electrolytes are used in the calculations, including dimethyl formamide (DMF) and tetraethylene glycol dimethyl ether (TEGDME). These are chosen as solvents because of their opposing high and low vapor pressures, respectively. TEGDME is a widely used low vapor pressure organic solvent (~1 Pa) in experimental studies, while DMF has a fairly high vapor pressure (516 Pa at standard condition). The associated properties of both solvents are listed in Table 4-3. The diffusion coefficients of the solvent vapor in air are calculated using the FSG/LaBas method [24]. Oxygen diffusivities in the electrolyte are estimated through the Stokes–Einstein relation based on solvent viscosity [25]. Other parameters used in the calculation are provided in Table 4-4.

Figure 4-3 shows a typical example of the domain and mesh deformation after discharge. The discharge current density is 0.5 A m^{-2}, the solvent is DMF, and the radius of the cathode opening is 0.5 mm. No obvious mesh skewness is observed. The displacement of the electrolyte level and anode bottom surface are denoted as d_1 and d_2, and are computed as the integration of V_1 and V_2 over time, respectively. Therefore, they are influenced by discharge current density, evaporation rate of solvent, and the cathode porosity averaged over the electrolyte surface.

4.3 Results and discussion

4.3.1 Model validation

The predicted results are compared with the experimental results of Read [26], in which PC:DME was used as electrolyte solvent. The evaporation of solvent is not considered in this comparison because of the lack of vapor pressure data for a PC:DME mixture. The open ratio of the cathode casing was assumed to be 100% and the air chamber was assumed to be filled with pure oxygen initially. The cathode rate constant, k_R, is adjusted to match experimental results. Figure 4-4 shows the dependence of cell voltage on cathode material specific capacity at different

discharge current densities for both simulation and experimental results [26]. In general, the predicted results agree well with available experimental results in literature.

4.3.2 Tracking the electrolyte level

Figure 4-5 indicates the position (*z* value) of the electrolyte level and anode/spring interface for two different electrolytes. Figure 4-5(a) shows the case with the DMF based electrolyte while Figure 4-5(b) shows the case with TEGDME based electrolyte. Discharge current densities for both cases are 0.5 A m^{-2} and the cathode opening radius is 0.5 mm. The upper solid line represents the drop in electrolyte level while the lower solid line depicts the rise of the bottom of the anode lithium foil. The anode bottom surface rises linearly over time due to a constant discharge current, and therefore V_2 remains constant according to eq. (33). The dashed line separates the displacement of electrolyte surface into two parts for both solvents: The upper region is caused by solvent evaporation while the lower area is attributed to solid phase volume decrease. Solvent evaporation occurs quickly and fills the air chamber in several hundred minutes. Solvent evaporation then gradually slows (see Figure 4-6) when the partial pressure of solvent vapor in the chamber approaches its saturated value. The electrolyte level displacement caused by the solvent evaporation correspondingly stops. The distance between the dashed line and the lower solid line represents the electrolyte level drop caused by the solid phase volume decrease. The electrolyte level drops faster towards the end of discharge because of a higher V_{1v}. The only non-constant parameter that influences V_{1v} is the average porosity ε_1, as noted in eq. (30), which changes due to the increased Li_2O_2 deposition. There are two features of significance when comparing Figure 4-5(a) and (b). The first is that DMF evaporation causes a much larger electrolyte level drop due to its higher vapor pressure. This is also evident in Figure 4-6 as V_{1e} is several times larger for the DMF based cell than for the TEGDME based cell. Secondly, the discharge time of the DMF based

cell is much greater than that of TEGDME, due to a much higher oxygen diffusivity in DMF (see Table 4-3).

Figure 4-7 shows the variation of DMF solvent vapor concentration with time at the cell opening (⑤ in Figure 4-2) and at the air chamber wall (⑧ in Figure 4-2). The vapor concentration at the cell opening is 90% of the saturated level (0.215 mol m^{-3}) after just several minutes into discharge. This is reasonable because the gas diffusion layer is very thin. At the same time, vapor concentration at the air chamber wall is still very low, which results in a large concentration gradient in the air chamber, and drives solvent vaporization. The solvent vapor in the air chamber also reaches saturation at 300 minutes. Accordingly, the flux of solvent vapor on the electrolyte surface and V_{1e} are very low at this time, as evidenced by Figure 4-6(a).

4.3.3 Effect of electrolyte level change

It seems intuitive that a model accounting for electrolyte level change would predict a lower discharge capacity because of the loss of electrolyte. However, the predicted result indicates the opposite trend. Figure 4-8 compares the discharge curves of models with and without consideration of electrolyte level drop during discharge. The present model predicts a 22.5% higher discharge capacity for a DMF based cell at 5 A m^{-2} and a 14.9% higher discharge capacity for a TEGDME based cell at 0.5 A m^{-2}. Therefore, neglect of electrolyte level drop during discharge would result in an underestimation of cell discharge capacity. To better explain this conclusion, the effects of electrolyte level drop need to be examined.

There are three primary effects of electrolyte level drop on Li-air battery operation. The first is less cathode soaked in electrolyte and consequently less reaction surface. A higher overpotential must then be maintained for the required current output, which yields a smaller discharge time and capacity. The distribution of volumetric current density $A_{ED}j_R$ along the z direction (r=0) is shown

in Figure 4-9, which is a direct indicator of reaction rate. It can be seen that the electrochemical reaction takes place only in a small section of the cathode adjacent to the electrolyte surface (where the sharp drop of the line is located). This is more pronounced at the second half of the discharge period, which reveals that only a small percentage of the cathode reaction surface is used. Therefore, the loss of reaction surface only has a small influence on discharge capacity.

The second effect caused by electrolyte level drop is a decrease in electrolyte thickness, and consequent lower ion migration resistance and higher discharge capacity. The overpotential caused by the finite electrolyte conductivity can be approximated as:

$$\eta_2 = \frac{I\left(h_{cath}/2 + h_{sep}\right)}{k_e}$$

where h_{cath} is the thickness of the electrolyte in the cathode (which decreases) and h_{sep} is the thickness of the separator. The electrolyte level drops 0.17 mm for a DMF based cell and 0.013 mm for a TEGDME based cell at the end of discharge, when the discharge current density is 0.5 A m^{-2}. This corresponds to a 0.03 mV and 0.05 mV decrease of η_2, for DMF and TEGDME based cells, respectively. These value are negligible compared to other overpotentials, such as that for reaction activation. The decreased ion migration resistance caused by electrolyte level drop is also relatively insignificant.

Compared to the above two phenomena, the third effect caused by electrolyte level drop is significant based on the model prediction. Figure 4-10(a) illustrates the Li_2O_2 deposition on the cathode solid phase surface with a constant electrolyte level during discharge. The electrolyte level remains unchanged during discharge. The reaction rate and Li_2O_2 generation rate are at their highest because the oxygen concentration at this surface is also at its highest at any location in the cathode. This leads to the thickest deposition layer of Li_2O_2 at the cathode/GDL interface. Most

existing modeling studies showed a similar Li_2O_2 distribution profile [5,8,27]. However, if electrolyte level drop is considered, this distribution profile is no longer valid. Figure 4-10(b) shows the electrolyte level at various times during discharge. As the electrolyte level drops, the position with maximum reaction rate and Li_2O_2 deposition drops accordingly. This leads to a final Li_2O_2 volume fraction (ε_s) distribution curve that peaks where the electrolyte surface is located at the end of the discharge. At each time interval, the maximum reaction rate area is lowered slightly. This alleviates electrode blocking and predicts a better electrode utilization than for a constant electrolyte level. Figure 4-11 shows the predicted final ε_s distribution with and without consideration of electrolyte level change. The results match with the qualitative analysis of Figure 4-10. An integration of ε_s over the entire cathode volume shows that without considering electrolyte drop, 22.0% of the cathode pore volume is used at the end of discharge while inclusion of the electrolyte level drop increases this value to 24.3%. This agrees with the prediction of increased cathode specific capacity.

4.3.4 Effect of air chamber size

Solvent evaporation causes a large part of electrolyte level drop for a DMF based cell, as evidenced by Figure 4-5(a). The size of the air chamber directly affects the amount of solvent evaporation. The larger the chamber, the more solvent vapor can be accommodated before saturation, which affects cell discharge capacity. The chamber size was chosen to make sure that less than 5% of the oxygen original stored in the chamber was used during discharge. This was to ensure that during discharge the pressure in the chamber keeps at a constant pressure. Figure 4-12 shows the discharge curves of a cell using DMF based electrolyte undergoing a 0.5 A m^{-2} discharge. It reveals that cathode specific capacity increases 72% from 530 mAh g^{-1} to 910 mAh g^{-1} when the air chamber radius is increased from 5 cm to 15 cm. However, with a 15 cm radius,

33.8% of the cathode is exposed to air instead of immersed in electrolyte at the end of discharge, about half of which is caused by solvent evaporation. In comparison, for a cell with a 5 cm air chamber radius, only 8.2% of the cathode is exposed to air at the end of discharge. The same calculation was done for a TEGDME based cell, with the result showing that air chamber size has negligible effect on cell performance because of a very low vapor pressure. The current model only considers the first discharge of the battery. The charging process needs to be included in future models to study the effect of chamber size on cycling performance of the battery. It should also be noted that if it is assumed that the air chamber is already saturated with solvent vapor at the start of the discharge, the effect of chamber size on electrolyte level change would be negligible.

4.4 Conclusions

In a non-aqueous Li-air battery, the electrolyte level drops during discharge. This is caused by two phenomena, the decrease of the solid phase volume and electrolyte solvent evaporation. A 2-D Li-air coin cell physical model is developed with mesh deformation to track the electrolyte level during discharge. The position of electrolyte surface and its velocity are calculated. The diffusion of solvent vapor in the cell GDL and air chamber are also considered. The following conclusions are made:

1. The electrolyte surface velocity caused by solvent evaporation is at its highest at the beginning of discharge and then decreases to zero when the air chamber is saturated with solvent vapor. The surface velocity imposed by solid volume decrease gradually rises because of increased Li_2O_2 deposition and decreased porosity.

2. A Li-air battery model would predict a higher cathode specific discharge capacity by including the effect of electrolyte level drop. The increase can be up to 22.5% for a cell using DMF based electrolyte and 14.9% for a cell using TEGDME based electrolyte.

3. The proposed model describes a different Li_2O_2 distribution profile than those shown in previous studies. When electrolyte level drops during discharge, the position of the greatest Li_2O_2 deposition gradually moves with the surface. The final distribution of the Li_2O_2 volume fraction shows a peak in the middle of the cathode.

4. The air chamber has significant influence on discharge capacity for cells that use DMF based electrolyte. The discharge capacity increased by 72% when the radius of the chamber increased from 5 cm to 15 cm. This is accompanied by a large amount of solvent loss. At the end of discharge, 33.8% of the cathode volume is exposed in air instead of immersed in electrolyte.

Nomenclature

A	specific area (m^{-1})
c	concentration (mol m^{-3})
D	diffusivity (m^2 s^{-1})
d	displacement (m)
E^0	thermodynamic equilibrium voltage (V)
F	Faraday constant (96,485 C mol^{-1})
$f_{\pm}$	Salt activity coefficient
I	discharge current density (A m^{-2})
i	current density (A m^{-2})
j	transfer current density between electrode and electrolyte (A m^{-2})
k_e	ionic conductivity (S m^{-1})
k_c	electron conductivity in carbon phase of electrode (S m^{-1})
k_D	diffusion conductivity (A m^{-1})
k_R	reaction rate constant (A m^{-2})
M	molecular weight (kg mol^{-1})
N	molar flux (mol m^{-2} s^{-1})
O_r	cathode casing open ratio
p	pressure (Pa)
R	universal gas constant (8.314 J mol^{-1} K^{-1}), electrical resistivity (Ω m^2), radius (m)
r	generation rate (mol m^{-3} s^{-1})
T	temperature (K)
t	time (s)

t_+	transference number
V	velocity (m s^{-1})
α	transfer coefficient
β	Bruggeman coefficient
ε	porosity
η	overpotential (V)
ρ	density (kg m^{-3})
ϕ	electric potential (V)

Superscripts and Subscripts

1	electrode solid phase
2	electrolyte phase
a	anode
c	cathode
eff	effective value
oa	oxygen in air
sa	solvent vapor in air

References

[1] S.S. Sandhu, J.P. Fellner, G.W. Brutchen, Diffusion-Limited Model for a Lithium/air Battery with an Organic Electrolyte, J. Power Sources. 164 (2007) 365–371. doi:10.1016/j.jpowsour.2006.09.099.

[2] P. Albertus, G. Girishkumar, B. McCloskey, R.S. Sánchez-Carrera, B. Kozinsky, J. Christensen, et al., Identifying Capacity Limitations in the Li/Oxygen Battery Using Experiments and Modeling, J. Electrochem. Soc. 158 (2011) A343–A351. doi:10.1149/1.3527055.

[3] Y. Wang, S.C. Cho, Analysis of Air Cathode Perfomance for Lithium-Air Batteries, J. Electrochem. Soc. 160 (2013) A1847–A1855. doi:10.1149/2.092310jes.

[4] U. Sahapatsombut, H. Cheng, K. Scott, Modelling of Electrolyte Degradation and Cycling Behaviour in a Lithium-Air Battery, J. Power Sources. 243 (2013) 409–418. doi:10.1016/j.jpowsour.2013.06.043.

[5] U. Sahapatsombut, H. Cheng, K. Scott, Modelling the Micro–macro Homogeneous Cycling Behaviour of a Lithium–air Battery, J. Power Sources. 227 (2013) 243–253. doi:10.1016/j.jpowsour.2012.11.053.

[6] X. Li, A. Faghri, Optimization of the Cathode Structure of Lithium-Air Batteries Based on a Two-Dimensional, Transient, Non-Isothermal Model, J. Electrochem. Soc. 159 (2012) A1747–A1754. doi:10.1149/2.043210jes.

[7] A.A. Franco, K.-H. Xue, Carbon-Based Electrodes for Lithium Air Batteries: Scientific and Technological Challenges from a Modeling Perspective, ECS J. Solid State Sci. Technol. 2 (2013) M3084–M3100. doi:10.1149/2.012310jss.

[8] K.-H. Xue, T.-K. Nguyen, a. a. Franco, Impact of the Cathode Microstructure on the Discharge Performance of Lithium Air Batteries: A Multiscale Model, J. Electrochem. Soc. 161 (2014) E3028–E3035. doi:10.1149/2.002408jes.

[9] X.J. Chen, V. V. Bevara, P. Andrei, M. Hendrickson, E.J. Plichta, J.P. Zheng, Combined Effects of Oxygen Diffusion and Electronic Resistance in Li-Air Batteries with Carbon Nanofiber Cathodes, J. Electrochem. Soc. 161 (2014) A1877–A1883. doi:10.1149/2.0721412jes.

[10] C.O. Laoire, S. Mukerjee, K.M. Abraham, E.J. Plichta, M.A. Hendrickson, Influence of Nonaqueous Solvents on the Electrochemistry of Oxygen in the Rechargeable Lithium−Air Battery, J. Phys. Chem. C. 114 (2010) 9178–9186. doi:10.1021/jp102019y.

[11] X. Zhang, L. Hua, E. Yang, Z. An, J. Chen, X. Chen, et al., A Simple Method of Making a Li-Air Battery with Longevity, Int. J. Electrochem. Sci. 7 (2012) 10562–10569.

[12] G. a Elia, J. Hassoun, W.-J. Kwak, Y.-K. Sun, B. Scrosati, F. Mueller, et al., An Advanced Lithium-Air Battery Exploiting an Ionic Liquid-Based Electrolyte., Nano Lett. 14 (2014) 6572–7. doi:10.1021/nl5031985.

[13] J. Yuan, J.-S. Yu, B. Sundén, Review on Mechanisms and Continuum Models of Multi-Phase Transport Phenomena in Porous Structures of Non-Aqueous Li-Air Batteries, J. Power Sources. 278 (2015) 352–369. doi:10.1016/j.jpowsour.2014.12.078.

[14] K. Yoo, S. Banerjee, P. Dutta, Modeling of Volume Change Phenomena in a Li–air Battery, J. Power Sources. 258 (2014) 340–350. doi:10.1016/j.jpowsour.2014.02.044.

[15] M. Balaish, A. Kraytsberg, Y. Ein-Eli, A Critical Review on Lithium-Air Battery Electrolytes., Phys. Chem. Chem. Phys. 16 (2014) 2801–22. doi:10.1039/c3cp54165g.

[16] J. Newman, K.E. Thomas-Alyea, Electrochemical Systems, 3rd ed., John Wiley & Sons, Hoboken, NJ, 2004.

[17] A. Nyman, M. Behm, G. Lindbergh, Electrochemical Characterisation and Modelling of the Mass Transport Phenomena in $LiPF_6$–EC–EMC Electrolyte, Electrochim. Acta. 53 (2008) 6356–6365. doi:10.1016/j.electacta.2008.04.023.

[18] P. Andrei, J.P. Zheng, M. Hendrickson, E.J. Plichta, Modeling of Li-Air Batteries with Dual Electrolyte, J. Electrochem. Soc. 159 (2012) A770–A780. doi:10.1149/2.010206jes.

[19] A. Faghri, Y. Zhang, Transport Phenomena in Multiphase Systems, Academic Press, 2006. doi:10.1016/0167-2738(81)90101-6.

[20] W. Lai, F. Ciucci, Mathematical Modeling of Porous Battery electrodes—Revisit of Newman's Model, Electrochim. Acta. 56 (2011) 4369–4377. doi:10.1016/j.electacta.2011.01.012.

[21] H. Bahrami, A. Faghri, Review and Advances of Direct Methanol Fuel Cells: Part II: Modeling and Numerical Simulation, J. Power Sources. 230 (2013) 303–320. doi:10.1016/j.jpowsour.2012.12.009.

[22] A.J. Bard, L.R. Faulkner, Electrochemical Methods: Fundamentals and Applications, 2nd ed., John Wiley & Sons, 2001.

[23] J. Donea, A. Huerta, J. Ponthot, A. Rodr, Arbitrary Lagrangian – Eulerian Methods, in: Encycl. Comput. Mech., 1999: pp. 1–25. doi:10.1002/0470091355.ecm009.

[24] W.A. Tucker, L.H. Nelken, No Title, in: W.J. Lyman, W.F. Reehl, D.H. Rosenblatt (Eds.), Handb. Chem. Prop. Estim. Methods, American Chemical Society, Washington DC, 1982.

[25] J. Read, K. Mutolo, M. Ervin, W. Behl, J. Wolfenstine, A. Driedger, et al., Oxygen Transport Properties of Organic Electrolytes and Performance of Lithium/Oxygen Battery, J. Electrochem. Soc. 150 (2003) A1351–A1356. doi:10.1149/1.1606454.

[26] J. Read, Characterization of the Lithium/Oxygen Organic Electrolyte Battery, J. Electrochem. Soc. 149 (2002) A1190–A1195. doi:10.1149/1.1498256.

[27] C.Y. Jung, T.S. Zhao, L. An, Modeling of Lithium–oxygen Batteries with the Discharge Product Treated as a Discontinuous Deposit Layer, J. Power Sources. 273 (2015) 440–447. doi:10.1016/j.jpowsour.2014.09.103.

[28] T.E. Daubert, R.P. Danner, Physical and Thermodynamic Properties of Pure Chemicals: Data Compilation, Taylor & Francis, Washington, DC, 1989.

[29] D.T. Sawyer, G. Chlerlcato, C.T. Angells, E.J. Nannl, T. Tsuchlya, Effects of Media and Electrode Materials on the Electrochemical Reduction of Dioxygen, 2 (1982) 1720–1724.

[30] J.P. Southall, H.V.S.A. Hubbard, S.F. Johnston, V. Rogers, G.R. Davies, J.E. McIntyre, et al., Ionic Conductivity and Viscosity Correlations in Liquid Electrolytes for Incorporation into PVDF Gel Electrolytes, Solid State Ionics. 85 (1996) 51–60.

[31] B.T. Ahn, H. Jeon, B.Y. Hur, K. Kim, J.W. Park, Effect of Various Lithium Salts in TEGDME Based Electrolyte for Li/Pyrite Battery, Solid State Phenom. 124-126 (2007) 971–974. doi:10.4028/www.scientific.net/SSP.124-126.971.

[32] K.M. Abraham, Z. Jiang, A Polymer Electrolyte-Based Rechargeable Lithium/Oxygen Battery, J. Electrochem. Soc. 143 (1996) 1. doi:10.1149/1.1836378.

[33] Y.R. Dougassa, J. Jacquemin, L. El Ouatani, C. Tessier, M. Anouti, Viscosity and Carbon Dioxide Solubility for $LiPF_6$, LiTFSI, and LiFAP in Alkyl Carbonates: Lithium Salt Nature and Concentration Effect, J. Phys. Chem. B. 118 (2014) 3973–3980. doi:10.1021/jp500063c.

[34] S.G. Stewart, J. Newman, The Use of UV/vis Absorption to Measure Diffusion Coefficients in $LiPF_6$ Electrolytic Solutions, J. Electrochem. Soc. 155 (2008) F13–F16. doi:10.1149/1.2801378.

[35] Y.-C. Lu, D.G. Kwabi, K.P.C. Yao, J.R. Harding, J. Zhou, L. Zuin, et al., The Discharge Rate Capability of Rechargeable Li-O_2 Batteries, Energy Environ. Sci. 4 (2011) 2999–3007. doi:10.1039/c1ee01500a.

Table 4-1 Structural parameters of the Li–air coin cell

Radius [mm]		Original thickness [mm]				Original porosity		
Electrodes	Opening	GDL	Cathode	Separator	Anode	GDL	Cathode	Separator
2.5	0.1	0.1	0.8	0.025	0.2	0.75	0.73	0.5

Table 4-2 Effective domains of each dependent variable and corresponding boundary and initial conditions

Variable	Effective Domain	Boundary Condition (BC) and Initial Condition (IC)
c_{Li}, eq. (6)	Sep*, Cath*	①**: $\frac{\partial c_{\mathrm{Li}}}{\partial z}=0$; ③: $-D_{\mathrm{Li}}^{eff}\frac{\partial c_{\mathrm{Li}}}{\partial z}=\frac{1-t_+}{\mathrm{F}}I$; IC: c_{Li}=1 M
c_{O_2}, eq. (8)	Sep, Cath	①: $c_{\mathrm{O}_2}=\frac{c_{oa}}{c_0}c_{\mathrm{O}_2,sat}$; ③: $\frac{\partial c_{\mathrm{O}_2}}{\partial z}=0$; IC: $c_{\mathrm{O}_2}=c_{\mathrm{O}_2,sat}$
ϕ_2, eq. (12)	Sep, Cath	①: $\frac{\partial \phi_2}{\partial z}=0$; ③: $-k^{eff}\frac{\partial \phi_2}{\partial z}=I+\frac{k_D}{c_{\mathrm{Li}}}\frac{\partial c_{\mathrm{Li}}}{\partial z}$ IC: $\phi_2=0$
ϕ_{1c}, eq. (15)	Cath, GDL*	④: $\frac{\partial \phi_{1c}}{\partial z}=0$; ⑤: $\frac{\partial \phi_{1c}}{\partial z}=0$; ⑥: $-k_c^{eff}\frac{\partial \phi_{1c}}{\partial z}=\frac{I}{1-O_r}$ IC: $\phi_{1c}=E_0^c$
c_{oa}, eq. (16)	GDL, AC*	①: $N_{oa}=N_{\mathrm{O}_2}$; ⑧: $N_{oa}=0$ IC: $c_{oa}=0.21c_0$
c_{sa}, eq. (17)	GDL, AC	①: $c_{sa}=\frac{p_{sa}}{p_0}c_0$; ⑧: $N_{oa}=0$ IC: $c_{sa}=0$
ϕ_{1a}, eq. (27)	Ano*	②: $\phi_{1a}=0$; ③: $-k_{Li}\frac{\partial \phi_{1a}}{\partial z}=I$ IC: ϕ_{1a}=0
ε_{s}, eq. (21)	Sep, Cath	IC: ε_{s}=0

* Sep: Separator; Cath: Cathode; GDL: Gas Diffusion Layer; AC: Air Chamber; Ano: Anode.
** ① – ⑧: Boundaries shown in Figure 4-2.

Table 4-3 Solvent/Electrolyte properties of the Li-air coin cell

		DMF	TEGDME
Diffusion coefficient in air [$\times 10^{-6}$ m^2 s^{-1}]	D_{so}	9.49	5.13
Vapor pressure [Pa]	p_s	516 [28]	1.33
Molecular weight [g mol^{-1}]	M_s	73.09	78.13
Density [kg m^{-3}]	ρ_s	948	1100.4
O_2 solubility [mol m^{-3}]	$c_{O_2,sat}$	4.8 [29]	4.84[25]
O_2 diffusivity [$\times 10^{-9}$ m^2 s^{-1}]	D_{O_2}	1.93	0.217[10]
Ionic conductivity [S/m]	k_e	1.0[30]	0.06 [31]

Table 4-4 Parameters used in the simulation model of a Li-air coin cell

Parameter	Symbol	Value
Cathode specific area [m^2 m^{-3}]	$A_{ED,0}$	3.75×10^6 [4]
Cathode rate constant [A m^{-2}]	k_R	2.5×10^{-9}
Transfer coefficient	α_c, α_a	0.5
Cathode theoretical potential [V]	E_c^0	3.1 [32]
Anode exchange current density [A m^{-2}]	i_0	1 [5]
Density of lithium [g cm^{-3}]	ρ_{Li}	0.534
Density of carbon [g cm^{-3}]	ρ_c	2.0
Density of lithium peroxide [g cm^{-3}]	$\rho_{Li_2O_2}$	2.14
Density of PTFE [g cm^{-3}]	ρ_{PTFE}	2.2
Electric resistivity of Li_2O_2 [Ω m^2]	$R_{Li_2O_2}$	50 [4]
Diffusivity of O_2 in electrolyte [m^2 s^{-1}]	D_{O_2}	3.98×10^{-10} [33]
Salt diffusivity in electrolyte [m^2 s^{-1}]	D_{Li}	1.5×10 [34]
Molecular weight of lithium [g mol^{-1}]	M_{Li}	6.94
Molecular weight of Li_2O_2 [g mol^{-1}]	$M_{Li_2O_2}$	45.88
Transference number	t_0^+	0.43 [35]
Thermodynamic factor	$1+d\ln f_{\pm}/d\ln c$	$\frac{0.28687c_{Li}^{\ 2}-0.74678c_{Li}+0.44103}{0.1287c_{Li}^{\ 3}-0.4106c_{Li}^{\ 2}+0.4717c_{Li}+0.5508}$ [17]

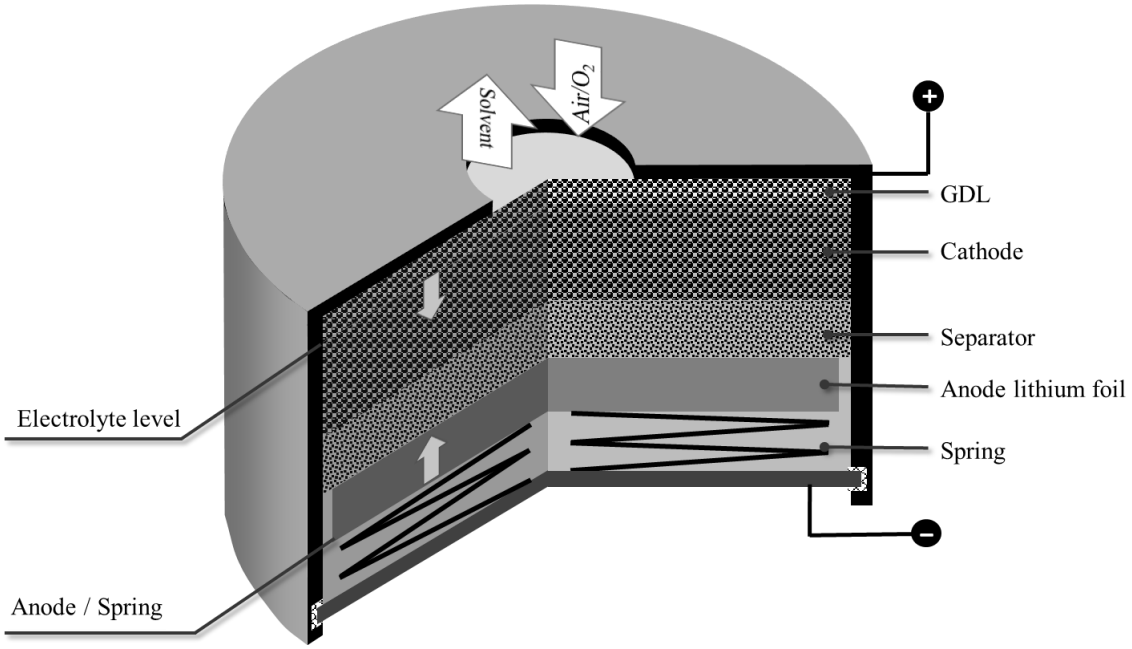

Figure 4-1 Structure of a Li-air coin cell.

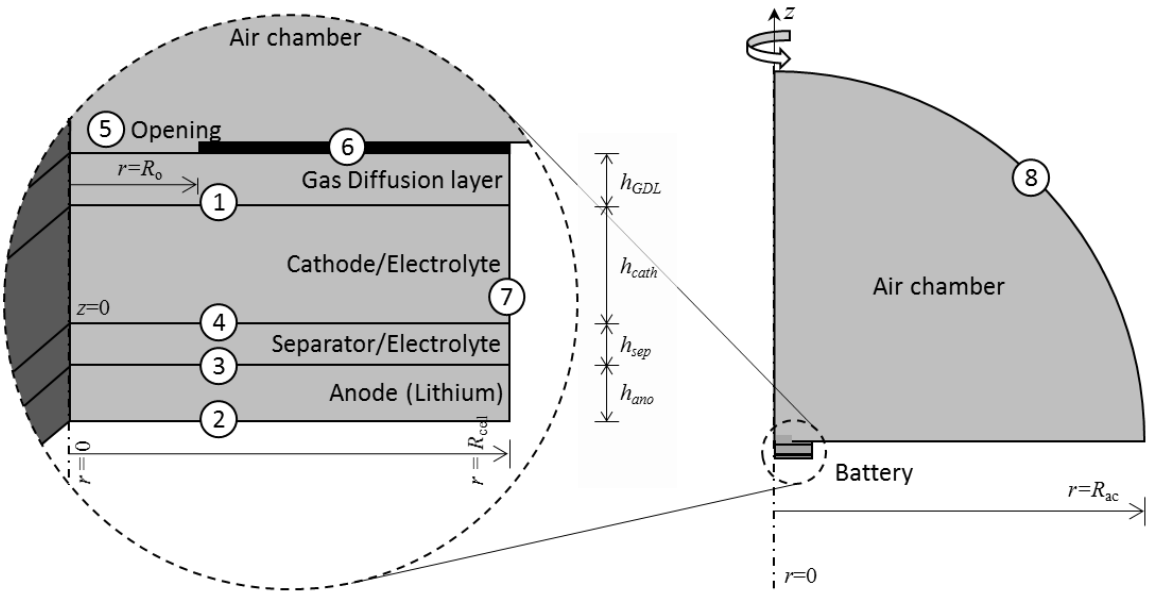

Figure 4-2 Computational domain and boundaries of the Li-air coin cell.

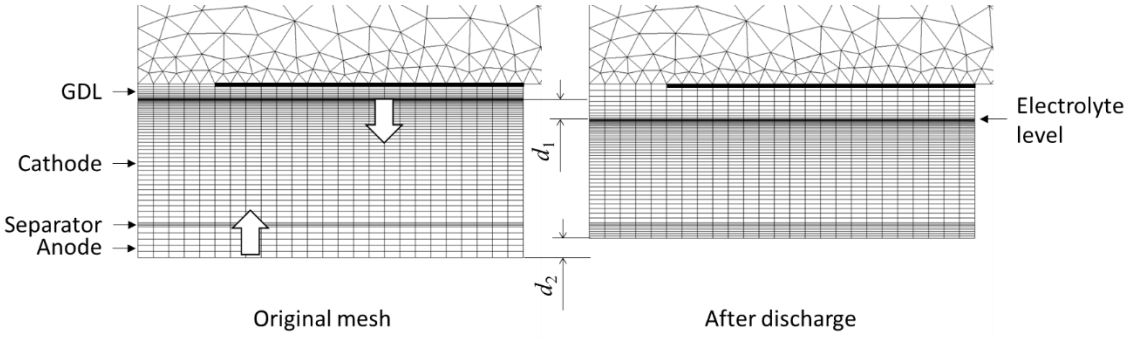

Figure 4-3 Boundary movement and mesh deformation of the Li-air coin cell.

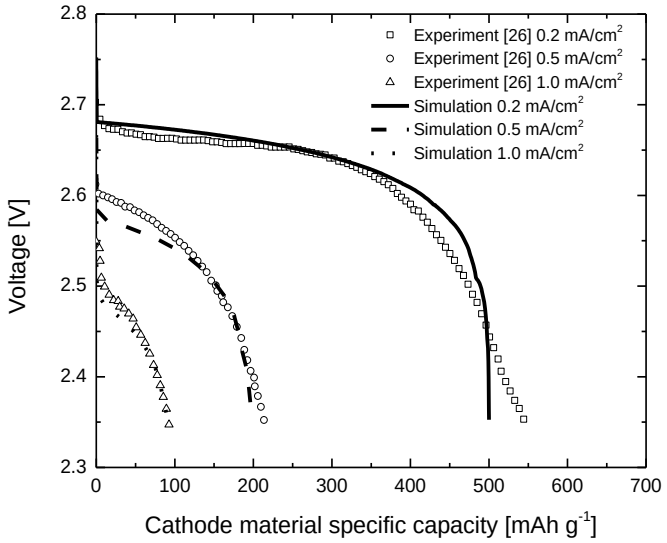

Figure 4-4 Comparison of predicted battery discharge curves at various current densities with experimental results from Read [26].

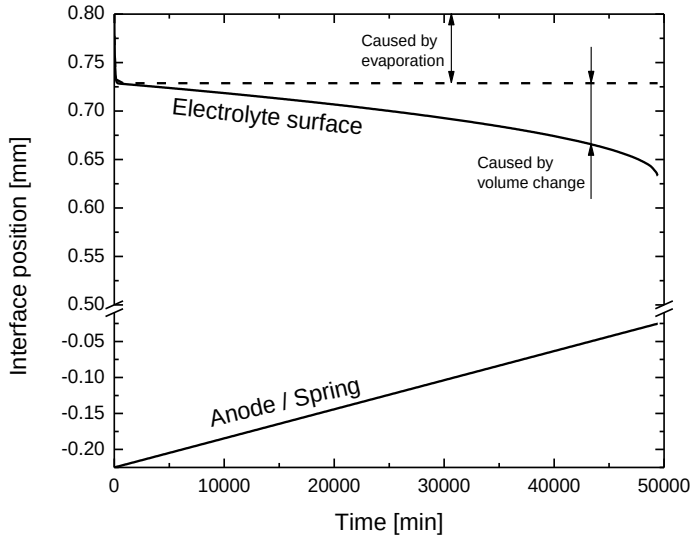

(a) Solvent: DMF

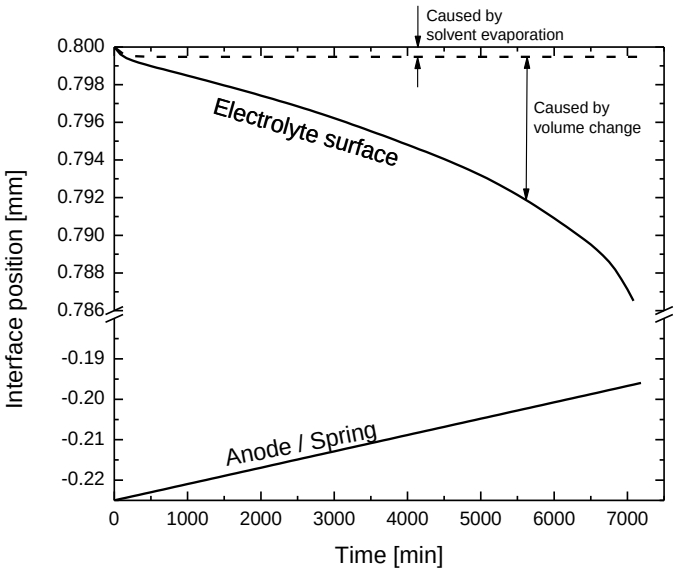

(b) Solvent: TEGDME

Figure 4-5 Variation of electrolyte surface and anode/spring interface position with time for a Li-air coin cell using (a) DMF and (b) TEGDME as electrolyte solvent.

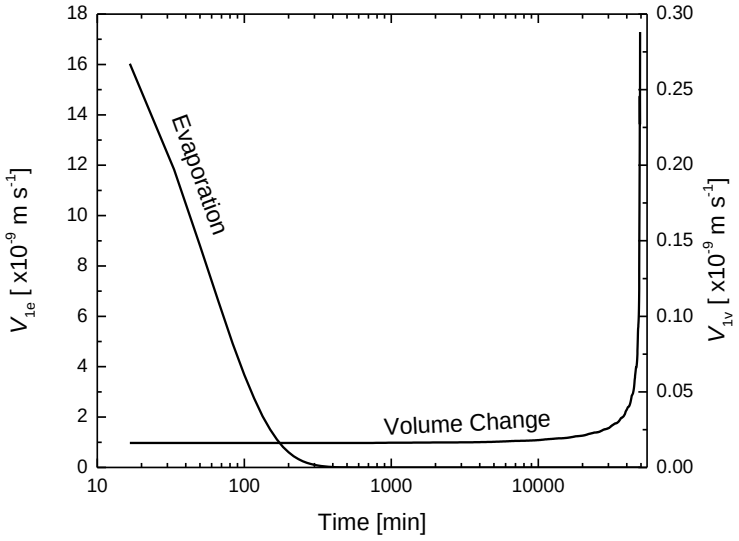

(a) Solvent: DMF

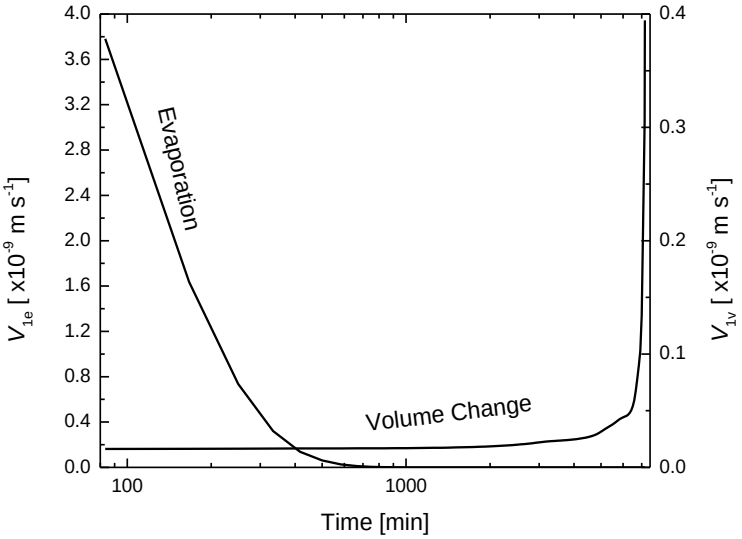

(b) Solvent: TEGDME

Figure 4-6 Velocities of electrolyte surface caused by solvent evaporation (V_{1e}) and solid volume change (V_{1v}) for a Li-air coin cell using (a) DMF and (b) TEGDME as electrolyte solvent.

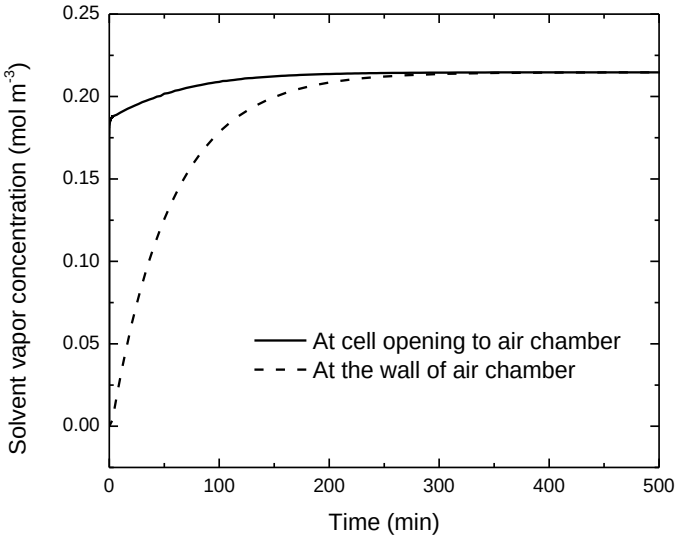

Figure 4-7 Variation of solvent vapor concentration with time at the cell opening and at the air chamber wall (DMF, R_o = 0.5 mm, R_{ac} = 10 cm).

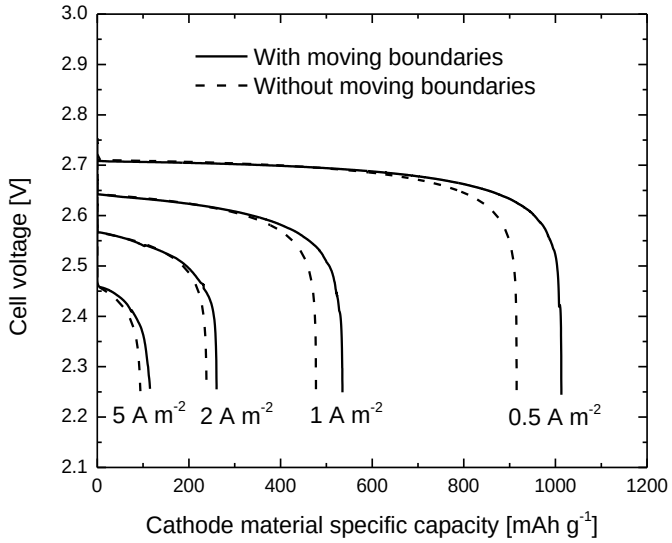

(a) Solvent: DMF

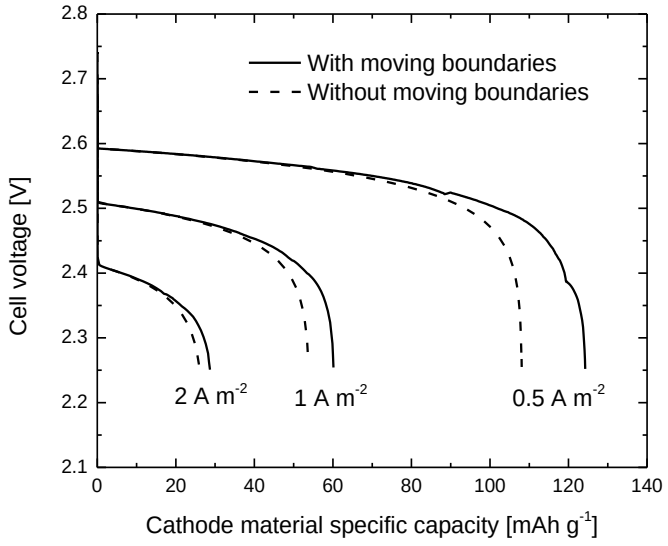

(b) Solvent: TEGDME

Figure 4-8 Discharge curves with and without consideration of electrolyte level change for a Li-air coin cell using (a) DMF and (b) TEGDME as electrolyte solvent.

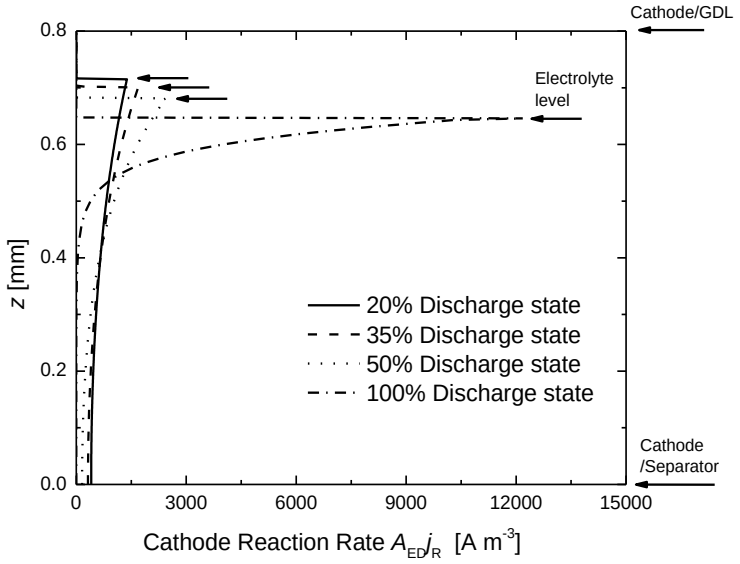

Figure 4-9 Reaction rate distribution at different states of discharge.

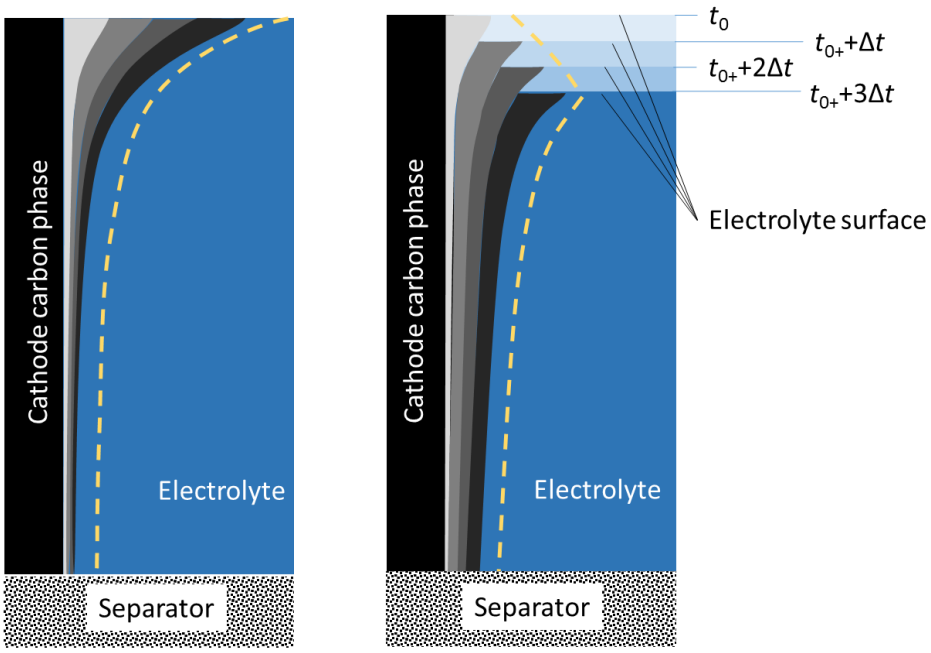

(a) (b)

Figure 4-10 Li_2O_2 deposition on the cathode solid phase surface (a) with constant electrolyte level and (b) with electrolyte level drop.

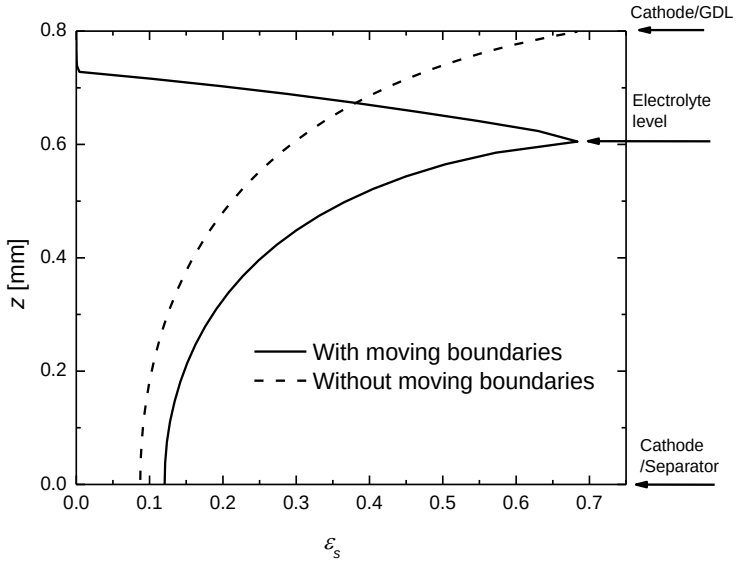

Figure 4-11 Distribution of Li_2O_2 deposition volume fraction, ε_s, with and without consideration of electrolyte level drop.

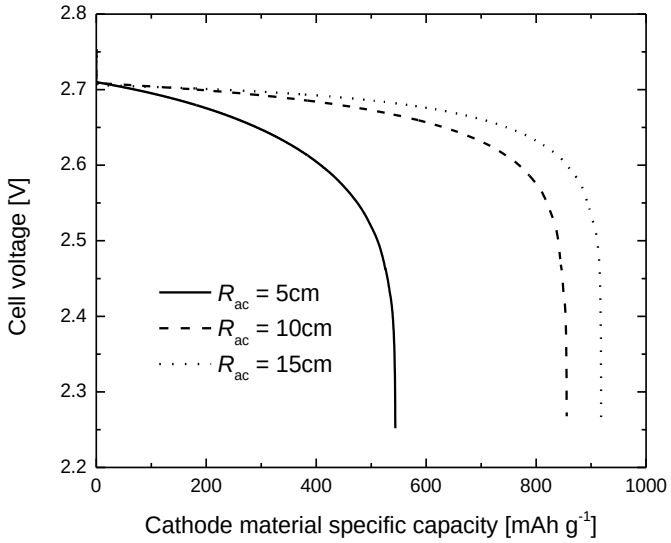

Figure 4-12 Discharge curve with various air chamber radii and DMF as electrolyte solvent.

Chapter 5 Analysis of a Permselective Membrane-Free Alkaline Direct Ethanol Fuel Cell

A physical model is developed to study the coupled mass and charge transport in a permselective membrane-free alkaline direct ethanol fuel cell. This type of fuel cell is not only free of expensive ion exchange membranes and platinum based catalysts, but also features a facile oxygen reduction reaction due to the presence of alkaline electrolyte. The proposed model is first validated by comparing its predictions to the experimental results from literature and then used to predict the overall performance of the cell and reveal the details of ion transport, distribution of electrolyte potential and current density. It is found that: (i) KOH concentration lower than 1 M notably impairs cell performance due to low electrolyte conductivity; (ii) the concentration gradient and electrical field are equally important in driving ion transport in the electrolyte; (iii) the current density distributions in the anode and cathode catalyst layers keep non-uniform due to different reasons. In the anode, it is caused by the ethanol concentration gradient, while in the cathode it is because of the electrolyte potential gradient; and (iv) at low cell voltage, current density distribution in the catalyst layer shows stronger non-linearity in the anode than in the cathode.

5.1 Introduction

With the advancement of material and electrochemical engineering, alkaline fuel cells regained research interests over the last several years. Among them, those using liquid fuels such as ethanol are regarded as good candidates to replace the once-promising direct methanol fuel cell (DMFC) as a portable power supply. In these fuel cells, because the charge transfer ion is OH^- instead of H^+, anion exchange membranes (AEM) are used instead of proton exchange membrane as in DMFC. They could conquer some fundamental problems of the DMFC by offering more facile

electrochemical kinetics in alkaline environment and a cheaper price due to the use of non-noble catalysts. Furthermore, fuel crossover is alleviated, leading to a higher efficiency and power density.

The state-of-the-art AEMs are still expensive and have relatively low ionic conductivities, however. They also face the problem of rapid performance degradation [1]. After a close inspection of the working mechanism of these fuel cells, it is found that AEM is not an indispensable part for them to operate. The liquid fuel is usually an aqueous solution of alcohol and alkali hydroxide, which can serve as electrolyte itself. At the same time, the cathode catalysts are usually highly tolerant to alcohol. Thus, the AEM can simply be replaced by a very low cost dielectric separator. This separator does not prevent the transport of reactants as an AEM does. Its only function is to prevent short circuits between the anode and cathode. In 2009, Zhang et al. [2] applied for a US patent which proposed a fuel cell called a permselective membrane-free direct fuel cell (PMFDFC). It lowers the cost of the fuel cell and avoids the problem of low conductivity of AEMs. The membrane-free alkaline fuel cell is the focus of this study.

Among the many choices of liquid fuels for compact fuel cells, including ethanol [3, 4], methanol [5], and borohydride [6], ethanol owns many merits over other candidates, such as low toxicity, lower cost, low carbon footage and market-readiness. A PMFDFC that uses an aqueous solution of ethanol and KOH as fuel will be referred to as a permselective membrane-free alkaline direct ethanol fuel cell (PMF-ADEFC) in this study.

The reported studies on membrane-free fuel cells are still very scarce, both in experimental and modeling approach. Some relevant modeling studies are briefly reviewed as follows.

Verma and Basu [7] provided an analytical model on the traditional dissolved fuel alkaline fuel cell, which has the same working principle as PMF-ADEFC. The model can predict the overall

performance of an alkaline fuel cell using ethanol, methanol or sodium borohydride as fuel [8, 9]. Since it is an analytical model, however, it cannot predict the mass transport characteristics such as the distribution of fuel, electrolyte concentrations and potentials.

Laminar Flow Fuel Cell (LFFC) is another kind of membrane-free fuel cell. It relies on the smooth interface between two laminar flow layers to separate the anode and cathode reactants and transfer ions. It uses neither ion exchange membrane nor a porous separator. The simulation model developed by Sprague and Dutta [10] on LFFC is a two-dimensional model based on Nernst-Planck and Poisson equations. It successfully illustrates the flow and mass transport in a LFFC and the effects of electric double layer on the surface of electrode. However, since it treats the electrode as a one-dimensional flat surface, the effect of electrode parameters such as porosity, liquid saturation in cathode layers cannot be evaluated through this model.

Jo and Yi [11, 12] developed a simulation model on classical alkaline fuel cells. It is the most comprehensive simulation study in literature on alkaline fuel cells. The simulation results agree with experimental data on NASA's Orbiter fuel cell and the model is used to predict the effect of electrolyte concentration and operating pressure on cell performance.

Bahrami and Faghri [13-15] developed a numerical model on an anion exchange membrane direct ethanol fuel cell which was the first physical model provided for this kind of fuel cell.

A one-dimensional numerical model on a PMF-ADEFC is developed in this study, with the following uniqueness and merits: (*i*) it is the first numerical model on PMF-ADEFCs predicting the cell performance in terms of polarization curves, the effect of fuel concentrations and electrode parameters; (*ii*) it provides the details on ion distribution, fuel and oxidant distribution in porous electrode and the roles of concentration gradient and electric field on ion transport.

5.2 Physical Model

Figure 5-1 shows the operating principles of a PMF-ADEFC. The fuel reservoir contains an aqueous solution of ethanol and potassium hydroxide (KOH). Ethanol diffuses through the anode diffusion layer (ADL), a porous layer built of carbon powder (XC72) and PTFE. The anode catalyst layer (ACL) consists of carbon supported palladium particles and anion exchange ionomers, where ethanol is oxidized into acetic acid and releases electrons [16]:

$$CH_3CH_2OH + 4\,OH^- \rightarrow CH_3COOH + 3\,H_2O + 4\,e^- \quad (1)$$

At the cathode side, oxygen diffuses from ambient through cathode diffusion layer (CDL) with a similar structural material to the ADL. In the cathode catalyst layer (CCL), Oxygen combines with water to generate hydroxyl ions in the presence of carbon supported catalyst particles, usually iron, copper or manganese oxide:

$$O_2 + 2\,H_2O + 4\,e^- \rightarrow 4\,OH^- \quad (2)$$

OH^- ions then move through the porous separator (SEP), reach ACL and take part in the ethanol oxidation reaction (EOR) of eq. (1). The separator is a dielectric porous layer where reactants and ions are free to move through. The five-layer structure shown in Figure 5-1 is similar to that of the alkaline fuel cells using an AEM with the difference being that the separator does not serve as a barrier for fuel and electrolyte solution between the anode and cathode, therefore, the reactants and ions are distributed across all of the layers.

In this study, a physical model is developed to predict the operating principals of the PMF-ADEFC described above. The following assumptions are made:

- Consistent to the application of direct alcohol fuel cells for compact portable power supplies, a passive mode of cell operation is considered. The bulk velocity, and consequently the convective terms in mass transport equations, are thus assumed to be negligible;

- Due to the relatively low power density and heat generation, the cell operates in an isothermal condition;
- The concentration of water is much higher than that of ethanol and KOH. Thus, it is constant throughout all layers;
- The kinetics of oxygen reduction reaction (ORR) and ethanol oxidation reaction are approximated by Tafel expressions;
- The anode is fully saturated with ethanol and KOH aqueous solution. The liquid saturation in the cathode is set to 0.2;
- Diffusion is considered by Fick's law, and the multi-component effects are neglected;
- Ethanol consumption in the CCL is negligible due to the low activity of cathode catalyst for the ethanol oxidation;
- The reaction between acetic acid and potassium hydroxide is neglected.
- The effect of potassium hydroxide concentration on the electrochemical kinetics is neglected due to the lack of an appropriate kinetics model.

5.2.1 Governing equations

The computation domain shown in Figure 5-1 includes five porous layers. While ethanol and ions (K^+ and OH^-) exist in all layers, oxygen mainly remains in the cathode side in gas phase. Ethanol and oxygen are not charged species, so the electrical field has no effect on their transports, which are described by [17]:

Ethanol: $\nabla \cdot \left(D_{\mathrm{E}}^{eff} \nabla C_{\mathrm{E}} \right) + S_{\mathrm{E}} = 0$ (3)

Oxygen: $\nabla \cdot \left(D_{\mathrm{O}}^{eff} \nabla C_{\mathrm{O}} \right) + S_{\mathrm{O}} = 0$ (4)

where subscript E and O stand for ethanol and oxygen, respectively, and *S* is the source term due to the consumption of ethanol and oxygen by electrochemical reactions in the catalyst layers, respectively:

$$S_{\mathrm{E}} = \begin{cases} -R_{ox}/4F & \text{ACL} \\ 0 & \text{others} \end{cases} \tag{5}$$

$$S_{\mathrm{O}} = \begin{cases} -R_{red}/4F & \text{CCL} \\ 0 & \text{others} \end{cases} \tag{6}$$

where R_{ox} and R_{red} are the oxidation and reduction reaction rates in the catalyst layers, respectively, and will be defined later by the electrochemical kinetics.

The effective diffusion coefficients in porous media, D^{eff}, are calculated from bulk diffusivity using the Bruggeman correction [7]:

$$D_{\mathrm{E}}^{eff} = D_{\mathrm{E}} \left(\varepsilon \cdot s\right)^{\tau} \tag{7}$$

$$D_{\mathrm{O}}^{eff} = D_{\mathrm{O}} \left[\varepsilon \cdot (1-s)\right]^{\tau} \tag{8}$$

where τ is a constant coefficient, D_{E} and D_{O} are respectively the bulk diffusion coefficients of oxygen and ethanol, ε is the porosity, and s is the liquid saturation.

The transports of ions are governed by the Nernst-Plank equation, considering the effect of both concentration gradient and electrical field:

$$\mathrm{OH^-}: \nabla \cdot \left(D_{\mathrm{OH}}^{eff} \nabla C_{\mathrm{OH}}\right) + z_{\mathrm{OH}} \nabla \cdot \left(\mu_{\mathrm{OH}}^{eff} C_{\mathrm{OH}} \nabla \Phi_e\right) + S_{\mathrm{OH}} = 0 \tag{9}$$

$$\mathrm{K^+}: \nabla \cdot \left(D_{\mathrm{K}}^{eff} \nabla C_{\mathrm{K}}\right) + z_{\mathrm{K}} \nabla \cdot \left(\mu_{\mathrm{K}}^{eff} C_{\mathrm{K}} \nabla \Phi_e\right) = 0 \tag{10}$$

where subscripts OH and K represent OH^- and K^+, respectively, *e* denotes the electrolyte phase and μ^{eff} is the effective electrical mobility of the ions in the liquid phase. Electrical mobility is the

ratio of the drift velocity of a charged particle to the magnitude of the electric field it is in. The effective electric mobility of an ion in porous media can be estimated by:

$$\mu^{eff} = \mu \left(\varepsilon \cdot s\right)^{\tau} \tag{11}$$

S_{OH} in eq. (9) is the source term due to the consumption of OH^- in the catalyst layers:

$$S_{OH} = \begin{cases} -R_{ox}/F & \text{ACL} \\ R_{red}/F & \text{CCL} \\ 0 & \text{others} \end{cases} \tag{12}$$

To maintain electro-neutrality, the following relation must be fulfilled:

$$C_{OH} = C_K = C_{KOH} \tag{13}$$

Since potassium ions do not take part in the electrochemical reactions, there should be no net flux of K^+ across interface (I) as numbered in Figure 5-1. Therefore:

Interface (I): $D_K^{eff} \nabla C_K + z_K \mu_K^{eff} C_K \nabla \Phi_e = 0$ (14)

Combining eqs. (10), (13) and (14), the governing equation for K^+ transport reduces to a first order differential equation:

$$z_K \mu_K^{eff} C_{KOH} \nabla \Phi_e + D_K^{eff} \nabla C_{KOH} = 0 \tag{15}$$

Equation (15) is substituted into eq. (9) to eliminate $\nabla \Phi_e$:

$$\nabla \cdot \left(D_{OH}^{eff} \nabla C_{KOH} \right) + z_{OH} \nabla \cdot \left(\frac{-D_K^{eff} \mu_{OH}^{eff}}{z_K \mu_K^{eff}} \nabla C_{KOH} \right) + S_{OH} = 0 \tag{16}$$

Having set the governing equation for electrolyte concentration C_{KOH} by eq. (16), eq. (15) is used to solve for the electrolyte potential, Φ_e.

The carbon phase potential in the catalyst layers and diffusion layers are governed by Ohm's law [18]:

$$\nabla \cdot \left(\sigma_C \nabla \Phi_C \right) - R_{ox} + R_{red} = 0 \tag{17}$$

where subscript C represents the carbon phase.

5.2.2 Boundary conditions

The boundary conditions at interfaces (I) through (VI) for all the variables are summarized in Table 5-1 and explained as follows:

Electrolyte potential (Φ_e) and Hydroxide potassium concentration (C_{KOH}):

At steady state, the OH^- ions generated in the CCL are transported to and then consumed in the ACL. Therefore, there is no net flux of OH^- through interface (I):

Interface (I): $z_{OH}\mu_{OH}^{eff}C_{KOH}\nabla\Phi_e + D_{OH}^{eff}\nabla C_{KOH} = 0$ (18)

Combining this restriction with eq. (15), the following boundary conditions is concluded at interface (I):

Interface (I): $\nabla\Phi_e = 0,\ \nabla C_{KOH} = 0$ (19)

The boundary conditions of eq. (19) can also be physically proved by considering two possible scenarios, illustrated in Figure 5-2: (*i*) If the slopes of Φ_e and C_{OH} distribution have the same signs at interface (I), as in Figure 5-2(a), the concentration gradient drives both K^+ and OH^- to the right, while the electrical field drags K^+ to the right and OH^- to the left. Thus, eq. (18) is satisfied, but eq. (15) is not; (*ii*) If Φ_e and C_{OH} have opposite slopes, as in Figure 5-2(b), this configuration fulfills eq. (15) but not eq. (18). Therefore, the only possible boundary conditions at this interface are $\nabla\Phi_e = 0$ and $\nabla C_{KOH} = 0$.

The two boundary conditions in eq. (19) are not independent, however. If one is fulfilled, so will be the other through eq. (15). Therefore, another boundary condition must be set at this boundary:

Interface (I): $C_{KOH} = \text{constant}$

This reflects the assumption of a constant KOH concentration in the reservoir.

Ethanol:

The boundary condition of ethanol at interface (I) is similar to that of KOH. A constant ethanol concentration is assumed because of a stable supply from the large fuel reservoir. At cathode side, because of the volatility of ethanol, its evaporation into the ambient must be considered. The mass transfer coefficient at this interface is taken from the natural convection correlations on a horizontal surface facing up [19]:

Interface (VI): $Sh = 0.54\left(Gr \cdot Sc\right)^{0.25}$ (20)

where the Grashof number is:

$$Gr = \frac{g\rho\left|\Delta\rho\right| L_{ch}^3}{\mu^2}$$

where L_{ch} is the characteristic length, chosen to be 2 cm, and μ is viscosity.

Oxygen:

Since the solubility of oxygen in the liquid phase is much lower than that in the gas phase, a zero oxygen mass flux is considered at interface (IV). At interface (VI), a natural convection mass transfer similar to ethanol is considered and the same correlation as eq. (20) is used.

Carbon phase potential:

The carbon phase potential is set to zero at interface (I) and to V_{cell} at interface (VI). Thus, the cell voltage is fixed:

$$V_{cell} = \Phi_{\text{C},c}\left(\text{L}\right) - \Phi_{\text{C},a}\left(0\right) \quad (21)$$

where subscript *a* and *c* stand for anode and cathode, respectively.

At interface (III) and (IV), since there is no net current flux, the corresponding boundary conditions are specified:

$$\nabla \Phi_{\mathrm{C}} = 0 \tag{22}$$

5.2.3 Electrochemical kinetics

Electrochemical reaction rates in eqs (5), (6) and (12) are determined by the electrochemical kinetics model. The overpotentials driving electrochemical reactions are defined as [18]:

Anode: $\eta_a = \Phi_{\mathrm{C},a} - \Phi_e - U_{\mathrm{E}}$ (23)

Cathode: $\eta_c = \Phi_{\mathrm{C},c} - \Phi_e - U_{\mathrm{O}}$ (24)

where U refers to the thermodynamic equilibrium voltage and sets to be -0.766 V and 0.401 V for U_{E} and U_{O}, respectively.

The electrochemical kinetics adopted in this study follows the model proposed by Bahrami and Faghri [13]. The EOR rate is approximated by the Tafel model:

$$R_{ox} = J_{0,\mathrm{E}}^{ref} \left(\frac{C_{\mathrm{E},a}^{\mathrm{CL}}}{C_{\mathrm{E},a}^{ref}} \right)^{\gamma_a} \exp\left(\frac{\alpha_a \eta_a F}{R_u T} \right) \tag{25}$$

where the superscripts CL and *ref* denote the catalyst layer and the reference value, respectively. $J_{0,\mathrm{E}}^{ref}$ is the anode exchange current density, α is the transfer coefficient, η is the overpotential as defined in eq. (23), F is Faraday's constant, R_u is the universal gas constant, T is the temperature and γ_a is the order of oxidation reaction rate, determined by the ethanol concentration in the ACL:

$$\gamma_a = \begin{cases} 0 & C_{\mathrm{E},a}^{\mathrm{CL}} > C_{\mathrm{E},a}^{ref} \\ 1 & C_{\mathrm{E},a}^{\mathrm{CL}} \le C_{\mathrm{E},a}^{ref} \end{cases} \tag{26}$$

At the cathode, the ORR rate is also modeled by following the Tafel kinetics:

$$R_{red} = J_{0,O}^{ref} \left(\frac{C_{O,c}^{CL}}{C_{O,c}^{ref}} \right)^{\gamma_c} \exp\left(\frac{\alpha_c \eta_c F}{R_u T} \right) \tag{27}$$

where

$$\gamma_c = \begin{cases} 0 & C_{O,c}^{CL} > C_{O,c}^{ref} \\ 1 & C_{O,c}^{CL} \le C_{O,c}^{ref} \end{cases} \tag{28}$$

5.2.4 Physical properties

Ethanol and oxygen diffusion coefficients are determined as [18, 20]:

$$D_{\mathrm{E}} = \left(-5.7939 x_{\mathrm{E}}^3 + 11.696 x_{\mathrm{E}}^2 - 6.1678 x_{\mathrm{E}} + 1.3679\right) \times 10^{-9} \tag{29}$$

$$D_{\mathrm{O}} = 1.775 \times \left(\frac{T}{273.15}\right)^{1.823} \times 10^{-5} \tag{30}$$

where x_{E} is the molar fraction of ethanol. It is calculated from ethanol and KOH concentrations based on ideal solution approximation.

The diffusion coefficients of ions in a binary KOH electrolyte solution are expressed as [12, 21]:

$$D_{\mathrm{K}} = \frac{D_{\mathrm{KOH}}}{2\left(1 - t_{\mathrm{K}}\right)} \tag{31}$$

$$D_{\mathrm{OH}} = \frac{D_{\mathrm{KOH}}}{2\left(1 - t_{\mathrm{OH}}\right)} \tag{32}$$

where D_{KOH} is the diffusion coefficient of KOH in water, and t_{OH} and t_{K} are the transference numbers of OH^- and K^+, respectively.

The KOH diffusion coefficient at 313K is obtained from the experimental data reported in [22] and fitted to a polynomial function:

$$\begin{aligned} D_{\mathrm{KOH}} = {} & 2.805 \times 10^{-9} - 1.808 \times 10^{-11} C_{\mathrm{OH}}{}^{0.5} + 6.333 \times 10^{-13} C_{\mathrm{OH}} \\ & -4.820 \times 10^{-15} C_{\mathrm{OH}}{}^{1.5} + 1.066 \times 10^{-17} C_{\mathrm{OH}}{}^{2} \end{aligned} \tag{33}$$

The transference numbers t_{OH} and t_{K} are assumed to be independent of the electrolyte concentration. Therefore, they are calculated based on an infinite dilute KOH solution:

$$t_{\mathrm{OH}} \cong t_{\mathrm{OH}}^{0} = \frac{\lambda_{\mathrm{OH}}^{0}}{\lambda_{\mathrm{OH}}^{0} + \lambda_{\mathrm{K}}^{0}} \tag{34}$$

$$t_{\mathrm{K}} \cong t_{\mathrm{K}}^{0} = \frac{\lambda_{\mathrm{K}}^{0}}{\lambda_{\mathrm{OH}}^{0} + \lambda_{\mathrm{K}}^{0}} \tag{35}$$

where λ^0 is the limiting ionic equivalent conductance of an ion [23].

The electrical mobility of ion *i* is expressed as [24]:

$$\mu_i = \frac{\lambda_i}{|z_i| F} \tag{36}$$

where λ_i is the equivalent ionic conductivity of ion *i*, and is related to the equivalent conductance of the KOH solution Λ_{KOH} by:

$$\lambda_i = t_i \Lambda_{\mathrm{KOH}} \tag{37}$$

Λ_{KOH} is calculated through:

$$\Lambda_{\mathrm{KOH}} = \frac{\kappa_{\mathrm{KOH}}}{C_{\mathrm{KOH}}} \tag{38}$$

where κ_{KOH} is the specific ionic conductivity of aqueous KOH solution, and obtained as [25]:

$$\begin{aligned} \kappa_{\mathrm{KOH}} &= -0.2041 C_{\mathrm{KOH}} - 0.28 \times 10^{-6} {C_{\mathrm{KOH}}}^{2} + 0.5332 \times 10^{-3} C_{\mathrm{KOH}} \cdot T \\ &+ 20.72 \frac{C_{\mathrm{KOH}}}{T} + 0.1043 \times 10^{-9} {C_{\mathrm{KOH}}}^{3} - 0.3 \times 10^{-10} {C_{\mathrm{KOH}}}^{2} \cdot T^{2} \end{aligned} \tag{39}$$

The Finite Volume Method (FVM) is employed to solve the coupled governing equations [26]. An iteration based on the bisection method is implemented to solve for $\Phi_e(0)$ in eq. (15) and achieve the overall charge balance in the computation domain, i.e.:

$$I_{cell} = \int_{\mathrm{ACL}} R_{ox} = \int_{\mathrm{CCL}} R_{red} \tag{40}$$

5.3 Results and discussion

Using the model described above, numerical simulations are conducted with different fuel cell parameters to study their effects on mass transport processes and cell performance.

First, the proposed model is calibrated against the experimental results of [2]. The calibrated parameters are listed in Table 5-2 with asterisk. All predictions in this study are based on the values provided in Table 5-2 unless otherwise specified. The cell temperature is 313 K. Concentrations of ethanol and KOH in the reservoir are 1M and 2.4 M, respectively. The cathode is exposed to ambient air. Figure 5-3 shows the comparison between the present numerical prediction and the experiment values of [2].

In the following sections, if not otherwise specified, the concentration of ethanol and KOH are both kept at 1 M. Cell temperature is 313K and cathode is exposed to ambient air.

5.3.1 Effect of ethanol and potassium hydroxide concentration on the cell performance

Figure 5-4 shows the polarization curves for various reservoir ethanol concentrations from 0.5 M to 2 M. $C_{KOH,res}$ is kept at 1 M. It is seen that ethanol concentration has a great impact on the maximum power density. With 0.5 M ethanol in reservoir, the highest power density is 14.5 mW/cm^2, while 2 M ethanol in reservoir enhances the highest power density to 40.5 mW/cm^2.

The concentration of KOH influences the cell performance by changing the electrolyte conductivity in the separator and catalyst layers. Figure 5-5 shows the polarization curves for various reservoir KOH concentrations ranging from 0.1 M to 2 M. Ethanol concentration in the reservoir is kept at 1 M. When KOH concentration is 0.1 M, maximum power density is 21.9 mW/cm^2, whereas with 2 M KOH the maximum power density is 25.9 mW/cm^2. Figure 5-4 and Figure 5-5 also show that the effect of KOH and ethanol concentrations is more significant in the vicinity of maximum power density.

In order to further investigate the effect of the electrolyte concentration on the cell performance, Figure 5-6 decomposes overpotential into three parts: (*i*) anode overpotential that drives the EOR, (*ii*) ohmic overpotential over electrolyte, and (*iii*) cathode overpotential that drives the ORR. It is seen that in order to reach higher current density, overpotential caused by ohmic resistance increases and higher anode and cathode overpotentials are needed. With higher KOH concentration, hence lower ionic resistance, the ohmic overpotential is largely alleviated. It is also seen that the overpotential over anode and cathode are at the same level at low current densities, while at higher current densities anode overpotential dominates because ethanol transport is more limited, which will be discussed below.

5.3.2 Mass transport

Concentration of reactants and reaction rates are interconnected, as evident by eqs. (25) and (27). While higher reaction rates lead to a faster consumption of reactants, lack of reactants decelerate the reaction rates. The distribution of ethanol concentration is a result of this relation. Figure 5-7 shows the distribution of ethanol concentration under different cell potentials. In the ADL, ethanol distribution is nearly linear and C_E decreases toward the ACL where it is consumed. With the decrease in cell voltage, current density increases, resulting in faster EOR and lower ethanol concentration in the ACL. When the cell voltage is 0.1 V, the ethanol in the ACL is nearly depleted, causing the fuel cell to operate in the mass transport limit condition.

Figure 5-8 shows the distribution of oxygen concentration in the CCL and the CDL. Since the diffusion coefficient of oxygen in the gas phase is much higher than in liquid phase, the separator is nearly impermeable to oxygen. Infinitesimal oxygen is available in the separator with a zero oxygen concentration gradient at interface IV. In the CCL and CDL, the oxygen distribution is almost linear. However, the decrease in oxygen concentration in the cathode from the ambient is

less than 1 M in all cases. The oxygen concentration never drops to zero in the CCL, even under very low cell voltage. This means that the mass limit condition is caused by the anode mass transport rather than the cathode.

Figure 5-9(a) shows the normalized reaction rate distributions in the ACL. The reaction rate in the ACL decreases along the *x*-direction. This is because the reaction rate directly scales with the ethanol concentration. Furthermore, it is evident that the non-linearity of R_{ox} increases with higher current density. This is consistent with the trend of ethanol distribution in the ACL shown in Figure 5-7. Similar phenomenon was also proved by the result of [27]. Figure 5-9(b) shows the ORR rate in the CCL. Unlike the reaction rate distribution in ACL, the reaction rate is higher where the reactant concentration is lower (smaller *x*). To explain this, another factor that influences the reaction rate other than reactant concentration should be considered, the overpotential that drives the electrochemical reaction. As defined by eq. (24), cathode overpotential is determined by carbon phase potential, electrolyte potential and equilibrium potential of oxygen reduction in alkaline environment. Because the conductivity of carbon is very high, the potential drop in carbon phase is usually very small, in the order of 10^{-2} mV, therefore the difference in overpotential at different parts of the catalyst layer is mainly governed by electrolyte potential. Therefore, the distribution of electrolyte potential needs to be analyzed.

Figure 5-10 shows the electrolyte potential distribution. Because the level of electrolyte potential varies in a wide range under different cell voltages, to compare them, all of the values are subtracted by the electrolyte potential at the center point of the separator, $\Phi_e(x = L/2)$. It shows that the potential drop in the separator layer is nearly linear, while in the CCL, a significant non-linear drop along *x* is observed. This is mainly because ions can only be transported in the liquid phase electrolyte while liquid saturation in the CCL is only 0.2. This leads to a larger ion

concentration change, and in turn influences the electrolyte potential. The large electrolyte potential gradient in the CCL results in a higher overpotential in the CCL further away from interface VI (smaller *x*) , providing more driving force for the ORR and explaining the higher reaction rate, as shown in Figure 5-9.

The movements of ions in the electrolyte are governed by electrical field and the electrolyte concentration, as evident by eqs. (15) and (16). Figure 5-11 shows the KOH concentration distribution under difference cell voltages. At the left boundary, KOH concentration is kept constant by the reservoir supply. OH^- ions are generated in the CCL, causing a lift in the local electrolyte concentration. They are then driven by the concentration gradient and electrical field to the ACL where they are consumed. With a lower cell voltage, hence a higher current density, more OH^- ions are generated as shown by the higher local KOH concentration in the CCL. This also means that in the CCL and CDL, the K^+ concentration is the highest. At the same time, these layers are closer to air supply, which makes these places more vulnerable to carbonate precipitation.

As discussed above, the movements of ions are driven by both diffusion and migration. Figure 5-12(a) shows the molar flux of K^+ ion by migration and diffusion. Diffusion and migration have the same magnitude but opposite signs in the ACL, separator and CCL, which leads to a zero net flux of K^+ ion. Figure 5-12(b) shows the molar flux of OH^- ion. In comparison to K^+ ions, the molar fluxes of OH^- ion caused by diffusion and migration have the same signs. This means that concentration gradient and electrical field drives the OH ion in the same direction, from cathode to anode. At the same time, the magnitude of both flux are almost the same. Thus, neither can be neglected in simulation models. This can be explained by inspecting eq. (16), where the first and second terms on the left side represent the local gradient of the diffusion and migration flux,

respectively. In an infinite solution, the mobility of the ions is related to their diffusivities by the Einstein relation [28]:

$$\mu = \frac{DF}{k_B T N_A} \tag{41}$$

Thus, the coefficient in the second term of eq. (16) would equal the coefficient in the first term. Another ion transfer characteristic observed from Figure 5-12 is that the flux distribution in the ACL shows more non-linearity than in the CCL at low cell voltages. This is because the ion flux is directly influenced by the reaction rate, which deviates from linear distribution a lot more in the ACL than in the CCL at low cell voltages, as shown in Figure 5-9.

5.3.3 Fuel utilization rate

Not all the ethanol transported from the fuel reservoir is used to generate electricity. Some evaporated through interface (VI) into the ambient and is thus wasted, while the rest reacts in the ACL. As evident in Figure 5-7 at interface (VI), there exists a concentration gradient for ethanol, creating a net flux of ethanol exiting the system into ambient. This ethanol flux decreases with a lower cell voltage because of a lower ethanol concentration at interface (VI). A fuel utilization rate *u* is defined as:

$$u = \frac{I_{cell}}{4FN''_{E,vap} + I_{cell}} \tag{42}$$

Figure 5-13 shows the dependence of the fuel utilization rate on the cell voltage and fuel concentration in the reservoir. As seen for a high cell voltage (a low current density), most of ethanol remains unreacted. Thus, a high concentration of ethanol at interface (VI) results in an increase in the evaporation rate and a waste of ethanol. Fuel Utilization rate approaches 1 when the cell voltage approaches zero. In this condition, however, the power density and thermodynamic efficiency of the fuel cell is very low. Therefore, in practice an optimal working voltage should be

a balance between cell voltage, power density, efficiency and fuel utilization rate. Figure 5-13 also shows that higher ethanol concentration in reservoir leads to lower fuel utilization rate.

5.3.4 Effect of separator thickness on cell performance

The variation of the cell current versus the separator thicknesses for a constant cell voltage is shown in Figure 5-14. It shows that for a constant cell voltage the fuel cell with a thinner separator has higher current density and the dependence is almost linear. This is because thickening of the separator linearly increases ohmic resistance of the fuel cell. Another phenomenon observed is that the variation of current density with different separator thickness is larger when V_{cell} is 0.3 V. When the cell voltage is either very high, such as 0.5 V, or very low, such as 0.1 V, the current density is not sensitive to separator thickness. This is because at higher voltage, current density is mainly controlled by electrochemical kinetics, whereas at low voltage, the cell is mass transport controlled. In both situations, electrolyte conductance plays a minor role in current output. It should be noted that in an actual cell, the optimal separator thickness is also influenced by other factors, such as mechanical strength, catalyst migration, etc. It is not always true that a thinner separator leads to a higher current density.

5.4 Conslusions

A physical model is developed to investigate the operation of a PMF-ADEFC. Details on mass and charge transport are obtained for a better understanding of the operational principle and achieving the optimal fuel cell design. The following conclusions are made upon analyzing the simulation results:

(*i*) Concentration of ethanol influences power density greatly. With 0.5 M ethanol in the reservoir, the highest power density is 14.5 mW/cm^2 while 2 M ethanol in the reservoir enhances

the highest power density to 40.5 mW/cm^2. KOH concentration has little effect on cell performance when it is above 1M.

(*ii*) Anode and cathode kinetic overpotential contribute almost equally to the overall overpotential; overpotential caused by the ionic resistance of electrolyte is only significant when KOH concentration is as low as 0.1M.

(*iii*) Diffusion and migration are equally important in driving ion transport in the electrolyte.

(*iv*) The current density distribution in the anode and cathode catalyst layers keeps non-uniform due to two different reasons. In the anode it is caused by the ethanol concentration gradient, whereas in the cathode it is because of the electrolyte potential gradient. Current density distribution in the anode catalyst layer shows stronger non-linearity at low cell voltages;

(*v*) Variation of current density with different separator thickness' is larger when V_{cell} = 0.3 V because electrolyte conductance plays a major role in current output around this potential range.

Nomenclature

C	Molar concentration, mol m^{-3}
D	Diffusivity, m^2 s^{-1}
F	Faraday constant, 96485.3415 Coulomb mol^{-1}
Gr	Grashof number
I	Current density, A m^{-2}
J_0	Exchange current density, A m^{-3}
k_B	Boltzmann's constant, J K^{-1}
L_{ch}	Characteristic length, m
N''	Molar flux, mol m^{-2} s
N_A	Avogadro constant, mol^{-1}
P	Power density, mW cm^{-2}
R	Reaction rate, A m^{-3}
R_u	Universal gas constant, 8.31446 J mol^{-1} K^{-1}
s	Liquid saturation
S	Source term
Sc	Schmidt number
Sh	Sherwood number
t	transference number
T	Temperature, K
u	Fuel utilization rate
U	Thermodynamic equilibrium voltage, V
V	Voltage, V

x Coordinate, m, or molar fraction

z Charge number of ions

Greek

α_a Oxidation transfer coefficient

α_c Reduction transfer coefficient

γ Order of reaction

ε Porosity

η Overpotential, V

κ Specific conductivity, S m^{-2}

λ^0 Limiting ionic equivalent conductance, $m^2\ \Omega^{-1}\ eq^{-1}$

λ *E*quivalent ionic conductivity, $m^2\ \Omega^{-1}\ eq^{-1}$

Λ Equivalend conductance, $m^2\ \Omega^{-1}\ eq^{-1}$

μ Mobility, $m^2\ S^{-1}\ V^{-1}$; Viscosity, kg $m^{-1}\ s^{-1}$

ρ Density, kg m^{-3}

σ Conductivity, S m^{-1}

τ Constant coefficient in Bruggeman correction

Φ Potential, V

Superscripts

CL Catalyst layer

eff Effective value

ref Reference value

Subscripts

a Anode

am Ambient condition

c Cathode

C Carbon phase

CCL Cathode catalyst layer

CDL Cathode gas diffusion layer

e Electrolyte

E Ethanol

g Gas phase

i Species i

K K^+ ion

KOH Potassium hydroxide

l Liquid phase

max Maximum value

min Minimum value

O Oxygen

OH OH^- ion

ox Oxidation

red Reduction

res reservoir

w Water

vap Vaporization

References

[1] E.H. Yu, U. Krewer, K. Scott, Principles and Materials Aspects of Direct Alkaline Alcohol Fuel Cells, Energies. 3 (2010) 1499–1528. doi:10.3390/en3081499.

[2] R. Zhang, J. Pope, Y. Pan, Permselective Membrane-Free Direct Fuel Cell and Components Thereof, US20110123902 A1, 2011.

[3] Y.S. Li, T.S. Zhao, Z.X. Liang, Effect of Polymer Binders in Anode Catalyst Layer on Performance of Alkaline Direct Ethanol Fuel Cells, J. Power Sources. 190 (2009) 223–229. doi:10.1016/j.jpowsour.2009.01.055.

[4] Y.S. Li, T.S. Zhao, Z.X. Liang, Performance of Alkaline Electrolyte-Membrane-Based Direct Ethanol Fuel Cells, J. Power Sources. 187 (2009) 387–392. doi:10.1016/j.jpowsour.2008.10.132.

[5] S.J. Lue, W.H. Pan, C.M. Chang, Y.L. Liu, High-Performance Direct Methanol Alkaline Fuel Cells Using Potassium Hydroxide-Impregnated Polyvinyl Alcohol/carbon Nano-Tube Electrolytes, J. Power Sources. 202 (2012) 1–10. doi:10.1016/j.jpowsour.2011.10.091.

[6] R. Jamard, A. Latour, J. Salomon, P. Capron, A. Martinent-Beaumont, Study of Fuel Efficiency in a Direct Borohydride Fuel Cell, J. Power Sources. 176 (2008) 287–292. doi:10.1016/j.jpowsour.2007.10.036.

[7] M.M. Mench, Fuel Cell Engines, John Wiley & Sons, Hoboken, NJ, 2008. doi:10.1002/9780470209769.

[8] A. Verma, S. Basu, Direct Use of Alcohols and Sodium Borohydride as Fuel in an Alkaline Fuel Cell, J. Power Sources. 145 (2005) 282–285. doi:10.1016/j.jpowsour.2004.11.071.

[9] A. Verma, S. Basu, Experimental Evaluation and Mathematical Modeling of a Direct Alkaline Fuel Cell, J. Power Sources. 168 (2007) 200–210. doi:10.1016/j.jpowsour.2007.02.069.

[10] I. Sprague, P. Dutta, Role of the Diffuse Layer in Acidic and Alkaline Fuel Cells, Electrochim. Acta. 56 (2011) 4518–4525. doi:10.1016/j.electacta.2011.02.060.

[11] J.H. Jo, S.C. Yi, A Computational Simulation of an Alkaline Fuel Cell, J. Power Sources. 84 (1999) 87–106.

[12] J.H. Jo, S.K. Moon, S.C. Yi, Simulation of Influences of Layer Thicknesses in an Alkaline Fuel Cell, J. Appl. Electrochem. 30 (2000) 1023–1031. doi:10.1023/A:1004046721157.

[13] H. Bahrami, A. Faghri, Multi-Layer Membrane Model for Mass Transport in a Direct Ethanol Fuel Cell Using an Alkaline Anion Exchange Membrane, J. Power Sources. 218 (2012) 286–296. doi:10.1016/j.jpowsour.2012.06.057.

[14] H. Bahrami, A. Faghri, Start-up and Steady-State Operation of a Passive Vapor-Feed Direct Methanol Fuel Cell Fed with Pure Methanol, Int. J. Hydrogen Energy. (2012).

[15] H. Bahrami, A. Faghri, Water Management in a Passive DMFC Using Highly Concentrated Methanol Solution, J. Fuel Cell Sci. Technol. 8 (2011) 021011. doi:10.1115/1.4002315.

[16] Z.X. Liang, T.S. Zhao, J.B. Xu, L.D. Zhu, Mechanism Study of the Ethanol Oxidation Reaction on Palladium in Alkaline Media, Electrochim. Acta. 54 (2009) 2203–2208. doi:10.1016/j.electacta.2008.10.034.

[17] A. Faghri, Y. Zhang, Transport Phenomena in Multiphase Systems, Academic Press, 2006. doi:10.1016/0167-2738(81)90101-6.

[18] H. Bahrami, A. Faghri, Transient Analysis of a Passive Direct Methanol Fuel Cell Using Pure Methanol, J. Electrochem. Soc. 157 (2010) B1762. doi:10.1149/1.3491449.

[19] A. Faghri, Y. Zhang, Advanced Heat and Mass Transfer, Global Digital Press, Columbia, MO, 2010.

[20] L. Zhang, Q. Wang, Y.C. Liu, L.Z. Zhang, On the Mutual Diffusion Properties of Ethanol-Water Mixtures, J. Chem. Phys. 125 (2006). doi:10.1063/1.2244547.

[21] J. Koryta, J. Dvorak, L. Kavan, Principles of Electrochemistry, 2nd ed., John Wiley & Sons, 1993.

[22] R.N. Bhatia, K.E. Gubbins, R.D. Walker, Mutual Diffusion in Concentrated Aqueous Potassium Hydroxide Solutions, Trans. Faraday Soc. 64 (1968) 2091–2099.

[23] S. Quist, L. Marshall, A.S. Quist, L. William, Assignment of Limiting Equivalent Conductances for Single Ions to 400°, 69 (1966) 2984–2987.

[24] A.J. Bard, L.R. Faulkner, Electrochemical Methods: Fundamentals and Applications, 2nd ed., John Wiley & Sons, 2001.

[25] R.J. Gilliam, J.W. Graydon, D.W. Kirk, S.J. Thorpe, A Review of Specific Conductivities of Potassium Hydroxide Solutions for Various Concentrations and Temperatures, Int. J. Hydrogen Energy. 32 (2007) 359–364.

[26] S. V. Patankar, Numerical Heat Transfer and Fluid Flow, First, CRC Press, New York, 1980.

[27] H. Bahrami, A. Faghri, Exergy Analysis of a Passive Direct Methanol Fuel Cell, J. Power Sources. 196 (2011) 1191–1204.

[28] J. Newman, K.E. Thomas-Alyea, Electrochemical Systems, 3rd ed., John Wiley & Sons, Hoboken, NJ, 2004.

Table 5-1 Boundary conditions

Variables	Boundary	Boundary condition
Ethanol, C_E	Reservoir-ADL (I)	C_E = constant
	CDL - Ambient (VI)	Eq. (20)
Oxygen, C_O	CDL - Ambient (VI)	Eq. (20)
	Separator – CCL (IV)	$\nabla C_O=0$
Electrolyte concentration, C_{KOH}	Reservoir-ADL (I)	C_{KOH} = constant
	CDL - Ambient (VI)	$\nabla C_{KOH}=0$
Electrolyte potential, Φ_e	Reservoir-ADL (I)	$\nabla \Phi_e=0$
	CDL - Ambient (VI)	$\nabla \Phi_e=0$
Cathode carbon phase potential , $\Phi_{C,c}$	Separator-CCL (IV)	$\nabla \Phi_{C,c}=0$
	CDL-Ambient (VI)	$\nabla \Phi_{C,c}=V_{cell}$
Anode carbon phase potential, $\Phi_{C,a}$	Reservoir-ADL (I)	$\Phi_{C,a}=0$
	ACL-Separator (III)	$\nabla \Phi_{C,a}=0$

Table 5-2 Simulation parameters

Thickness	L_{ADL}	0.26	mm
	L_{ACL}	0.04	mm
	L_{SEP}	0.40	mm
	L_{CDL}	0.04	mm
	L_{CCL}	0.26	mm
Porosity	ε_a	0.7	
	$\varepsilon_{\mathrm{SEP}}$	0.6	
	ε_c	0.7	
Liquid saturation	s_a	1.0	
	s_c	0.2	
Electrochemical kinetics	α_a^*	0.5	
	$J_{0,\mathrm{E}}^{ref\,*}$	2.0×10^5	$\mathrm{A/m^3}$
	$C_{\mathrm{E},a}^{ref}$	1000	$\mathrm{mol/m^3}$
	α_c^*	0.5	
	$J_{0,O}^{ref\,*}$	1.7×10^5	$\mathrm{A/m^3}$
	$C_{\mathrm{O},c}^{ref}$	41.6	$\mathrm{mol/m^3}$

*: calibrated parameters

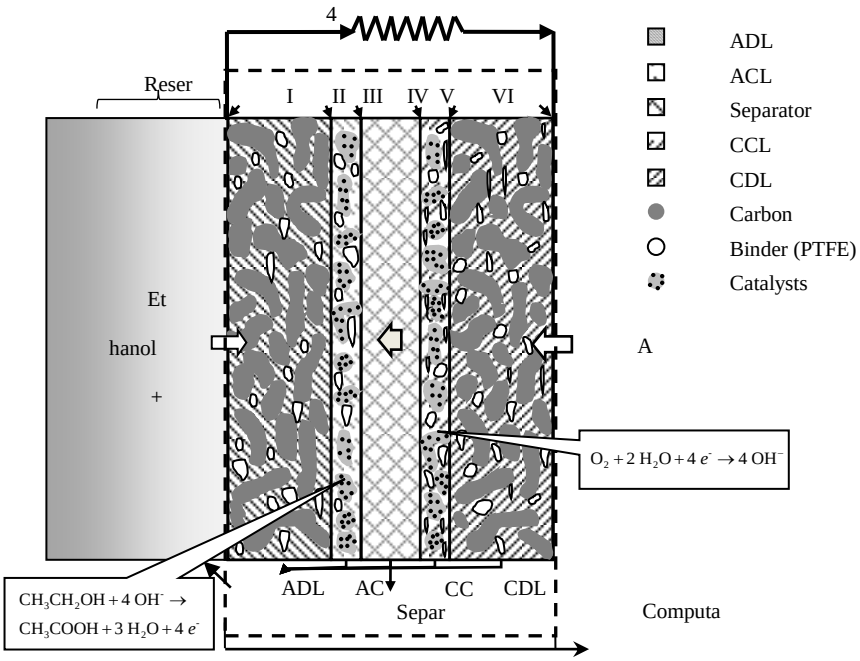

Figure 5-1 Structure of a PMF-ADEFC

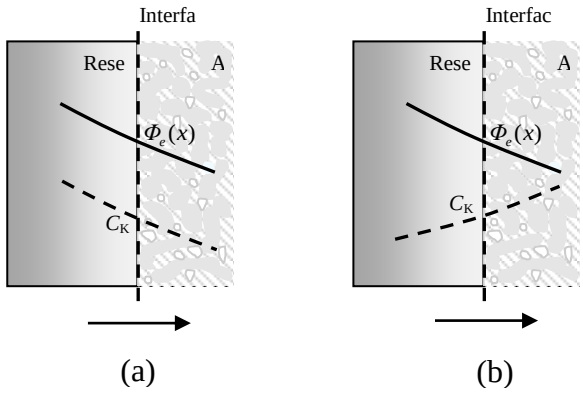

Figure 5-2 Possible scenarios of electrolyte potential and electrolyte concentration distribution at the reservoir-ADL boundary

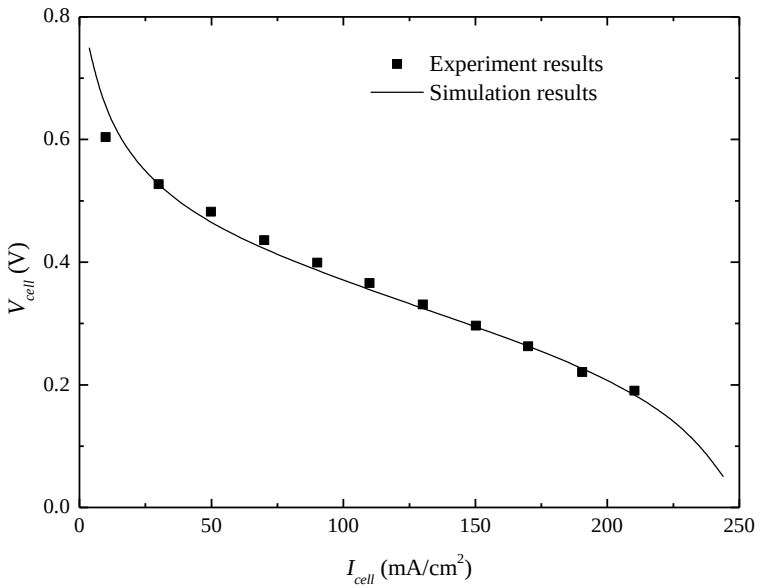

Figure 5-3 Comparison of the predictions by this study and and the experimental results of [2] ($C_{E,res}$ = 2.4 M, $C_{KOH,res}$ = 1 M, Ambient Air, 313 K)

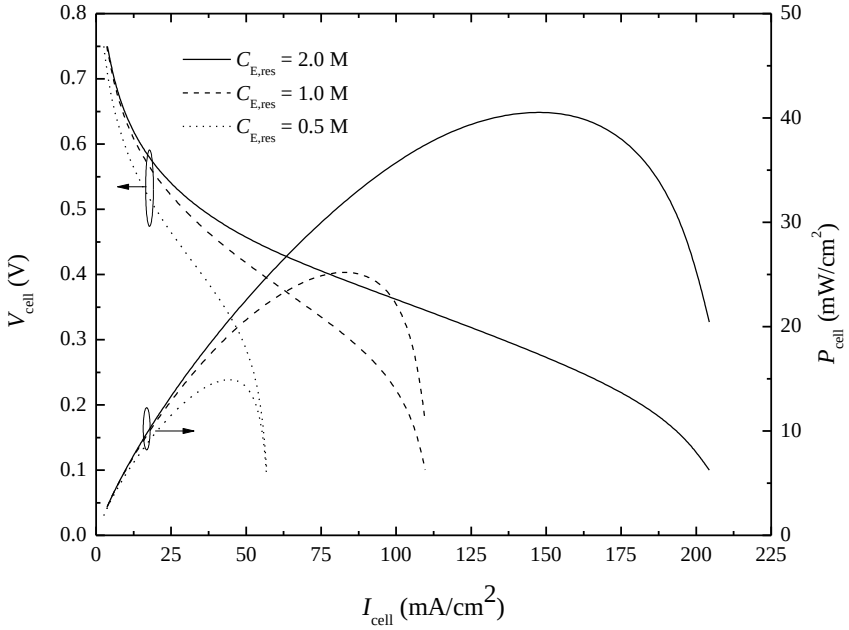

Figure 5-4 Influence of ethanol concentration on performance

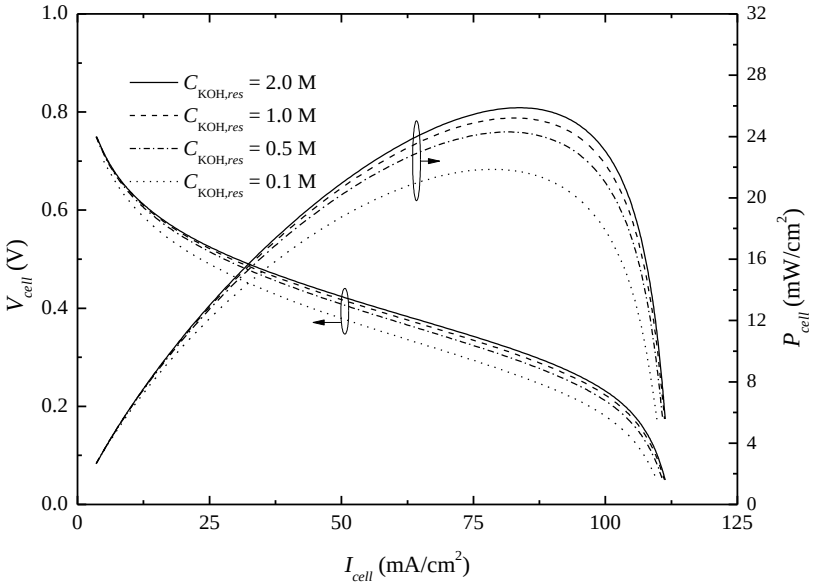

Figure 5-5 Influence of KOH concentration on polarization

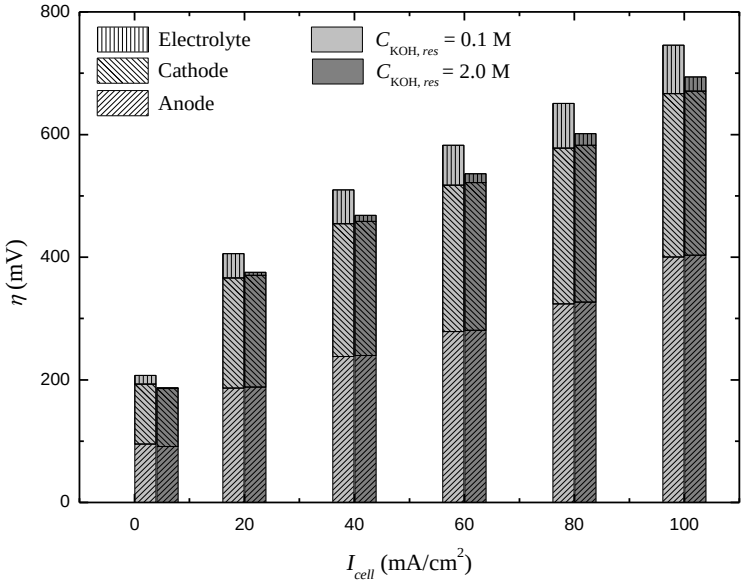

Figure 5-6 Overpotential breakdown

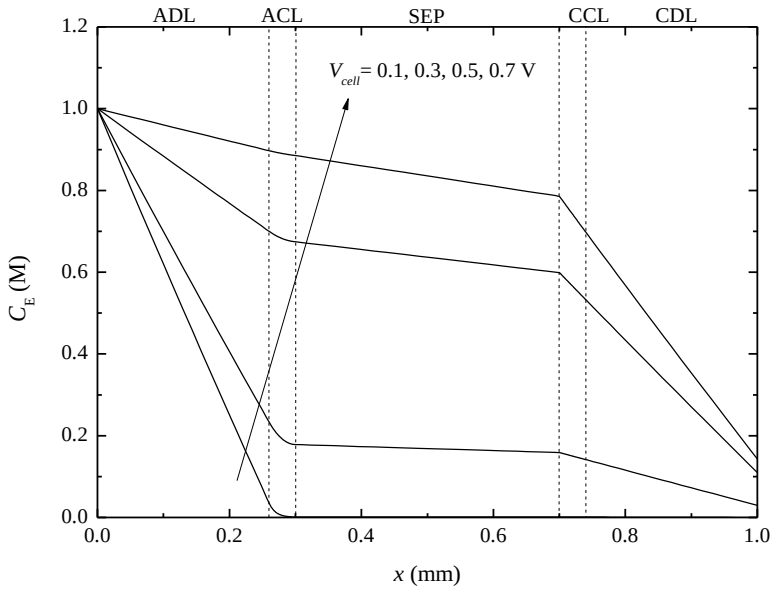

Figure 5-7 Distribution of ethanol concentration for various cell voltages

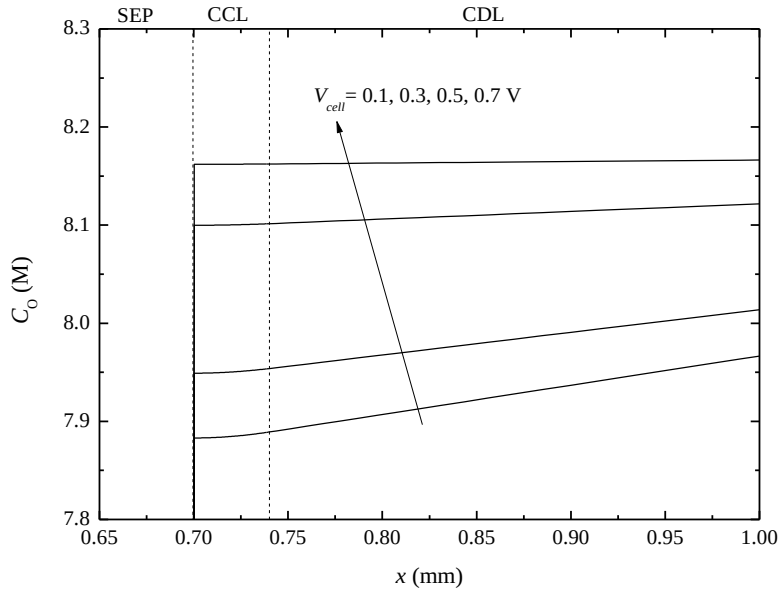

Figure 5-8 Distribution of oxygen concentration for various cell voltages

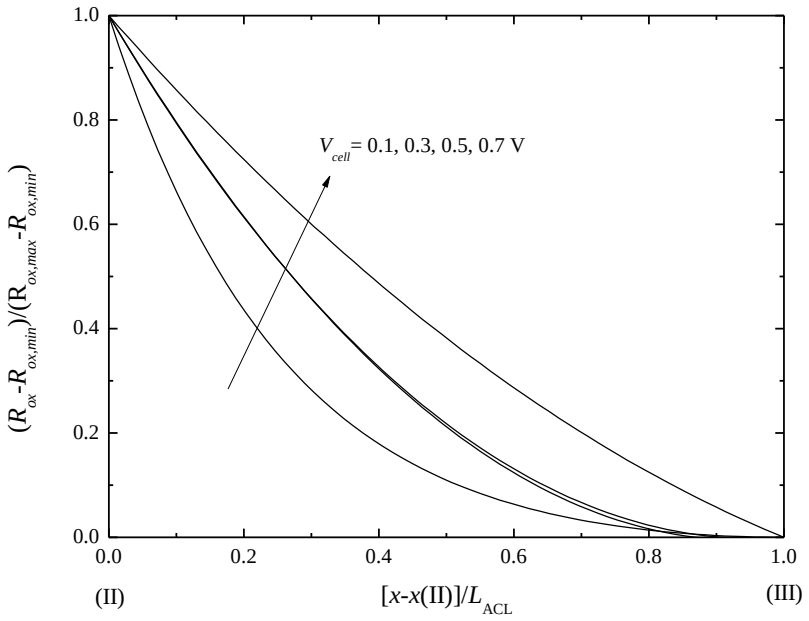

(a)

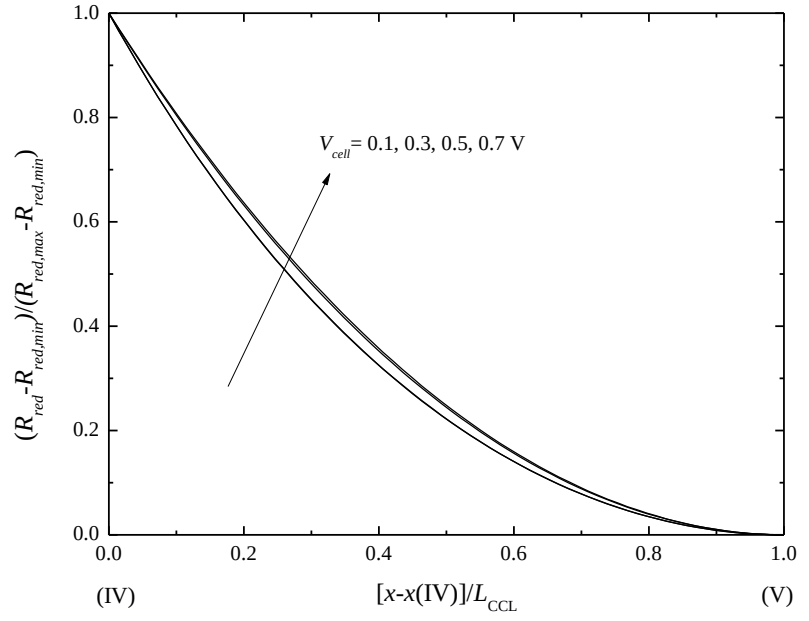

(b)

Figure 5-9 Distribution of normalized (a) oxidation reaction rate in the ACL and (b) reduction reaction rate in the CCL

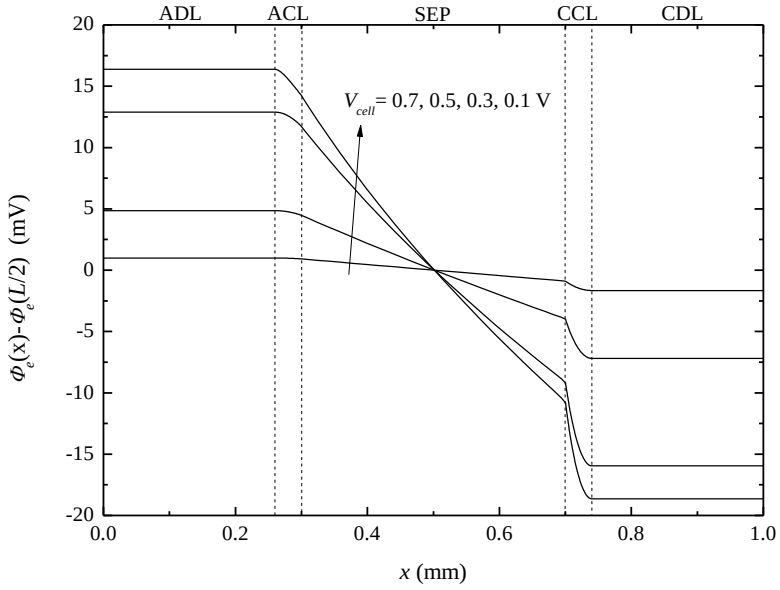

Figure 5-10 Distribution of electrolyte potential

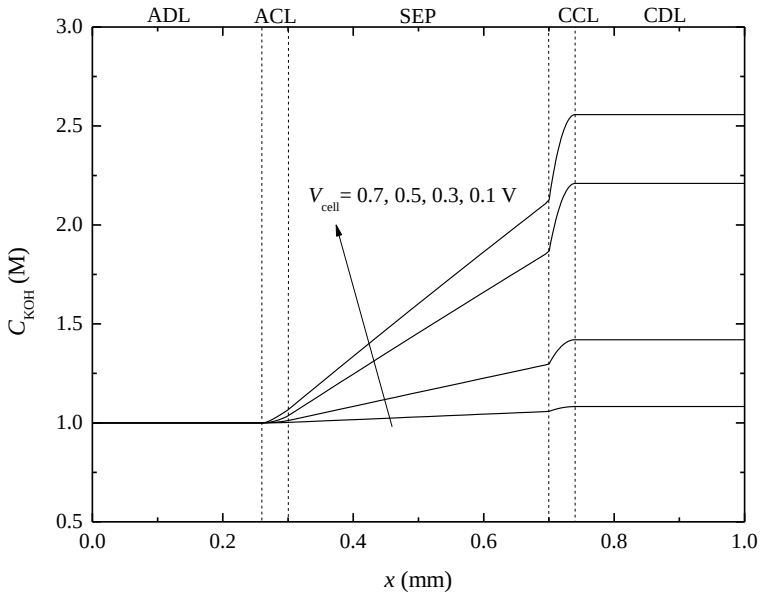

Figure 5-11 Distribution of KOH concentration

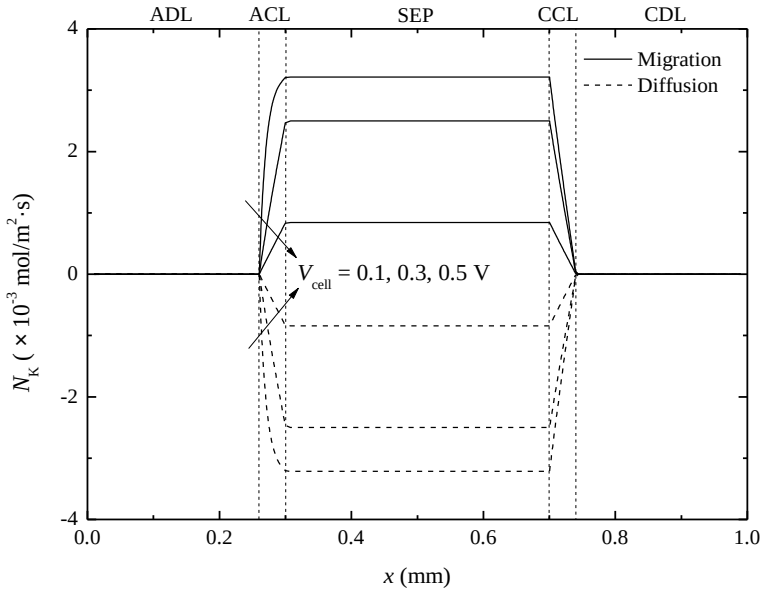

(a)

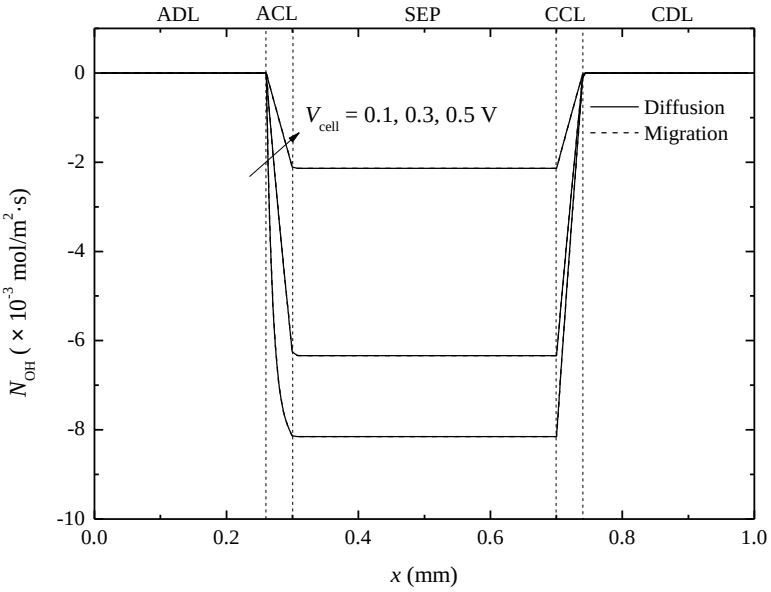

(b)

Figure 5-12 Diffusion and migration molar flux of (a) K^+ and (b) OH^- ions under various voltages

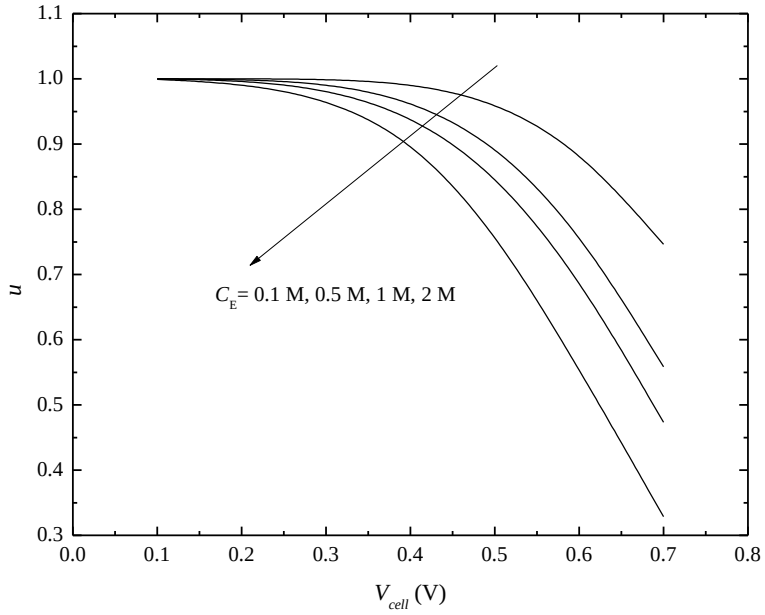

Figure 5-13 Change of fuel utilization with different cell voltage

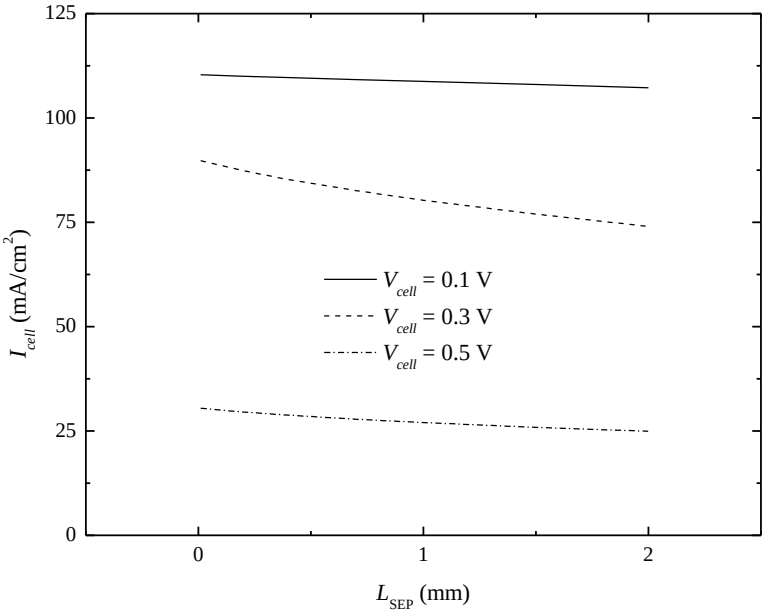

Figure 5-14 Influence of separator thickness

Chapter 6 Comparison of Alkaline Direct Ethanol Fuel Cells with and without Anion Exchange Membrane

The performance of three alkaline direct ethanol fuel cells (ADEFCs) is investigated. All three use identical anode and cathode electrodes, but one uses an anion exchange membrane (AEM) and the other two use non-permselective porous separators. Ethanol was chosen as the fuel because of its low toxicity, low carbon footage and market readiness. A direct comparison between ADEFCs with and without AEM is reported. The performance of each cell is studied under different operation conditions of temperature, reactants flow rate, ethanol and KOH concentrations. The results show that with low cost porous separator, the ADEFC can reach similar power output as those using expensive AEMs. With 1 M ethanol and 1 M KOH aqueous solution, the maximum power densities of 26.04 mW/cm^2 and 24.0 mW/cm^2 are achieved for the ADEFC employing AEM and porous separator, respectively. This proves the feasibility of replacing AEM with non-permselective separators. The results suggest that improving the cathode structure in order to provide a better oxygen supply is the key factor to enhance the performance of an anion exchange membrane free ADEFC.

6.1 Introduction

As one of the earliest fuel cell technologies that entered real applications, alkaline fuel cells (AFCs) have been used to power spacecraft since the Apollo-series missions and on space shuttles. However, they had very limited impact outside of space and naval applications. When air instead of oxygen is used as oxidant, the carbon oxide causes metal carbonate precipitation and severely hinders AFC's wider applications. In the last several years, interests in AFCs were re-established because of the progress in better anion exchange membranes (AEMs). By replacing liquid electrolyte with solid AEMs, the problem of carbonate precipitation is alleviated while the

advantages of traditional AFCs remain. These advantages include good oxygen reduction reaction (ORR) kinetics in the alkaline environment, and a wide range of low cost non-noble catalysts available in contrast to the Pt-based catalysts usually used in fuel cells operating in acidic media.

AEM is a category of polymer membranes that only allow anions, such as OH^-, to permeate through while blocking other substances including cations and electrons [1]. On the molecular level, AEMs consist of quaternized functional groups that adhere to a large polymer substrate, so the anions can move through the membrane by hopping over the functional groups [2]. Among the AFCs that using AEMs as electrolyte, some use liquid alcohol as fuel, typically ethanol, aiming at replacing the direct methanol fuel cell (DMFC) as a portable power source. Usually the fuel is an aqueous solution of ethanol and potassium hydroxide (KOH), therefore it is named alkaline direct ethanol fuel cell (ADEFC). KOH is added into the fuel to enhance reaction kinetics and the ionic conductivity of AEMs. A201-Tokuyama membrane, Pd-based catalysts for the anode and Fe-Co based catalysts for the cathode are the most commonly used materials in reported studies.

The state-of-the-art membranes still face many performance issues [3], such as low ion conductivity, poor mechanical strength, and fast performance degradation. In addition, the price of ion exchange membranes is also a financial obstacle of fuel cell systems. For example, the price for A201 Tokuyama membrane is over $\$1000/m^2$ while the research grade separator films for batteries cost only $\$20/m^2$. Although large scale production may significantly decrease the projected price, the cost of the membrane will still account for a considerate portion of the total cost of fuel cell stacks. Reports by Yang [4,5] on the cost analysis of proton exchange membrane fuel cells (PEMFCs) using hydrogen or methanol as fuels show that the price of membranes usually contributes to 8% of the manufacturing cost of a fuel cell stack.

The above issues justify the efforts to replace the AEMs with non-permselective porous separators. This is possible for the aforementioned alkaline direct liquid fuel cells (ADLFC) because: (i) The fuel is usually an alkaline aqueous solution, which is able to serve as electrolyte. (ii) The cathode catalysts for ORR in an alkaline environment are usually highly tolerant of the fuels such as ethanol. The sole function of the separator is to prevent an electronic short circuit between the anode and cathode electrodes. The permeation of ethanol and KOH through the separator is also much higher than that through AEMs [6,7]. There is a wide range of materials that can be selected for this function.

A 2011 US patent filed by Zhang et al. [8] proposed a fuel cell called a permselective membrane-free direct fuel cell. A porous PEEK (poly-etheretherketone) mesh was used as the separator. The disclosed experimental results showed that the fuel cell using ethanol as fuel could output 44 mW/cm^2 power by using ambient air as the oxidant. The patent filed by Yang et al. in 2006 [9], titled Dissolved Fuel Alkaline Fuel Cell, had a very similar structure to that in Zhang's patent [8], but it used potassium borohydride as fuel. Yang et al. [10] proposed an alkaline direct methanol fuel cell that uses a polymer fiber membrane as the separator, $LaNiO_3$/CNT as the cathode catalyst and commercial PtRu/C as the anode catalyst. The maximum power density reached 103 mW/cm^2 at 65^oC under an active operation mode. The polymer fiber membrane is electrolyte permeable. It is much cheaper than ion exchange membranes and it is widely used in NiMH batteries as the separator. A 140 hour continuous discharging test determined that cell performance degradation was caused by anode catalyst poisoning. The same group also tested similar cells with sodium borohydride as fuel which obtained a peak power density of 663 mW/cm^2 [10,11,12]. Table 6-1 summarized several recent studies on alkaline direct liquid fuel cells using

AEM or a porous separator. It shows that without AEMs, the fuel cell performance is still comparable to those using AEMs.

One concern for eliminating AEM in ADEFCs is the precipitation of carbonate, same as in traditional alkaline fuel cells. However, as reported in [8], researchers showed a successful 3746 hours operation of such a fuel cell with air as the oxidant. At the same time, a study by Naughton et al. showed that performance of AFC with flow electrolyte could be resilient to a broad range of carbonate concentrations [13].

It should be mentioned that there is another kind of low temperature fuel cell that also eliminates the using of ion exchange membranes. Laminar flow fuel cells (LFFC) takes advantage of the fact that two streams of solution in micro channel keep laminar flow and do not mix. The interface between the two streams thus serves as the ion transfer medium and therefore does not need an ion exchange membrane [14].

Although there has been works reported on ADEFCs both with and without AEMs, as reviewed above, no direct comparison between them has been reported. In this study, three identical sets of anode and cathode electrodes were fabricated. One set of the electrodes was used to assemble an ADEFC using an AEM as electrolyte. Another two sets of the electrodes were used to assemble an ADEFC using porous separators. Ethanol was chosen as the fuel because it has the advantages of low toxicity, low carbon footprint and market readiness. The performance of the fuel cells under different operation conditions were compared, including temperature, reactants flow rate, ethanol and KOH concentrations. The results prove the feasibility of replacing AEM with porous separators and provide viable direction to further improve the cell performance.

6.2 Experimental

6.2.1 Fuel Cell Assembly

Membrane/Separator Electrode Assemblies: Three sets of ADEFCs are as follows: For Cell #1, Tokuyama A201 was used as the AEM. It was soaked in 1M KOH solution for 24 hours before assembling. Anode electrode, membrane, and cathode electrode are simply pressed together (without hotpress) in the fuel cell test hardware provided by FuelCell Technology Inc. Cell #2 uses a Hydroknit® non-woven fabric from Kimberly Clark Inc. with a thickness of 0.01″. The structure of this AEM-free ADEFC assembly is shown in Figure 6-1. Cell #3 uses a cotton fabric provided by McMASTER-CARR, the thickness was 0.026″.

In this study, geometric surface areas of all fuel cells tested are 5 cm^2. Figure 6-2 shows the membrane electrode assembly of Cell #1 (left) and the separator electrode assembly of Cell #2 (right).

Anode electrodes preparation: Nickel foam obtained from MTI (EQ-bcnf-16m, purity > 99.99%) was used as the anode support. The anode electrodes were prepared by dipping the Nickel foam into catalyst ink then air-drying repeatedly. The catalyst ink is made of a commercial anode catalyst (5% Pd on carbon black, A102023-5 from Johnson Matthey Catalysts), 5 wt% of PTFE (on dry weight basis) and water that is stirred in ultrasonic bath for 30 minutes. The electrodes were air dried until their weights were stable and reached a predetermined catalyst loading. Then they were hot pressed under 300 psi and 60^oC for 15 minutes. The anode catalyst loading was 15 mg/cm^2.

Cathode electrodes preparation: The cathode electrodes were prepared by brushing the cathode ink on carbon cloth (GDL-CT from FuelCellsEtc). The cathode catalyst ink was prepared

by mixing Hypermec® 4014 from ACTA S.p.A. with 10 wt% PTFE (on dry weight basis) and water. The cathode catalyst loading was at 3.5 mg/cm^2.

6.2.2 Testing procedure

An integrated fuel cell test stand, Scribner 850C, was used to apply the load and record the current, power, internal resistance, and operating temperature of the cell. Internal resistance was measured by a current interrupt method. An aqueous solution containing ethanol and KOH was supplied by a peristaltic pump. At the cathode, 99.9% oxygen was fed with humidification and temperature control. The fuel cell fixture is heated by two electrical heating rods installed in anode and cathode fixture plates and temperature is controlled by the 850C test station. A mixed metal oxide (MMO) reference electrode (Hg|HgO|KOH, 0.098V vs. SHE), provided by Koslow Scientific Company, was placed at the inlet of anode fuel supply. The anode voltage was measured by subtracting the reference potential from the anode current collector potential. The cathode voltage was then calculated by adding the anode potential to the iR-corrected cell voltage.

All the experiments were performed with a room temperature of 24 ~ 27°C and an ambient relative humidity of 40 ~ 60%. Cell temperature was varied from 30 to 60 ^{o}C. Fuel solutions were prepared from ACS reagent grade ethanol (Sigma-Aldrich) and potassium hydroxide (Alfa Aesar) with deionized water. The ethanol concentration was varied from 1 M to 12 M. KOH concentration was varied from 1 M to 6 M. Each fuel cell was activated by continuously feeding 1 M ethanol and 1 M KOH solution to the anode with a flow rate of 0.5 ml/min, and O_2 to the cathode at 50 sccm for 10 hours. During activation, the cell voltage was set at 0.35 V. Polarization curves were obtained every 1 hour until they are repeatable.

If not otherwise specified in the experiments, ethanol concentration is 1 M, KOH concentration is 1 M, cell temperature is 60 ^{o}C, anode flow rate is 0.5 ml/min and cathode flow rate is 50 sccm.

6.3 Results and discussion

6.3.1 General performance and comparison

Figure 6-3 shows the polarization and power density curves of the three fuel cells introduced above (Cell#1-3) under the same conditions. An aqueous solution of 1 M ethanol mixed with 1 M KOH is pumped into the anode at a rate of 0.5 ml/min. Oxygen humidified at 30^{o}C is fed into the fuel cell at a rate of 50 sccm to the cathode. The cell temperature is kept constant at 60^{o}C. The maximum power density of Cell #1 which uses AEM as the electrolyte membrane reaches 26.05 mW/cm^2 at 0.28 V of cell voltage. This is at the same performance level with the cell under the same condition reported in [15] which used a similar structure and materials. For Cell #2, the maximum power density is also obtained at 0.28V, with a value of 24.0 mW/cm^2. For Cell #3, the maximum power density is obtained at 0.24V, with a value of 13.1 mW/cm^2. This result shows that by replacing AEM with a porous separator, the ADEFC performance can be maintained at the same level, but with a lower cost. It also shows that the selection of a porous separator greatly influences the cell performance. More effort should be taken to seek a better material for the separator, which has a high porosity and small thickness, but still provide enough structural support and electrical insulation. Another phenomenon observed from this figure is that at a very low cell voltage, Cell #2 provides even better current density than Cell #1, which is attributed to the better conductivity of aqueous KOH solution than the AEM.

It can be seen from Figure 6-3 that the open circuit voltages (OCV) of the three cells are 0.835V, 0.827V and 0.817V for Cell #1, 2 and 3 ,respectively. Although ethanol can crossover from the anode through the electrolyte membrane/separator and reach cathode catalyst layer (CCL) directly, the reaction of ethanol with oxygen is slow in the CCL and does not cause notable parasitic overpotential as in the direct methanol fuel cells (DMFC) or direct ethanol fuel cells

(DEFC). This is due to the use of non-Pt catalysts at the cathode which is not catalytic to ethanol oxidation and thus leads to a high OCV.

Figure 6-4 shows the iR-corrected electrode potentials for Cell #1 and #2. It can be seen that the anode electrode potentials are similar at most current density ranges for the two different cells. The cathode potential of Cell #2 dropped a little lower than Cell #1 because the cathode is more water flooded without AEM which causes less sufficient oxygen supply. Since a lower voltage causes a lower power density of the cell, efforts should be focused more on cathode improvement for the fuel cell with a porous separator to enhance the cell performance.

6.3.2 Effect of temperature

Temperature is one of the most important parameters influencing the performance of an ADEFC. Higher temperature enhances the electrochemical reaction kinetics, electrolyte conductivity and the mass transport, hence causing better power density. This is true for an ADEFC using both AEM and a porous separator. Since there are already reports on the effects of temperature on ADEFC with AEM, only the influence of temperature on Cell #2 is shown in Figure 6-5. By increasing cell temperature from 30^{o}C to 60^{o}C, maximum power density increases from 11.5 mW/cm^2 at 0.24V to 25.5 mW/cm^2 at 0.27 V. For AEM-ADEFCs, the cell temperature is usually under 60^{o}C because of the thermal stability issues of most AEMs [16]. By replacing the AEM with a porous separator, this is no longer an issue. A pressurized system is preferred to avoid vaporization of fuel to reach a higher operation temperature and a high power density.

6.3.3 Effect of reactants flow rate

Since the separators have a porous structure, it has a very limited function to prevent liquid or gas permeation. Therefore, in comparison to denser anion exchange membrane, the reactants flow rate will have a more significant influence on the cell performance. Since the current experimental

system is not pressurized, a delicate pressure balance between anode and cathode flow channel must be maintained to maintain a fully saturated separator and a proper liquid/oxygen interface in the CCL. Because the outlets of both anode and cathode flow channels are at ambient pressure, the pressure balance between the two sides can be achieved by adjusting the two streams' flow rates.

The effect of cathode oxygen flow rate, under a fixed anode flow rate of 0.5 ml/min, on the performance of all three cells is shown in Figure 6-6. The oxygen flow rate ranges between 10 to 400 ml/min. For Cell #1 and #3, the influence of oxygen flow rate is insignificant, as shown in Figure 6-6(a) and (c). For Cell #2, the maximum power density increases until oxygen flow rate reaches 100 ml/min. With higher oxygen flow rates, the higher pressure in the cathode gas channel pushes oxygen through the catalyst layers and the porous separator into anode flow channel. Large amount of gas bubbles can be observed in the anode stream with an oxygen flow rate of 400 ml/min and anode flow rate of 0.05 ml/min. This oxygen crossover decreases power density and causes a very unstable power output, which can be seen from the polarization curve at high current density. Cell #3 also use a porous separator, but because the cotton fabric is much thicker than the non-woven fabric used in Cell #2, it can prevent oxygen crossover at a higher pressure difference between anode and cathode flow channel caused by higher flow rate.

Different anode flow rates are also tested with a fixed cathode flow rate of 50 ml/min. The results are shown in Figure 6-7. As seen in Figure 6-7(a), anode flow rate has a more significant influence on Cell #1 than the cathode flow rate does. By increasing anode flow rate from 0.5 ml/min to 15 ml/min, maximum power density increases from 25.1 mW/cm^2 at 0.31 V to 29.7 mW/cm^2 at 0.24 V. This is mainly because the anode electrode used in the cell is relatively thicker than the cathode. The thickness of the anode electrode is about 0.5 mm while for cathode it is 0.2 mm. Thus a higher flow rate is needed for a better reactant transport. At higher anode flow rates,

the fuel utilization rate is also lower, thus a recirculation system is needed in this condition to utilize unused fuel. For Cell #2, the same trend shows for a flow rate under 5 ml/min. When the flow rate increases further, cell performance deteriorates rapidly. During the experiment, a considerable amount of fuel solution can be observed in the cathode channel exit. The severe flooding of CCL blocks oxygen supply and restricts ORR rate at the cathode. For Cell #3, the anode flow rate does not show obvious negative effects until it reaches 20 ml/min. This is attributed to the thick separator providing more flow resistance between anode and cathode. This trend is a balance between the above two factors, higher flow rate provides better mass transport, but it aggravates cathode flooding.

6.3.4 Effect of reactant concentration

One severe issue for the DMFC is the methanol crossover from the anode to the cathode which causes a parasitic overpotential and fuel waste. A lot of research works have been done to deal with this problem [17,18]. However, in an ADEFC, this is no longer an issue. First of all, the non-Pt cathode electrode is not catalytic to the ethanol oxidation. Secondly, the charge transfer ions (OH^-) moves from the cathode to the anode, which brings ethanol molecules back to the anode by electromostic force [19]. Figure 6-8(a) shows the effect of ethanol concentration on the performance of Cell #1. By increasing the ethanol concentration from 1 to 3 M, the maximum power density increases from 24.0 to 31.8 mW/cm^2. Maximum power density increases slightly from 31.9 to 32.5 mW/cm^2 with an increasing ethanol concentration from 3 to 10 M. The cell voltage that achieves the maximum power density slightly increases from 0.32 to 0.36 V. When ethanol concentration further increases to 14 M, the cell performance deteriorates rapidly. One explanation is the lack of water in the fuel which is essential for the ORR in cathode. However, it should be noted that this deterioration is irreversible, even if the fuel is changed back to a lower

concentration such as 1 M ethanol, cell performance cannot recover to its original level with 1 M ethanol fuel. This means more complex mechanisms such as catalyst poisoning causing the cell performance to drop by using high concentration ethanol solutions, though some works shows that CO poisoning on Hypermec® catalysts is not a serious problem [20]. The ethanol concentration has similar effects on the performance of Cell #2, which is shown in Figure 6-8(b). From 1 M to 3 M, maximum power density increases from 24.0 to 27.9 mW/cm^2. From 3 to 8 M, power density increases from 27.9 to 29.9 mW/cm^2, but current density starts to decrease at low cell voltage. At 10 M concentration of ethanol, cell performance shows irreversible deterioration.

For ADEFCs using AEM as the electrolyte, potassium hydroxide is not mandatory for the cell to work. However, with the existence of KOH in the anode fuel stream, cell performance is greatly enhanced. This is because KOH both boosts the AEM conductivity and the ethanol oxidation kinetics. For ADEFCs without AEMs, KOH is necessary as a supporting electrolyte. Figure 6-9(a) shows the influence of KOH concentration on Cell #1. It can be seen that by increasing the KOH concentration from 1 M to 6 M, maximum power density increases from 25.5 to 29.3 mW/cm^2. With 6 M KOH, it is obvious that current density at cell voltage below 0.4 V is restricted. This can be explained by the existence of KOH occupying part of the catalyst surface, restricting both anode and cathode reaction rates. For cell #3, the effect of the KOH concentration is more significant. By increasing the KOH concentration from 1 M to 6 M, maximum power density increases from 11.4 to 24.2 mW/cm^2. This is because a higher KOH concentration directly increases its conductivity and lowers Ohmic loss in the cell.

For PEMFCs that use Nafion® as the electrolyte membrane, maintaining a hydrated membrane is crucial for the cell operation because conductivity of the Nafion® membrane greatly depends on its water content. This is why in most PEMFCs, the cathode's oxygen supply is fully humidified.

In ADEFCs, this is not the case. Figure 6-10 shows the influence of cathode oxygen humidity on cell performance in Cell #1. It shows that with higher oxygen humidity, cell performance is actually impaired. Although water is essential for ORR in an alkaline environment, the water permeated through AEM from the anode to the cathode is already enough. The results for AEM-free ADEFCs are similar.

6.4 Conclusions

Three alkaline direct ethanol fuel cells are built with identical anode and cathode electrodes. Cell #1 uses an anion exchange membrane as the electrolyte while Cell #2 and #3 use a porous fabric as the separator. Their performances are compared under different temperatures, flow rates, fuel concentrations and KOH concentrations. The following conclusions are drawn from experimental results:

1. Replacing the AEM with a porous separator, the ADEFC performance can be maintained at the same level. Cell #2, which uses a non-woven fabric as separator, produces 24.0 mW/cm^2 power density. Under the same conditions (1 M KOH, 1 M ethanol, 60 ^oC), Cell #1, which uses an AEM, reaches a maximum power density of 26.05 mW/cm^2.

2. The porous separator has a great impact on the cell performance. Cell #2 and #3 use different materials as the separator. The maximum power densities produced under the same conditions (1 M KOH, 1 M ethanol, 60 ^oC) are 24.0 and 13.1 mW/cm^2 by Cell #2 and #3 respectively.

3. Reactant flow rate has a greater influence on AEM-free ADEFCs, because maintaining a pressure balance in the CCL to avoid flooding is crucial. A lower anode flow rate causes ethanol transport limitation and reduces the limiting current density, however, increasing the anode flow rate too much may aggravate cathode flooding and impairs the oxygen supply. A thicker separator performs better under higher anode flow rates but they also lead to a higher Ohmic loss.

4. Ethanol concentration has an obvious influence on cell performance under 3 M. Between 3 to 10 M, the maximum power density is slightly enhanced but the limiting current density is decreased.

5. Combining the above results, it is clear that for AEM-free ADEFCs to maintain a high performance it is very important to avoid cathode flooding and ensure a good oxygen supply. This can be done by building a super hydrophobic cathode, which is the aim for the experiments in our next study.

References

[1] J.R. Varcoe, R.C.T. Slade, Prospects for Alkaline Anion-Exchange Membranes in Low Temperature Fuel Cells, Fuel Cells. 5 (2005) 187–200. doi:10.1002/fuce.200400045.

[2] S. Maurya, S.H. Shin, M.K. Kim, S.H. Yun, S.H. Moon, Stability of Composite Anion Exchange Membranes with Various Functional Groups and Their Performance for Energy Conversion, J. Memb. Sci. 443 (2013) 28–35. doi:10.1016/j.memsci.2013.04.035.

[3] Y.-J. Wang, J. Qiao, R. Baker, J. Zhang, Alkaline Polymer Electrolyte Membranes for Fuel Cell Applications., Chem. Soc. Rev. 42 (2013) 5768–87. doi:10.1039/c3cs60053j.

[4] Y. Yang, Portable Power Fuel Cell Manufacturing Cost Analyses, San Antonio, 2010.

[5] Y. Yang, Cost Analysis of Direct Hydrogen PEM Fuel Cell/Lithium Ion Battery Hybrid Power Source for Transportation, Orlando, 2011.

[6] L. An, T.S. Zhao, Y. Li, Q. Wu, Charge Carriers in Alkaline Direct Oxidation Fuel Cells, Energy Environ. Sci. 5 (2012) 7536–7538.

[7] L. An, T.S. Zhao, Q.X. Wu, L. Zeng, Comparison of Different Types of Membrane in Alkaline Direct Ethanol Fuel Cells, Int. J. Hydrogen Energy. 37 (2012) 14536–14542. doi:10.1016/j.ijhydene.2012.06.105.

[8] R. Zhang, J. Pope, Y. Pan, Permselective Membrane-Free Direct Fuel Cell and Components Thereof, US20110123902 A1, 2011.

[9] L. Yang, B.Z. Jang, Dissolved Fuel Alkaline Fuel Cell, US 20060078764A1, 2006.

[10] X. Yang, Y. Liu, S. Li, X. Wei, L. Wang, Y. Chen, A Direct Borohydride Fuel Cell with a Polymer Fiber Membrane and Non-Noble Metal Catalysts, Sci. Rep. 2 (2012) 567. doi:10.1038/srep00567.

[11] Y. Liu, J. Ma, J. Lai, Y. Liu, Study of LaCoO3 as a Cathode Catalyst for a Membraneless Direct Borohydride Fuel Cell, J. Alloys Compd. 488 (2009) 204–207. doi:10.1016/j.jallcom.2009.08.079.

[12] J. Ma, Y. Liu, Y. Yan, P. Zhang, A Membraneless Direct Borohydride Fuel Cell Using LaNiO3-Catalysed Cathode, Fuel Cells. 8 (2008) 394–398. doi:10.1002/fuce.200800048.

[13] M.S. Naughton, F.R. Brushett, P.J.A. Kenis, Carbonate Resilience of Flowing Electrolyte-Based Alkaline Fuel Cells, J. Power Sources. 196 (2011) 1762–1768. doi:10.1016/j.jpowsour.2010.09.114.

[14] E. Kjeang, N. Djilali, D. Sinton, Microfluidic Fuel Cells: A Review, J. Power Sources. 186 (2009) 353–369. doi:10.1016/j.jpowsour.2008.10.011.

[15] Y.S. Li, T.S. Zhao, Z.X. Liang, Performance of Alkaline Electrolyte-Membrane-Based Direct Ethanol Fuel Cells, J. Power Sources. 187 (2009) 387–392. doi:10.1016/j.jpowsour.2008.10.132.

[16] H. Zarrin, J. Wu, M. Fowler, Z. Chen, High Durable PEK-Based Anion Exchange Membrane for Elevated Temperature Alkaline Fuel Cells, J. Memb. Sci. 394-395 (2012) 193–201. doi:10.1016/j.memsci.2011.12.041.

[17] X. Li, A. Faghri, Review and Advances of Direct Methanol Fuel Cells (DMFCs) Part I: Design, Fabrication, and Testing with High Concentration Methanol Solutions, J. Power Sources. 226 (2013) 223–240. doi:10.1016/j.jpowsour.2012.10.061.

[18] H. Bahrami, A. Faghri, Review and Advances of Direct Methanol Fuel Cells: Part II: Modeling and Numerical Simulation, J. Power Sources. 230 (2013) 303–320. doi:10.1016/j.jpowsour.2012.12.009.

[19] H. Bahrami, A. Faghri, Multi-Layer Membrane Model for Mass Transport in a Direct Ethanol Fuel Cell Using an Alkaline Anion Exchange Membrane, J. Power Sources. 218 (2012) 286–296. doi:10.1016/j.jpowsour.2012.06.057.

[20] J.S. Spendelow, A. Wieckowski, Electrocatalysis of Oxygen Reduction and Small Alcohol Oxidation in Alkaline Media, Phys. Chem. Chem. Phys. 9 (2007) 2654–2675. doi:10.1039/b703315j.

[21] X. Yang, Y. Liu, Y. Fang, L. Wang, S. Li, X. Wei, A Direct Methanol Fuel Cell without the Use of a Polymer Electrolyte Membrane or Precious Metal Cathode Catalyst, J. Power Sources. 234 (2013) 272–276. doi:10.1016/j.jpowsour.2013.01.176.

[22] G.K.K.S. Prakash, F.C. Krause, F.A. Viva, S.R.R. Narayanan, G.A. Olah, Study of Operating Conditions and Cell Design on the Performance of Alkaline Anion Exchange Membrane Based Direct Methanol Fuel Cells, J. Power Sources. 196 (2011) 7967–7972. doi:10.1016/j.jpowsour.2011.05.056.

[23] Y.S. Li, T.S. Zhao, A High-Performance Integrated Electrode for Anion-Exchange Membrane Direct Ethanol Fuel Cells, Int. J. Hydrogen Energy. 36 (2011) 7707–7713.

[24] N.A. Choudhury, J. Ma, Y. Sahai, High Performance and Eco-Friendly Chitosan Hydrogel Membrane Electrolytes for Direct Borohydride Fuel Cells, J. Power Sources. 210 (2012) 358–365. doi:10.1016/j.jpowsour.2012.03.013.

Table 6-1 Reported performance of ADLFCs with and without AEM

Ref.	Operation Mode	catalyst		Fuel	Oxidant	Separator/AEM	Peak power density (mW/cm^2)
		Anode	Cathode				
Zhang, R.M. [8]	Semi-Active	Pd/C, on Ni Foam	Co/C, loading N/A	10% wt KOH, 10% wt Ethanol	Ambient air	Separator: PEEK mesh	44@0.3V
Yang, X. [10]	Active	CoO, 70 mg/cm^2 on Ni Foam	$LaNiO_3$/ CNT, loading N/A	0.8 M KBH_4 and 6 M KOH 20ml/min	O_2, 5sccm	Separator: Polymer fiber	663 @0.6V, 65°C
Yang, X. [21]	Active	PtRu/C, 6 mg/cm^2 on Ni Foam	$LaNiO_3$/ CNT, loading N/A	5 M methanol and 4 M KOH 20ml/min	O_2, 5sccm	Separator: Polymer fiber	103 @0.3V, 65°C
Prakash, G.K.S. [22]	Active	Pt black, 8mg/cm^2	PtRu black, 8 mg/cm^2	2 M KOH + 1 M methanol	O_2, 1270 sccm	AEM: Tokuyama A-006	170@0.38V, 90°C
Li, Y.S. [23]	Active	PdNi/C, 2 mg/cm^2 on Ni foam	Hypermec K14	5M KOH+3M EtOH	O_2, 100 sccm	AEM: Tokuyama A-201	130@0.3V, 80°C
Choudhury, N.A. [24]	Active	Pd/C	Pt/C	$NaBH_4$	O_2	AEM: Chitosan hydrogel membrane	810@0.48V, 70°C

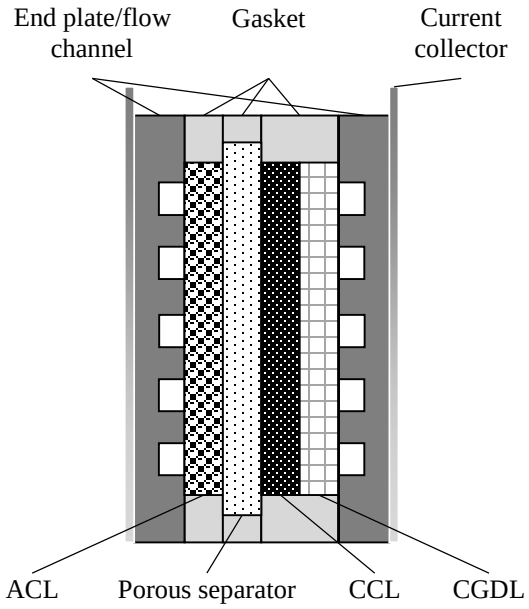

Figure 6-1 Structure of an AEM-free ADEFC

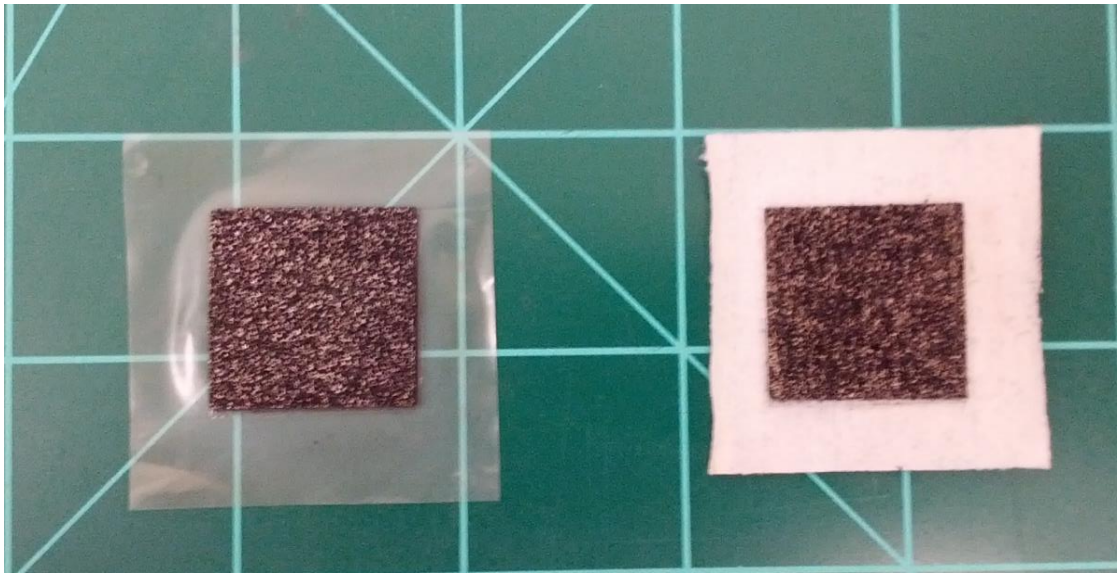

Figure 6-2 ADEFCs that use anion exchange membrane as electrolyte (left, Cell #1) and non-woven fabric as separator (right, Cell #2)

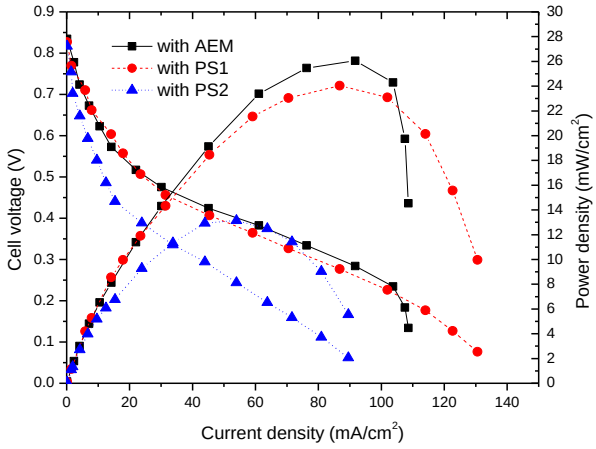

Figure 6-3 Comparison between three fuel cells that using identical anode and cathode electrodes but different separators or anion exchange membrane

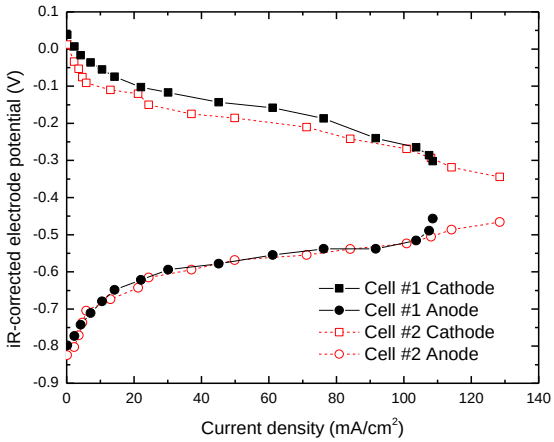

Figure 6-4 iR-corrected anode and cathode potential and overpotential

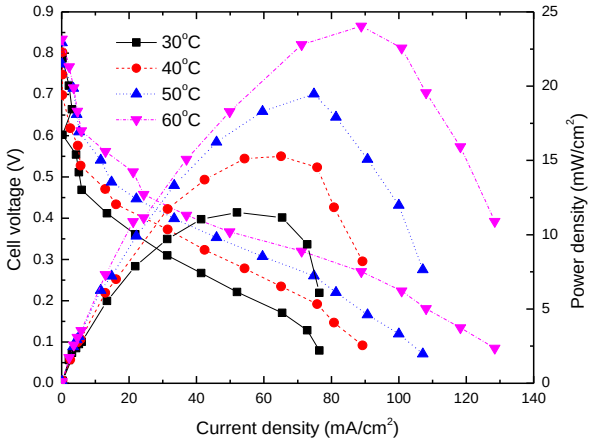

Figure 6-5 Influence of temperature on the cell performance (Cell #2)

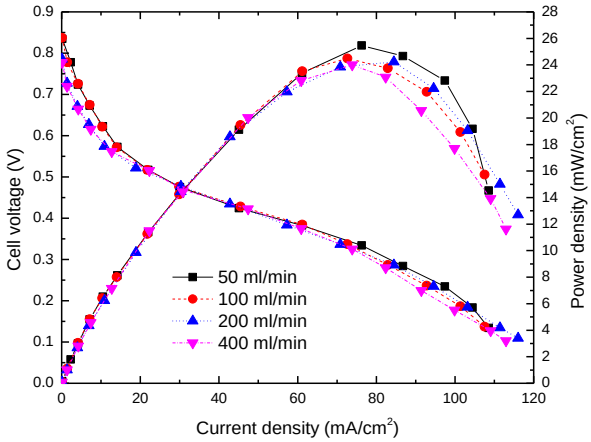

(a) Cell #1

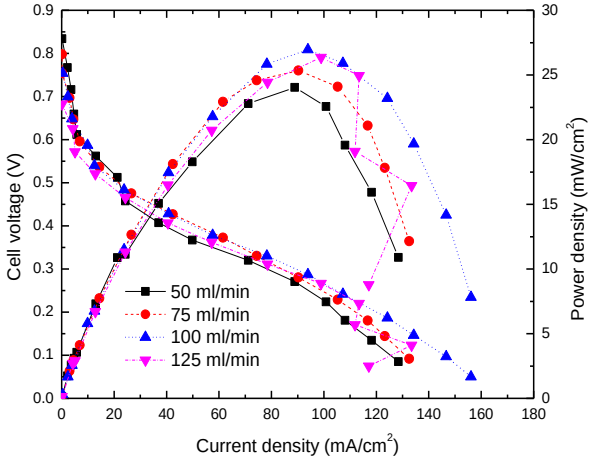

(b) Cell #2

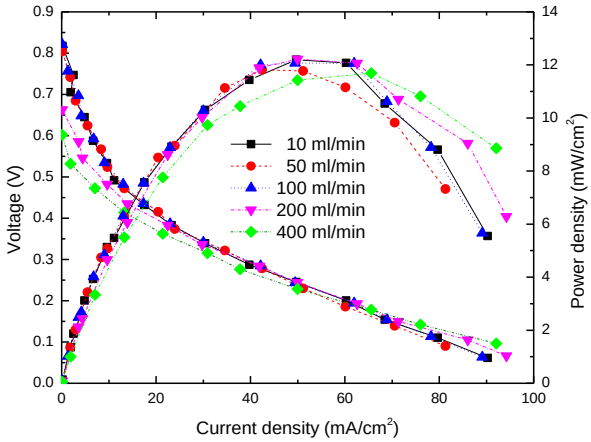

(c) Cell #3

Figure 6-6 Influence of cathode flow rate on (a) Cell #1, (b) Cell #2, and (c) Cell #3

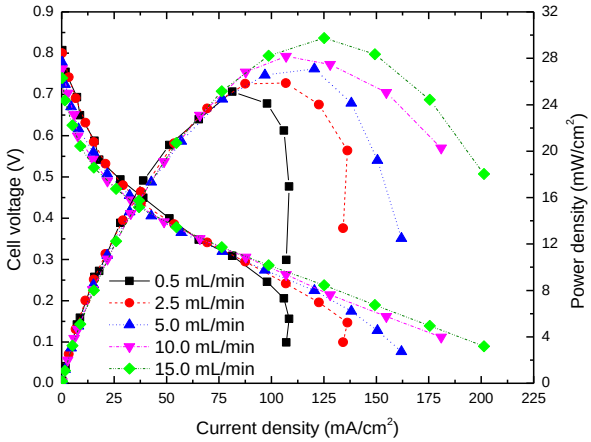

(a) Cell #1

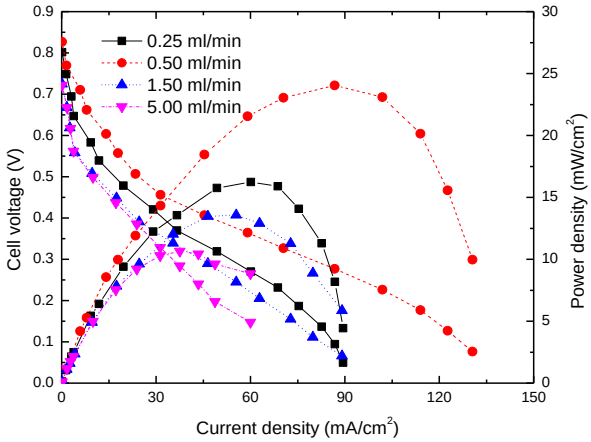

(b) Cell #2

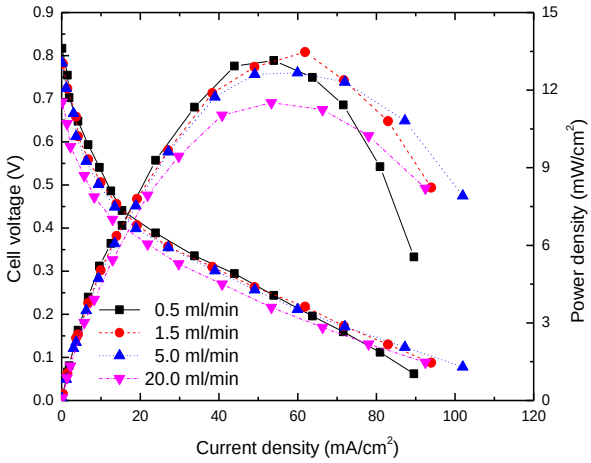

(c) Cell #3

Figure 6-7 Influence of anode flow rate on (a) Cell #1, (b) Cell #2, and (c) Cell #3

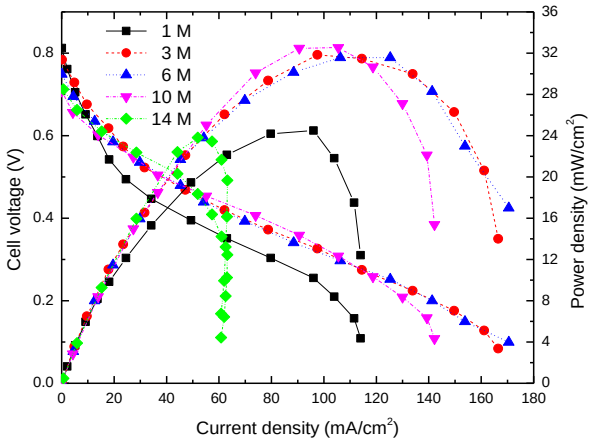

(a) Cell #1

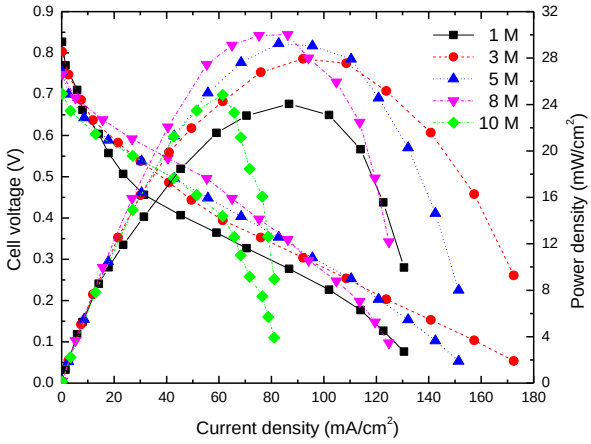

(b) Cell #2

Figure 6-8 Influence of the ethanol concentration on (a) Cell #1, (b) Cell #2

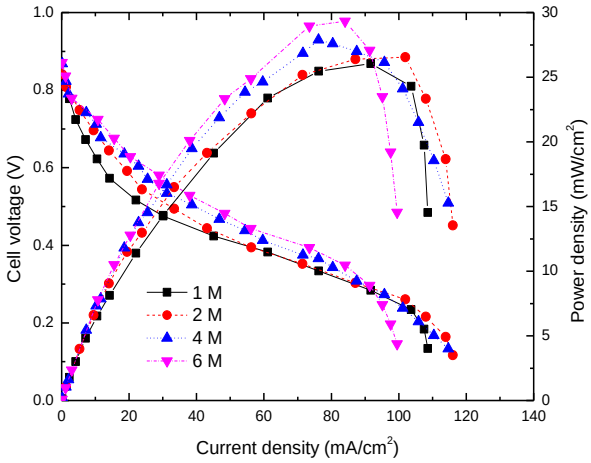

(a) Cell #1

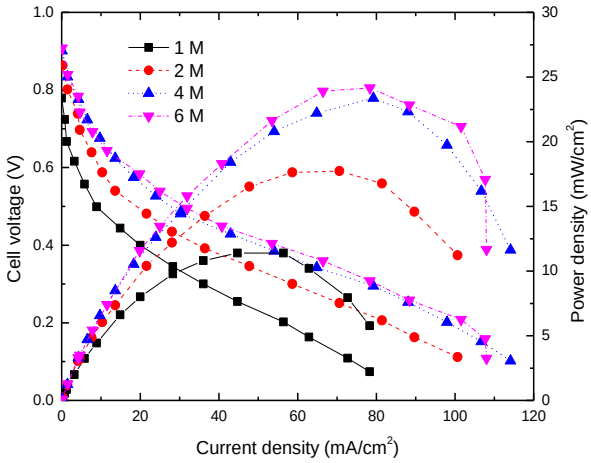

(b) Cell #2

Figure 6-9 Influence of KOH concentration on (a) Cell #1, (b) Cell #2

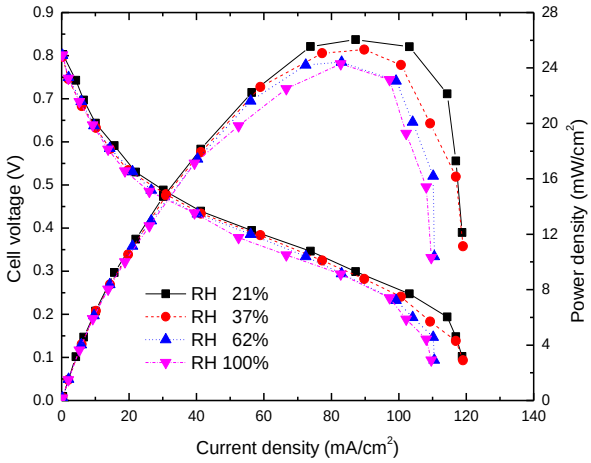

Figure 6-10 Influence of oxygen humidity (cell #1)

Chapter 7 Optimizing the Anode Structure of a Passive Tubular-Shaped Direct Methanol Fuel Cell to Operate with High Concentration Methanol

In order to take full advantage of the high energy density available in the methanol fuel, one must use high concentration methanol in Direct Methanol Fuel Cells (DMFCs). However, this causes severe methanol crossover and leads to low power density and fuel efficiency. In this work, tubular shape is adopted to generate higher volumetric power density; Porous PTFE membranes at anode are used to control methanol transport with high concentration fuel. A novel passive, tubular-shaped DMFC is improved to achieve stable operation with methanol concentrations up to 20M. It is observed that a balance between fuel transport resistance, power density, energy density and fuel efficiency exists. Increased resistance enhances fuel efficiency hence energy density but limits fuel supply and causes low power density. With the improved anode structure and higher concentration fuel (1M to 15M), the energy output of the tubular DMFC increases 591%, from 0.094 Wh to 0.65 Wh with 2ml fuel. The power density keeps the same level as 16 mW/cm^2. For different fuel concentrations, there exists an optimum structure to generate the highest power density, which is a result of minimizing the methanol crossover while also providing sufficient fuel. The discharge characteristic at constant voltage and its effect on fuel efficiency are also discussed.

7.1 Introduction

As one of the most promising portable power supply solutions, direct methanol fuel cells (DMFCs) have attracted tremendous research and industrial interest in the last decade. One of the most extraordinary merits of the DMFCs is their potential of providing high energy density. In the premise of complete electro-oxidization, a liter of methanol can produce 4820 Wh of electricity, which is much higher than its competitors, such as Li-ion batteries (250~620 WhL^{-1}) and hydrogen

PEM fuel cells (1556 Wh L^{-1} at 700 bar). However, in current applications, the performance of DMFC's is impaired by a low power density, which is caused by slow electrochemical kinetics and methanol/water crossover through the electrolyte membrane.

Traditional polymer electrolyte membrane fuel cells (PEMFC) have a planar shape because of the straightforward structure design. Several research efforts, however, have shown that a tubular-shaped PEMFC would provide a larger active area without increasing the overall volume occupied by the fuel cell [1-3]. For DMFC, this is especially important because one of the problems of regular DMFC is relatively low power density.

A tubular DMFC has several other significant advantages compared to a planar-shaped one: (1) It can operate in all orientations without lack of methanol contacting the Anode Catalyst Layer (ACL); (2) Because of a decreased volume, the fabrication cost is reduced; (3) It has the same shape as existing AA, AAA, D, and C batteries, which would allow easier conversion between batteries and fuel cells in the future; (4) With the elimination of flow fields at the cathode, uniform pressure can be applied across the membrane electrode assembly (MEA) [3].

The tubular direct alcohol fuel cells can be divided into two categories. The first is a tubular-cast membrane type, and the second is a wrapped MEA type. For the first type, the membrane is cast into a tubular shape and the catalyst is then sprayed to the inner and outer sides of the membrane [4-6]. However, this type of tubular DMFCs usually have very poor performance (10~15 mW/cm^2) because of low conductivity and high contact resistance. The second type uses a regular MEA wrapped onto a tubular shaped frame, which serves as the fuel reservoir and the anode current collector [1,2,7]. An outer frame presses the MEA and other layers together. In 2007, Cao put forward a conceptual design of fuel cell stack composed of tubular single cells [8]. Some theoretical evaluation indicated that the stack design may potentially increase the reactive surface

area by more than 10 times. Thus, with the same power density per unit active area, tubular DMFCs have higher volumetric power density, hence a higher total power output with same volume.

Another issue of DMFC is methanol crossover. In most existing works on tubular DMFCs, dilute methanol were used to alleviate this problem. However, it decreased the energy density which should be one of the most attractive characteristics of DMFC. Recently, the concept of a passive vapor feed DMFC has attracted more attention because of its potential to directly utilize high concentration methanol and its elimination of the issues related to CO_2 bubble removal. A simple vaporizer was used to passively convert liquid methanol solutions stored in a fuel tank to vapor in order to drive the fuel cell [9-11]. Ren et al. used a silicone membrane as a vaporizer in a passive DMFC. Water crossover was controlled by an optimized passive water management system through back diffusion and back convection [12,13]. Guo and Faghri utilized the advantage of a porous wick structure to separate the methanol reservoir from the MEA without the need for a complex micro-fluidics subsystem. Pure methanol in a fuel tank was wicked to an evaporation pad to produce methanol vapor. Successful thermal fluids management enabled prototype cells to operate for 6 months without obvious degradation [14-17]. Xu et al. studied the effect of the anode structure on the methanol vapor generation rate of a passive vapor-feed DMFC which had a membrane vaporizer and a hydrophobic vapor transport layer (VTL). The parameters studied included VTL thickness, vaporizer open ratio and water management layer thickness. The optimized structure enabled the fuel cell to operate with a fuel efficiency of 62% with neat methanol and output a peak power density of 34 mW/cm^2 [18].

In this work, we investigate the effect of adapting different anode structures to a passive tubular-shaped DMFC for high concentration methanol solutions, which has not been reported in literature. Knowledge and techniques obtained through optimizing the performance of planar

DMFCs are adopted. These include adding micro-porous PTFE membranes to increase the transport resistance to methanol, using a Nafion 117 membrane between the methanol reservoir and gas diffusion layer to serve as a pervaporation layer, and changing the open ratio of the fuel reservoir exposed to the anode electrode. After optimization of the structure, the passive tubular-shaped DMFC operated stably for over 5 hours with 2 mL of 20 M methanol solution. It is worthwhile to note that this is the first experimental work describing the modification of a tubular-shaped, passive DMFC to achieve stable, repeatable, high concentration methanol operation.

7.2 Experimental

7.2.1 Structure of the passive tubular-shaped DMFC

The structure of the passive, tubular-shaped DMFC frame, Catalyst Coated Membrane (CCM), and Membrane Electrode Structure (MEA) are the same as our previous work, as described in ref. [1]. This work focuses on the structural enhancement to the anode side of the fuel cell to improve fuel cell performance and fuel efficiency with high concentration methanol up to 20 M. Similar materials and structures were applied to the anode to increase the mass transport resistance as explained previously in [18].

Six different structures were considered at the anode in our experimental work as shown in Figure 7-1. The MEAs used in the tests are provided by BCS Fuel Cells, Inc. Nafion® 115 was chosen as electrolyte membrane with consideration of the balance between ion conductivity, mechanical strength, and methanol crossover. The active area is 4×5.3 cm^2. Catalyst loadings are 5 mg/cm^2 Pt and 5 mg/cm^2 PtRu for the cathode and anode, respectively. Porous PTFE membranes (Saint-Gobain Zitex® G-110) were placed on the outside of the anode diffusion layer to increase the mass transfer resistance from the methanol channel to the reaction sites in the catalyst layer. Nafion® 117 was used as a pervaporation membrane in structures S4, S5 and S6. To control the

pervaporation rate, a layer of regular, nonporous PTFE membrane was placed between the fuel reservoir and the pervaporation membrane. A specific number of holes were perforated on this PTFE membrane to achieve different open ratios (3%, 10%, and 50%) and reduce the total mass transport from the methanol channels to the gas diffusion layer. Structure S3 was considered to have a 100% open ratio. It should be pointed out that one problem with a tubular fuel cell is the flexibility of the cell frame. For planar ones, adding more layers to the cell is not difficult while for a tubular one, adding more layers to the cell increases the thickness so that the frame needs to be re-designed and fabricated.

7.2.2 Testing

The tests were performed using a Scribner Associates 850e test station. This apparatus is equipped with an electronic load that can record the current, voltage, internal resistance, and temperature of the fuel cell. It is capable of applying a variable voltage or current to the fuel cell and recording the resulting polarization curve. All tests were performed in a controlled laboratory setting with ambient temperatures that ranged between 24 – 28 ºC and relative humidities that ranged between 5% - 50%.

Prior to installation on the tubular fuel cell, each MEA was activated by H_2/O_2 and 1 M methanol solutions/humidified air in an active mode. Polarization curves were obtained and compared to make sure all the MEAs used in the tests had similar performance. The differences in peak power density between each MEA were smaller than 5%.The tests that were conducted on each unique fuel cell structure included determining the polarization curve and fuel cell efficiency. The polarization curve was generated by scanning the voltage from open circuit conditions (OCV) down to 0.05 V in steps of 0.05 V and recording the average current density produced by the fuel cell for each voltage. The results were plotted as voltage versus current density (VI curve) and

power density vs. current density to compare the range of voltages, current density, and maximum power density that each cell structure produced. The fuel cell efficiency is a measurement of how much fuel is used by the fuel cell compared to the quantity of fuel provided to the fuel cell, which is useful for concluding how much fuel is lost due to crossover, evaporation, or leakage. It was determined based on the constant voltage discharge as follows:

$$\eta = \frac{M_{\mathrm{MeOH}} \cdot \int_0^T i(t)\,\mathrm{d}t \Big/ 6F}{m_{\mathrm{MeOH,sup}}}, \tag{1}$$

where t is the time of the discharging process, M_{MeOH} the molecular weight of methanol, T the total discharging time, $i(t)$ the transient discharging current density, F Faraday's constant, and $m_{\mathrm{MeOH,sup}}$ the mass of methanol provided to the fuel reservoir.

For each structure, methanol solutions with different concentrations, ranging from 1~20 M, were tested. For each case, several polarization curves were obtained until the performance of the cell was stable. Fuel efficiency tests were then carried out. 2 ml of methanol solution was injected into the reservoir. After stable open circuit voltage was achieved, a constant voltage (0.35 V) discharge was performed until there was no current output to determine fuel efficiency.

7.3 Results and discussion

7.3.1 Effect of structure on performance

Figure 7-2 presents the polarization curves for a range of methanol concentrations and structure S4 which has a 50% open ratio pervaporation membrane. For all methanol concentrations less than 15 M, the peak power density increases with each higher methanol concentration. For low concentrations, such as 3 M and 5 M, the factor limiting the power density is mainly mass transfer, since the VI curves dropped sharply under high current density. The peak power density reaches 16.5 mW/cm^2 with 15 M solution. For the case with 18 M solution, the peak power density and

current density drops drastically in contrast to the results presented with the 15 M solution. During this test, mass transfer no longer limits the fuel supply for electrochemical reactions; the main reason for the drop in performance is the methanol crossover which causes parasitic voltage loss on the cathode side and, at the same time, accelerates the depletion of methanol on the anode side. The effect of methanol concentration on the crossover rate can also be seen by the different open circuit voltages, as shown in Figure 7-2(b). The OCV for the 3 M solution is 0.545 V, while the OCV for the 18 M solution drops to 0.449 V.

Figure 7-3 presents the influence of the anode side structures on the fuel cell polarization curves during operation with a 15 M methanol solution. With the increase of open ratio from 3% to 50%, the mass transport resistance from the fuel reservoir to the catalyst layer is reduced, which permits better fuel supply to the catalyst layer and leads to higher power and current density. When the open ratio is higher than 50 %, however, the methanol concentration at the catalyst layer is too high and, as a result, methanol crossover impairs the performance. This is reflected in Figure 7-3 with anode structure S3, in which the power and current both decrease due to significant methanol crossover.

During the experiments, we tested each of the six structures with different fuel concentrations ranging from 1 M ~ 20 M. To simultaneously compare the results, Figure 7-4 shows the peak power density achieved considering each methanol concentration and structure. Generally, for each anode structure, increasing the concentration of methanol solution increases the power density until a peak value, and then it reduces due to increased methanol crossover. This is the point at which a given structure cannot operate with any higher methanol concentration since the methanol permeates through each of the layers and crosses over the membrane, reducing the performance of the fuel cell. For structure S1, the maximum power density is 18.99 mW/cm^2,

which occurs at a concentration of 5 M. The performance then deteriorates sharply with fuel of higher concentration. For structure S4, the maximum power density occurs at 15 M, which is 16.5 mW/cm^2. One can concluded, thus, that by optimizing the mass transfer at anode side, the methanol crossover can be well controlled and the ability of the fuel cell to handle high concentration methanol is enhanced without impairing the performance significantly. With structure S6 (3% open ratio), the tubular fuel cell is operated in a stable condition for over 5 hours with 2 ml of 20 M methanol solution. The power output, however, is less than 5 mW/cm^2 which is caused by a limited fuel supply.

The maximum current density follows a similar trend as the peak power density and is plotted in Figure 7-5. The decreased current density during higher concentration operation is caused by water crossover from the anode to cathode. The mechanism of water crossover is quite similar to that of methanol. It is also caused by electro-osmotic drag during proton transport, diffusion by water concentration gradients, and convection by hydraulic pressure gradients. To achieve higher current density, more protons need to be transported through the Nafion® membrane which causes more water crossover. This impairs the cell performance in two ways. First, more water crossover from anode to cathode causes flooding on the cathode side, which limits the oxygen supply. Secondly, water crossover depletes the water supply on the anode side and, consequently, decreases the methanol oxidization rate. These problems can be alleviated by introducing a water management layer on the cathode side to optimize water distribution across the entire cell.

Figure 7-6 provides a comparison of the peak power densities for different anode structures with the same methanol concentration. For low concentrations, such as 3 M, the power density decreases monotonically from structure S1 to S6 because of decreasing methanol supply. For higher concentrations, such as 18 M, the peak power density is achieved with the 50% open ratio

pervaporation membrane (structure S4). When the open ratio is higher than 50%, the methanol crossover dominates and impairs fuel cell performance. Therefore, for each specific methanol concentration, there exists an optimum structure to achieve the highest power density. For higher concentrations of methanol, a higher mass transport resistance is needed at the anode in conjunction with a layer added at the cathode to provide back flux of water from the cathode to the anode.

The temperature of the fuel cell rises as a direct result of methanol crossover. Due to the existence of Pt at the cathode, methanol that crosses over reacts with oxygen exothermically giving off heat and causing the cell temperature to rise. During our test, the cell temperature is recorded by a thermocouple placed in the cathode air channel and in contact with the cathode diffusion layer. The original temperature of the cell is the same as the ambient air present at the start of each test. The highest temperature is usually measured after 30 minutes of the fuel efficiency testing since the concentration of fuel in the anode catalyst layer is highest at this point and most of the methanol is likely to cross over to the cathode. Following this point, the concentration of fuel in the anode gradually drops along with the current density, both resulting in reduced methanol crossover, so that the cell temperature reduces back to the ambient value. Figure 7-7 provides a comparison of the highest temperature rises for each cell structure. For the 10 M fuel, structure S3 shows a maximum temperature rise of 24 ^{o}C while for structure S6 it is only 6 ^{o}C. This trend is more evident with higher methanol concentrations, which indicates that by applying a higher mass transfer resistance the methanol crossover can be well controlled for high concentration tubular-shaped DMFCs.

7.3.2 Effect of structure on fuel efficiency

One of the main advantages of DMFCs over hydrogen PEM fuel cells is the high energy density of DMFCs, which is due to the fact that methanol exists as a liquid at normal pressure/temperature conditions. In real applications, this advantage is compromised due to many limiting factors with the DMFC. The theoretical energy density of a DMFC cannot be achieved because of the necessity of using dilute methanol, fuel loss due to methanol crossover, fuel leakage from the gas outlet, etc. To study the influence of the anode structure on fuel utilization, fuel efficiency tests are performed with different structures and fuel concentrations. The results are summarized in Figure 7-8.

For structures S2 and S3, in which the anode does not have a high mass transport resistance, higher methanol concentrations always cause a lower fuel efficiency, which has been reported in elsewhere as well [18] and can be explained by higher methanol crossover. However, when the pervaporation open ratio is reduced, the fuel efficiency for dilute methanol is not always higher than that at high concentration as shown by the curves for structures S5 and S6 in Figure 7-8. This is surprising since it proved contrary to what is expected. An explanation might be that the dilute solution leads to a longer operating time because of a lower discharging current, so that fuel escapes by evaporation over the long period and reduces the fuel efficiency. However, this is not always true. As shown in Figure 7-9, with lower concentrations, such as 3M, the current is very low, as expected and the discharge process is still the shortest. Combining this result with Figure 7-4, we can find that when the cell operates at a very small power density, hence low current, the fuel efficiency is always low. This may be caused by incomplete oxidation of methanol due to the very sluggish methanol oxidation reaction. In other words, the methanol is not completely converted to carbon dioxide in the anode catalyst layer and does not release the expected 6 protons and electrons for each molecule of methanol. Under this assumption, the fuel efficiency is very

low even when the crossover is not severe. Plotting the data of Figure 7-8 in another way to emphasize the effect of structure on fuel efficiency leads to Figure 7-10. It can be seen that for structures with higher mass transport resistance, such as for structures S5 and S6, the fuel efficiency is not as sensitive to fuel concentration. For structures S1 and S2, however, increasing the fuel concentration decreases the fuel efficiency sharply.

For this study, one of the most important goals is to emphasize the high energy density of DMFC's by utilizing higher centration methanol solutions. So we compare the work done by the same volume (2 ml) of methanol solution under the same discharge voltage for different structures and concentrations. The result is plotted in Figure 7-11. Comparing this result with Figure 7-10, we can conclude that although a lower open ratio leads to higher mass transport resistance and subsequently lower power density even with high concentrations of fuel, the higher fuel concentration provided a large quantity of total work produced by the fuel cell. Dilute solutions, such as 3 M, exhibit very low electricity generation while structure S6 (3% open ratio) generates up to 0.86 Wh of electricity at 0.35 V by utilizing a 18 M methanol solution, which is much higher than the results provided by low concentration fuels. Compared with original structure (MEA without extra layers) using 1M methanol solution [1], Structure S4 using 15M methanol solution increases the energy output of the tubular DMFC by 591%, from 0.094Wh to 0.65Wh with 2ml fuel. The power density remains the same level as 16 mW/cm^2.

7.3.3 Future improvement to operate with neat methanol

The focus of this work is to improve the anode structure of the DMFC. The goal is to enhance methanol transport resistance enough to prevent methanol crossover while also allowing sufficient power generation by the fuel cell. However, methanol crossover is only part of the problem associated with DMFCs. As discussed in section 7.3.1, water management is equally important,

especially for high concentration operation where less water is available at the anode for methanol oxidization. By providing water management layers on the cathode side to force some water back to the anode side, the methanol crossover problem can be further prohibited and the DMFC can operate stably with high concentrations of methanol.

7.4 Conclusions

In this chapter, the anode structure of a DMFC is improved to allow the tubular-shaped DMFC to operate with high concentration methanol up to 20 M. By adopting the passive vapor feed concept to the anode, including a methanol-impermeable PTFE membrane with different open ratios and porous PTFE membranes, the methanol transport resistance from the fuel reservoir to the anode catalyst layer can be controlled. By comparing the polarization curves and fuel efficiency of six different structures with different methanol concentrations ranging from 1 M to 20 M, the following conclusions are made:

(1) There exists an optimum fuel concentration to achieve the highest power density for a certain cell structure. Cells with higher methanol transport resistance operate best at a higher fuel concentration. For structure S4, the maximum power density of 16.5 mW/cm^2 is obtained with a 15 M methanol solution.

(2) For a specific methanol concentration, there exists a best structure to achieve the best power density. For higher concentrations, higher mass transport resistance is needed. For a 3 M methanol, structure S1 achieves the highest power density while for the 15 M solution, Structure S4 achieves a higher power density.

(3) Although higher mass transport resistance may impair power density, the fuel efficiency is higher. The higher concentration compensates on the total electricity generation for a specific amount of fuel supply. With a 18 M methanol solution, structure S6 generates the most electricity

at 0.86 Wh, while for a 15 M methanol, structure S5 generates the most electricity, which is 0.75 Wh.

(4) The aim of the section is to improve energy output without impairing power density. Compared with original structure (MEA without extra layers) using 1M methanol solution, Structure S4 using 15M methanol solution increases the energy output of the tubular DMFC by 591%, from 0.094Wh to 0.65Wh with 2ml fuel. The power density remains the same level as 16 mW/cm^2.

References

[1] T. Ward, X. Li, A. Faghri, Performance Characteristics of a Novel Tubular-Shaped Passive Direct Methanol Fuel Cell, J. Power Sources. 196 (2011) 403–414.

[2] T. Ward, C. Xu, A. Faghri, X.U. CHAO, Performance and Design Analysis of Tubular-Shaped Passive Direct Methanol Fuel Cells, Int. J. Hydrogen Energy. 36 (2011) 9216–9230.

[3] M.A.R. Sadiq Al-Baghdadi, Three-Dimensional Computational Fluid Dynamics Model of a Tubular-Shaped PEM Fuel Cell, Renew. Energy. 33 (2008) 1334–1345.

[4] R.-J. Yu, G.-Y. Cao, X.-Q. Liu, Z.-F. Li, W. Xing, X.-J. Zhu, Fabrication of Support Tubular Proton Exchange Membrane for Fuel Cell, J. Fuel Cell Sci. Technol. 4 (2007) 520–524. doi:10.1115/1.2759501.

[5] Z.G. Shao, W.F. Lin, F. Zhu, P.A. Christensen, H. Zhang, B. Yi, A Tubular Direct Methanol Fuel Cell with Ti Mesh Anode, J. Power Sources. 160 (2006) 1003–1008.

[6] H. Qiao, T. Kasajima, M. Kunimatsu, N. Fujiwara, T. Okada, Evaluation of a Passive Microtubular Direct Methanol Fuel Cell with PtRu Anode Catalyst Layers Made by Wet Chemical Processes, J. Electrochem. Soc. 153 (2006) A42–A47.

[7] http://www.swri.edu/3pubs/ttoday/summr96/subass.htm, (n.d.).

[8] Y.D. Cao, Fuel Cell Stacks Based on Micro Fuel Cell Units for a Substantially Increased Power Density, in: MicroNanoChina07, 2007: p. 21471.

[9] M.A. Abdelkareem, N. Nakagawa, A Key Factor for the Actual Application of a Vapor Feed Passive DMFC Operated with High Concentration of Methanol, Key Eng. Mater. 459 (2011) 78–83.

[10] F.R. Brushett, P.J.A. Kenis, Design and Characterization of a Vapor Feed Methanol Fuel Cell with a Flowing Electrolyte, in: AIChE 100 - 2008 AIChE Annu. Meet. Conf. Proc., 2008.

[11] S. Eccarius, X. Tian, F. Krause, C. Agert, Completely Passive Operation of Vapor-Fed Direct Methanol Fuel Cells for Portable Applications, J. Micromechanics Microengineering. 18 (2008) 104010.

[12] X. Ren, F.W. Kovacs, K.J. Shufon, S. Gottesfeld, Passive Water Management Techniques in Direct Methanol Fuel Cells , 2007.

[13] X. Ren, J.J. Becerra, R.S. Hirsch, S. Gottesfeld, F.W. Kovacs, K.J. Shufon, Direct Oxidation Fuel Cell Operating with Direct Feed of Concentrated Fuel under Passive Water Management , 2008.

[14] A. Faghri, Z. Guo, An Innovative Passive DMFC Technology, Appl. Therm. Eng. 28 (2008) 1614–1622.

[15] Z. Guo, A. Faghri, Vapor Feed Direct Methanol Fuel Cells with Passive Thermal-Fluids Management System, J. Power Sources. 167 (2007) 378–390.

[16] G. Jewett, Z. Guo, A. Faghri, Performance Characteristics of a Vapor Feed Passive Miniature Direct Methanol Fuel Cell, Int. J. Heat Mass Transf. 52 (2009) 4573–4583.

[17] J. Rice, A. Faghri, Analysis of a Passive Vapor Feed Direct Methanol Fuel Cell, Int. J. Heat Mass Transf. 51 (2008) 948–959.

[18] C. Xu, A. Faghri, X. Li, Development of a High Performance Passive Vapor-Feed DMFC Fed with Neat Methanol, J. Electrochem. Soc. 157 (2010) B1109–B1117. doi:10.1149/1.3435256.

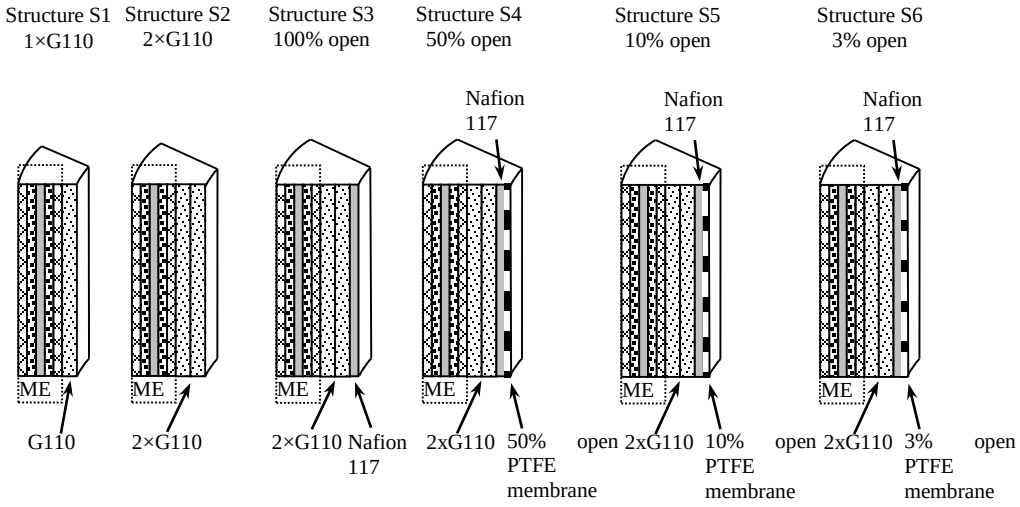

Figure 7-1 Different anode structures tested

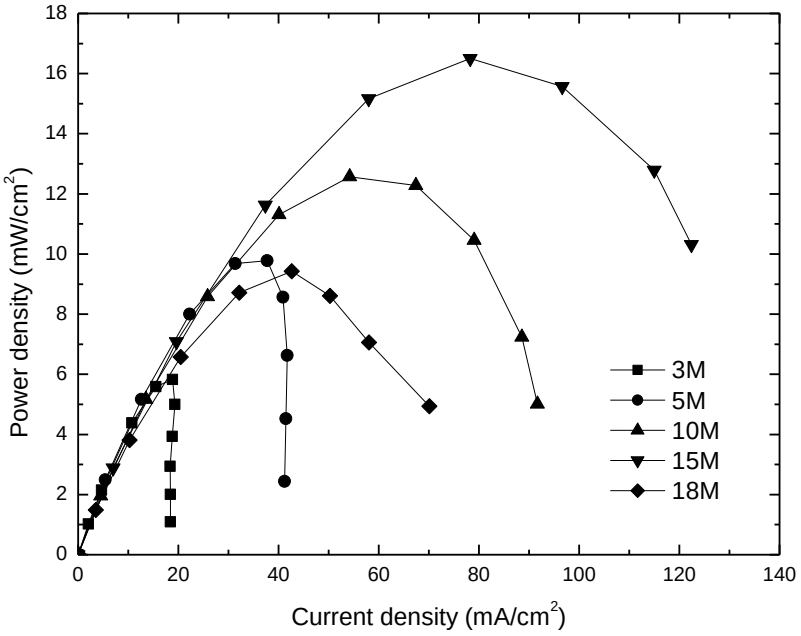

(a)

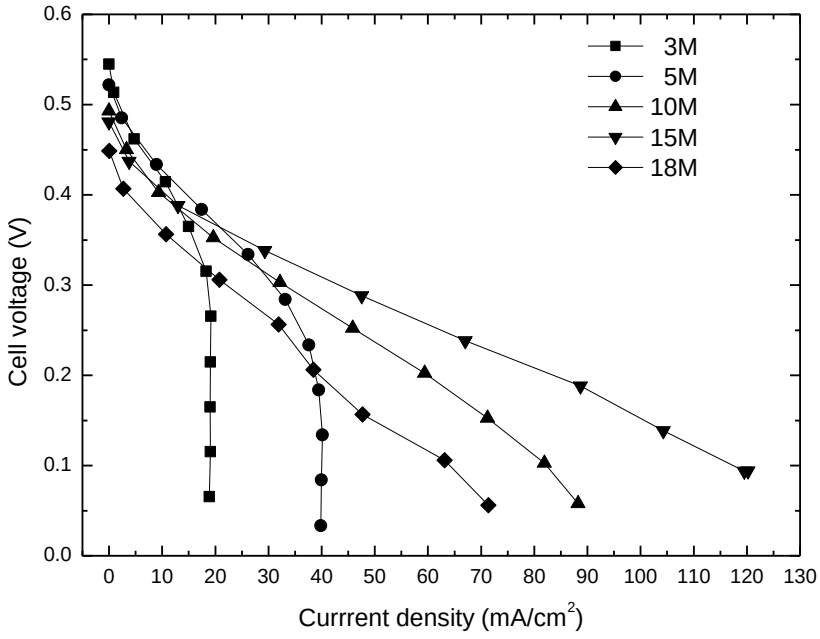

(b)

Figure 7-2 (a) Power density and (b) polarization curves for different concentrations of methanol using structure S4

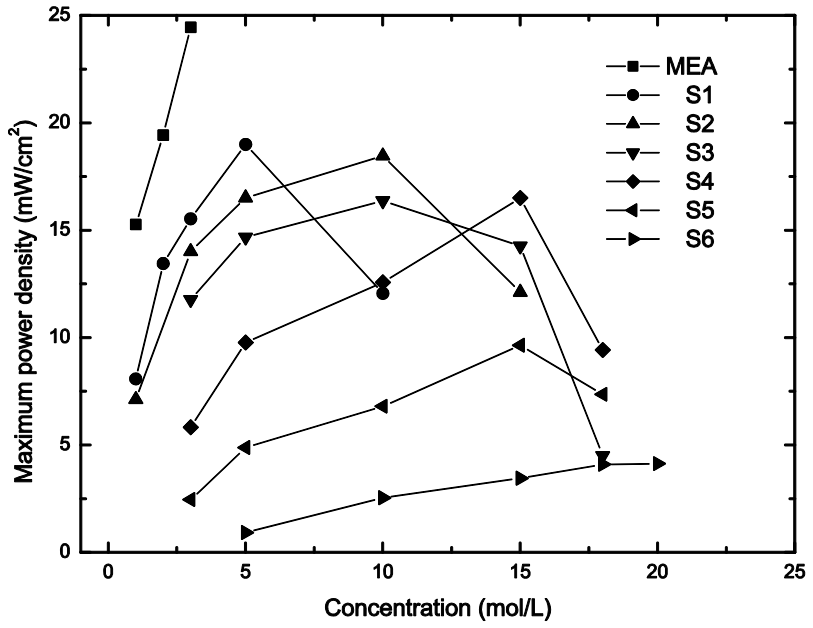

(a)

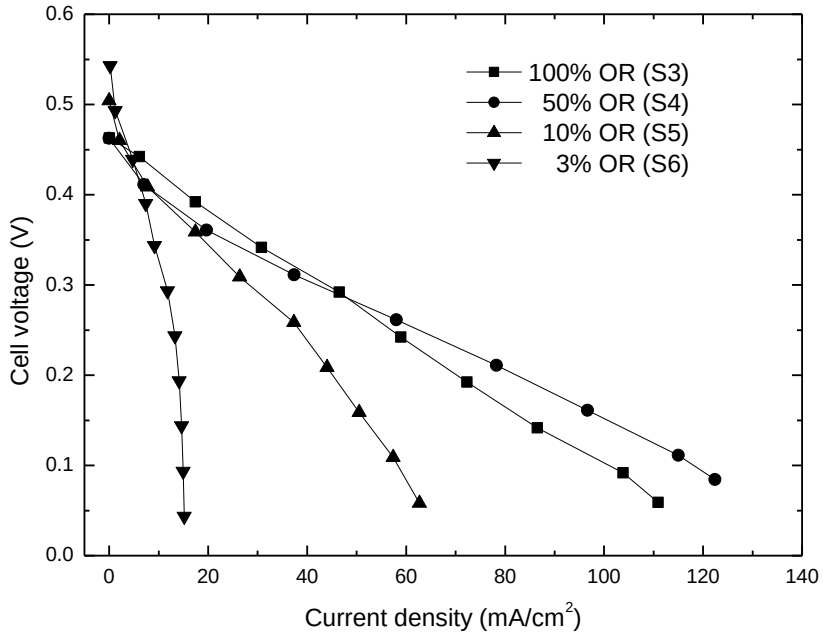

(b)

Figure 7-3 (a) Power density and (b) polarization curves for different anode side structures with a 15 M methanol solution

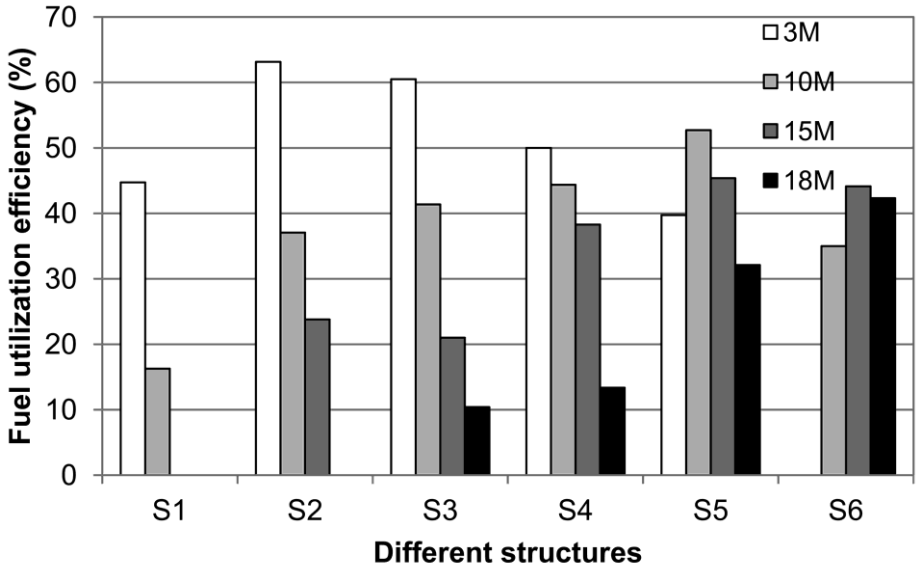

Figure 7-4 Peak power density versus methanol solution concentration for different anode structures

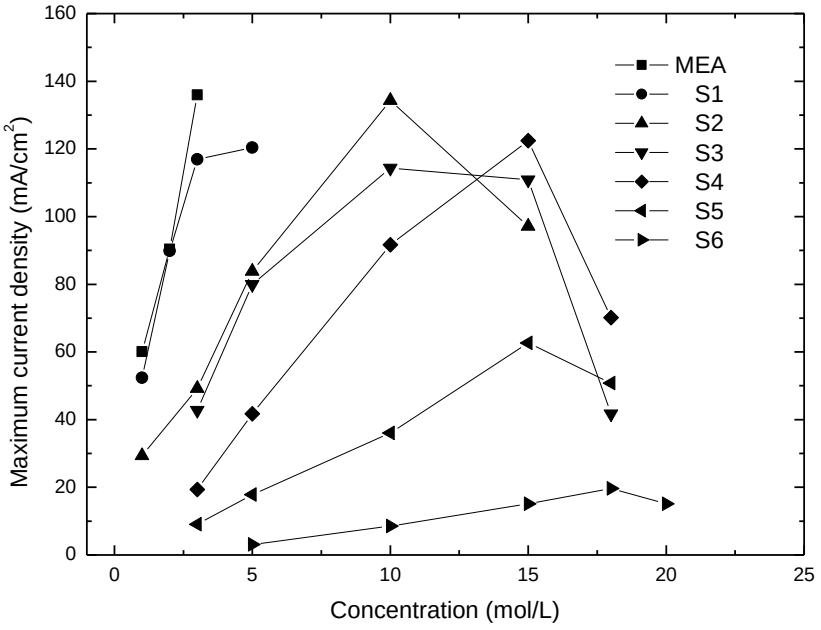

Figure 7-5 Maximum current density versus methanol solution concentration

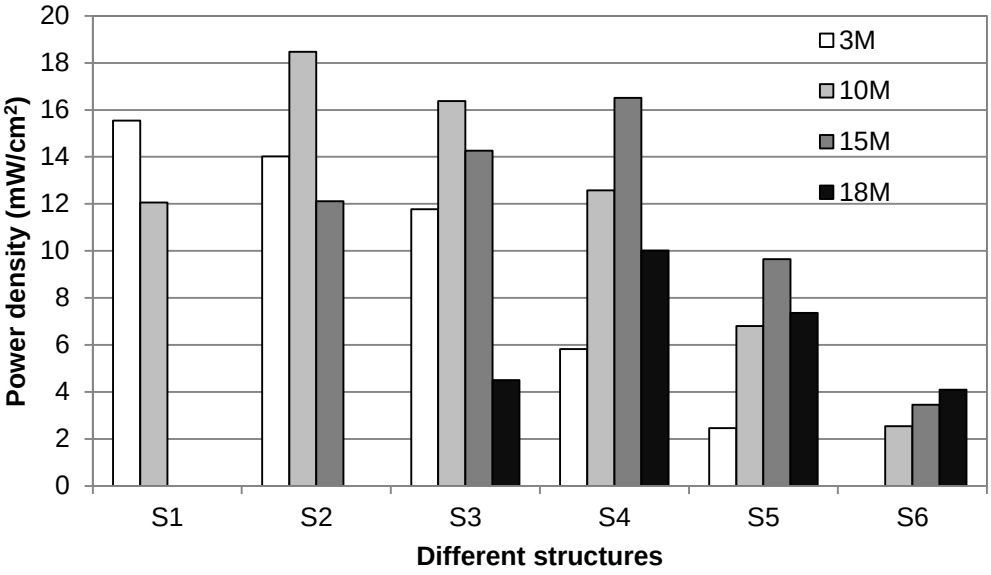

Figure 7-6 Maximum power density versus anode structure

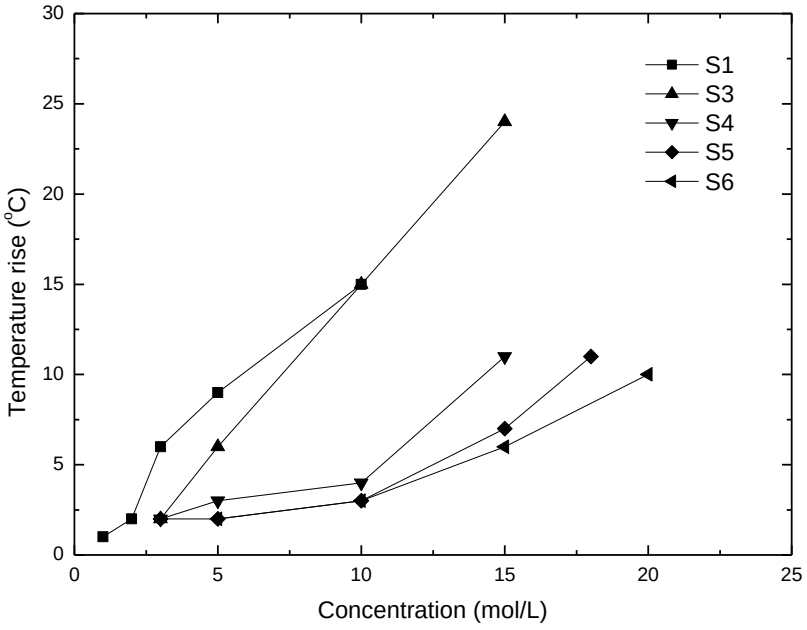

Figure 7-7 Maximum temperature rise with different methanol concentrations and structures

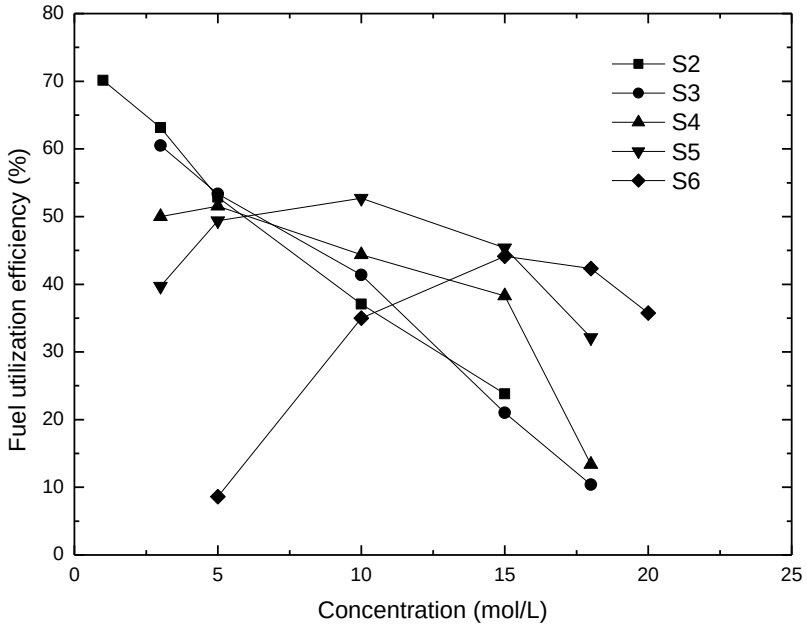

Figure 7-8 Fuel efficiency versus methanol solution concentration

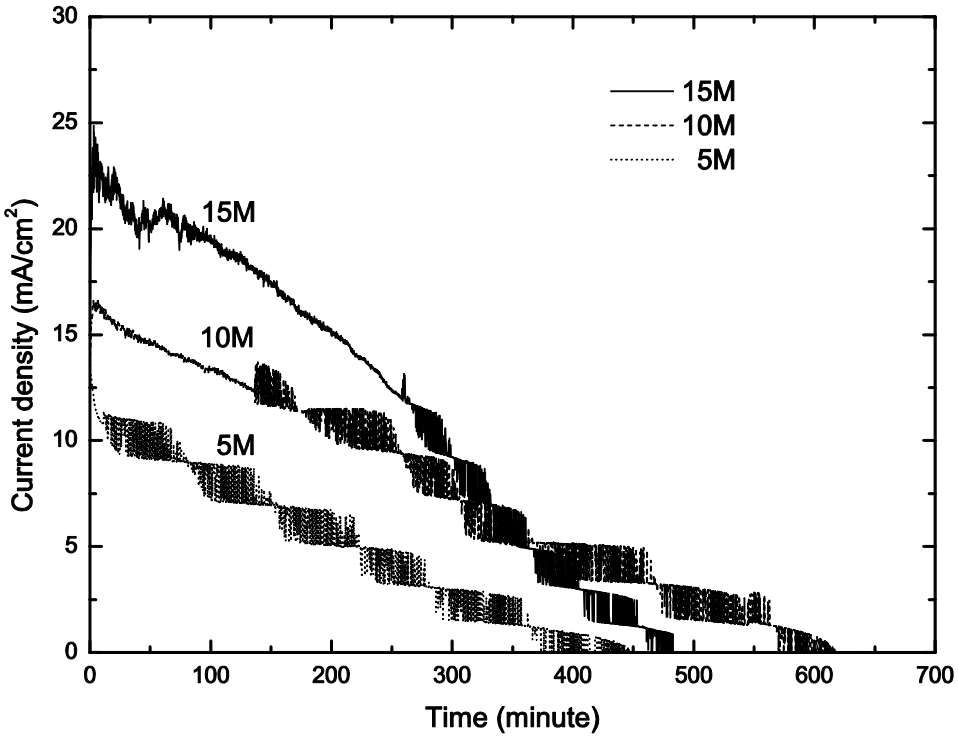

Figure 7-9 Constant voltage discharge with the same strucutre under different methanol concentrations

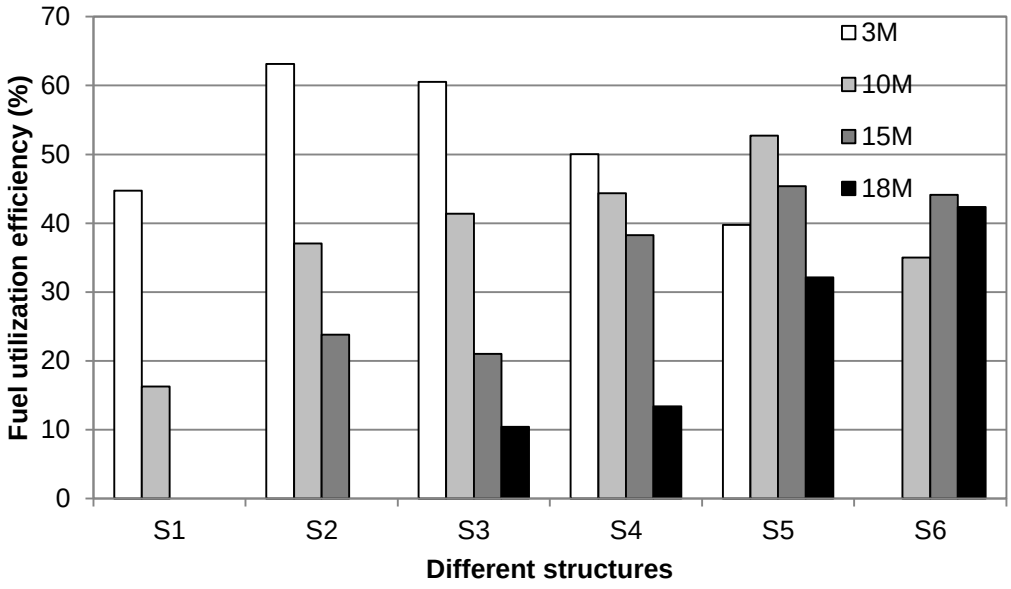

Figure 7-10 Fuel efficiency versus anode structure

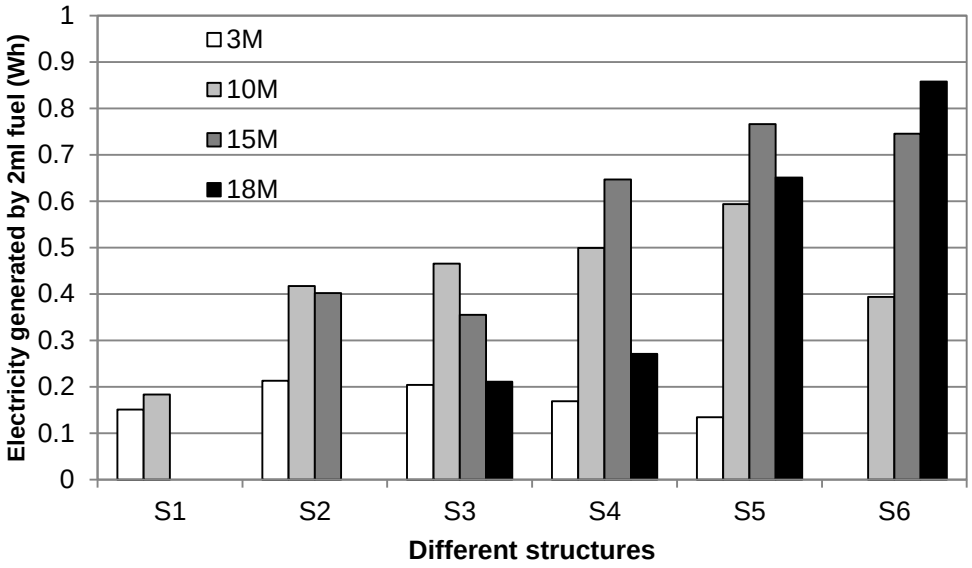

Figure 7-11 Electricity generated by 2 ml methanol solution at 0.35 V